Development of a Novel Detector Response Formulation and Algorithm in RAPID and its Benchmarking

Meng-Jen Wang

Dissertation submitted to the faculty of
Virginia Polytechnic Institute and State University
in partial fulfillment of the requirements for the degree of

Doctor of Philosophy
in
Nuclear Engineering

Alireza Haghighat, Chair
Céline Hin
Glenn E. Sjoden
Roop L. Mahajan
Yang Liu

September 17, 2019
Falls Church, Virginia

Keywords: Particle Transport Theory, Real-time, Detector Response Function Methodology, Pressure Vessel Fluence Calculations, Dosimeter/Detector Response, Dry Storage Cask External Dosimetry

Development of a Novel Detector Response Formulation and Algorithm in RAPID and its Benchmarking

Meng-Jen Wang

(ABSTRACT)

Solving radiation shielding problems, i.e. deep penetration problems, is a challenging task from both computation time and resource aspects in field of nuclear engineering. This is mainly because of the complexity of the governing equation for neutral particle transport - Linear Boltzmann Equation (LBE). The LBE includes seven independent variables with presence of integral and differential operators. Moreover, the low successive rate of radiation shielding problem is also challenging for solving such problems.

In this dissertation, the Detector Response Function (DRF) methodology is proposed and developed for real-time and accurate radiation shielding calculation. The real-time capability of solving radiation shielding problem is very important for: (1) Safety and monitoring of nuclear systems; (2) Nuclear non-proliferation; and (3) Sensitivity study and Uncertainty quantification. Traditionally, the difficulties of solving radiation problem are: (1) Very long computation time using Monte Carlo method; (2) Extremely large memory requirement for deterministic method; and (3) Re-calculations using hybrid method. Among all of them, the hybrid method, typically Monte Carlo + deterministic, is capable of solving radiation shielding problem more efficiently than either Monte Carlo or deterministic methods. However, none of the aforementioned methods are capable of performing "real-time" radiation shielding calculation.

Literature survey reveals a number of investigation on improving or developing efficient methods for radiation shielding calculation. These methods can be categorized by: (1) Using variance reduction techniques to improve successive rate of Monte Carlo method; and (2) Developing numerical techniques to improve convergence rate and avoid unphysical behavior for deterministic method. These methods are considered clever and useful for the radiation transport community. However, real-time radiation shielding calculation capability is still missing although the aforementioned advanced methods are able to accelerate the calculation efficiency significantly. In addition, very few methods are "Physics-based"

For example, the mean free path of neutrons are typically orders of magnitude smaller than a nuclear system, i.e. nuclear reactor. Each individual neutron will not travel too far before its history is terminated. This is called the "loosely coupled" nature of nuclear systems. In principle, a radiation shielding problem can be potentially decomposed into pieces and solved more efficient. In the DRF methodology, the DRF coefficients are pre-calculated with dependency of several parameters. These coefficients can be directly coupled with radiation source calculated from other code system, i.e. RAPID (Real-time Analysis for Particle transport and In-situ Detection) code system. With this arrangement, detector/dosimeter response can be calculated on the fly.

Thus far, the DRF methodology has been incorporated into the RAPID code system, and applied on four different benchmark problems: (1) The GBC-32 Spent Nuclear Fuel (SNF) cask flooded with water with a ^{3}He detector placed on the cask surface; (2) The VENUS-3 experimental Reactor Pressure Vessel (RPV) neutron fluence calculation benchmark problem; (3) RPV dosimetry using the Three-Mile Island Unit-1 (TMI-1) commercial reactor; and (4) A Dry storage SNF cask external dosimetry problem.

The results show that dosimeter/detector response or dose value calculations using the DRF methodology are all within 2σ relative statistical uncertainties of MCNP5 + CADIS (Consistent Adjoint Driven Importance Sampling) standard fixed-source calculation. The DRF methodology only requires order of seconds for the dosimeter/detector response or dose value calculations using 1 processor if the DRF coefficients are appropriately prepared. The DRF coefficients can be reused without re-calculations when a model configuration is changed. In contrast, the standard MCNP5 calculations typically require more than an hour using 8 processors, even using the CADIS methodology. The DRF methodology has enabled the capability of real-time radiation shielding calculation.

The radiation transport community can be greatly benefited by the development of DRF methodology. Users can easily utilize the DRF methodology to perform parametric studies, sensitivity studies, and uncertainty quantifications. The DRF methodology can be applied on various radiation shielding problems, such as nuclear system monitoring and medical radiation facilities. The appropriate procedure of DRF methodology and necessary parameters on DRF coefficient dependency will be discussed in detail in this dissertation.

Development of a Novel Detector Response Formulation and Algorithm in RAPID and its Benchmarking

Meng-Jen Wang

(GENERAL AUDIENCE ABSTRACT)

Since the beginning of nuclear era, enormous amount of radiation applications have been proposed, developed, and applied in our daily life. The radiation is useful and beneficial when they are under control. However, there will be some "unwanted radiation" from these applications, which have to be shielded. For this, radiation shielding has become a very important task. To effectively shield the unwanted radiations, studying the thickness and design of the shields is important. Instead of directly performing experiments, computation is a more affordable and safer approach. The radiation shielding computation is typically an extremely difficult task due to very limited "communication" between the radiation within the shield and detector outside the shield. In general, it is impractical to simulate the radiation shielding problems directly because the extremely expensive computation resources. Most of interactions of radiation are within the shield while we are only interested in how many of them penetrate through the shield. This is typically called "deep penetration" problems in the radiation transport community.

Since it is almost impossible to directly simulate the radiation shielding problem, scholars in this field have proposed and developed various approaches for performing more efficient radiation shielding calculations. These techniques are either using numerical techniques to accelerate the calculation efficiency or biasing the physics but preserving the outcome when performing calculations. However, none of these techniques are capable of performing online examination of nuclear systems with real-time radiation shielding calculations. The radiation shielding calculations, even with current advanced techniques, typically require order of hours or days using parallel computation. Moreover, if the system configuration is changed, i.e. shuffling the nuclear fuel assemblies or changing detector locations, the whole computation process has to be re-performed. This will be impractical for examining some large nuclear system, such as Spent Nuclear Fuel (SNF) pool or commercial nuclear reactor. Therefore, an accurate and fast radiation shielding calculation algorithm is needed.

In this dissertation, a Physics based method - Detector Response Function (DRF) methodology is proposed and developed for enabling real-time radiation shielding calculation capability. The new methodology cleverly quantifies and bypasses the unimportant segments of radiation shielding problems, which are making negligible contribution to the outcome, i.e. dose or dosimeter/detector response. In the DRF methodology, the radiation shielding problems are divided into stages. A series of physical quantities, i.e. the DRF coefficients, are pre-calculated depending on various parameters. Similar to different size of nails, the nails are pre-manufactured with different sizes and will be used on different purposes, such

as hanging a paint on wall. Since the size, geometry, and most of the materials of a nuclear system, such as a nuclear reactor, are determined at the first place, the DRF coefficients are pre-calculated for a specific system. These coefficients can be reused and no re-calculations are required.

The results show that excellent agreement is observed between the traditional Monte Carlo fixed-source calculation method and the DRF methodology. Real-time capability is enabled with the DRF methodology. The DRF methodology calculates the detector/dosimeter response or dose with order of seconds using 1 computer processor while the traditional method requires at least few hours using 8 computer processors. This provides an excellent capability for online nuclear system examination.

Acknowledgments

For my 5 years of doctoral student career, I am truly thankful and happy it has come to the end with a fruitful outcome. First, I would like to thank my academic advisor, Professor Alireza Haghighat, for his patience, tremendous help on my research, and the constant encouragement. Through his guidance, my knowledge in particle transport has been elevated to the level that I have never expected. I would also like to express my gratitude to my committee members, Dr. Roop L. Mahajan from Mechanical Engineering Department, for his patient and helpful mentoring on how to become a good researcher and a better person, Dr. Glenn E. Sjoden from University of Utah, for providing very helpful comments on my work, and Drs. Yang Liu and Céline Hin for participating my preliminary and final defense.

I would like to express my sincere gratitude to my colleagues, Dr. Nathan J. Roskoff, for providing tremendous help on both research and life when I firstly joined the VT^3G as roommate and colleague, Mr. Valerio Mascolino, for providing a lot of good comments and help on this dissertation at the early stage, and Dr. William Walters, for providing consultant on the RAPID code system. Also, I would like to give my thanks to Mr. James (Jimmy) M. Butler, Mr. Jacob Bartel, Mr. Quinn Dircks, and Mr. Mohsen Hosseinian, for providing chance for me to learn how to guide young researchers in their early stage, also the encouragement and warm atmosphere you have created in in the office. Also, I would like to thank for Mr. Jiong-Ting Wu, Mr. Congchao Wang, Ms. Lulu Chen, and Ms. Debbie Change from the ECE Department, for support from the friendship during my graduate career.

I would like to give thanks to Mr. James (Jim) Murphy from the TLOS team, for mentoring me on learning the sense of humor, and providing help during my difficult time. Also, thanks for the members of TLOS team, Ms. Fanglan Chen, Mr. Abdulaziz Alhamadani, Mr. Usman Shaikh, Mr. Rene Fabrega, Ms. Aizhan Sheraliyeva, Mrs. Farida Mohamed, and Mr. Zhiqian Chen, for the support from friendship during the time working with you.

I would also like to express a big gratitude to the one who always encourage me, Dr. I-Chen Lee, for her constant encouragement and support during my doctoral student career.

I am very thankful for my parents, Mr. Kung-Yin Wang and Mrs. Yueh-Li Lai Wang, and grandparents, Mr. Jui-Rong Wang and Mrs. Jin-Chen Cheng Wang, for their love and

constant support not only during my doctoral student life, but also in my life as a whole. Without their support, my dream of studying abroad will never come true.

I also would like to express my gratitude to all the brothers and sisters from Church in Dunn Loring, Church in Fairfax, and Church in Washington DC. Without the connection with the saints, the life will definitely become miserable here. I truly thank God for having you around me.

Finally, I thank God for all the arrangement on me, and let me have the wisdom to finish the dissertation. I would always take the verse as a reminder for myself: "Knowledge puffs up, but love builds up" 1 Corinthians 8:1.

Contents

List of Figures

List of Tables

Chapter 1

Introduction

In this dissertation, a new radiation shielding calculation algorithm - Detector Response Function (DRF) methodology is proposed and developed. The DRF methodology is capable of performing accurate, efficient, and real-time (online) radiation shielding calculations. The real-time capability is very important from various aspects such as: (1) Safety of commercial nuclear reactor operation; and (2) Safety of radiation workers; and (3) Nuclear non-proliferation. Note that the real-time here is defined as seconds and minutes. It means to enable the online computational examination to nuclear systems.

1.1 Motivation

The radiation transport calculation is very important for various applications in the field of nuclear engineering. One of the important application is the radiation shielding calculation. When designing a reactor, we are obviously more interested in how much power can be extracted from the nuclear fuel. However, the following tasks, usually are referring to radiation shielding problems, are always the "by-product" problems that have to be solved:

1. Reactor Pressure Vessel (RPV) Neutron Fluence Calculation
2. Spent Nuclear Fuel Pool Monitoring
3. Spent Nuclear Fuel Cask External Dosimetry

Although they are called "by-product" problems, they are very important from the safety aspect of any nuclear systems, sometime more than power generation. Among all of the problems above, a new methodology is urgently required for RPV neutron fluence calculations recently. The purpose of RPV neutron fluence calculations is monitoring the material aging from radiation bombardment. For the standard 40 years of operation lifetime, the

RPV neutron fluence calculations are commonly performed at beltline region with the maximum neutron flux. The regions with welding and accumulated neutron fluence reaching certain amount, e.g. 10^{17} neutrons/cm^2 [8], at the end of reactor lifetime are especially important. Fig. 1.1 shows an example of a commercial Pressurized Water Reactor (PWR) beltline region.

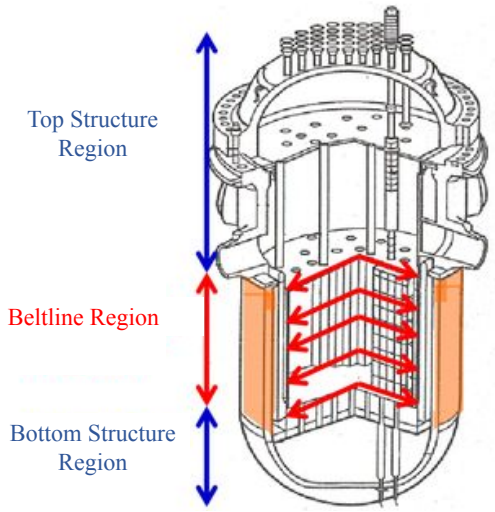

Figure 1.1 Beltline Region for a Pressurized Water Reactor(PWR) [1]

However, some of the commercial nuclear reactors in the U.S. have extended their operation licenses for another 20 to 40 years, which gives total reactor operating lifetime of 60 to 80 years. Potential license extension to lifetime of 80 years is under evaluation [8]. Therefore, neutron fluence calculation on extended regions of the reactor will be important. For this, the widely used calculation methodology for beltline region may suffer from long calculation time and accuracy of the solution. Therefore, a robust and efficient new method is needed.

To perform radiation transport simulations, three approaches are typically used:

1. Deterministic method - Solving the Linear Boltzmann Equation (LBE)
2. Monte Carlo method
3. Hybrid method

The deterministic method discretizes the LBE, and solves it with power iteration technique. The Monte Carlo method does not directly solve the LBE. The physics are represented with probability density functions in this method. By random sampling technique, an averaged system behavior can be obtained with a statistical uncertainty. The hybrid methods are developed for the purpose of more efficient calculation, which can be combinations of the

methods. Pros and cons of all the three methods and the past works will be discussed in this chapter.

Since the LBE has seven independent variables, it is expected that significant amount of computation expense is required no matter which approach is selected. From the past, the approaches for enhancing calculation efficiency are either via numerical techniques or variance reduction techniques. However, these improvements still cannot enable the "real-time" radiation shielding calculation capability.

1.2 Literature Review

There are various applications relying on the solution of the LBE. For this dissertation, the focus is on the radiation shielding problems, which is typically called "***deep penetration***" problems in the community. Obviously, we are not expecting to detect large amount of radiation from outside of a radiation shield. With all the radiation interaction inside the shield, very few of them will penetrate and make contribution to detector/dosimeter responses. Solving the deep penetration problem is challenging no matter which method is selected. This section will briefly introduce the past work of solving deep penetration problems, including methods, issues, and performances. Note that significant amount of effort in the field of radiation shielding calculation was spent on the RPV neutron fluence calculation. Therefore, a large part of literature review will address the RPV neutron fluence calculation.

1.2.1 Comparisons for the Traditional Approaches of Solving Radiation Transport Problems

Traditionally, two approaches for solving radiation transport problems are: (1) Monte Carlo method [2]; and (2) Deterministic method [9]. During the old days, the capability of computers are not as powerful as what we have nowadays. The Monte Carlo method was not widely used due to the expensive computation cost. The deterministic method mainly requires memory rather than CPU resources, and therefore was widely used for solving the radiation transport problems. However, the capability of computer has evolved significantly that the Monte Carlo method can be more affordable than it was in the old days. To compare the two methods, the pros and cons of the both methods are listed in the Table 1.1. Note that the bold fonts represent the advantages of the method.

By the first glance, it is obvious that the Monte Carlo method has more advantages than the deterministic method. However, it is always good to extract as much details as you can for analysis of radiation transport problems. Although the Monte Carlo method has a lot of advantages, limited amount of information is one of the major disadvantage. The deterministic method, in contrast, is capable of providing details.

Table 1.1 Comparison between Monte Carlo and Deterministic Methods

Item	Monte Carlo Method	Deterministic Method
Geometry	**Exact**	Discrete/Exact
Energy Treatment - Cross-section	**Exact**	Discrete
Direction	**Exact**	Discrete
Input Preparation	**Easy**	Difficult
Computer memory	**Small**	Large
Computer time (Expense)	Large	**Relatively Small**
Numerical Issues	Source Convergence	Iterative Convergence
Amount of Information	Small	**Large**
Parallel Processing	**Trivial**	Complex

1.2.2 Methods for Solving the LBE

The most widely used method for solving the LBE is the discrete ordinate method [9]. The discrete ordinate method discretizes the phase spaces into segments, and solve it with power iteration technique. The angular variable is represented by a set of discrete ordinates and associated weights (i.e., angular quadrature). The spatial variable is discretized based on the finite volume or finite element techniques. The energy variable is discretized with a pre-selected energy group structure.

Detailed representation of a 3D model requires significant amount of memory and computer hours. Therefore, for practical applications such as the RPV neutron fluence calculation, techniques such as synthetic method [10] were developed for beltline region calculations.

1.2.2.1 Discrete Ordinate Method Synthetic Method

The 3D discrete ordinate approach may requires significant amount of memory. With limited computation resources in the old day, this is not practical even with approximated geometry. For this, the ASTM (American Society for Testing and Materials) standard [8] and the U.S. NRC (United State Nuclear Regulatory Commission) Regulatory Guide 1.190 [10] suggest that the simple synthetic method [10] can be used. The synthetic method assumes the 3D spatial dependent neutron flux can be decomposed into two independent functions. Furthermore, the following assumptions are also made:

1. The axial source distribution for all important peripheral fuel assemblies is approximately the same or is bounded by a conservative axial power shape.
2. The attenuation characteristics do not vary axially over the region of interest.

By doing this, it is possible to perform multiple 2D calculations to emulate the 3D behavior.

However, the U.S. NRC Regulatory Guide 1.190 indicated that this method may underpredict the result by $5 \sim 10\%$ [10].

When simple synthesis techniques are not applicable, the multichannel synthesis method [10] can be used. The multichannel synthesis method calculates a series of basis flux solution, which typically represents specific region of the core and vessel geometries. A weighting coefficient for each basis flux solution will be calculated for optimizing the prediction of the vessel fluence. However, this method is sensitive to the selection of the basis functions, especially at the region interfaces. The ASTM standard Designation: E2956-14 [8] also indicated that this method might not be appropriate for regions of extended beltline. This approach has been applied to the VENUS-3 experimental benchmark problem [11], which will be used for benchmarking the DRF methodology in this dissertation.

1.2.2.2 Full 3D Discrete Ordinate Method

At the time synthetic method was proposed, the computers were not capable of performing full 3D deterministic calculations. However, the computer nowadays has evolved rapidly that full 3D discrete ordinate neutron transport calculation has become possible. The developments of various code systems have evolved from 1D [12][13][14] and 2D [15][16] to 3D [17][18][19][20][21][22][23]. Currently, the available full 3D discrete ordinate particle transport codes are:

1. THREETRAN (Hex, Z) [17] - A 3D discrete ordinate neutral particle transport code in hexagonal coordinate system. The code was developed by the Los Alamos National Laboratory.

2. TORT [18] - A 3D discrete ordinate neutron/photon transport code with options of Cartesian and cylindrical coordinate. The code is developed by the Oak Ridge National Laboratory (ORNL).

3. THREEDANT [23] - A 3D discrete ordinate code system for neutron/photon transport. The code system is developed by the Los Alamos National Laboratory.

4. PARTISN [19] - A 3D time-dependent semi paralleled neutron/photon particle transport code system with options of Cartesian and cylindrical coordinate. The code system is developed by Los Alamos National Laboratory.

5. TITAN [20] - A hybrid deterministic 3D Cartesian coordinate code system with both Method of Characteristic (MOC) and discrete ordinate. It is capable of performing hybrid deterministic calculation with paralleled capability. The code system was originally developed by Yi [20].

6. PENTRAN^{TM} [21] - A fully paralleled 3D Cartesian coordinate system neutral particle transport code with features of various adaptive differencing scheme. The code system was originally developed by Sjoden [24].

7. DENOVO [22] - A 3D discrete ordinate code system in SCALE package. It is developed by the ORNL to replace the TORT code system.

Although the full 3D discrete ordinate approach is more accurate, there were still some problems remained unsolved at the time. The intrinsic problems due to the phase space discretizations such as ray effect [9], negative flux [25], and flux unphysical oscillation [26] are the disadvantages of the discrete ordinate method.

Several advanced differencing schemes, such as Theta Weighted (TW) in the TORT code system [18], Directional Theta Weighted (DTW) by Petrović and Haghighat [27], Exponential Directional Weighted (EDW) by Sjoden and Haghighat [28], and Exponential Directional Iterative (EDI) by Sjoden [29] are developed from time to time. These techniques are capable of accelerating the iterative convergence, avoiding the negative flux, and alleviating the unphysical oscillation. These advanced differencing scheme will be used in this dissertation, and their theory will be introduced in the theory section.

For the angular variable, the S_N method [9] has been widely used. Several advanced approaches [30][31][32] to increase the accuracy and calculation efficiency have been proposed and developed into different code systems.

For the energy phase space discretization, the multi-group cross-section with conservation of reaction rate by pre-calculated spectrum weighting [33] is widely used. Some advanced method [34] and code system [35][36] for determining appropriate group numbers for radiation shielding calculations has been proposed and developed.

1.2.3 Monte Carlo Method

The Monte Carlo method is capable of performing exact radiation shielding calculations. No approximations are used in the Monte Carlo method, including geometry, cross-sections of material, and angular distribution. The Monte Carlo method does not directly solve the LBE. Instead, it represents the physics by the Probability Density Functions (PDF). Using random sampling technique, an averaged system behavior can be obtained. A statistical uncertainty will be calculated at the end to give a confidence range of the solution. The result of Monte Carlo calculations always has to be examined to guarantee the convergence. For example, if the Central Limit Theorem (CLT) is valid, the trend calculated statistical uncertainty should be proportional to $\frac{1}{\sqrt{N}}$, where N is the number of sample.

1.2.4 Variance Reduction Techniques for the Monte Carlo Method

To perform radiation shielding calculations using Monte Carlo method, one of the difficulty will be large variance even with large amount of sample and long computation wallclock time. The intrinsic physics of deep penetration problem is the low probability of penetration rate. To overcome this issue, variance reduction techniques [2] are proposed. The commonly used variance reduction techniques for the deep penetration problems can be grouped into:

1. Probability Density Function (PDF) biasing - Implicit Capture, Russian Roulette, Path Length Biasing, Exponential Transformation, and Forced Collision
2. Splitting Techniques - Geometry Splitting with Russian Roulette, Energy Splitting with Russian Roulette, Angular Splitting with Russian Roulette, and Weight-Window Techniques

Among all of them, the weight window technique has been used heavily in deep penetration problems. Originally, selection of the appropriate weight windows was mainly replied on user's experiences. However, more advanced technique, such as the Consistent Adjoint Driven Importance sampling (CADIS) methodology [37] has elevated the use of weight window. Selected variance reduction techniques will be discussed in more details in the theory chapter.

1.2.5 Advanced Hybrid Methods

We have discussed the comparison between the Monte Carlo method and deterministic method. Since each of them are with their intrinsic pros and cons, so why not take advantage from the pros and bypass the cons by using "hybrid" method. The hybrid method can be:

1. Deterministic + Deterministic
2. Monte Carlo + Monte Carlo
3. Monte Carlo + Deterministic - the most popular and effective one
4. Physics Based Method (Deterministic + Monte Carlo) - will be discussed in the following section

Example of Deterministic + Deterministic is the TITAN code system [20]. The TITAN code system is capable of performing different deterministic approaches in each coarse mesh unit. It is known that the discrete ordinate method can be not very effective for problem with optically thick material and ratio of within-group scatter to total cross-section ~ 1 [9] while

Method of Characteristic (MOC) [9] may be better for such scenario. By this arrangement, the problem can be solved with a more efficient way.

For the Monte Carlo + Monte Carlo approach, several works has utilized the Monte Carlo approach to obtain the importance function for use of variance reduction. However, the importance function calculation is intrinsically same as forward deep penetration problems. This means that the statistical uncertainties of the calculated importance function will be extremely high except large amount of sampling is performed. For this, Louvin [38][39] has proposed iteratively solving the forward deep penetration with improving the resolution of the importance function at the same time. The calculation efficiency of this approach is better than Monte Carlo calculation without variance reduction. However, the speedup is still not considered significant. Some code systems such as the SERPENT [40] and MCNP [41] have their in-built importance function calculation capability using Monte Carlo method.

The Monte Carlo + Deterministic approach is considered the most popular and effective hybrid method. The development of the Consistent Adjoint Driven Importance sampling (CADIS) methodology [37] has elevated the variance reduction to another level. The CADIS methodology includes two parts: (1) Source Distribution Biasing; and (2) Transport Biasing. Instead of performing analog Monte Carlo simulation with Bernoulli process, the particles are represented by weights. The transport biasing selects the weight of a particle by either splitting or playing particle survival game with Russian Roulette while the source biasing biases the probability density function (*pdf*) of the sampling process. The weight window bounds are determined based on an approximated importance function calculation using the deterministic method. Several code packages have been developed based on the Monte Carlo + Deterministic approach:

1. MCBEND [42] - The code is developed by the United Kingdom. The importance function is calculated using a diffusion theory deterministic solver with corrections. The diffusion solver is developed into the MCBEND code system as a package. The importance function is used for geometry splitting and Russian Roulette of MCBEND Monte Carlo calculation.

2. AVATAR [43] - The code is a processing code developed by the Los Alamos National Laboratory (LANL). The importance function is calculated by the THREEDANT deterministic code [23], converted into weight window bounds, and feed into the MCNP code. Note that angular biasing is applied in this code.

3. A^3MCNP [44] - The code is a processing code developed by Wagner and Haghighat. It is an automated code system using TORT code system [18] for importance function calculation, and MCNP4A for Monte Carlo calculations. The performance of the A^3MCNP is considered excellent in applications of reactor shielding problems [45][46][47].

4. DXTRAN [48] - A built in analytical solver in MCNP6 for determining particle weight for problem with void.

5. ADVANTG [49] - It is a newer version of the A^{3}MCNP developed by Wagner when he worked at the Oak Ridge National Laboratory (ORNL). The theory part of the processing code is exactly the same as A^{3}MCNP, but replace the TORT deterministic code with the DENOVO deterministic code [22]. An extension capability of CADIS - Forward Weighted CADIS (FW-CADIS) [50] has been developed into the code system. Note that the FW-CADIS methodology is developed for global variance reduction.

A recent literature [51] has summarized the Monte Carlo variance reduction development with a preliminary discussion of angular variance reduction. Detailed theory and recent development status can be found in the article. The performance comparisons of different advanced variance reduction methods can be found in another recent article [52].

1.2.6 Physics Based Response Function Method (Deterministic + Monte Carlo)

All the aforementioned methods are either improving the calculation efficiency of the Monte Carlo method using variance reduction techniques or improving convergence performance and speed of the deterministic method. However, none of the techniques are considered "real-time" particle transport calculations. Moreover, radiation transport problems have to be re-calculated if configurations are changed. For this, a new methodology to enable real-time detector/dosimeter response is needed.

Recently, the response function based methodology has been proposed and developed [53][54] [55][56][57]. The response function based methodology is a Physics based methodology. It partitions the radiation transport problem into stages. In each stages, response functions or coefficients are pre-calculated. All the stages can be combined by iteratively or directly solving a linear system of equation using the pre-calculated response functions or coefficients. The coefficients or response functions are typically obtained by performing a 3D heterogeneous Monte Carlo fixed-source radiation transport calculations. The coefficients or response function are a discretized sets of numbers, and will be feed into a deterministic solver. Therefore, this method is intrinsically a Deterministic + Monte Carlo hybrid method. The code systems developed for different purposes are listed below:

1. AIMS-IFLEX [54] (Active Interrogation for Monitoring of Special nuclear materials (SNMs) Incident Flux EXpansion) - For examing cargo that contains Special Nuclear Materials (SNM).

2. INSPCT-s [53] (Inspection of Nuclear Spent fuel-Pool Calculation Tool ver. Spreadsheet) - A Real-time Spent Nuclear Fuel (SNF) system monitoring code system with some approximations on the coefficient calculations for subcritical multiplication calculations.

3. RAPID [56] (Real-time Analysis for Particle-transport and In-situ Detection) - A Real-time nuclear system simulations and monitoring with some clever approach. The clever approaches, which will be discussed in the RAPID code system chapter, is currently designed for Light Water Reactor (LWR) nuclear systems.

4. COMET [57] - An interface current based hybrid method developed by Rahnema and his research group in the Georgia Institute of Technology.

In the past, for detector response calculation, the adjoint (importance function) methodology was used in RAPID. To pre-calculate importance function, the PENTRAN^{TM} deterministic code system is used. To avoid the limitations of the deterministic methods in representing geometry and nuclear data, i.e. nuclear cross-section, this dissertation develops a novel methodology which relies on the determination of an importance function using the forward Monte Carlo simulation.

1.3 Objective and Scope

In this dissertation, the Detector Response Function (DRF) methodology is proposed and developed for enabling accurate real-time radiation shielding calculations. The content of following chapters are:

- Chapter 2 - The theory that supports the DRF methodology development will be introduced. This chapter will include a detailed discussion on the deterministic method, Monte Carlo method, and some advanced techniques for solving radiation shielding calculations. Since radiation source is required for shielding calculations, approaches to calculate radiation source will also be discussed.

- Chapter 3 - Since the DRF methodology is incorporated into the RAPID code system, it is important to discuss the structure of RAPID code system. The advantages and current limitations of RAPID code system will be discussed in this section.

- Chapter 4 - The theory and procedures of the DRF methodology will be introduced and discussed. Some sensitivity and uncertainty parameters for DRF methodology will also be discussed. Here, we mainly apply the DRF methodology on the RPV surveillance and SNF cask external detection. The sensitivity and uncertainty parameters will be selected based on these systems.

- Chapter 5 - A mock up benchmark problem with the GBC-32 SNF Cask flooded with water and a ^{3}He detector placed on the external surface of the cask will be studied. This study is mainly for demonstration of the DRF methodology.

- Chapter 6 - It is important to compare calculations with experiments for a new methodology. For this, the DRF methodology will be applied on the experimental RPV surveillance benchmark problem VENUS-3.
- Chapter 7 - After experimental and computational benchmark, the DRF methodology will be applied on the TMI-1 commercial PWR RPV surveillance.
- Chapter 8 - A dry storage SNF cask will be used for external dosimetry benchmark study. This section will include a comprehensive study on the dry storage cask external dosimetry using the DRF methodology.
- Chapter 9 - This chapter will summarize and give a guidance for use of DRF methodology.
- Chapter 10 - Conclusion of this dissertation will be made.
- Chapter 11 - Potential future work will be introduced.

The objective of this dissertation is to generalize the DRF methodology and give a guideline for applications of any radiation shielding problem.

Chapter 2

Theory

The theory supporting the development of the DRF methodology will be presented in this chapter. For radiation transport calculations, the governing equation is the Linear Boltzmann Equation (LBE) [9]. Three forms of LBE for neutrons will be discussed: (1) Eigenvalue; (2) Subcritical Multiplication; and (3) Fixed source. Briefly, the LBE for photon transport will be discussed also. Both forward LBE and importance equation [58] will be discussed with the application of their solutions for detector/dosimeter response calculations. Note that the detector response is used for radiation detector while dosimeter response is used for dosimeters. Detailed approaches to solve the LBE and their issues and advantages will also be discussed in this chapter.

2.1 Forward Linear Boltzmann Equation for Neutron

The general form of forward time-independent (or steady-state) LBE for neutron is shown by the Eq.(2.1). It represents the particle balance within phase space $d^3rdEd\Omega$, shown in the Fig. 2.1, at position $\underline{r}$, direction $\hat{\Omega}$, and energy E.

$$\underbrace{\hat{\Omega}\cdot\nabla\psi(\underline{r},E,\hat{\Omega})}_{1}+\underbrace{\sigma(\underline{r},E)\psi(\underline{r},E,\hat{\Omega})}_{2}=\underbrace{S(\underline{r},E,\hat{\Omega})}_{3} \tag{2.1}$$

where $\psi(\underline{r},E,\hat{\Omega})$ is the forward angular flux at position $\underline{r}$, direction $\hat{\Omega}$, and energy E.

The above three terms are described below:

1. Particle streaming term - it describes the loss of particle by leakage from the phase space $d^3rdEd\Omega$ at position $\underline{r}$, direction $\hat{\Omega}$, and energy E

2. Collision term - It describes the particle loss due to the collision process from the phase

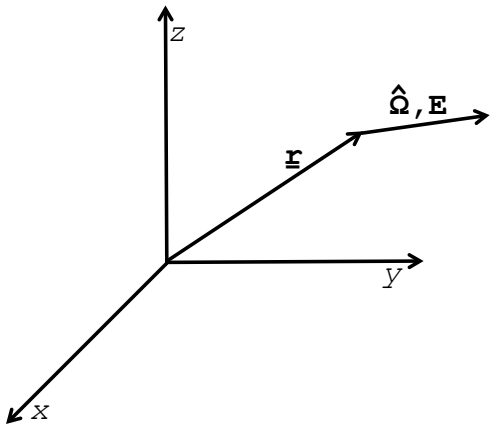

Figure 2.1 Phase Space of LBE.

space $d^3rdEd\Omega$ at position $\underline{r}$, direction $\hat{\Omega}$, and energy E

3. Source term - It describes the gain of particle in the phase space $d^3rdEd\Omega$ at position $\underline{r}$, direction $\hat{\Omega}$, and energy E

The source $S(\underline{r}, E, \hat{\Omega})$ represents the total production of particles from independent angular sources, scattering, and fission. Eq.(2.2) shows the form of the source for subcritical multiplication

$$S(\underline{r}, E, \hat{\Omega}) = \int_0^\infty dE' \int_{4\pi} d\Omega' \sigma_s(\underline{r}, E' \to E, \hat{\Omega}' \to \hat{\Omega}) \psi(\underline{r}, E', \hat{\Omega}') + \frac{\chi(\underline{r}, E)}{4\pi} \int_0^\infty dE' \nu(E') \sigma_f(\underline{r}, E') \phi(\underline{r}, E') + q(\underline{r}, E, \hat{\Omega}), \tag{2.2}$$

where $\sigma_s(\underline{r}, E' \to E, \hat{\Omega}' \to \hat{\Omega})$ is the differential macroscopic scattering cross-section for a particle of energy E' and traveling in direction of $\hat{\Omega}'$ scattering into dE at energy E and solid angle $d\Omega$ in direction of $\hat{\Omega}$, the $\hat{\Omega}' \to \hat{\Omega} = \hat{\Omega} \cdot \hat{\Omega}' = \mu_0$, which is the product between angles of before and after scattering, $\nu(E)\sigma_f(\underline{r}, E')$ is the fission cross-section multiplied by the number of fission neutrons produced per fission, $\chi(\underline{r}, E)$ is the fission spectrum, i.e, the probability density function for fission neutron energy, $q(\underline{r}, E, \hat{\Omega})$ is the independent particle source and the scalar flux is defined by

$$\phi(\underline{r}, E) = \int_{4\pi} d\Omega \psi(\underline{r}, E, \hat{\Omega}). \tag{2.3}$$

The first term in Equation (2.2) represents particles from all other energies and angles $dE'd\hat{\Omega}'$ that scatter into the phase space of interest $dEd\hat{\Omega}$. The second term represents

fission neutrons born in dE due to induced fissions at all neutron energies. If the system is a non-multiplying system, the source term will be

$$S(\underline{r}, E, \hat{\Omega}) = \int_0^\infty dE' \int_{4\pi} d\Omega' \sigma_s(\underline{r}, E' \to E, \hat{\Omega}' \to \hat{\Omega}) \psi(\underline{r}, E', \hat{\Omega}') + q(\underline{r}, E, \hat{\Omega}). \tag{2.4}$$

If we want to determine how far is the system from nuclear critical state, the source term will be

$$\begin{aligned} S(\underline{r}, E, \hat{\Omega}) = \int_0^\infty dE' \int_{4\pi} d\Omega' \sigma_s(\underline{r}, E' \to E, \hat{\Omega}' \to \hat{\Omega}) \psi(\underline{r}, E', \hat{\Omega}') \\ + \frac{1}{k_{eff}} \frac{\chi(\underline{r}, E)}{4\pi} \int_0^\infty dE' \nu(E') \sigma_f(\underline{r}, E') \phi(\underline{r}, E'), \end{aligned} \tag{2.5}$$

where k_{eff} is the system multiplication factor, which the physical interpretation is

1. $k_{eff} < 1$ - Subcritical System
2. $k_{eff} = 1$ - Critical System
3. $k_{eff} > 1$ - Super Critical System

Typically, the independent neutron source term, $q(\underline{r}, E, \hat{\Omega})$, becomes negligible if $k_{eff} \geq 1$. Note that Eq. (2.5) is typically called the eigenvalue form of the LBE.

2.2 Neutron Importance Equation

The neutron importance equation is similar to the mathematical adjoint of LBE, which is valid with vacuum BC. The importance equation is expressed by

$$\underbrace{-\hat{\Omega} \cdot \nabla \psi^*(\underline{r}, E, \hat{\Omega})}_{1} + \underbrace{\sigma(\underline{r}, E) \psi^*(\underline{r}, E, \hat{\Omega})}_{2} = \underbrace{S^*(\underline{r}, E, \hat{\Omega})}_{3} \tag{2.6}$$

where $\psi^*(\underline{r}, E, \hat{\Omega})$ is the angular importance function at position $\underline{r}$, direction $\hat{\Omega}$, and energy E.

Similar to the forward LBE, the terms 1, 2, and 3 in the Eq.(2.6) are particle streaming, collision, and source terms, respectively. The importance source $S^*(\underline{r}, E, \hat{\Omega})$ represents the total

production from independent angular importance sources, scattering, and fission. Eq.(2.10) shows the form of the angular importance source in general form

$$S^*(\underline{r}, E, \hat{\Omega}) = \int_0^\infty dE' \int_{4\pi} d\Omega' \sigma_s(\underline{r}, E \to E', \hat{\Omega} \to \hat{\Omega}') \psi^*(\underline{r}, E', \hat{\Omega}') + \frac{\nu(E)\sigma_f(\underline{r}, E)}{4\pi} \int_0^\infty dE' \chi(\underline{r}, E') \phi^*(\underline{r}, E') + q^*(\underline{r}, E, \hat{\Omega}), \tag{2.7}$$

where $\sigma_s(\underline{r}, E \to E', \hat{\Omega} \to \hat{\Omega}')$ is the macroscopic differential scattering cross-section for a particle's importance to energy E' and direction $\hat{\Omega}'$ with its original energy E and direction $\hat{\Omega}$, $\nu(E)\sigma_f(\underline{r}, E)$ is the number of particle per fission multiplied by the fission cross-section at location $\underline{r}$ and energy E, $\chi(\underline{r}, E')$ is the fission spectrum at energy E', this means the importance of particle created by fission process isotropically at energy E has an importance of $\phi^*(\underline{r}, E')$ to the particle produced at energy E', $q^*(\underline{r}, E, \hat{\Omega})$ is the independent angular importance source and the scalar importance function is defined by

$$\phi^*(\underline{r}, E) = \int_{4\pi} d\Omega \psi^*(\underline{r}, E, \hat{\Omega}). \tag{2.8}$$

Similar to Eq. (2.4), the angular importance source term for non-multiplying system will be

$$S^*(\underline{r}, E, \hat{\Omega}) = \int_0^\infty dE' \int_{4\pi} d\Omega' \sigma_s(\underline{r}, E \to E', \hat{\Omega} \to \hat{\Omega}') \psi^*(\underline{r}, E', \hat{\Omega}') + q^*(\underline{r}, E, \hat{\Omega}), \tag{2.9}$$

Similar to Eq. (2.5), the source of eigenvalue form for importance equation can be written by

$$S^*(\underline{r}, E, \hat{\Omega}) = \int_0^\infty dE' \int_{4\pi} d\Omega' \sigma_s(\underline{r}, E \to E', \hat{\Omega} \to \hat{\Omega}') \psi^*(\underline{r}, E', \hat{\Omega}') + \frac{1}{k^*_{eff}} \frac{\nu(E)\sigma_f(\underline{r}, E)}{4\pi} \int_0^\infty dE' \chi(\underline{r}, E') \phi^*(\underline{r}, E'), \tag{2.10}$$

where k^*_{eff} is the eigenvalue for the importance equation, which is same to the k_{eff} in Eq. (2.5) for the fundamental mode. The physical interpretation is exactly the same as well.

2.3 Linear Boltzmann Equation for Photon

So far, we have discussed the forward LBE and importance equation for neutrons. For photon transport, the LBE is similar, except (1) there will be no fission term; and (2) the scattering

term will be expressed in a different form. The time independent photon LBE [59] can be written by

$$\hat{\Omega}\cdot\nabla\psi_\gamma(\underline{r},\lambda,\hat{\Omega})+\sigma_\gamma(\underline{r},\lambda)\psi_\gamma(\underline{r},\lambda,\hat{\Omega})=S_\gamma(\underline{r},\lambda,\hat{\Omega})+\int_{\lambda'}d\lambda'\int_{\Omega'}d\Omega' K(\underline{r},\lambda'\to\lambda,\hat{\Omega}'\to\hat{\Omega})\psi_\gamma(\underline{r},\lambda',\hat{\Omega}'), \tag{2.11}$$

where $\psi_\gamma(\underline{r},\lambda,\hat{\Omega})$ is the angular photon flux, the $S_\gamma(\underline{r},\lambda,\hat{\Omega})$ is the angular independent photon source, the $K(\underline{r},\lambda'\to\lambda,\hat{\Omega}'\to\hat{\Omega})$ is the photon scattering kernel. According to the Klien-Nishina Theory [60], the scattering kernel can be written by

$$K(\underline{r},\lambda'\to\lambda,\hat{\Omega}'\to\hat{\Omega})=\frac{m_e c}{h}\rho\frac{N_A}{A}Z\pi r_e^2(\frac{\tilde{\lambda}'}{\tilde{\lambda}})[\frac{\tilde{\lambda}}{\tilde{\lambda}'}+\frac{\tilde{\lambda}'}{\tilde{\lambda}}-(1-\mu^2)]\frac{1}{2\pi}\delta(1+\tilde{\lambda}'-\tilde{\lambda}-\mu), \tag{2.12}$$

where

1. $\tilde{\lambda}=\dfrac{\lambda h}{m_e c}$, $\tilde{\lambda}'=\dfrac{\lambda' h}{m_e c}$;
2. $\lambda=\dfrac{hc}{E}$, $\lambda'=\dfrac{hc}{E'}$, which is the wavelength of the photon after and before scattering that corresponding to the energy E and E';
3. $r_e=\dfrac{e^2}{m_e c}\sim 2.81777\times10^{-13}$ cm is the classical electron radius, m_e is the classical electron mass, c is the speed of light;
4. ρ is the material density, A is the material atomic number, N_A is the Avogadro constant;
5. μ is the cosine projection of the solid angle $\hat{\Omega}$.

Note that the term $\dfrac{1}{2\pi}\delta(1+\tilde{\lambda}'-\tilde{\lambda}-\mu)$ is the energy conserving Dirac delta function, which maintains the one-to-one correspondence final wavelength λ and initial wavelength λ'.

The importance equation for photon can be written by

$$-\hat{\Omega}\cdot\nabla\psi^*_\gamma(\underline{r},\lambda,\hat{\Omega})+\sigma_\gamma(\underline{r},\lambda)\psi^*_\gamma(\underline{r},\lambda,\hat{\Omega})=S^*_\gamma(\underline{r},\lambda,\hat{\Omega})+\int_{\lambda'}d\lambda'\int_{\Omega'}d\Omega' K(\underline{r},\lambda\to\lambda',\hat{\Omega}\to\hat{\Omega}')\psi^*_\gamma(\underline{r},\lambda',\hat{\Omega}'), \tag{2.13}$$

where the ψ^*_γ is the photon angular importance function, the $S^*_\gamma(\underline{r},\lambda,\hat{\Omega})$ is the angular photon importance source. Note that there is a minus sign in the first streaming term, and the final and initial photon wavelengths in the scattering kernel are reversed.

2.4 Deterministic Methods for Solving the LBE

The deterministic method requires discretization on phase spaces from the LBE. Two methods are widely used: (1) Method of Characteristic (MOC) [61]; and (2) Discrete ordinate (or S_N) method [9]. The MOC is based on integral transport equation [9]. It is typically used for core lattice physics calculations, and usually used for cross-section collapsing. However, the MOC will not be used in this dissertation, and therefore will not be discussed. In this section, we will be focusing on the discrete ordinate method. The approaches on energy, angle, and space discretizations will be discussed.

2.4.1 The Discrete Ordinate Method

In the discrete ordinate method, the angle is discretized. Each direction is given a weight for achieving integral quantities such as moments of angular fluxes. The integration of the angular flux will be preserved by the weights. In the following three sections, methods for generation of discrete ordinates and their weights, and techniques for spatial and energy discretizations are discussed.

2.4.1.1 Energy

The energy variable is discretized using the multi-group approach [9]. The multi-group method integrates the LBE with an energy group g, the multi-group angular flux can be expressed by:

$$\psi_g(\underline{r},\hat{\Omega}) = \int_{E_g}^{E_{g-1}} dE\psi(\underline{r},E,\hat{\Omega}) \tag{2.14}$$

where the range of energy group g is from E_g to E_{g-1}.

Similarly, the angular multi-group importance functions and other terms in Eq.(2.1) and (2.6) can be obtained with the same approach. However, all the terms with multi-group form can be simply obtained by integration except the cross-sections. This is mainly because a multi-group expression of cross-section requires angular flux distribution to preserve reaction rates by:

$$\sigma_g(\underline{r}) = \frac{\int_{E_g}^{E_{g-1}} dE \int_{4\pi} d\Omega\sigma(\underline{r},E)\psi(\underline{r},E,\hat{\Omega})}{\int_{E_g}^{E_{g-1}} dE \int_{4\pi} d\Omega\psi(\underline{r},E,\hat{\Omega})} \tag{2.15}$$

Assuming a reactor with homogeneous core, if we only looking into the core multi-group

cross-section, Eq.(2.15) can be re-written by

$$\sigma_g^C = \frac{\int_{V_{core}} dV \int_{E_g}^{E_{g-1}} dE \int_{4\pi} d\Omega \sigma(E) \psi(\underline{r}, E, \hat{\Omega})}{\int_{V_{core}} dV \int_{E_g}^{E_{g-1}} dE \int_{4\pi} d\Omega \psi(\underline{r}, E, \hat{\Omega})} \tag{2.16}$$

where V_{core} is the reactor core volume, σ_g^C is the multi-group cross-section for energy group g for reactor core.

The denominator of the Eq.(2.16) without energy integration can be written by

$$\int\limits_{V_{core}} dV \int\limits_{4\pi} d\Omega \psi(\underline{r}, E, \hat{\Omega}) = f(E) \tag{2.17}$$

where the $\int\limits_{E_g}^{E_{g-1}} dE f(E)$ is typically a pre-calculated multi-group spectrum with finer group structures or approximated continuous distribution (i.e. Maxwelliam distribution for thermal range) for specific purpose. The BUGLE-96 data library [62] is an example of collapsed multi-group cross-section data library using pre-calculated spectrum 1-D PWR or BWR model. It is assumed that spectrum of Light Water Reactor (LWR) are similar. Therefore, the pre-calculated spectrum can be applied to most of the LWR problems.

2.4.1.2 Angle

For the angular variable, two approaches can be found from literatures: (1) P_N method [58]; and (2) S_N method [9]. The P_N method expands the angular variable with polynomial while S_N method discretizes the angles into pieces and calculates their associated weights by conservation law. The weights of discretized angles are called "quadrature sets". These values are selected such that the integral quantities of the angular flux are preserved. The P_N method requires significant amount of memory to preserve the angular flux with vacuum boundary condition. Therefore, P_N method is rarely used.

The most widely-used method to calculate the angular quadrature sets is the Level-Symmetry method [9]. However, literatures have indicated that part of the quadrature sets may become negative if more than S_{20} is selected [31]. For this, the Legendre-Chebyshev (or P_N-T_N) method is proposed and developed [31]. The quadrature sets calculated by P_N-T_N method can be as high as the user wants without negative weights. Some adaptive angular quadrature sets selection algorithm has also been developed for more efficient computation [30][32].

2.4.1.3 Space

The space variable can be discretized by different approaches such as finite element method or finite volume method. In this dissertation, the finite volume method will be used and

therefore will be discussed. Here, the remaining question is the spatial distribution of the flux within a finite volume (or mesh/cell). This is typically referred to the spatial differencing scheme. Appropriate differencing scheme is important for accurately represent the flux behavior. In deep penetration problem, the flux distribution will be close to exponential drop. False selection on the differencing scheme may leads to unconverged, even diverged solution.

The simplest spatial differencing method is the Diamond Difference (DD) scheme [9]. The DD scheme simply balance the cell-centered point flux by equally weighted flux from two surfaces of the cell. However, this may leads to negative flux and unphysical oscillation [26]. For this, Lathrop and Brinkley [63] proposed the "zero-fixup" (or "linear-zero") method by simply adjusting the negative flux to zero, and perform the sweeping process again based on the assumption. Later in 1982, Rhode and Childs [15] developed a weighted differencing scheme, which typically referred as "$\theta-$weighted" scheme. Instead of balance the cell-centered point flux by equal weights, the θ value is selected from 0 to 1 for optimizing the cell-centered point flux balance. The performance of the $\theta-$weighted differencing scheme is better than the DD and zero-fixup scheme, but not yet optimized. The θ value has to be selected manually, which is inconvenience for users.

After the development of $\theta-$weighted scheme, Petrovič and Haghighat [27] developed the "Directional $\theta-$Weighted" (DTW) differencing scheme. The DTW scheme is able to automatically select the $\theta-$ depending on the flux distribution. The method is not only convenient to use, but also alleviates the problems of unphysical oscillation and negative flux.

Although the DTW scheme is considered robust, it is still a linear differencing scheme, which might not be able to handle some extreme condition with very sharp slope, such as exponential function. For this, Sjoden and Haghighat developed the Exponential Directional Weighted (EDW) scheme [28]. The EDW uses the DTW scheme to predict a solution that is later corrected by an exponential fit. The EDW scheme is more stable and accurate than DTW alone. Further development by Sjoden on Exponential Directional Iterative (EDI) scheme [29] has improved the constants prediction in EDW scheme.

The general mathematical formulation of finite volume method differencing scheme can be written by

$$\psi_{n,i,j,k} = a_{n,i,j,k}\psi_{n,i+\frac{1}{2},j,k} + (1 - a_{n,i,j,k})\psi_{n,i-\frac{1}{2},j,k} \tag{2.18}$$

$$\psi_{n,i,j,k} = b_{n,i,j,k}\psi_{n,i,j+\frac{1}{2},k} + (1 - b_{n,i,j,k})\psi_{n,i,j-\frac{1}{2},k} \tag{2.19}$$

$$\psi_{n,i,j,k} = c_{n,i,j,k}\psi_{n,i,j,k+\frac{1}{2}} + (1 - c_{n,i,j,k})\psi_{n,i,j,k-\frac{1}{2}} \tag{2.20}$$

where $\psi_{n,i,j,k}$ is the discretized angular flux in direction n, and cell location i, j, k, $a_{n,i,j,k}$, $b_{n,i,j,k}$, $c_{n,i,j,k}$ are the coefficient to be determined by differencing scheme, $\psi_{n,i+\frac{1}{2},j,k}$ and $\psi_{n,i-\frac{1}{2},j,k}$ are the outgoing and incoming angular flux in x direction, $\psi_{n,i,j+\frac{1}{2},k}$, $\psi_{n,i,j-\frac{1}{2},k}$, $\psi_{n,i,j,k+\frac{1}{2}}$ and $\psi_{n,i,j,k-\frac{1}{2}}$ are the same things except for y and z directions, Fig. 2.2 shows

an example of one computation cell with its incoming and outgoing angular flux $\psi_{n,i,j,k}$. Typically, the outgoing fluxes are the values to solve in the three formulations.

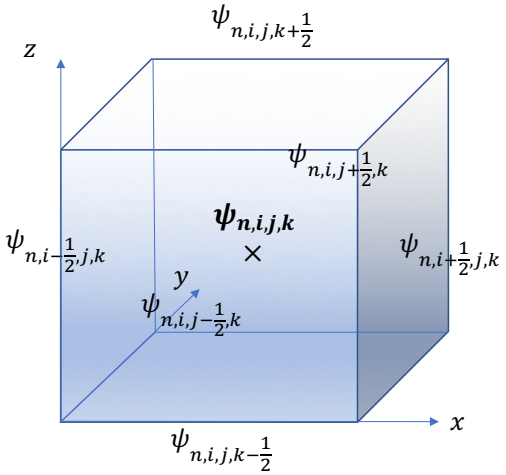

Figure 2.2 Example of a Computation Cell

Diamond Difference. Simply select $a_{n,i,j,k} = b_{n,i,j,k} = c_{n,i,j,k} = \dfrac{1}{2}$.

θ-Weighted. The coefficients are selected as follow

$$a_{n,i,j,k} = 1 - \frac{q_{n,i,j,k} + \frac{|\mu_n|}{\Delta x}\psi_{n,i-\frac{1}{2},j,k} + \theta(\frac{|\eta_n|}{\Delta y}\psi_{n,i,j-\frac{1}{2},k}) + \frac{|\xi_n|}{\Delta z}\psi_{n,i,j,k-\frac{1}{2}})}{(2\frac{|\eta_n|}{\Delta y} + 2\frac{|\xi_n|}{\Delta z} + \sigma_{i,j,k})\psi_{n,i-\frac{1}{2},j,k}} \tag{2.21}$$

$$b_{n,i,j,k} = 1 - \frac{q_{n,i,j,k} + \frac{|\eta_n|}{\Delta y}\psi_{n,i,j-\frac{1}{2},k} + \theta(\frac{|\mu_n|}{\Delta x}\psi_{n,i-\frac{1}{2},j,k}) + \frac{|\xi_n|}{\Delta z}\psi_{n,i,j,k-\frac{1}{2}})}{(2\frac{|\mu_n|}{\Delta x} + 2\frac{|\xi_n|}{\Delta z} + \sigma_{i,j,k})\psi_{n,i,j-\frac{1}{2},k}} \tag{2.22}$$

$$c_{n,i,j,k} = 1 - \frac{q_{n,i,j,k} + \frac{|\xi_n|}{\Delta z}\psi_{n,i,j,k-\frac{1}{2}} + \theta(\frac{|\mu_n|}{\Delta x}\psi_{n,i-\frac{1}{2},j,k}) + \frac{|\eta_n|}{\Delta y}\psi_{n,i,j-\frac{1}{2},k})}{(2\frac{|\mu_n|}{\Delta x} + 2\frac{|\eta_n|}{\Delta y} + \sigma_{i,j,k})\psi_{n,i,j,k-\frac{1}{2}}} \tag{2.23}$$

where $q_{n,i,j,k}$ and $\sigma_{i,j,k}$ are the volumetric angular source and macroscopic cross-section at cell i, j, k, the μ_n, η_n, and ξ_n are the discretized angle projection along x, y, and z directions, respectively, the Δx, Δy, and Δz are the cell length in x, y, and z directions, respectively.

The implication of Eq.(2.21), (2.22), and (2.23) are the 3D space are not decomposable. The 3D angular neutron flux couples the x, y, and z directions. If simply select $a_{n,i,j,k} = b_{n,i,j,k} = c_{n,i,j,k} = \dfrac{1}{2}$, it means that the three directions are independent from the others. In the θ-Weighted scheme, the θ is a constant selected manually.

Directional θ-Weighted. The DTW scheme select the θ value depending on the directions by the following formulations:

$$\theta(\mu_n) = \mu_n^2 \quad \theta(\eta_n) = \eta_n^2 \quad \theta(\xi_n) = \xi_n^2 \tag{2.24}$$

By doing this, the angular flux weighting factors are subsequently used to obtain the DTW average cell angular flux, given by

$$\psi_{n,i,j,k} = \frac{q_{n,i,j,k} + \frac{|\mu_n|}{a_{n,i,j,k}\Delta x}\psi_{n,i-\frac{1}{2},j,k} + \frac{|\eta_n|}{b_{n,i,j,k}\Delta y}\psi_{n,i,j-\frac{1}{2},k} + \frac{|\xi_n|}{c_{n,i,j,k}\Delta z}\psi_{n,,j,k-\frac{1}{2}}}{\frac{|\mu_n|}{a_{n,i,j,k}\Delta x} + \frac{|\eta_n|}{b_{n,i,j,k}\Delta y} + \frac{|\xi_n|}{c_{n,i,j,k}\Delta z} + \sigma_{i,j,k}} \tag{2.25}$$

Exponential Directional Weighted. In the EDW scheme, the angular flux behavior within a cell is expressed by

$$\psi_{n,i,j,k} = \frac{1}{\beta}(e^{\frac{2\lambda_i}{|\mu_n|}} - 1)(e^{\frac{2\lambda_j}{|\eta_n|}} - 1)(e^{\frac{2\lambda_k}{|\xi_n|}} - 1)(q_A + \frac{|\mu_n|}{\Delta x}\psi_{in\ x} + \frac{|\eta_n|}{\Delta y}\psi_{in\ y} + \frac{|\xi_n|}{\Delta z}\psi_{in\ z}) \tag{2.26}$$

$$\begin{aligned}\beta = {} & \frac{2\lambda_i}{\Delta x}e^{\frac{2\lambda_i}{|\mu_n|}}(e^{\frac{2\lambda_j}{|\eta_n|}} - 1)(e^{\frac{2\lambda_k}{|\xi_n|}} - 1) + \frac{2\lambda_j}{\Delta y}e^{\frac{2\lambda_j}{|\eta_n|}}(e^{\frac{2\lambda_i}{|\mu_n|}} - 1)(e^{\frac{2\lambda_k}{|\xi_n|}} - 1) + \\ & \frac{2\lambda_k}{\Delta z}e^{\frac{2\lambda_k}{|\xi_n|}}(e^{\frac{2\lambda_j}{|\eta_n|}} - 1)(e^{\frac{2\lambda_i}{|\mu_n|}} - 1) + \sigma_{i,j,k}(e^{\frac{2\lambda_i}{|\mu_n|}} - 1)(e^{\frac{2\lambda_j}{|\eta_n|}} - 1)(e^{\frac{2\lambda_k}{|\xi_n|}} - 1)\end{aligned} \tag{2.27}$$

where the $\sigma_{i,j,k}$ is the macroscopic total cross-section of cell i, j, k, the λ_i, λ_j, and λ_k are the constants to be determined by

$$\lambda_i \sim \frac{(\hat{\psi}_{n,i+\frac{1}{2},j,k} - \hat{\psi}_{n,i-\frac{1}{2},j,k})|\mu_n|}{2\psi_{n,i,j,k}} \tag{2.28}$$

$$\lambda_j \sim \frac{(\hat{\psi}_{n,i,j+\frac{1}{2},k} - \hat{\psi}_{n,i,j-\frac{1}{2},k})|\eta_n|}{2\psi_{n,i,j,k}} \tag{2.29}$$

$$\lambda_k \sim \frac{(\hat{\psi}_{n,i,j,k+\frac{1}{2}} - \hat{\psi}_{n,i,j,k-\frac{1}{2}})|\xi_n|}{2\psi_{n,i,j,k}} \tag{2.30}$$

where the $\hat{\psi}$ are the DTW predicted incoming and outgoing flux.

Exponential Directional Iterative. The EDI is a predictor-corrector scheme with the exponential base in EDW. In the EDI scheme, the constants in Eq.(2.28), (2.29), and (2.30) are iteratively refined to improve the quality of EDW scheme.

2.5 Fixed-Source Monte Carlo Methods

The Monte Carlo (MC) method does not directly solve the LBE. Instead, it utilizes the statistical approach to represent the Physics by using the Probability Density Functions (*pdf*) [2][64][65]. The stochastic behavior of each individual particle are simulated using random sampling process using a pseudo random number generator. An averaged system behavior can be obtained by a series of individual particle simulations. A statistical uncertainty for the confidence of the mean value will be obtained by using the MC method. The statistical uncertainty has to be reasonable low such that if the solution is meaningful is determined by this. This section will briefly discuss the fundamentals of probability, which governs the Monte Carlo method. A discussion of the pros and cons of the Monte Carlo method are also provided.

2.5.1 Random Variables

Typically, the outcomes of a process are mapped onto a value for numerical treatments. This value is called a random number. Any random numbers are governed by their corresponding Probability Density Functions (*pdf*) and Cumulative Density Functions (*cdf*). The definition of the *pdf* is the probability that the outcome of a random process is x, which the integration of a *pdf* is always unity:

$$\int_a^b dx' p(x') = 1 \tag{2.31}$$

where $p(x)$ is the *pdf* with range from $[a,b]$.

The *cdf*, $P(x)$, represents the probability that the random variable is *less than* x. The *cdf* is defined as

$$P(x) = \int_a^x dx' p(x') \tag{2.32}$$

The *pdf* and *cdf* of a random variable have a few important characteristics:

1. *pdf* is always positive.
2. *cdf* is always positive and nondecreasing function of its random variable.
3. *pdf* is normalized such that the corresponding *cdf* varies in a range of [0,1].

2.5.2 Fundamental Formulation of Monte Carlo (FFMC)

With the knowledge of random variable, *cdf* and *pdf*, we want to use them to simulate the physics process via the Monte Carlo method. To achieve this, we need random number η. Here, the question is how to relate the random number to the random variable and *pdf*. The *pdf* are typically the know physics. Haghighat [2] suggested that we can consider the relationship:

$$p(x)dx = q(\eta)d\eta \tag{2.33}$$

where $q(\eta)$ is the density function of the random number.

By performing integration from both side on Eq.(2.33), the relationship between x and η, referred to as the Fundamental Formulation of Monte Carlo (FFMC) [2], can be written by

$$P(x) = \eta, \tag{2.34}$$

where

$$0 \leq \eta \leq 1.$$

To obtain the physics outcome x, we can simply inverse the Eq.(2.34) by

$$x = P^{-1}(\eta), \tag{2.35}$$

By obtaining the random number η from Pseudo Random Number Generator (PRNG) [2], we can simulate the physics process by obtaining a series of random numbers. This process is called random sampling. Two difficulties will be encountered here:

1. The inversion of *cdf* $\mathrm{P}^{-1}(\eta)$ is typically not easy, which will require numerical techniques. The numerical inversion has to be checked such that the probability of outcome will be preserved.

2. The PRNG is typically used since true randomness of random number generation still remain an unsolved problem in scientific community. The randomness of PRNG has to be tested.

2.5.3 Modeling Neutral Particle Transport

Here, we consider a simplified shielding problem for describing the Monte Carlo fixed-source neutral particle transport simulation. We can assume the problem is 1D, one-speed with purely absorbing material in the shield and isotropic scattering process only. Fig. 2.3 shows the configuration of this problem.

With the assumptions, three distinct processes are required to be simulated in this problem:

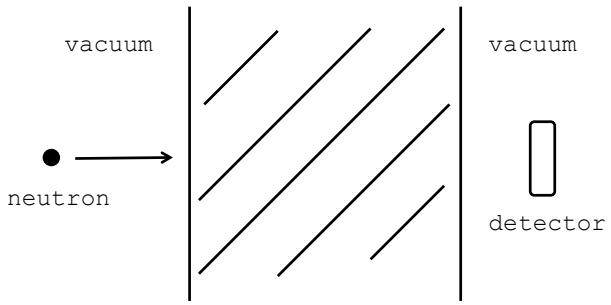

Figure 2.3 A Simple 1D Shielding Problem [2]

1. Free-flight or path-length between interactions
2. Selection of interaction type
3. Selection of scattering angle

The corresponding *pdf*s and their FFMCs are listed in the Table 2.1. where σ_t and σ_s are

Table 2.1 FFMC for the 1D Simplified Shielding Problem

Process	*pdf* Type	*pdf*	FFMC
Path-Length	Continuous	$p(r) = \sigma_t e^{-\sigma_t r}$	$r = \dfrac{-\ln \eta_1}{\sigma_t}$
Interaction Type	Discrete	σ_a/σ_t	Absorption if $\eta_2 \leq \sigma_a/\sigma_t$, else: scatter
Scattering Angle (μ')	Continuous	$p(\mu_0) = 2\pi \dfrac{\sigma_s(\mu_0)}{\sigma_s}$	$\mu' = \mu\mu_0$
		$p(\varphi_0) = \dfrac{1}{2\pi}$	$+\sqrt{(1-\mu^2)}\sqrt{(1-\mu_0^2)}\cos(\varphi_0)$, where: $\mu_0 = 2\eta_3 - 1$, $\varphi_0 = 2\pi\eta_4$

macroscopic total and scattering cross-sections, $\sigma_s(\mu_0)$ is the angular differential scattering cross-section, which we have select isotropic process and can be expressed by

$$\sigma_s(\mu_0) = \frac{\sigma_s}{4\pi} \tag{2.36}$$

The η_1, η_2, η_3, and η_4 are the random numbers, the μ' and μ are the cosine of angle after and before scattering, the μ_0 is the cosine between μ' and μ, which the relationship can be described by the Fig. 2.4.

The Ω and Ω' are the angle before and after scattering, which μ' and mu are the azimuthal part of them. The μ_0 is the cosine of θ'.

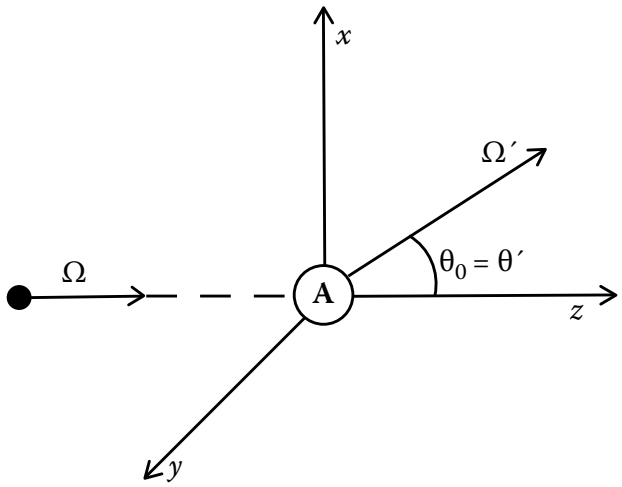

Figure 2.4 Scattering Angles [2]

The procedure of modeling the particle transport for the 1D shielding problem is

1. Sample the path-length of the particle by selecting the origin of the particle from the inner side of the shield
2. Determine if the particle is still within the shield range, if still within it, continue, if leave, then restart a new particle from the step 1. If the particle enter the shield and leave without interaction, it is called a free-flight particle.
3. If the particle is still within the shield, sample the interaction type, if the particle is absorbed, start a new particle from the step 1, if the particle is undergoing scattering process, continue.
4. Sample the scattering angle if the particle is scattered.
5. Sample the path-length of the scattered particle, determine if the particle is still within the shield, it leave the shield, start a new particle from step 1, otherwise, perform the interaction type sampling from step 3 again, and keep going.

Typically, we will need to perform N particles for simulating the particle transport process. After finishing all the sampling, an averaged quantity can be obtained, depending on the interest, with a statistical uncertainty. The larger the number of particle N, the lower the statistical uncertainty will be obtained. In other word, confidence of the outcome is higher with more particles are sampled.

2.5.4 Figure of Merit

The result of a Monte Carlo simulation includes an averaged quantity and its associated uncertainty. The Monte Carlo calculation is typically performed with a pre-selected number of history. Considering the number of history N is very large, the variance that corresponding to the sample mean is used, i.e. $\sigma_{\bar{x}}^2 = \frac{\sigma_x^2}{N}$, based on the validity of Central Limit Theorem (CLT) [2]. Here, a figure of merit has to be defined to measure the effectiveness of the Monte Carlo particle transport simulations. The Figure of Merit (FOM) is defined as

$$FOM = \frac{1}{TR_{\bar{x}}} = \frac{1}{T\frac{\sigma_x^2}{N}} \tag{2.37}$$

where T is the computation time, R is the relative statistical uncertainty. If the CLT is valid, then the σ_x is converged to a constant value C_1 with statistical fluctuation only. The computation time T will be proportional with number of history N with a proportionality constant of C_2. The FOM will reduced to

$$FOM = \frac{1}{C_2 N \frac{C_1}{N}} = C \tag{2.38}$$

Therefore, the Monte Carlo particle transport simulation is converged if constant FOM is observed with increase of history. Note that according to the CLT, the relative statistical uncertainty $R_{\bar{x}}$ should be proportional to $1/\sqrt{N}$ [2].

2.6 Monte Carlo Criticality (Eigenvalue) Calculation

The most widely-used procedure of the Monte Carlo eigenvalue simulation is

1. Partition the region in the model that contains fissile and fertile materials into I regions.
2. Distribute the N_0 fission neutrons over the subregions S_i, which $i = 1, I$. The k at a given iteration is given by
$$k^n = \frac{1}{N^0} \sum_{i=1}^{I} S_i^{(n)}. \tag{2.39}$$
These fission neutrons are transported throughout the problem by the following steps, and a new distribution is obtained.
3. For each fission neutron, sample the energy and direction.

4. Transport the particle through the medium. The sampling process is the same as the fixed-sourced simulation discussed in the section 2.5.3, except it will be 3D and continuous energy. This part includes path-length, reaction type, and direction sampling. The particle will be terminate only if: (1) encountering absorption; or (2) leaving the system boundary. Otherwise, the simulation process will be repeated.

5. If the particle encounter absorption reaction, whether the particle undergoes fission reaction is determined. If yes, sample how many fission neutron are produced with their corresponding direction and energy. These neutrons represents the next generation of fission neutron.

The source distribution are typically not converged for the first few cycles, therefore directly using the above formulation may yield false converge. The standard remedy for solving this issue is to skip convergence checking for a number of generations and calculate the cumulative k only on following generations. This cumulative k is given by

$$k_c^n = \frac{1}{n - n_s} \sum_{n'=n_s+1}^{n} k^{(n')}. \tag{2.40}$$

where k_c^n is the converged k at n^{th} iteration, the n_s is the skip cycle selected to avoid false convergence from unconverged flux distribution. Note that this study typically has to be performed by users via selection of different sets of n_s.

The source distribution has to be normalized in order to prevent over or under populated source distribution. The expression of this can be written by

$$q_i^{(n)} = \left(\frac{S_i^{(n)}}{\sum_{i=1}^{I} S_i^{(n)}} \right) N^{(0)}. \tag{2.41}$$

2.7 Difficulties with the Eigenvalue Monte Carlo Calculation

Although the Monte Carlo method can provide exact simulation, there are some issues with the method when it is applied on eigenvalue (criticality) calculations. Three issues still remaining unsolved in the radiation transport community are:

1. Cycle to cycle correlation [66] - The literature [66] has indicated that a factor of 5 underestimation on the tallied quantity can be possible from the cycle to cycle correlation for a spent nuclear fuel cask criticality problem. This may further yields inaccurate sampling process since the source sampling of eigenvalue Monte Carlo calculation is depending on the previous generation. Note that this is for a specific case, and is not generalized. The impact of cycle to cycle correlation has to be studied case by case.

2. Undersampling [67] - the undersampling appears when problem has significant discontinuity on the source distribution. The source distribution can be nearly converge, but still are distorted by the undersampling problem [68]. This issue usually shows up at the low neutron population regions, such as presence of absorber or peripheral of a nuclear system.

3. High dominance ratio [2] - The high dominance ratio typically appears when the ratio of first moment and fundamental mode of eigenvalue, i.e. $\frac{k_1}{k_0}$, is close to 1. Under such condition, the eigenvalue from the first iteration will dominate the final result [2][68]. More iteration steps will be required for decaying of the higher mode of neutron flux distribution.

Several approaches have been proposed to diagnose these issues [69][70]. However, no direct solution on these issues has been proposed. With these intrinsic issues, users have to carefully examine the neutron source convergence when using the Monte Carlo method for eigenvalue calculations.

2.8 Fission Matrix Method

Since the Monte Carlo eigenvalue has its intrinsic issues, a question raised here is: "Is it possible to bypass these issues if there is no direct solution to them?". The answer is yes. The Fission Matrix (FM) approach was proposed in the 1950s [71][72][73]. A complete theory was summarized by Carney [74] recently. The FM approach was originally proposed to accelerate the Monte Carlo simulations [75][76]. Dufek's research [77] further investigated the possibility to replace the skip cycle approach with the FM approach for eigenfunction convergence. The FM approach was formally used for the nuclear system analysis by Haghighat and his research group [53][78].

An eigenvalue Monte Carlo problem can be decomposed into a series of fixed-source problems. By doing this, there will be no need to perform Monte Carlo sampling process at each generation if the FM coefficients are appropriately calculated. The cycle to cycle correlation, undersampling, and high dominance ratio can be easily bypassed.

The criticality form of the transport equation is can be rewritten as

$$H\psi\left(\underline{r}, E, \hat{\Omega}\right) = \frac{1}{k}\chi\tilde{F}\psi\left(\underline{r}, E, \hat{\Omega}\right) \tag{2.42}$$

where

$$\tilde{F} = \frac{1}{4\pi}\int_0^\infty dE' \int_{4\pi} d\Omega' \nu\sigma_f(\underline{r}, E'). \tag{2.43}$$

Assuming the transport operator H is invertible, then we can solve for ψ, as

$$\psi = \frac{1}{k} H^{-1} \chi \tilde{F} \psi. \tag{2.44}$$

If we then multiply both sides of the above equation by $\tilde{F}$, we obtain

$$\tilde{F}\psi = \frac{1}{k} \left(\tilde{F} H^{-1} \chi \right) \tilde{F} \psi \tag{2.45}$$

which can be written in the form

$$S = \frac{1}{k} \mathbf{A} S, \tag{2.46}$$

where $S = \tilde{F}\psi$ and $\mathbf{A} = \tilde{F} H^{-1} \chi$. One may rewrite this expression in the following form

$$kS = \mathbf{A} S \tag{2.47}$$

which indicates that $\mathbf{A}$ operates on the present generation fission density to obtain the fission density of next generation. The next generation fission neutrons in a phase space $(d^3 r d\Omega dE)$ can be induced by fission neutrons in the same phase space plus any other phase space $(d^3 r' d\Omega' dE')$. Therefore, we can write

$$\mathbf{A} S \left(\underline{r}, E, \hat{\Omega} \right) = \int_V d^3 r' \int_{4\pi} d\Omega' \int_0^\infty dE' \; a \left(\underline{r}' \to \underline{r}, \hat{\Omega}' \to \hat{\Omega}, E' \to E \right) S \left(\underline{r}', \hat{\Omega}', E' \right). \tag{2.48}$$

This FM formulation can be implemented on a computer by discretizing our model, which we partion the spatial domain into N volumes, then the eigenvalue formulation Equation (2.46) can be rewritten as

$$\underline{S} = \frac{1}{k} \underline{\underline{\mathbf{A}}} \; \underline{S} \tag{2.49}$$

or

$$S_i = \frac{1}{k} \sum_{j=1}^{N} a_{i,j} S_j, \tag{2.50}$$

where

$$a_{i,j} = \frac{\int_{V_i} d^3 r \int_{V_j} d^3 r' a \left(\underline{r}' \to \underline{r} \right) S \left(\underline{r}' \right)}{\int_{V_j} d^3 r' S \left(\underline{r}' \right)}. \tag{2.51}$$

This says that $a_{i,j}$ is the number of fission neutrons produced in cell i due to a fission neutron born in cell j.

An FM formulation can also be obtained within a subcritical multiplying nuclear system, i.e., where a fixed radiation source is necessary to achieve equilibrium. In the case of spent nuclear fuel, the fixed source is referred to as the "intrinsic" or independent source and is

generated by spontaneous fission, delayed neutrons, and (α, n) reaction. An equilibrium formulation can be written for a subcritical multiplication problem as

$$S_i = \sum_{j=1}^{N} \left(a_{i,j} S_j + b_{i,j} S_j^{intrinsic} \right), \tag{2.52}$$

where $b_{i,j}$ is the number of fission neutrons produced in cell i due to an independent neutron source born in cell j. Note that $a_{i,j}$ and $b_{i,j}$ are fundamentally different values, because S and $S^{intrinsic}$ have different spatial and spectral distributions with each cell. Their general behavior might be similar, but the values will not be exactly the same. The subcritical multiplication factor (M) can be expressed by

$$M = \frac{\sum_{j=1}^{N} \left(S_j + S_j^{intrinsic} \right)}{\sum_{j=1}^{N} \left(S_j^{intrinsic} \right)}. \tag{2.53}$$

Note that at equilibrium, i.e., when the number of generations goes to infinity with material homogeneous system, M reduces to

$$M = \frac{1}{1-k} \tag{2.54}$$

Equation (2.52) can also be written in the matrix form as

$$\underline{S} = \underline{\underline{\mathbf{A}}}\ \underline{S} + \underline{\underline{\mathbf{B}}}\ \underline{S}^{intrinsic}. \tag{2.55}$$

The fission matrix method results in a set of N linear equations, which can be solved for S and k, or k_{eff}, given the $a_{i,j}$ and $b_{i,j}$ coefficients are pre-calculated. The main effort is how to calculate the coefficients, and to decide on a computational cell size that is small enough to give detailed and accurate results, but not so large that the linear system becomes intractable. This will give a matrix with size of N^2. Unfortunately, there is no appropriate figure of merit as *a priori* to predict the appropriate size of mesh. Currently, it mainly rely on user's effort.

2.9 Variance Reduction Methods

Thus far, we have discussed the Deterministic and Monte Carlo methods for solving radiation transport problems. As mentioned above, the Monte Carlo method has the advantage of representing the physics without approximations. However, the drawback of the analog Monte Carlo simulation is the long computation time, especially for the radiation shielding problems. For this, numerous variance reduction techniques have been developed for more efficient Monte Carlo particle transport calculations. In this section, two major variance reduction techniques will be discussed:

1. Biasing of Density Functions
2. Splitting Techniques

2.9.1 Biasing of Density Functions

The main reason for inefficient analog Monte Carlo radiation shielding calculation is the low penetration rate. In principle, we can bias the *pdf* to increase the particle penetration rate and preserve the quantity of interest. To achieve this, we can no longer use the Bernoulli process for particle transport simulation. Here, a particle with its associated "weight" can be assigned. The weight indicates the importance of the particle while performing transport simulations. To obtain an unbiased objective, we can write the following formulation:

$$w_{biased} \cdot pdf_{biased} = w_{unbiased} \cdot pdf_{unbiased}. \tag{2.56}$$

The unbiased particle weight, $w_{unbiased}$, is typically 1 for the Bernoulli process. Therefore, the biased weight will be

$$w_{biased} = \frac{pdf_{unbiased}}{pdf_{biased}}. \tag{2.57}$$

The Eq.(2.57) shows that the biased particle weight is counter proportional to the biased *pdf*. Therefore, the averaged outcome will be preserved.

2.9.1.1 Implicit Capture (Survival Biasing)

An example is the implicit capture (or survival biasing). In this technique, the particle history is not terminated if undergoing absorption reaction. Instead, the particle is forced to undergo a scattering interaction, which the weight of particle is reduced. The unbiased scattering probability is $\frac{\sigma_s}{\sigma_t}$, and the unbiased weight is w_0. If we bias the *pdf* of the scattering process to 1, such that all particles are forced to undergo scattering interaction (no absorption). Using the Eq.(2.57), the biased weight of particle can be written by

$$w = w_o \frac{\sigma_s}{\sigma_t}. \tag{2.58}$$

where σ_s and σ_t are the scattering and total macroscopic cross-section of the media. If the particle undergoes n collision process, the weight will become

$$w = w_o (\frac{\sigma_s}{\sigma_t})^n. \tag{2.59}$$

This technique is especially useful in the deep penetration problems, in which most of the computation time are spent on tracking the particles that are not going to make contributions. Eq.(2.59) shows that the weight will be very low if the particle encounter a lot

of scattering interactions. This makes perfect sense that the particle encountering a lot of scattering will have less significant contribution to the outcome.

2.9.1.2 Russian Roulette

After the particle weight falls down to a certain value, they are less likely to make contribution to the outcome. Therefore, we can further play a "survival game" to it for enhancement of computation efficiency. One approach is to select a cutoff value d, and generate a random number η:

- If $\eta > \frac{1}{d}$, the history is terminated
- If $\eta \leq \frac{1}{d}$, the history is continued with a particle weight increase by factor of d.

The value d is typically between 2 to 10 [2]. The value d conserves the particle weight if it survives the Russian Roulette survival game. More *pdf* biasing based method, such as path-length biasing, exponential transform, and forced collision [2], are developed and implemented into some Monte Carlo code system such as MCNP [41].

2.9.2 Splitting Techniques

The splitting techniques was proposed based on the fact that different particle has their corresponding "importance". Therefore, it is desirable to increase the survivability of the "important" particles and simultaneously judiciously eliminate the "less important" particles. The splitting technique can be applied on spatial, energy, and angle phase spaces. Here, we use a 1D shielding problem as an example for spatial geometry splitting. Fig. 2.5 shows a 1D 2 region radiation shielding problem.

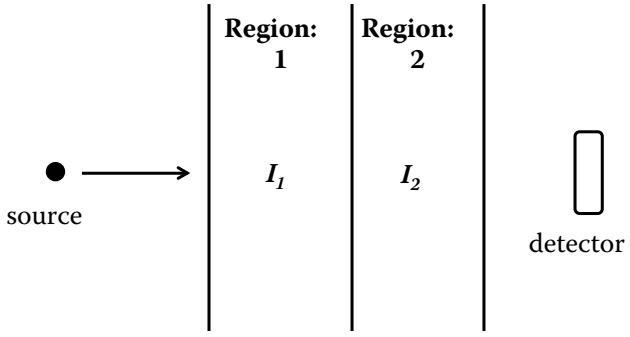

Figure 2.5 Example for Geometry Splitting [2]

Assuming the absorption cross-section of the two regions are not very different, the particle in region 2 are obviously more important than those in region 1. If a particle with a weight of w is moving in the direction of higher importance region, i.e., from region 1 to region 2, the particle is split into a number of identical particles with lower weights depending on the importances of the regions, i.e. I_2/I_1, as follows:

1. If $n = \frac{I_2}{I_1}$ is an integer ≥ 2, the particle is split into n identical particles with the same weights of $\frac{w}{n}$.
2. If $r = \frac{I_2}{I_1}$ is a real number with decimals and ≥ 2, a random number η is generated and compared with
$$\Delta = \frac{I_2}{I_1} - INT(\frac{I_2}{I_1}) = r - n. \tag{2.60}$$
   (a) If $\eta \leq 1 - \Delta$, the particles is split into n particles.
   (b) If $\eta > 1 - \Delta$, the particle is split into $(n + 1)$ particles.

The weight of the new particles are adjusted accordingly. If a particle is moving from region 2 to 1, which is toward the "less important" direction, a russian Roulette procedure is used:

1. A random number η is generated.
2. If $\eta \leq r^{-1}$, the particle survives with a weight of $w \cdot r$; ptherwise, it is killed.

Several recommendations from the MCNP5 manual [41] are listed below for geometry splitting:

1. Keep the ratio between the adjacent cells from 2 to 4.
2. Consider a single region size of 2 mean-free-path of particle.
3. Maintain the same number of particles for all regions.
4. Do not split particle in void or vacuum region.

The major difficulty of the splitting technique is the selection of appropriate importances of the regions. From the past, this selection mainly reply on user's experience. In 1998, Wagner and Haghighat has proposed and developed an automatic novel technique [37], which has elevated the use of splitting technique to another level. This technique will be discussed in the following section. For the energy and angular phase space splitting, similar process can be performed.

2.9.3 Weight-Window Technique

This technique combines the three splitting techniques mentioned in the previous section with a procedure to control the particle weights. Note that this technique can be extended to time variable as well. For each discretized phase space, a weight window is defined. Each window has a user defined lower and upper weights, w_l, and w_u. If a particle with a weight within [w_l,w_u], the particle transport simulation will be continued without any action; otherwise, it is treated via one of the following procedures:

1. If the particle weight is lower than the lower window w_l, Russian roulette is performed and the particle is either terminated or the weight of the particle is increased to a value w_s within an acceptable range.
2. If the particle weight is larger than the upper window w_u, the particle is split into new particles of weight within the acceptable range.

Generally, the w_u and w_s are related to the lower bound w_l. The MCNP manual [41] suggests the value of $w_u = 5w_l$ and $w_s = 2.5w_l$. Proper selection of the weight window distribution for a complex system is difficult. From the past, this is performed based on user's experience.

2.10 The CADIS Methodology

The CADIS methodology stands for Consistent Adjoint Driven Importance Sampling. It was proposed and developed in 1998 by Wagner and Haghighat [37]. The CADIS methodology utilizes the importance function to select the weight windows in each phase spaces. The importance function are usually obtained from an approximated calculation using deterministic approach. The advantage of using deterministic approach is the calculation speed. An approximated deterministic model with very coarse mesh will be able to provide sufficient information for variance reduction. There are two parts in the CADIS methodology:

1. Source biasing, and
2. Transport biasing.

The forward approach for detector response calculation is

$$R = \int dV \int_0^\infty dE \int_{4\pi} d\Omega \sigma_d(\underline{r}, E)\psi(\underline{r}, E, \hat{\Omega}), \tag{2.61}$$

where the $\sigma_d(\underline{r}, E)$ is the detector macroscopic cross-section, the $\psi(\underline{r}, E, \hat{\Omega})$ is the angular neutron flux, which can be obtained by solving Eq. (2.1) in the fixed-source form.

The adjoint approach for detector response calculation is

$$R = \int dV \int_0^\infty dE \int_{4\pi} d\Omega \psi^*(\underline{r}, E, \hat{\Omega}) q(\underline{r}, E, \hat{\Omega}), \tag{2.62}$$

where $q(\underline{r}, E, \hat{\Omega})$ is the angular source distribution, $\psi^*(\underline{r}, E, \hat{\Omega})$ is the angular importance function, which can be obatined by solving Eq. (2.6) in the fixed source form by selecting

$$q^*(\underline{r}, E, \hat{\Omega}) = \frac{1}{4\pi} \sigma_d(\underline{r}, E). \tag{2.63}$$

or

$$Q^*(\underline{r}, E) = \sigma_d(\underline{r}, E). \tag{2.64}$$

2.10.1 Source Biasing

From the adjoint methodology, we can determine the detector response by Eq. (2.62). Since the response is an integral quantity, an optimal *pdf* for restimating this integral would be $\frac{\psi^*(\underline{r}, E, \hat{\Omega}) q(\underline{r}, E, \hat{\Omega})}{R}$ based on the importance sampling technique. Therefore, the biased source distribution will be

$$\hat{q}(\underline{r}, E, \hat{\Omega}) = \frac{\psi^*(\underline{r}, E, \hat{\Omega}) q(\underline{r}, E, \hat{\Omega})}{R}. \tag{2.65}$$

The statistical weight $w(\underline{r}, E, \hat{\Omega})$ corresponding to the biased source will be

$$w(\underline{r}, E, \hat{\Omega}) = \frac{R}{\psi^*(\underline{r}, E, \hat{\Omega})} \tag{2.66}$$

Here, the value of $\psi^*(\underline{r}, E, \hat{\Omega})$ and R are all approximated value. If they are exactly correct, there will be no need to perform more calculation since the accurate R is the quantity of interest.

2.10.2 Transport Biasing

The integral form of the LBE can be written by

$$\psi(\underline{r}, E, \hat{\Omega}) = \int dV' \int_0^\infty dE' \int_{4\pi} d\Omega' K(\underline{r}' \to \underline{r}, E' \to E, \hat{\Omega}' \to \hat{\Omega}) \psi(\underline{r}', E', \hat{\Omega}') + q(\underline{r}, E, \hat{\Omega}) \tag{2.67}$$

where K is the transfer kernel. If we multiply the above equation by $\frac{\psi^*}{R}$ from the both side, we will have

$$\hat{\psi}(\underline{r}, E, \hat{\Omega}) = \int dV' \int_0^\infty dE' \int_{4\pi} d\Omega' \hat{K}(\underline{r}' \to \underline{r}, E' \to E, \hat{\Omega}' \to \hat{\Omega}) \hat{\psi}(\underline{r}', E', \hat{\Omega}') + \hat{q}(\underline{r}, E, \hat{\Omega}) \tag{2.68}$$

where

$$\hat{\psi}(\underline{r}, E, \hat{\Omega}) = \frac{\psi^*(\underline{r}, E, \hat{\Omega}) \psi(\underline{r}, E, \hat{\Omega})}{R}, \tag{2.69}$$

$$\hat{K}(\underline{r}' \to \underline{r}, E' \to E, \hat{\Omega}' \to \hat{\Omega}) = K(\underline{r}' \to \underline{r}, E' \to E, \hat{\Omega}' \to \hat{\Omega}) (\frac{\psi^*(\underline{r}, E, \hat{\Omega})}{\psi^*(\underline{r}', E', \hat{\Omega}')}), \tag{2.70}$$

In the Eq. (2.70), the biased kernel $\hat{K}$ is proportional to the importance function $\psi^*(\underline{r}, E, \hat{\Omega})$. However, this expression is not practical since the kernel K is unknown. Here, the above formulations are shown to elaborate the transport biasing.

In the CADIS methodology, the source particle are sampled from the following foumulation:

$$\hat{Q}(\underline{r}, E) = \frac{\phi^*(\underline{r}, E) Q(\underline{r}, E)}{R}. \tag{2.71}$$

where $Q(\underline{r}, E)$ is the total source, which can be obtained from integrating angular source distribution. The weights of the particles are controlled using the following form

$$w(\underline{r}, E) = \frac{R}{\phi^*(\underline{r}, E)}. \tag{2.72}$$

During the particle transport process between the phase spaces $(\underline{r}, E)$ and $(\underline{r}', E')$, particles are split if the importance ratio $\frac{\phi^*(\underline{r}, E)}{\phi^*(\underline{r}', E')}$ is greater than 1, otherwise, the Russian Roulette is applied. The particle weight is adjusted accordingly by

$$w(\underline{r}, E) = w(\underline{r}', E') \frac{\phi^*(\underline{r}', E')}{\phi^*(\underline{r}, E)}. \tag{2.73}$$

Note that in the CADIS methodology, only the spatial and energy phase spaces are included. The importance functions $\phi^*(\underline{r}', E')$ and $\phi^*(\underline{r}, E)$ are assumed to be known beforehand. Typically, the deterministic method is used to obtain the approximated importance functions. If the importance function are exact, an exact detector response R will be obtained with no variance.

Chapter 3

RAPID Code System

The RAPID code system is developed based on the MRT methodology [55], which utilizes: (1) The Fission Matrix (FM) approach for criticality and subcritical multiplication calculations; and (2) Detector Response Function (DRF) methodology or Adjoint methodology for detector/dosimeter response calculations. The criticality and subcritical multiplication neutron source calculations are originally developed by Walters, Roskoff, and Haghighat [56]. Originally, the RAPID code system is developed for the purposes of Spent Nuclear Fuel (SNF) system criticality analysis and monitoring. The capability of the code has been extended to other applications such as reactor core calculations.

Currently, the *b*RAPID [79] for reactor depletion calculation and *t*RAPID [80] for transient analysis are under development to extend the capability of the code system.

The RAPID code system has been benchmarked against various problems: (1) A Spent Nuclear Fuel (SNF) pool criticality problem [81]; (2) SNF Cask criticality problems [82][83]; (3) The Naval Academy Subcritical Reactor [84]; (4) The Organization for Economic Cooperation and Development (OECD)/Nuclear Energy Agency (NEA) Monte Carlo Performance PWR Benchmark Problem [56]; and (5) The Jozef Stefan Institute Research Reactor [85]. The RAPID code structure is shown in the Fig. 3.1.

The contribution of this dissertation is marked in the red frame as shown in the Fig. 3.1. The development of the DRF methodology means to improve upon the adjoint methodology for detector/dosimeter response calculations. In this dissertation, all parts of the RAPID code system will be used except directly using adjoint methodology for detector/dosimeter response calculations.

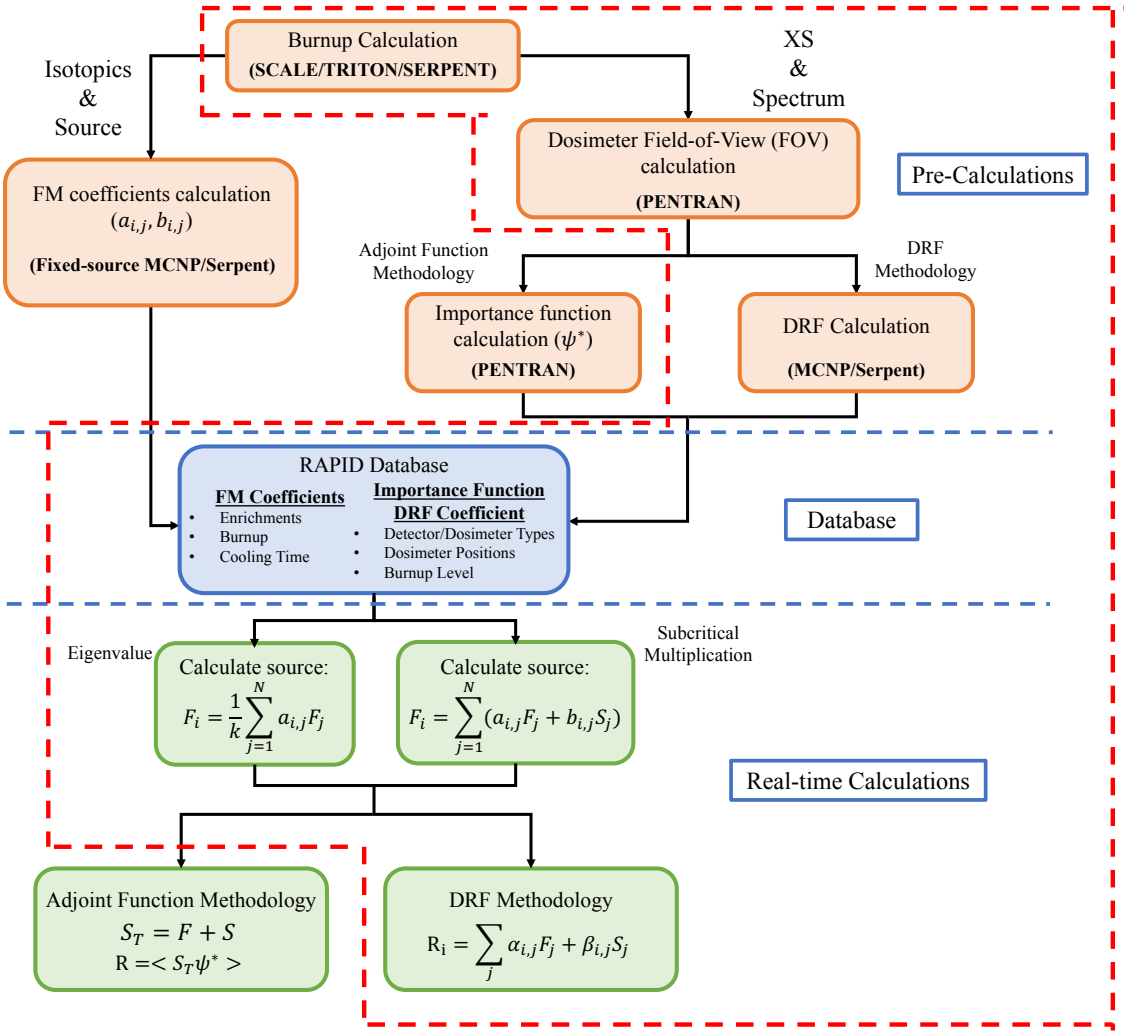

Figure 3.1 RAPID Code System Flow Chart

3.1 *p*RAPID and *Dp*RAPID Utility Code

To prepare the Monte Carlo model inputs for the coefficient calculations, there will be hundreds or even more than thousands of input files need to be prepared. To avoid human error and the tedious manual process, automation is very important. For this, the utility code systems *p*RAPID and *Dp*RAPID are created. The *p*RAPID code system was originally developed by Roskoff [4]. It was firstly written in Bash combining with FORTRAN 90/95, and later being updated using Python3.6. The Bash system is convenient from data extraction side while math operation is not very user friendly in the system. This is the main reason for the coupling with FORTRAN 90/95. In contrast, the Python3.6 is capable of handling both data extraction and math operation, although the math operation is in a different form using the NumPy package [86]. The *p*RAPID has been later extended to perform burnup

calculation used by the *b*RAPID code system. A few pseudo code scripts can be found in literature [4].

The *Dp*RAPID utility code is developed by the author of this dissertation, which is mainly written in FORTRAN 90/95. The *Dp*RAPID automatically prepare the Monte Carlo input files for the DRF coefficients calculation, process, and convert them into databases. An important function of the *Dp*RAPID utility code is flexible mesh for source volume definition of DRF coefficient calculations. An example for this capability is shown in the Fig. 3.2.

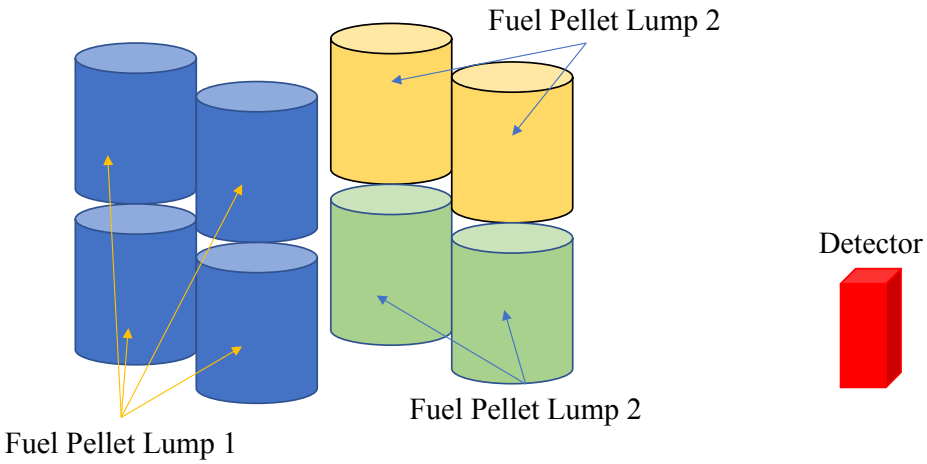

Figure 3.2 Example of DRF Mesh Distribution

Here, we assume uniform source distribution in all the four blue fuel pellets, and calculate an averaged DRF coefficient for these four fuel pellets. Similarly, the averaged DRF coefficients for light yellow and green pellets are calculate in the same way. The *Dp*RAPID utility code provides user with flexibility to define the lumping scheme in every fuel assemblies.

3.2 FM Approach for Neutron Source Calculations

In this section, the approaches in RAPID on utilizing the FM coefficients to perform neutron source calculations are introduced. Note that these clever approaches are designed for use for Light Water Reactor (LWR) currently.

3.2.1 Fission Matrix Coefficient Control Volume

Since the mean-free-path of neutrons are typically much smaller than the size of most of nuclear systems, it is expected that there are a lot of zeros in the $\underline{\underline{\mathbf{A}}}$ matrix from the Eq. (2.49). Here, we have to determine the "control volume" of FM coefficient before performing calculations. An example of the FM coefficient behavior in SNF cask flooded with water is shown

in the Fig. 3.3. The fuel assembly is standard 17 × 17 PWR with 4 wt% fresh fuel. Note that zeros are blanked out in the figure.

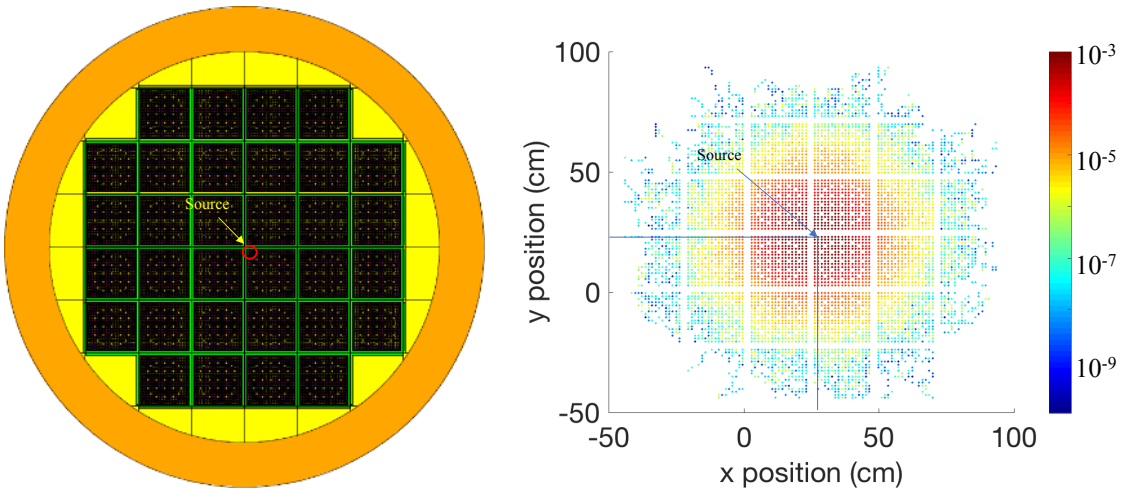

Figure 3.3 Sample FM Coefficient for SNF Cask flooded with water

As it is shown, the FM coefficients attenuate ∼ 3 and ∼ 6 orders of magnitude for 1 and 2 assembly away, respectively. Note that one assembly is ∼ 23.76 cm in pitch. The system is a perfect loosely coupled system. Rule of thumb indicated that for SNF cask flooded with water, presence of boron absorber plate in between, and filled with 17 × 17 PWR fuel assemblies, the control volume is 2 assembly away radially from the source assembly while it is 3 for commercial PWR core calculations. For the BWR 10 × 10 fuel assemblies, the control volume will be 4 assembly away since smaller size of single fuel assembly. The axial control volume for all the LWR nuclear facility are 76.2 cm away from the source location if 2.54 cm is selected for the source fuel pellet height, which is 30 axial levels away.

3.2.2 Octal Symmetry of the FM Coefficient

Since most of the fuel assemblies in commercial Light Water Reactor (LWR) are symmetry in geometry, it is reasonable to calculate an octant of FM coefficient and reflect them to the other octants. An example is shown in the Fig. 3.4.

In this example, the FM coefficient with neutron source in the yellow area are calculated first. The FM coefficients in the other 7 octants are then obtained by symmetric duplication from the calculated octant. Note that this arrangement hold with assumption of uniform fuel assembly material composition for FM coefficient calculations.

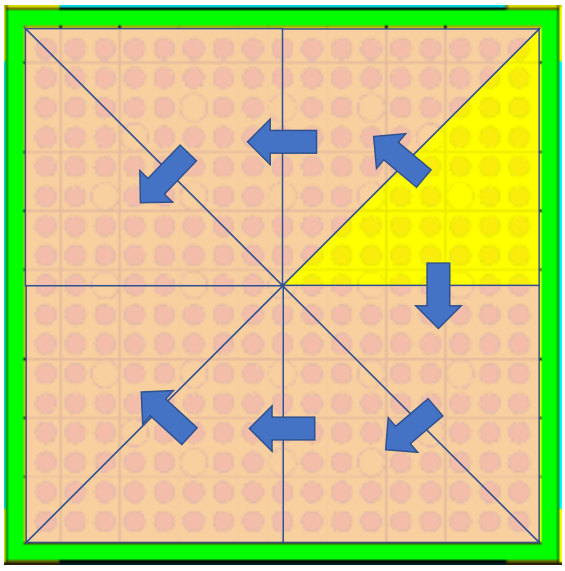

Figure 3.4 Sample Octal Symmetry for FM Coefficient Calculations

3.2.3 Fission Matrix Coefficient Translation

As indicated above, we can usually find geometric symmetry for most of the LWR system. The configurations of adjacent fuel assemblies are very similar to each others. for this, it is possible to translate the calculated FM coefficients from one assembly to others. Fig. 3.5 shows an example of radial FM coefficient translation.

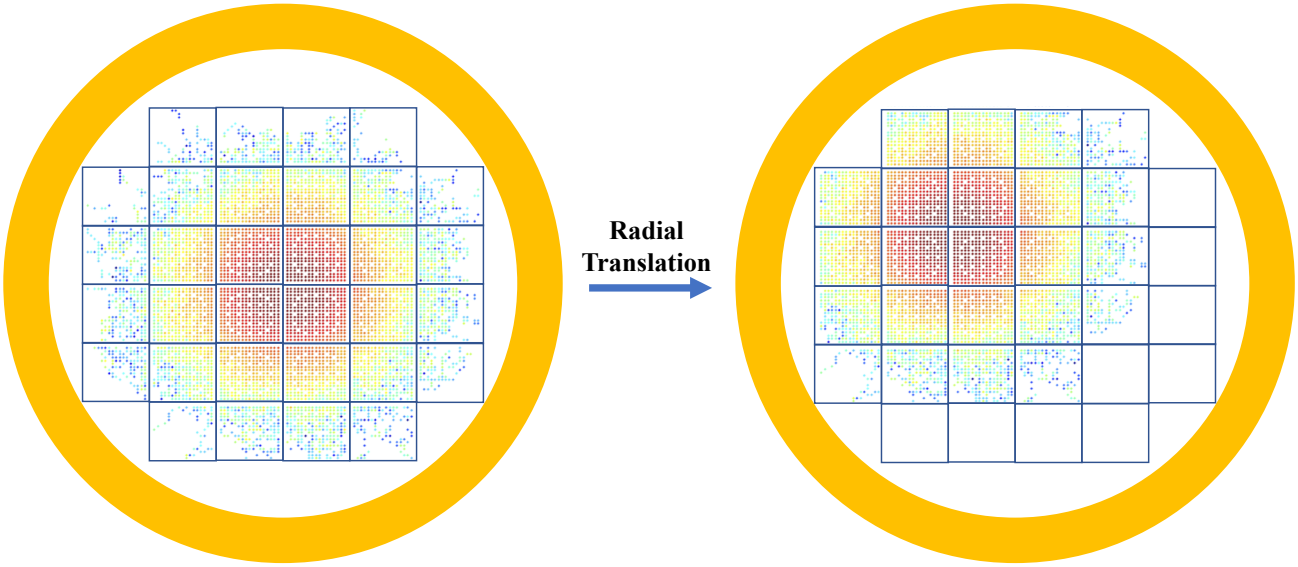

Figure 3.5 Radial FM Coefficient Translation

Similar translation scheme can be performed axially as well. This is shown in the Fig. 3.6.

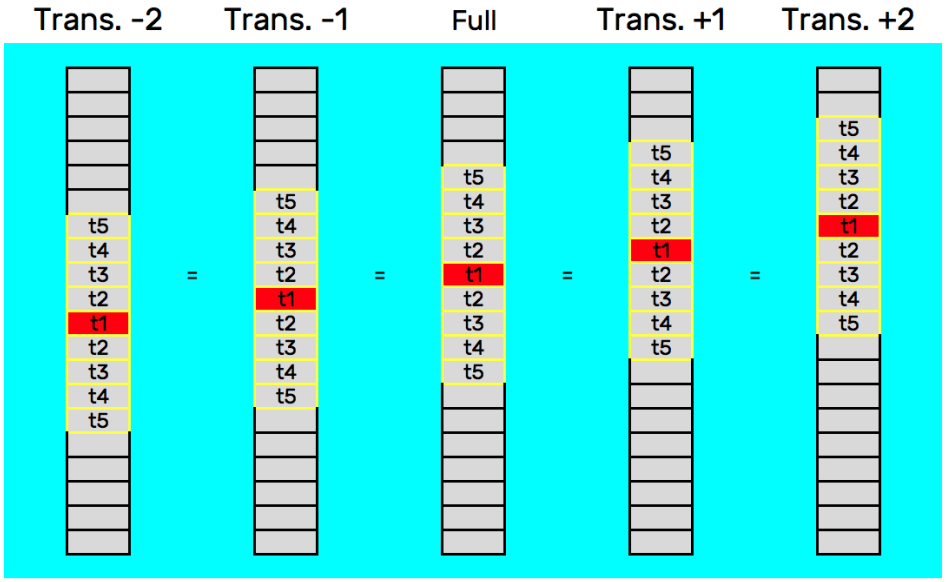

Figure 3.6 Axial FM Coefficient Translation [3]

The red segments are the fuel pellet with source. Since the axial materials are all fuel, only one axial source location has to be calculated. After that, translation is used for obtaining other FM coefficients. By doing so, the amount of FM coefficients that have to be calculated can be greatly reduced. Note that only the FM coefficients at top half of axial level are calculated. The bottom half of the FM coefficients are obtained by mapping the top half axial level.

3.2.4 Mixing Assembly Scenario

Currently, the FM coefficients are calculated by assuming uniform material compositions. This may not be true in real scenario. To overcome this issue, a routine with coefficient correction on the fly has been created in the RAPID code system. The FM coefficients are dependent on the neutron "destination" and "source" locations. The FM coefficient $\tilde{a_{i,j}}$ for a neutron born in the source assembly j with different material composition than the destination i will be corrected by the following formulation

$$\tilde{a_{i,j}} = \frac{c_i}{c_j} a_{i,j} \tag{3.1}$$

where $a_{i,j}$ is the FM coefficient with uniform destination i material distribution, the c_i and c_j are the summation of the coefficient within the database for uniform material distribution i and j, respectively.

This assumption hold true for most of the case in SNF system with absorber plate. However, relative large difference by this assumption may be found in reactor system [56][87]. The reported errors are maximum $\sim 5\%$ on the calculated fission sources, which is not considered significant, but definitely not negligible.

3.2.5 FM Coefficient Collapsing

Although we have used some clever approaches in the above sections, the $\underline{\underline{\mathbf{A}}}$ matrix still remains the same size. This means a large memory is required for the calculations. Poor convergence for such size of matrix might be encountered as well. For this, a homogenization-like approach is used here:

1. Currently, we have the FM coefficient of

$$a_{i,j} = a(x_d, y_d, x_s, y_s, z_{rel}, z_{slice}) \tag{3.2}$$

   where x_d, y_d are the location of neutron destination pin, x_s, y_s are the neutron source location, z_{rel} is the relative axial distance between i and j, z_{slice} refers to different material may be present in difference axial slice (e.g. axial burnup profile)

2. For such 3D FM coefficients, an approach can be performed is sum over the relative z-location and obtain a 2D FM with no axial leakage by:

$$a_{(2D)i,j} = \sum_{z_{rel}} a(x_d, y_d, x_s, y_s, z_{rel}, z_{slice}) \tag{3.3}$$

3. The 2D fission density for each z_{slice} is then calculated using the $a_{(2D)i,j}$ from the previous step. Each slice is considered independent from the others.

4. The fission density is then used to collapse the radial FM coefficient from (x, y) to a larger cell of $(x^{'}, y^{'})$ by:

$$a^{'}_{(3D)}(x^{'}_d, y^{'}_d, x^{'}_s, y^{'}_s, z_{rel}, z_{slice}) = \frac{\sum_{x_d, y_d \in x^{'}_d y^{'}_d} \sum_{x_s, y_s \in x^{'}_s y^{'}_s} a(x_d, y_d, x_s, y_s, z_{rel}, z_{slice}) f(x_s, y_s, z_{slice})}{\sum_{x_s, y_s \in x^{'}_s y^{'}_s} f(x_s, y_s, z_{slice})} \tag{3.4}$$

   where $f(x_s, y_s, z_{slice})$ is the fission density for each z slice from the third step, $x^{'}_d, y^{'}_d$ are the location of neutron destination pin in a larger cell, $x^{'}_s, y^{'}_s$ are the neutron source location in a larger cell.

5. The smaller size of fission matrix $a^{'}_{(3D)}(x^{'}_d, y^{'}_d, x^{'}_s, y^{'}_s, z_{rel}, z_{slice})$ is then used to calculate a 3D axial pin-wised fission density distribution.

6. After the calculation, the fine mesh fission source distribution can be obtained by using the 2D fission density from the second step:

$$f(x,y,z) = \frac{f(x,y,z_{slice})f(x^{'},y^{'},z^{'})}{\sum_{x,y\in x^{'}y^{'}} f(x,y,z_{slice})} \tag{3.5}$$

Thus far, this approach has been demonstrated its robustness on fast and accurate calculation on criticality and subcritical multiplication calculations.

3.2.6 Boundary Corrections

The radial and axial translation for FM coefficient introduced in the section 3.2.3 are generally appropriate in most of the cases, except at the boundaries. Different structure material such as water and stainless steels are usually found at the boundaries. The fission density distribution may be affected by the reflector effect of the boundaries. To capture this effect, axial and radial boundary correction factor are prepared. The radial boundary correction factor can be expressed by:

$$bnd(x,y) = \frac{f(x,y)}{\hat{f}(x,y)} \tag{3.6}$$

where $f(x,y)$ is calculated by performing a fixed source calculation assuming uniform source in the fuel pellet with fission option off, $\hat{f}(x,y)$ is calculated by modifying the original model with radial infinite fuel assembly and assuming the same uniform source in the fuel pellet.

Similarly, an axial boundary correction factor can be obtained by:

$$bnd(z) = \frac{g(z)}{\hat{g}(z)} \tag{3.7}$$

where $g(z)$ is calculated by performing a fixed source calculation assuming uniform source in the fuel pellet with fission option off, $\hat{g}(z)$ is calculated by modifying the original model with axial infinite fuel assembly and assuming the same uniform source in the fuel pellet.

The 3D boundary correction factor can be approximated by

$$bnd(x,y,z) \sim bnd(x,y)bnd(z) \tag{3.8}$$

The $bnd(x,y,z)$ is then used to correct the fission source distribution at every FM power iteration. This approach generally works for relatively large system such as SNF cask or power reactor core. However, the separation of the radial and axial boundary correction factors may not hold true when applied on some small system, such as a two assembly criticality experiment benchmark problem. This has been demonstrated by Butler [88].

3.2.7 Summary of RAPID Capability for Steady State Neutron Source Calculations

The robustness of neutron source distribution calculation of the RAPID code system on PWR nuclear system has been demonstrated. With the octal symmetry, FM coefficient translations, mixing assembly coefficient fixed-up, FM coefficient collapsing, and boundary corrections, only a very few sets of FM coefficients have to be pre-calculated. The criticality and subcritical multiplication can be calculated with order of seconds or minutes by the clever approaches. Note that for a smaller system such as a research TRIGA reactor [85], the FM coefficients are calculated within every fuel pellets. None of the aforementioned scheme will be applied.

Currently, limited amount of research has been performed on Boiling Water Reactor (BWR). The BWR fuel assembly configurations are more diverse, especially in SNF casks. For PWRs, the number of fuel rods per assembly are typically fixed, i.e. 17×17. The fuel rods of BWR assembly can be from 8×8 to 10×10 with mixing them in a same nuclear system. The two phase flow with different liquid to vapor ratio in a BWR core is also more complicated than the PWR core. All of these issues have to be handled with different approaches. However, the "loosely coupled" characteristic will still hold in BWR systems. Therefore, similar FM coefficient behavior can be found in BWR system with presence of water. More advanced approach can be potentially developed for extension of RAPID capability.

The nature of the "loosely coupled" system is mainly from the presence of water. With large amount of water, the neutrons will be slowed down very efficiently. This is one of the main reason for the successiveness of the RAPID code system. However, if the FM approach is applied on a nuclear system without water, such as High Temperature Gas Cooled Reactor (HTGCR) [89], the FM coefficient calculation time may be much longer due to the lower fission rate and longer neutron mean-free-path. The control volume of the FM coefficient will be larger. In other word, the system is "relatively more coupled".

Furthermore, the current RAPID code configuration is capable of performed calculations on solid fixed location fuel nuclear system. Liquid fuel system such as Molten Salt Reactor (MSR) [90] may be handled by dividing the fuel into sub-regions. However, the delayed neutron drift will be another difficulty for such computation. The most challenging reactor for RAPID would be Pebble Bed Reactor (PBR) [91] from my point of view. The moving fuel element with relative low fission rate due to presence of helium, i.e. not a good moderator for neutrons, can create more difficulties if using the FM approach. However, more interesting research with advanced approaches can be potentially developed for these Generation IV reactors [92].

3.3 *b*RAPID for Depletion Calculations

An extended capability of the RAPID code system has been developed for reactor depletion calculations. Fig 3.7 shows the flow chart of the *b*RAPID code system.

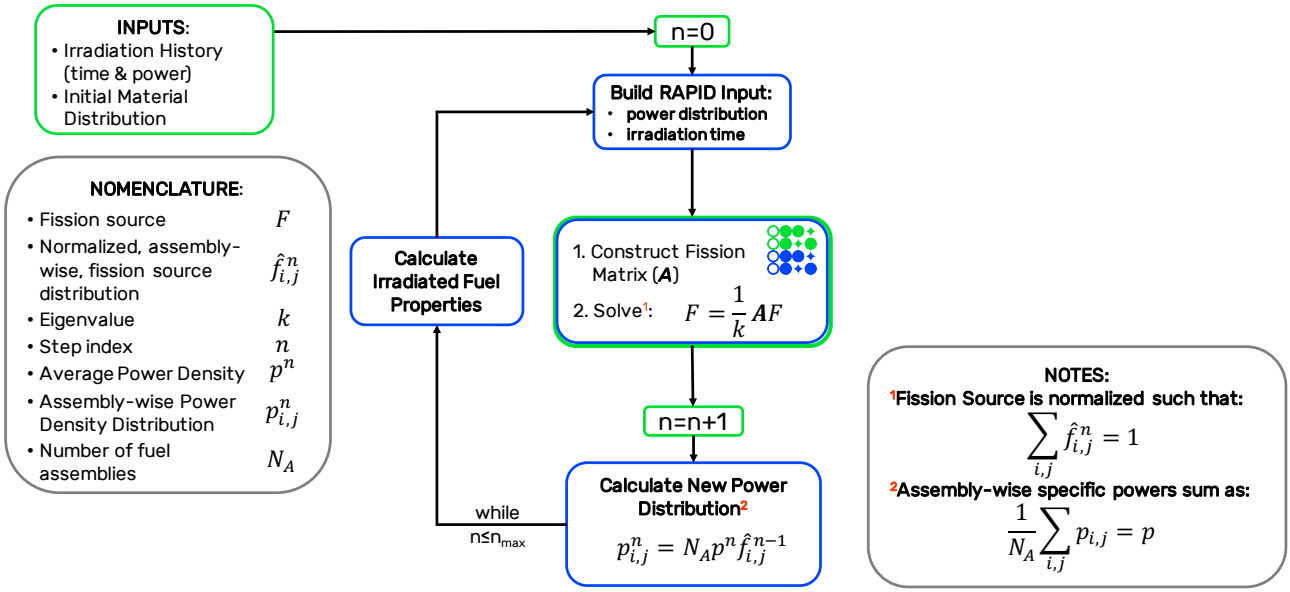

Figure 3.7 *b*RAPID Code System Flow Chart [4]

The code system pre-calculates the isotopic composition and FM coefficient for different combination of specific power and irradiation time. The RAPID code system provides the steady state fission source distribution at every burnup steps. The FM coefficients are updating on the fly between the burnup steps. The detailed 3D pin-wised fission source, system eigenvalue, and isotopic at each burnup steps can be obtained via this approach. This approach has been demonstrated to be robust with 1 year of irradiation time for PWR core. A minimum 1 pcm and maximum $\sim$ 200 pcm of eigenvalue differences are reported [4][93]. It is debatable whether the reference calculation is completely accurate. This is mainly because the difficulty to perform convergence study for Monte Carlo depletion calculation at every burnup steps. Although there are clearly space for improvement of the *b*RAPID algorithm currently, the code system is capable to provide detailed information with a very short time. This can be very useful for reactor design and fuel cycle study.

3.4 *t*RAPID for Transient Analysis

For the commercial reactors, one of the important task is the transient analysis. Under such condition, the neutron flux will change significantly with a very short time period. Example

of such conditions are reactor startup, shutdown, and overpower scenario. The steady state analysis under these condition no longer hold, and has to consider time dependent parameters, such as delayed neutron precursor. From the past, point kinetic [94] or quasi-static method [94] are typically used. However, the approximations under some condition may be questionable. The tFM methodology [95] provides a possible solution for better approach on transient analysis. In the tFM method, the time dependent LBE can be written by

$$(\underline{S_p} + \underline{S_d}) = \frac{1}{k_{eff}}[(\underline{\underline{A_{pp}}} + \underline{\underline{A_{pd}}})\underline{S_p} + (\underline{\underline{A_{dp}}} + \underline{\underline{A_{dd}}})\underline{S_d}] \tag{3.9}$$

where $\underline{S_p}$ is the criticality prompt neutron source, $\underline{S_d}$ is the criticality delayed neutron source, $\underline{\underline{A_{pp}}}$, $\underline{\underline{A_{pd}}}$, $\underline{\underline{A_{dp}}}$, $\underline{\underline{A_{dd}}}$ are the Fission Matrices of prompt neutron induced prompt neutron, prompt neutron induced delayed neutron, delayed neutron induced prompt neutron, and delayed neutron induced delayed neutron. Note that the Eq. 3.9 is originally from one of the reference article [80].

The coefficients in the four Fission Matrices in Eq. 3.9 are with time dependency. With this arrangement, similar translation scheme, as mentioned in the section 3.2.3, can be applied on the time domain and perform efficient calculations.

3.5 Adjoint Methodology for Detector/Dosimeter Response Calculations

Currently, the RAPID code system utilizes the adjoint methodology for detector/dosimeter response calculations. The importance functions for certain detector/dosimeter location are pre-calculated and stored as database. Typically, the deterministic approach is used for the calculations of importance function. The following reasons are the main difficulties for use of adjoint methodology:

1. The deterministic approach requires discretization in the phase spaces, which may yield bias on the results.

2. It is impossible to capture detailed fuel assembly geometry with deterministic approach. Therefore, homogeneous assemblies using volume as weighting function is typically used.

3. Convergence study, typically on spatial phase space, has to be always performed to guarantee the accuracy of the solution. This can be computationally expensive for importance function database calculations.

4. Mapping technique is required to couple with neutron source distribution for detector/dosimeter response calculation.

5. The database is larger due to multi-group importance function.

6. The neutron source calculated from RAPID are typically integrated over all energy (1 group only). In order to couple with the multi-group importance function, extra effort on preparation of multi-group fission neutron spectrum is needed, which might introduced another layer of uncertainty.

Due to all the above reasons, a new methodology for accurate and efficient importance function calculation is needed. For this, DRF methodology is proposed.

Chapter 4

Detector Response Function Methodology

In this chapter, the new proposed Detector Response Function (DRF) methodology will be introduced. Detailed mathematical derivation, procedure, and selection of the computer codes for calculations will be discussed. The DRF methodology is a Physics based method, which is based on the MRT methodology [55]. The DRF coefficients are pre-calculated and stored as database depending on various parameters. The coefficients can be reused without re-calculating it.

4.1 DRF Formulations

The forward approach for detector/dosimeter response calculation can be written by

$$R = \int_{V_d} d\boldsymbol{p}\psi(\boldsymbol{p})\sigma_d(\boldsymbol{p}) \tag{4.1}$$

where R is the detector/dosimeter response, $\psi(\boldsymbol{p})$ is the angular flux with phase space variable of $(\boldsymbol{p} = \underline{r}, E, \hat{\Omega})$, which is obtained from solving Eq.(4.5), $\sigma_d(\boldsymbol{p})$ is the detector/dosimeter cross-section.

Here, we can rewrite the Eq.(4.1) to

$$R = \int d\boldsymbol{p} \int d\boldsymbol{p}^{'} \alpha(\boldsymbol{p}^{'} \rightarrow \boldsymbol{p}) S(\boldsymbol{p}^{'}) \tag{4.2}$$

where $S(\boldsymbol{p}^{'})$ is the source at phase space $(\boldsymbol{p}^{'} = \underline{r}^{'}, E^{'}, \hat{\Omega}^{'})$, the $\alpha(\boldsymbol{p}^{'} \rightarrow \boldsymbol{p})$ is the DRF coefficient, which is intrinsically a mapping function from phase space $\boldsymbol{p}^{'}$ to $\boldsymbol{p}$. The DRF coefficient is defined as

$$\alpha(\boldsymbol{p}^{'} \rightarrow \boldsymbol{p}) = \frac{\int d\boldsymbol{p}\sigma_d(\boldsymbol{p})\psi(\boldsymbol{p})}{\int d\boldsymbol{p}^{'}S(\boldsymbol{p}^{'})} \tag{4.3}$$

where $\psi(\boldsymbol{p})$ can be obtained by solving the LBE in fixed source form

$$H\psi(\boldsymbol{p}) = S(\boldsymbol{p}) \tag{4.4}$$

where the H is the transport operator, and can be written by

$$H = \hat{\Omega} \cdot \nabla + \sigma_t(\underline{r}, E) - \int_0^{\infty} dE \int_{4\pi} d\Omega\sigma_s(\underline{r}, E^{'} \rightarrow E, \hat{\Omega} \rightarrow \hat{\Omega}^{'}) \tag{4.5}$$

By selecting the unit source volume V_j and detector/dosimeter volume V_i, the DRF coefficient from Eq.(4.3) can be written by

$$\alpha_{ij} = \frac{\int_{V_i} dV \int_0^{\infty} dE \int_{4\pi} d\Omega\sigma_d(\underline{r}, E)\psi(\underline{r}, E, \hat{\Omega})}{\int_{V_j} dV \int_0^{\infty} dE \int_{4\pi} d\Omega S(\underline{r}, E, \hat{\Omega})} \tag{4.6}$$

where α_{ij} refers to the DRF coefficient for detector/dosimeter type i from the source location j.

Similar to the Eq.(4.6), the source distribution $S(\boldsymbol{p}^{'})$ can be calculated in a discretized form of S_j as well. After the DRF coefficients are obtained, the detector/dosimeter response can be simply obtained by:

$$R_i = \sum_{j=1}^{N} \alpha_{i,j} S_j \tag{4.7}$$

where S_j is the source strength at location j with total number of mesh N. The discretized source distribution can be calculated by either Monte Carlo code, deterministic code, or the RAPID code system with the FM approach.

4.2 Comparison between Importance Function and DRF Formulations

Here, we can compare the Eq.(4.2) with the importance function form of detector/dosimeter response calculation [58]. Table 4.1 shows the formulation comparison.

where $\psi^*(\boldsymbol{p})$ is the importance function with the phase space $\boldsymbol{p}$. It is obvious that the only difference between the two formulations is the weighting function of source term $S(\boldsymbol{p})$. The main differences of DRF coefficient and importance function are:

Table 4.1 Comparison of Detector/Dosimeter Response Formulations

DRF Methodology	Importance Function Methodology
$R = \int d\boldsymbol{p} \int d\boldsymbol{p}^{'} \alpha(\boldsymbol{p}^{'} \rightarrow \boldsymbol{p}) S(\boldsymbol{p}^{'})$	$R = \int\limits_{V_d} d\boldsymbol{p} \psi^{*}(\boldsymbol{p}) S(\boldsymbol{p})$

1. The DRF methodology utilizes forward approach to obtain the energy and angle integrated "modified importance functions", which are the DRF coefficients. In the DRF methodology, the DRF coefficients are calculated by tallying detector/dosimeter reaction rate from a unit volume source while importance function methodology directly utilize the detector/dosimeter cross-section as importance source to calculate the importance function.

2. Typically, the importance function from the importance function methodology is calculated using deterministic approach, which require discretization from the phase space. This means there are approximations with the importance function methodology calculated importance function. For the DRF coefficient, there is no approximations. Except the statistical uncertainty, which can be reduced by performing more sampling.

3. The DRF coefficients are a discrete set of function while the importance function calculated from the importance function methodology is a distribution over all the phase space.

4. Mesh convergence study has to be performed for importance function methodology calculated importance function while it is not necessary for the DRF coefficient calculations.

5. Selection of the energy group structure for the importance function is required for importance function calculations while it is not required for the DRF coefficients.

6. It is easier to perform sensitivity study and uncertainty quantification using the DRF coefficient since no approximation on the Physics and fast calculation with the CADIS methodology. For the importance function methodology, the sensitivity of the parameters might be hidden by the errors introduced from phase space discretization and geometry homogenization.

4.3 DRF Coefficient Pre-Calculations

To implement the DRF methodology, the first step is to calculate the DRF coefficient database. Two options can be selected for the DRF coefficient calculations: 1) Monte Carlo method; and 2) Deterministic method. The deterministic method requires discretization on

variables, e.g. energy, angle, and space. For this, systematic convergence study has to be performed. Literature also shows that $\sim 20\%$ of difference on RPV dosimetry calculations may be encountered using deterministic approach [96]. Although deterministic approach is capable of provide detailed neutron flux distribution, it will not be used for the DRF coefficient calculation due to the approximations. The Monte Carlo method, in contrast, is capable of performing calculations without approximations. Therefore, the Monte Carlo method is considered the better calculation tool. However, the DRF coefficient calculation are intrinsically deep penetration calculations. Therefore, the calculations will not be feasible if no variance reduction is applied. To achieve this, the CADIS methodology [37] is used for the calculations. In other word, we utilize the hybrid method with discrete ordinate method + Monte Carlo method for the DRF coefficient calculations. The procedures of the DRF methodology are:

1. Prepare an importance function deterministic model for the problem of interest, the model doesn't have to be very exact.
2. Calculate the approximated importance function using the model prepared in the step 1.
3. Estimate the Field of View (FOV) and Group-wise Contribution (GC) using the calculated importance function from the step 2.
4. Calculate the lower weight window bounds using the following formula.

$$w_l = \frac{R}{\frac{C_u+1}{2}\phi^*} \tag{4.8}$$

5. Prepare a Monte Carlo model for the problem of interest, and trim down the problem according to the information from the step 3 for both spatial and energy phase spaces.
6. Define the source volume per DRF coefficient.
7. Calculate the DRF coefficients using the model prepared in step 5 and the lower weight window bounds from the step 4 and process them into database.
8. Calculate the dose value or detector/dosimeter response using the existing DRF coefficients.

Note that the w_l in Eq.(4.8) refers to the lower weight window bounds, the C_u refers to the ratio between upper weight window bound and lower weight window bound, the MCNP manual suggested C_u=5 is efficient for neutron transport, the R refers to the approximated dosimeter response calculated by importance function, the ϕ^* refers to the scalar importance

function, which can be obtained by integrating the angular importance function $\psi^*(\underline{r}, E, \hat{\Omega})$ in the angle phase space

$$\phi^*(\underline{r}, E) = \int_{4\pi} d\Omega \psi^*(\underline{r}, E, \hat{\Omega}) \tag{4.9}$$

In this work, the importance functions are calculated using the PENTRAN$^{\text{TM}}$ code system [21]. The DRF coefficient calculations are performed by the MCNP5 code system [41].

4.3.1 Field of View and Group-wise Contribution

In most of the cases, the detector or dosimeter are very small comparing with the size of the nuclear system. To avoid unnecessary calculations, the FOV and GC studies are required for efficient of DRF coefficient calculations. The FOV estimation is perform using the importance function form of dosimeter response calculations [9]

$$R = \int_0^\infty dE \int dV \int_{4\pi} d\Omega q(\underline{r}, E, \hat{\Omega}) \psi^*(\underline{r}, E, \hat{\Omega}) \tag{4.10}$$

where R refers to the dosimeter response, $q(\underline{r}, E, \hat{\Omega})$ refers to the angular source distribution, the $\psi^*(\underline{r}, E, \hat{\Omega})$ refers to the angular importance function. The partial contribution from the phase space $(\underline{r}, E, \hat{\Omega})$ can be written by

$$C(\underline{r}, E, \hat{\Omega}) = \frac{q(\underline{r}, E, \hat{\Omega}) \psi^*(\underline{r}, E, \hat{\Omega})}{\int_0^\infty dE \int dV \int_{4\pi} d\Omega q(\underline{r}, E, \hat{\Omega}) \psi^*(\underline{r}, E, \hat{\Omega})} \tag{4.11}$$

If we want only the spatial distribution, we can integrate over energy and angle, and define the FOV by

$$FOV(\underline{r}) = \frac{\int_0^\infty dE \int_{4\pi} d\Omega q(\underline{r}, E, \hat{\Omega}) \psi^*(\underline{r}, E, \hat{\Omega})}{\int_0^\infty dE \int dV \int_{4\pi} d\Omega q(\underline{r}, E, \hat{\Omega}) \psi^*(\underline{r}, E, \hat{\Omega})} \tag{4.12}$$

The physical interpretation of Eq.(4.12) is the dosimeter contribution from every each spatial source location. For convenience, the FOV formulation used in this study will be

$$FOV(\underline{r}) = \frac{\int_0^\infty dE Q(\underline{r}, E) \phi^*(\underline{r}, E)}{\int_0^\infty dE \int dV Q(\underline{r}, E) \phi^*(\underline{r}, E)} \tag{4.13}$$

where the $\phi^*(\underline{r}, E)$ is the scalar importance function, which can be obtained from Eq. (4.9), $Q(\underline{r}, E)$ is the neutron source, which can be obtained by

$$Q(\underline{r}, E) = \int_{4\pi} d\Omega q(\underline{r}, E, \hat{\Omega}) \tag{4.14}$$

Similar to the FOV, we can define the Group-wise Contribution by

$$GC(E) = \frac{\int dV \int_{4\pi} d\Omega q(\underline{r}, E, \hat{\Omega}) \psi^*(\underline{r}, E, \hat{\Omega})}{\int_0^\infty dE \int dV \int_{4\pi} d\Omega q(\underline{r}, E, \hat{\Omega}) \psi^*(\underline{r}, E, \hat{\Omega})}, \tag{4.15}$$

The physical interpretation of Eq.(4.15) is the dosimeter contribution from each energy group. Similarly, the following equation is used in the study for convenience

$$GC(E) = \frac{\int dV Q(\underline{r}, E) \phi^*(\underline{r}, E)}{\int_0^\infty dE \int dV q(\underline{r}, E) \phi^*(\underline{r}, E)}. \tag{4.16}$$

Similar angle dependent only function can be obtained by integrating the numerator of Eq. (4.11) over spatial and energy phase spaces. The physical interpretation of such function will be the directional contribution to the detector/dosimeter. This function will not be used in this study, and therefore no mathematical form is provided here.

Since we use the discrete ordinate approach to perform the importance function calculation, the FOV and GC used in this study will be

$$FOV_i = \frac{\sum_{g=1}^{G} Q_{i,g} \phi^*_{i,g}}{\sum_{i=1}^{N} \sum_{g=1}^{G} Q_{i,g} \phi^*_{i,g}}, \tag{4.17}$$

where N and G are the total number of spatial mesh and energy group, $\phi^*_{i,g}$ and $Q_{i,g}$ are the group-wised importance function and source for mesh i and energy group g, which are obtained by

$$\phi^*_{i,g} = \int_{E_g}^{E_{g-1}} dE \int_{V_i} dV \phi^*(\underline{r}, E), \tag{4.18}$$

$$Q_{i,g} = \int_{E_g}^{E_{g-1}} dE \int_{V_i} dV Q(\underline{r}, E), \tag{4.19}$$

where V_i is the volume for mesh i.

However, if we pay attention on the flow chart in Fig. 3.1, the source distribution is obtained after the FOV is estimated. In other word, the $Q_{i,g}$ in Eq. (4.17) is unknown at the stage. Therefore, we can assume $Q_{i,g} = 1$ for simplicity, then Eq. (4.17) will become

$$FOV_i = \frac{\sum_{g=1}^{G} \phi^*_{i,g}}{\sum_{i=1}^{N} \sum_{g=1}^{G} \phi^*_{i,g}}, \tag{4.20}$$

This is a valid approximation since the importance function drop more drastically than the source distribution in most of the case. This approximation will be examined in the benchmark chapter later on. Similarly, we will have discretized GC

$$GC_g = \frac{\sum_{i=1}^{N} Q_{i,g}\phi^*_{i,g}}{\sum_{i=1}^{N}\sum_{g=1}^{G} Q_{i,g}\phi^*_{i,g}}. \tag{4.21}$$

If uniform source assumption is applied, the above form becomes

$$GC_g = \frac{\sum_{i=1}^{N} \phi^*_{i,g}}{\sum_{i=1}^{N}\sum_{g=1}^{G} \phi^*_{i,g}}. \tag{4.22}$$

4.4 Mapping of the DRF Coefficients

Since the geometry of a nuclear systme is usually symmetry, the coefficients can be easily obtained by mapping technique. Taking a commercial Pressurized Water Reactor (PWR) core as example, Fig. 4.1 shows ann example of radial DRF coefficient mapping.

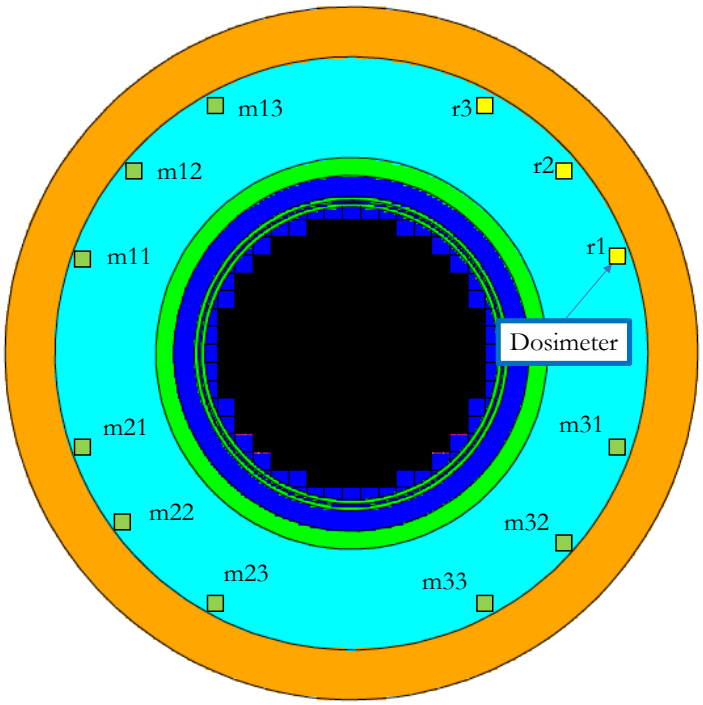

Figure 4.1 Example of DRF Coefficient Radial Mapping (TMI-1 Model)

Note that Fig. 4.1 is the TMI-1 (Three Mile Island Unit 1) model, which is the model for this study, and will be introduced in one of the benchmark chapters. The DRF coefficients

are calculated at the dosimeter radial location of r1, r2, and r3. Other three quarter's DRF coefficient can be simply obtained by mapping from the three locations:

1. r1 → m11, m21, and m31
2. r2 → m12, m22, and m32
3. r3 → m13, m23, and m33

Mathematical expression can be written by

$$\begin{aligned} DRF(numxa - x_{ai} + 1, y_{aj}, z_{slice}, z_{rel}, numxp - x_{pi} + 1, y_{pj}) \\ = DRF(x_{ai}, y_{aj}, z_{slice}, z_{rel}, x_{pi}, y_{pj}) \end{aligned} \tag{4.23}$$

$$\begin{aligned} DRF(x_{ai}, numya - y_{aj} + 1, z_{slice}, z_{rel}, x_{pi}, numyp - y_{pj} + 1) \\ = DRF(x_{ai}, y_{aj}, z_{slice}, z_{rel}, x_{pi}, y_{pj}) \end{aligned} \tag{4.24}$$

$$\begin{aligned} DRF(numxa - x_{ai} + 1, numya - y_{aj} + 1, z_{slice}, z_{rel}, \\ numxp - x_{pi} + 1, numyp - y_{pj} + 1) = DRF(x_{ai}, y_{aj}, z_{slice}, z_{rel}, x_{pi}, y_{pj}) \end{aligned} \tag{4.25}$$

where

- $numxa$, $numya$ - Number of fuel assemblies in x and y direction
- $numxp$, $numyp$ - Number of fuel pellets in x and y direction
- x_{ai},y_{aj} - Fuel assembly location
- x_{pi},y_{pj} - Fuel pellet location
- z_{slice} - the axial slice location of dosimeter
- z_{rel} - the axial relative DRF coefficient location to the z_{slice}

Similarly to the radial translation, the axial translation is performed using the following formulation

$$\begin{aligned} DRF(x_{ai}, y_{aj}, z_{slice} + N, z_{rel}, x_{pi}, y_{pj}) = DRF(x_{ai}, y_{aj}, z_{slice}, z_{rel}, x_{pi}, y_{pj}) \\ N = bnd, bnd + 1, ..., numza - bnd - 1, numza - bnd + 1 \end{aligned} \tag{4.26}$$

where $numza$ is the number of axial level of fuel assembly, the bnd is the axial level that DRF coefficient will not be affected by other structure materials. If the DRF coefficients are not sensitive to axial boundaries, the bnd will be 1.

4.5 Sensitivity of the DRF Coefficients to Different Parameters

For different applications, the dependency of the DRF coefficient on parameters can be different. It is important to study the sensitivity of the DRF coefficient on different parameters. Better DRF coefficient database management can be arranged from the information of sensitivity study. In this section, the parameters that may affect the DRF coefficient will be discussed. For radiation shielding calculations, the main focus of this dissertation is RPV neutron fluence calculation and SNF cask external dosimetry. Therefore, the parameters selected are according to these problems.

4.5.1 Sensitivity Parameters for RPV Neutron Fluence Calculations

For the RPV neutron fluence calculations, the DRF coefficients are expected to be sensitive to:

1. Dosimeter Type - Different dosimeter will have different reaction, energy threshold, and interaction rate (cross-section value).
2. Neutron Source Location - The DRF coefficient will be smaller when neutron source is further away from the dosimeter.

To ensure the aforementioned sensitivities, the following parameters have to be investigated:

1. Fission Spectrum - In the LWR, the nuclide that contribute to the thermal fission are mainly ^{239}Pu and ^{235}U. With different ratio of concentration between two of them, the fission neutron spectrum will be different. However, it is questionable if the dosimeter will "see" such change due to the nature of deep penetration problem.
2. Isotopic of Fuel Assemblies - When the fuel assembly undergoes irradiation by the neutrons, the isotopic will change. Since the neutrons has to travel through these assembly and exit the RPV, and finally contribute to the dosimeter response, it is questionable the DRF coefficient will be sensitive to the change of isotopic. This parameter combined with the previous one (fission spectrum) are mainly from the fuel assembly depletion.
3. Temperature of the Core - When the reactor is raised to full power for operation, the temperature of fuel assemblies and coolant will be high above the room temperature. Since temperature mainly affect the shape of resonance, the fast neutrons coming out of the RPV may not be affected. However, it has to be examined.

4. Coolant Density - When power of a nuclear reactor is raised to operating condition, the density of coolant will be changed by temperature. It is expected that the DRF coefficient will be sensitive to the coolant density.

5. Void Fraction - Under transient scenario, the coolant might become mixture of liquid and vapor. The DRF coefficients are expected to be sensitive to the void fraction since there will be a major change on the coolant density.

6. Boundary Structures - As indicated in the section 4.4, the DRF coefficient can be translated based on the geometry symmetry or similarity. However, when the DRF coefficients are translated to the location nearby the boundary structure, the behavior of neutrons might be different. Therefore, sensitivity of the DRF coefficients to the boundary structures has to be studied.

The extreme scenario such as fuel assembly melt down are not considered in the development of DRF methodology. It can be further studied. However, the DRF methodology might not be efficient under such condition due to uncertainties of radiation source location.

4.5.2 Sensitivity Parameters for SNF Cask External Detection

Similar to the RPV neutron fluence calculation, the DRF coefficients for SNF Cask External Detection will definitely be sensitive to (1) Detector/Dosimeter type; and (2) Source location. For the fuel assemblies in the SNF cask, typically they will be cooled in the SNF pool for more than 5 years before moving them to the cask. Therefore, there will be lesser parameters need to be considered. The parameters are:

The following parameters need to be examined for the SNF cask external dosimetry:

1. Source Spectrum - For SNF cask, the part that dominates the external dose is mainly primary photon for the first 50 to 100 years [97], depending on the cask material. The neutron and secondary photon will dominate the external dose for the remaining time up to 10,000 years. The source spectrum of photon and neutron will be different by assembly burnup and cooling time. Therefore, it is necessary to examine the DRF coefficient sensitivity to these parameters.

2. Isotopic of Fuel Assemblies - The isotopic change is always accompanied with spectrum change. However, it is possible to separate them for sensitivity study when performing computation. The isotopic affect the interaction between photon/neutron and the target nuclide while spectrum affect the energy distribution of the emitted particle.

3. Boundary Structures - Similar to the RPV neutron fluence calculation, the boundary structure may affect the particle behavior and thus have to be examined.

Chapter 5

Benchmark of the DRF Methodology: GBC-32 Cask with a ^{3}He Detector

In this chapter, a mock up Spent Nuclear Fuel (SNF) cask external detection problem is used for benchmarking the DRF methodology [98]. The SNF cask model used in this chapter is the GBC-32 [99], which stands for 32 SNF assembly in the General Burnup Credit benchmark problem. The GBC-32 cask is flooded with water. The ^{3}He detector is selected for study and placed on the surface of the cask. In this study, the MCNP5 [41] code system is used for DRF coefficients while the PENTRAN^{TM} code system is used for importance function calculations.

5.1 Burnup and Cooling Time Dependent Material Composition Calculations

Before performing detector response calculations, the first task is to calculate the material composition for different burnup levels and cooling times. The burnup dependent material compositions of the fuel are calculated using the TRITON depletion module [100] in SCALE6 code platform. There are 7 burnup levels with no cooling time being calculated. The burnup levels selected here are 5, 10, 16, 20, 30, 40, and 50 GWd/MTHM. A single 2D 17×17 fuel assembly NEWT [101] model with no burnable absorber and reflected boundary conditions is used for the depletion calculations.

To calculate the detector response, the DRF coefficients and FM coefficients are all required. For the DRF and FM coefficient calculations, the most important information from the depletion calculation is the neutron spectrum. The independent neutron spectrum is calculated by the ORIGEN [102] code in the TRITON module. Note that the ORIGEN code has incorporated the independent neutron source calculation code - SORCE [103], and used it

as a routine for calculating the independent neutron source strength and spectrum. For the fission neutron spectrum, the Watt fission spectrum [104] is used, which MCNP5 manual [41] has the suggested constants for different fissile nuclides. The Watt fission spectrum can be written by

$$f(E) = Ce^{-\frac{E}{a}} \sinh \sqrt{bE} \tag{5.1}$$

where C is a normalized constant, which is selected that $\int_0^\infty dEf(E) = 1$, the a and b are nuclide dependent constants. With depleted fuel, presence of ^{239}Pu will change the behavior of Watt fission spectrum. Therefore, for mixture with different fissile isotopes, the a and b coefficients can be obtained by

$$\bar{a} = \sum_i \frac{a_i \nu_i \sigma_{f,i} N_i}{\nu_i \sigma_{f,i} N_i} \tag{5.2}$$

$$\bar{b} = \sum_i \frac{b_i \nu_i \sigma_{f,i} N_i}{\nu_i \sigma_{f,i} N_i} \tag{5.3}$$

where the N_i is the atomic number density of fissile nuclide i, $\nu_i \sigma_{f,i}$ is the number of fission neutron multiplied b the fission cross-section of fissile nuclide i. The denominator of Eq.(5.2) and (5.3) are referring to a weighting function for calculating averaged Watt fission spectrum coefficients.

5.2 MCNP5 Model Description

The dimensions of the GBC-32 cask are 87.5 cm from inner radius, 107.5 cm from outer radius. The cask is loaded with 32 standard Westinghouse PWR 17 OFA/V5 fuel assemblies. There are 25 empty guide tubes filled with water per assembly. Fig. 5.1 and 5.2 show the radial projection of a single fuel assembly and the 3D model of radial and axial projection with multiple ^{3}He detector locations.

The active fuel assembly height is 365.76 cm with 144 axial level. The fuel assembly pitch is 23.7565 cm. The fuel pellet size is 0.3922 in radius and 2.54 cm in height. The inner cladding dimension is 0.40005 cm for inner radius and 0.4572 cm for outer radius. All the sizes of ^{3}He detectors are $2.5cm \times 2.5cm \times 10cm$.

Two assembly burnup loading patterns are selected as shown in the Fig. 5.3. Note that the axial burnup levels are uniform in this case.

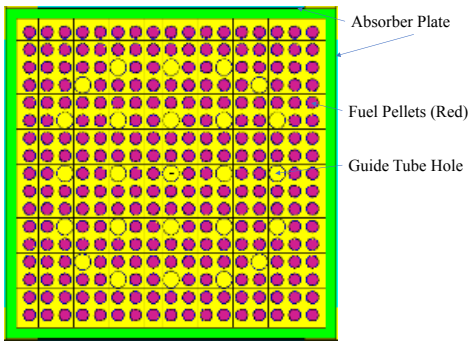

Figure 5.1 Radial Projection of a Westinghouse PWR 17 OFA/V5 Fuel Assembly

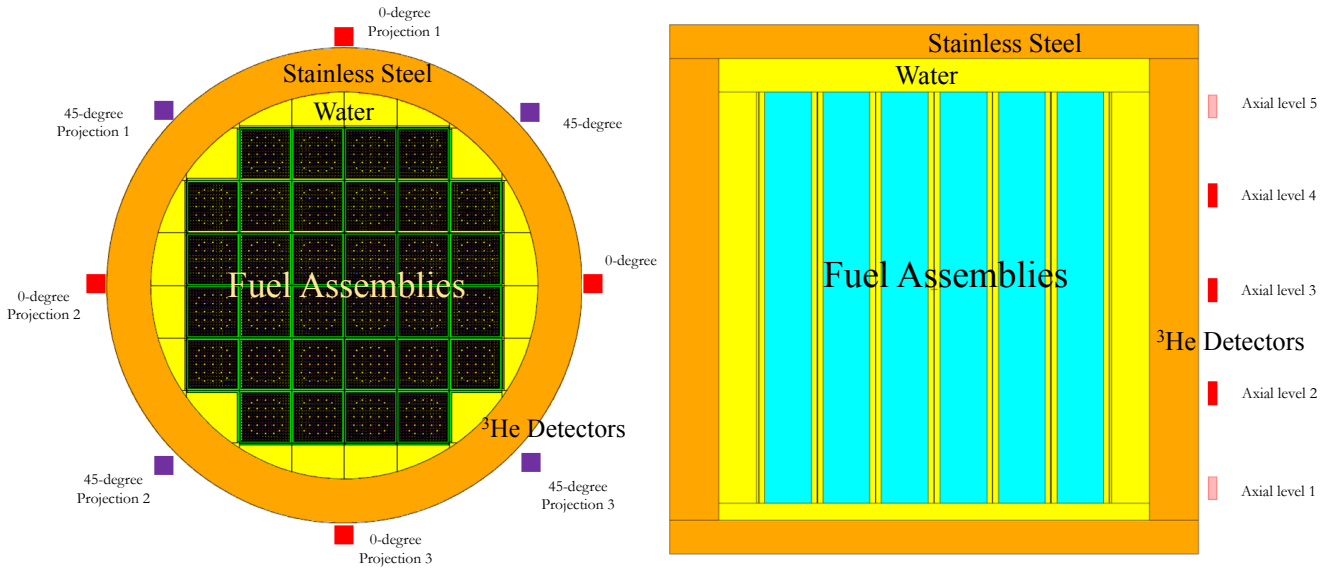

(a) Radial Projection

(b) Axial Projection

Figure 5.2 GBC-32 SNF Cask with ^{3}He Detectors MCNP5 Model

The first assembly profile is filled with fuel assembly with burnup level of 50 GWd/MTHM with and cooling time while the second profile replaces two of the peripheral fuel assemblies with burnup level of 30 GWd/MTHM and no cooling time. The independent neutron source distributions are assumed to be uniform within a single fuel assembly.

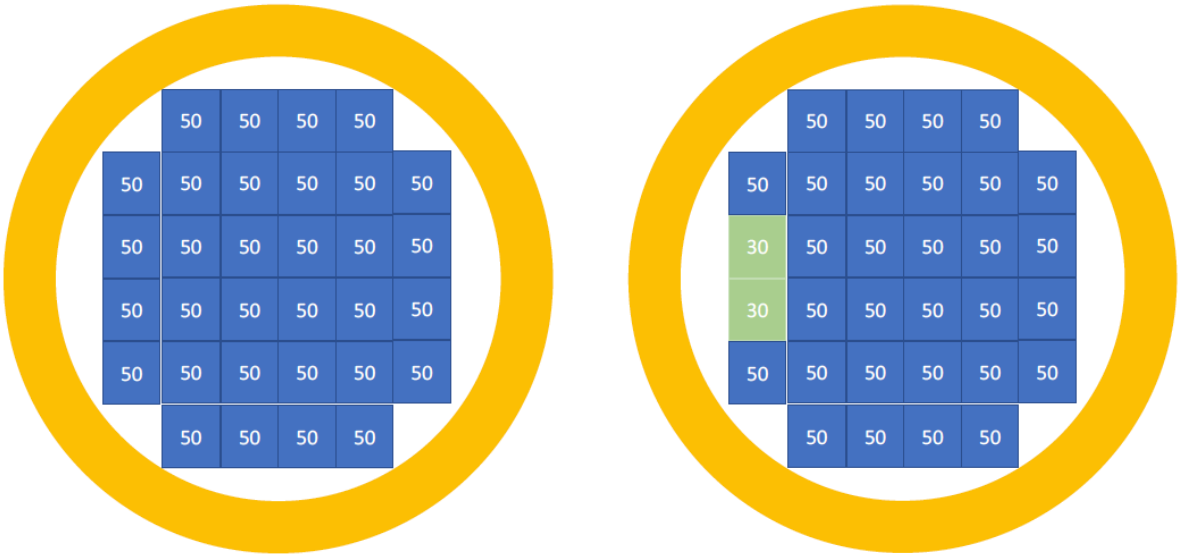

(a) Assembly Burnup Profile 1 **(b)** Assembly Burnup Profile 2

Figure 5.3 Assmebly Burnup Profiles (Units in GWd/MTHM with no Cooling Time)

5.3 Importance Function Calculations and Field of View

The importance functions are calculated using the PENTRAN^{TM} code system. This section will discuss the importance function calculations and the tasks required for efficient DRF coefficient calculations.

5.3.1 PENTRAN^{TM} Importance Model

The PENTRAN^{TM} GBC-32 Importance model with ^{3}He detector location at 0-degree and axial level 3 shown in the Fig. 5.2 is shown in the Fig. 5.4.

The detector does not really "see into" the system too much. Therefore, the importance function calculation only requires a segment of the GBC-32 cask near the ^{3}He detector. To be conservative at the beginning, two assemblies with axial level of $\sim$ 40 cm is selected for importance function calculations.

The mesh size of the importance model is from minimal 0.625 cm to maximum 5 cm. The anisotropic scattering Legendre expansion for differential scattering cross-section used is P3. The angular quadrature order selected is S8. The convergence criteria is 5×10^{-3}. The cross-section library used is the BUGLE96 47 group neutron cross-section [62]. The ^{3}He detector size is 2.5 cm$\times$2.5 cm$\times$10 cm. The ^{3}He absorption cross-section is used as the importance source. Fig. 5.5 shows the magnitude of microscopic ^{3}He absorption cross-section.

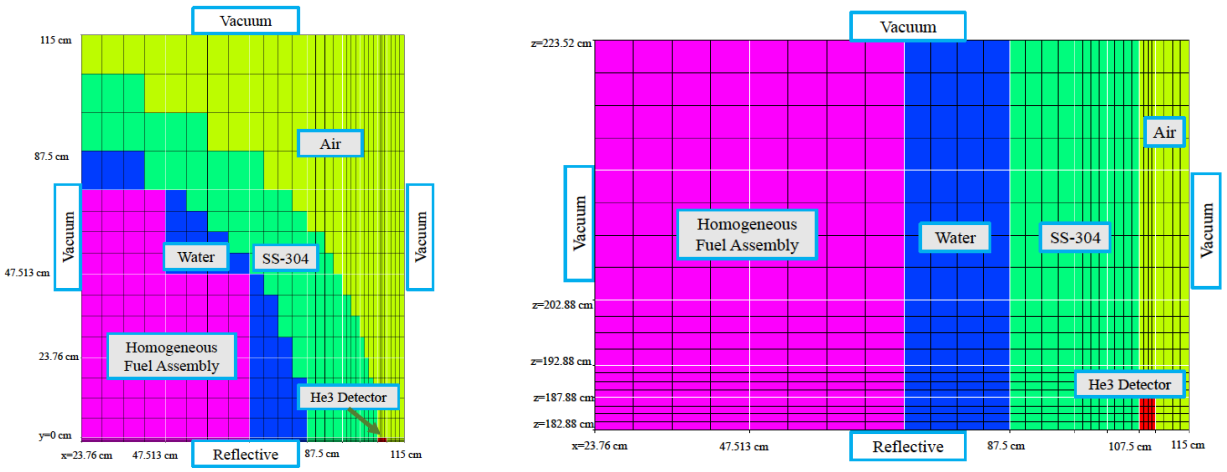

(a) Radial Projection **(b)** Axial Projection

Figure 5.4 PENTRAN^{TM} GBC-32 Cask with a ^{3}He Detector Importance Model

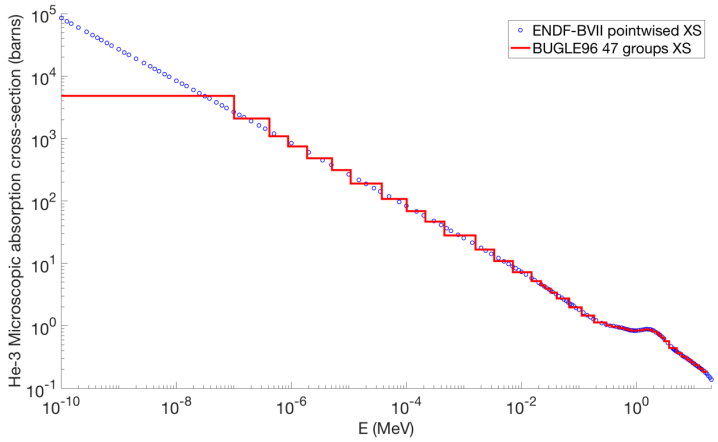

Figure 5.5 ^{3}He Microscopic Cross-section

5.3.2 PENTRAN^{TM} Calculated Importance Functions

Fig. 5.6 shows the PENTRAN^{TM} calculated ^{3}He detector importance functions for two selected energy groups. The calculation time of the importance function is 23 minutes on 2 processors.

The group 8 represents the fast neutron group, which is referring to neutron incident with higher energy. The group 43 represents the thermal energy group, which is referring to neutron incident with lower energy. It is shown that the slope of importance function of group 43 is steeper than group 8 when location moving further away from the detector. It is because the neutron with lower energy born far away from the detector is less likely to

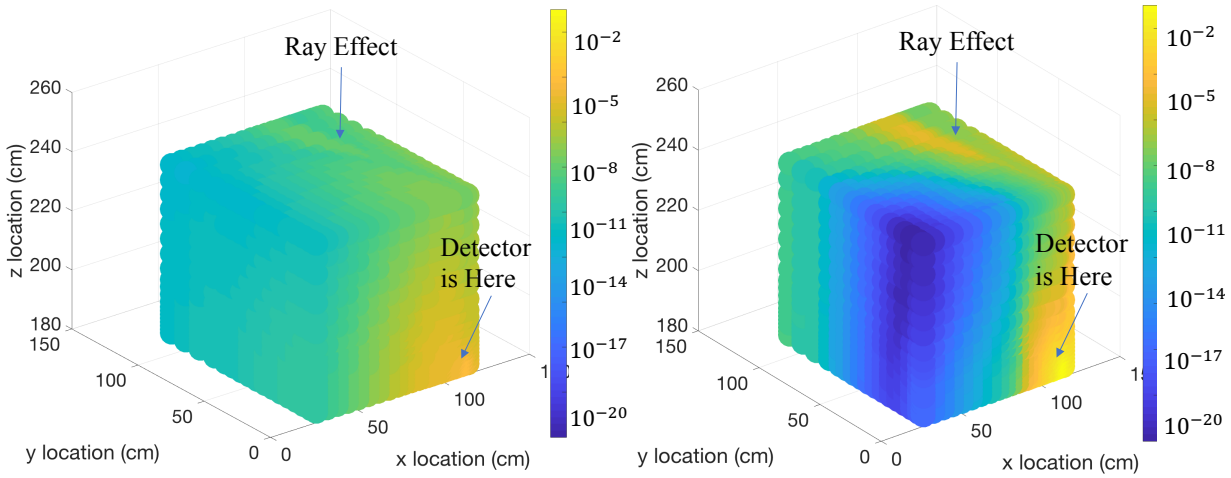

(a) Group 8: 3.68 MeV < E < 4.97MeV **(b)** Group 43: 1.86 eV < E < 5.04eV

Figure 5.6 ^{3}He Detector Importance Functions for 0-degree Detector

make contribution to the detector response. For fast neutron born at the same location, the probability to make contribution to the detector response is much higher. Note that ray effect can be found in Fig. 5.6 in the air region due to optical thick (or low interaction) media. Since the use of importance functions are variance reduction of Monte Carlo calculations, the ray effect will not affect the final results. However, the quality of importance functions may affect the efficiency of the variance reduction. The support of this statement can be found in the Appendix A.

5.3.3 Field of View Analysis by Importance Functions

As it was mentioned in section 4.3.1, the FOV is calculated as *a priori* for efficient DRF coefficient calculations. The FOV formulation from Eq.(4.20) is used with assumption of $Q_{i,g} = 1$, which gives the new FOV formulation by

$$FOV_i = \frac{\sum_{g=1}^{G} \phi^*_{i,g}}{\sum_{i=1}^{N} \sum_{g=1}^{G} \phi^*_{i,g}}. \tag{5.4}$$

This is a valid approximation for most of cases. The slope of importance functions are typically much steeper than the source distribution. Taking the 0-degree detector as example, the importance function drops minimal 6 orders of magnitude within a fuel assembly while the neutron source distribution only drops factor of 30. Under this condition, the importance function dominates the FOV. If there is a scenario that the source drops similar orders of magnitude as importance function, the Eq.(5.4) will under estimates the FOV.

The FOV for ^{3}He detector located at 0-degree and axial location 3 is shown in the Fig. 5.7. Four axial levels with 10.16 cm per segment are selected for FOV analysis.

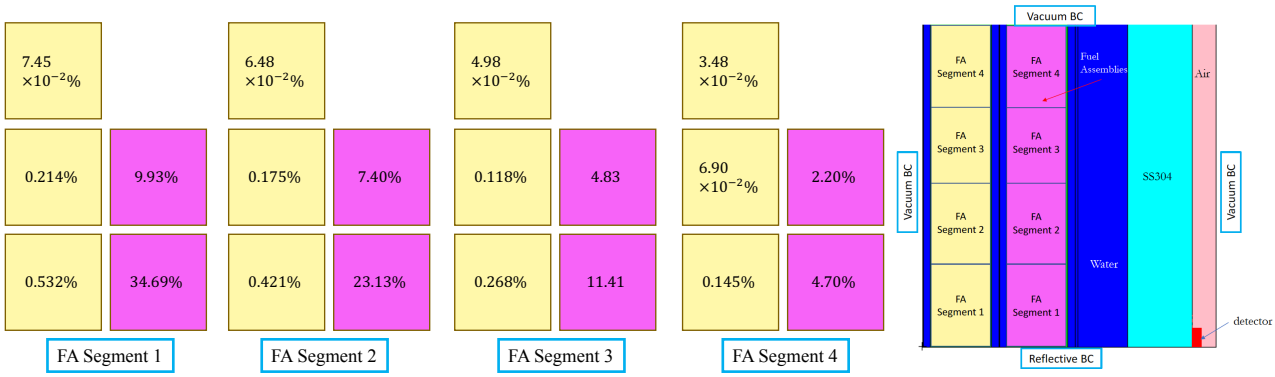

Figure 5.7 FOV for ^{3}He detector located at 0-degree and axial location 3

The results show that more than 95% of the detector responses are from the closest two assemblies (shown as purple in Fig. 5.7). This means that only the DRF coefficients from the two purple assembly need to be calculated.

5.3.4 Group-wised Contribution Analysis by Importance Functions

The GC is also important for the efficient DRF coefficient calculations. Using the Eq.(4.16) with the same assumption $Q_{i,g} = 1$, the GC for ^{3}He detector located at 0-degree and axial location 3 is shown in the Fig. 5.8.

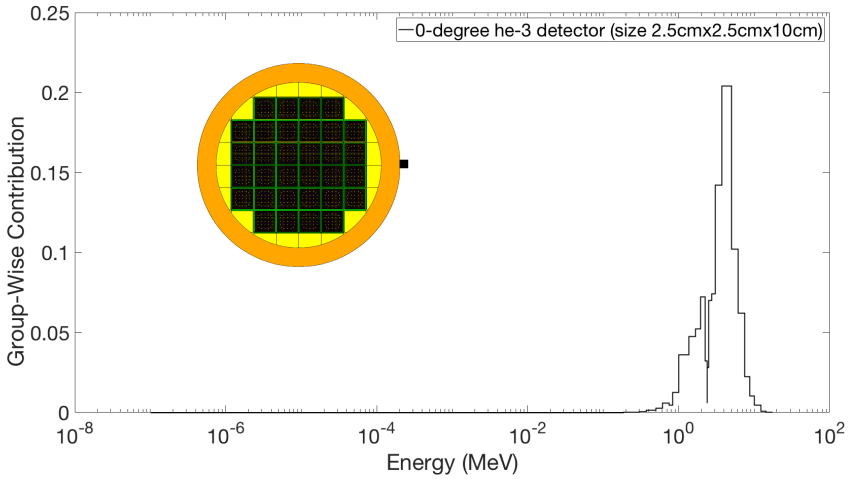

Figure 5.8 GC for ^{3}He detector located at 0-degree and axial location 3

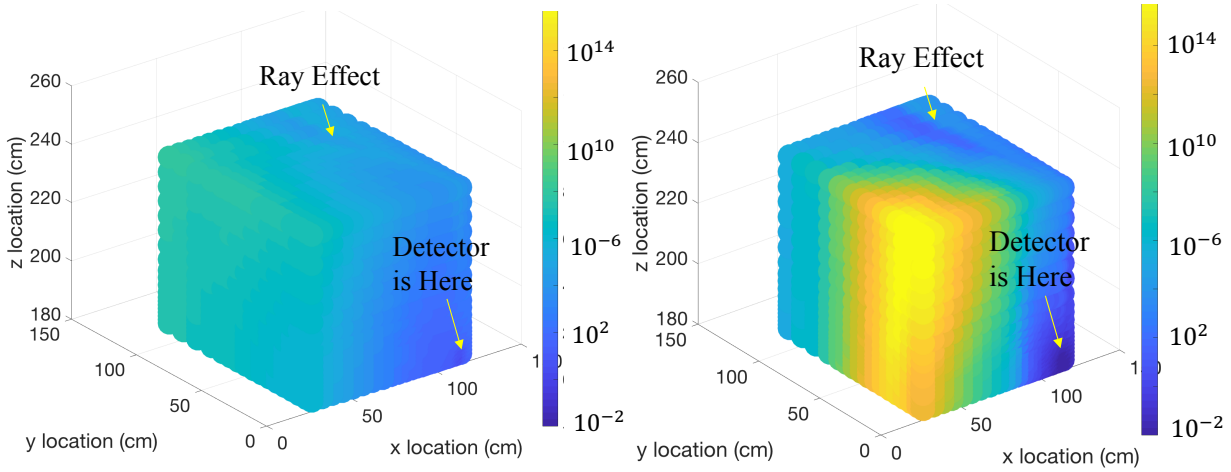

(a) Group 8: 3.68 MeV < E < 4.97MeV

(b) Group 43: 1.86 eV < E < 5.04eV

Figure 5.9 ^{3}He Detector Lower Weight Window Bounds for 0-degree Detector

The results show that with energy lower than ∼0.5 MeV, the detector response contribution almost drops to zero. Therefore, a cutoff energy for E=0.5 MeV can be selected for the ^{3}He detector located at 0-degree. A more detailed GC and FOV study for different ^{3}He detector locations and sizes can be found in the Appendix B.

5.3.5 Lower Weight Window Bounds Calculation

Another application of the calculated importance function is for the use of CADIS methodology. The CADIS methodology requires weight windows for transport biasing. Note that the source biasing will not be used here since the DRF coefficient calculations assume uniform source distribution over a singe fuel pellet. The corresponding lower weight window bounds calculated from Fig. 5.6 using Eq.(4.8) are shown in the Fig. 5.9.

The lower weight window bounds are intrinsically the inverse values of importance functions. Therefore, the lower weight window bounds of fast neutron (group 8) at fuel assembly location is lower than the thermal neutron (group 43). The neutron born at such location with high energy are more likely to survive while the thermal neutron are more likely to be killed by the high weight window bounds.

5.4 DRF Coefficient Calculations

The DRF coefficients are calculated using the fixed-source Monte Carlo calculations by MCNP5 with transport biasing technique in the CADIS methodology. The fresh fuel material

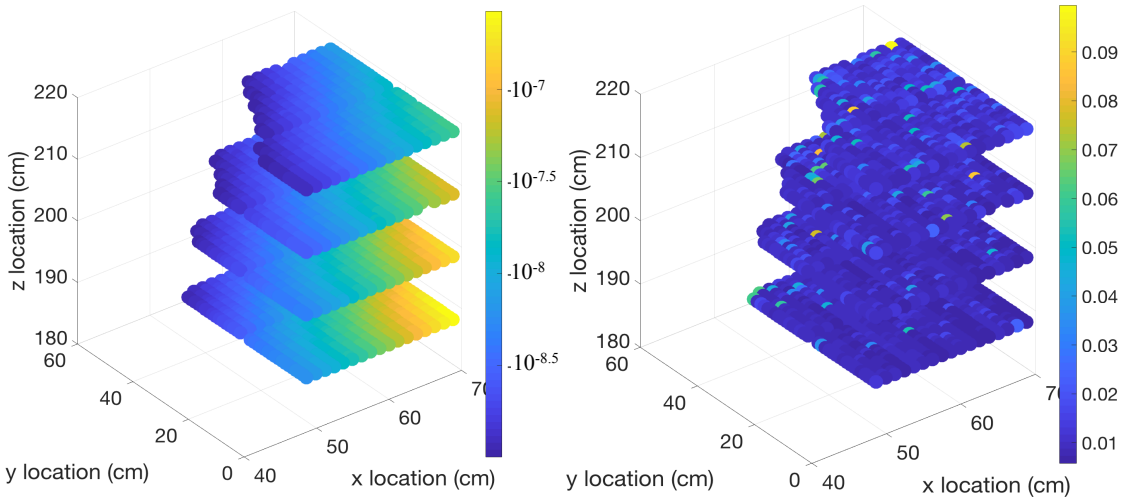

(a) DRF Coefficients **(b)** 1σ Statistical Uncertainties

Figure 5.10 DRF Coefficient of ^{3}He detector located at 0-degree and axial location 3

and fission spectrum are used for the DRF coefficient calculations by assuming they are not sensitive to the burnup levels. The unit neutron source region selected here is radius 0.3922 cm with height of 10.16 cm. Remark that a fuel pellet dimension is 0.3922 cm in radius and 2.54 cm in height. By doing this, we are assuming DRF source mesh of 4 fuel pellet lumping together axially. There are 5780 DRF coefficients calculated with individual calculation time $\sim$ 2 minutes using 8 processors. The total calculation is $\sim$ 1.15 days with 56 processors. The number of particle used for the DRF coefficient calculations are 5×10^6. Fig 5.10 shows the calculate DRF coefficients for two purple assemblies shown in the Fig. 5.7. Note that values below 10^{-9} are filtered out due to low contributions. The averaged statistical uncertainties of the DRF coefficients is $\sim$ 2%.

The DRF coefficients drop $\sim$2 orders of magnitude with one fuel assembly away (23.7565 cm) radially while it drops $\sim$1 order of magnitude with axial distance of $\sim$ 40 cm. The DRF coefficients have steeper slope in radial direction rather than axial direction in this case. This is mainly because the ^{3}He detector is long in axial direction in this case.

The DRF coefficients for detector at 45-degree axial location 3 are also provided in Fig. 5.11. Three fuel assemblies with 5 axial levels are selected for this detector location. This is mainly because the detector is closer to the fuel assemblies, and therefore more fuel assemblies will make contributions to the detector response. Note that the plot of DRF coefficients and their relative statistical uncertainties are rotated for 180-degree for convenience of analysis. The 45-degree DRF coefficients show a larger magnitude than 0-degree. This is mainly because the 45-degree detector is closer to the fuel assemblies.

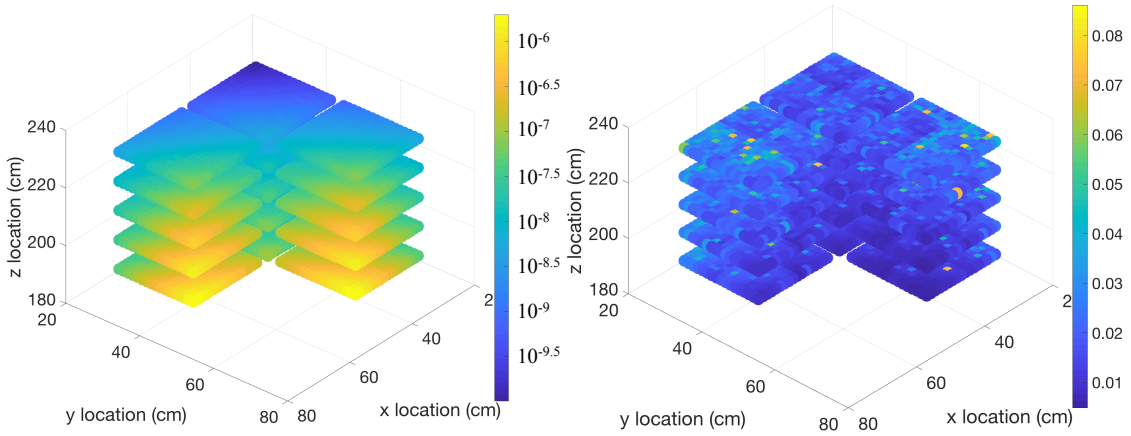

(a) DRF Coefficients **(b)** 1σ Statistical Uncertainties

Figure 5.11 DRF Coefficient of ^{3}He detector located at 45-degree and axial location 3 (Figures are rotated by 180-degree)

5.5 Neutron Source Calculations Using RAPID

To calculate the detector response, the neutron source distribution has to be calculated first. The subcritical multiplication mode of RAPID code system is used for calculating the fission source distributions. The FM coefficient are prepared with assembly initial enrichment of 4wt% and burnup level range from fresh fuel to 50 GWd/MTHM with no cooling time. The FM coefficients are calculated using the MCNP5 code system with $\sim$ 30 minutes on 8 processors for unit coefficient calculation. The total calculation time is $\sim$ 22 hours on 56 processors. The RAPID calculations parameters are:

- Radial single assembly FM coefficient collapsing scheme: 6 5 6 (summation=17, which is number of fuel pellets in x/y direction)
- Axial FM coefficient collapsing factor: 4 (Total 144 fine axial level, which is collapsed to 36 coarse axial level in this case)
- Fission density convergence tolerance: 10^{-5}
- Eigenvalue convergence tolerance: 10^{-7}
- Number of FM coefficient radial relative assembly: 2
- Number of FM coefficient relative axial level: 29

The details of FM coefficient collapsing and translation approaches can be found in one of the reference article [56] and the chapter 3. Figs. 5.12 and 5.13 show the calculated 2D

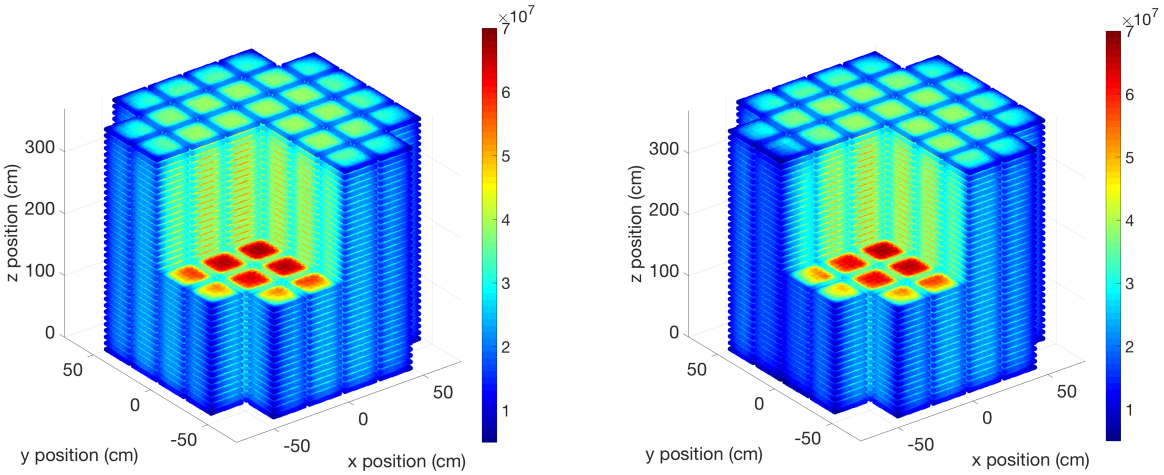

(a) Assembly Burnup Profile 1 **(b)** Assembly Burnup Profile 2

Figure 5.12 3D Pin-wised Fission Neutron Source (neutrons/sec)

and 3D fission neutron source distribution. Note that the independent neutron sources are assumed to be uniform axially.

Fig. 5.13b shows the $17^{th}/36^{th}$ slice of fission neutron source distribution for burnup profile 2. The spatial distribution of this case is symmetry due to uniform 50 GWd/MTHM fuel assembly placement. In contrast, the fission source distribution for burnup profile 2 is tilted toward right since the independent neutron sources of the 30 GWd/MTHM is lower than the 50 GWd/MTHM fuel assemblies. Lower strength of independent neutron sources will consequently induce lower fission rate. The detailed calculation and FM coefficient processing time and the subcritical multiplication factors are shown in the Table 7.2.

Table 5.1 Detailed RAPID Calculation Results and Times

Item	Burnup Profile 1	Burnup Profile 2
Input Read in	0.0011 seconds	0.0011 seconds
Database Read and Collapse	10.53 seconds	12.35 seconds
Database Summary	0.82 seconds	0.83 seconds
Interpolating	0.44 seconds	0.37 seconds
FM Coefficient Filling	7.75 seconds	7.63 seconds
Full 3D Calculations	4.78 seconds	6.30 seconds
2D Slice Cal. + FM Coeff. Collapsing	15.00 seconds	14.73 seconds
Total Time	39.32 seconds	42.21 seconds
Number of Iteration	25	33
Subcritical Multiplication Factor (M)	1.51571	1.57113

The results show that the subcritical multiplication factor of burnup profile 2 is a little

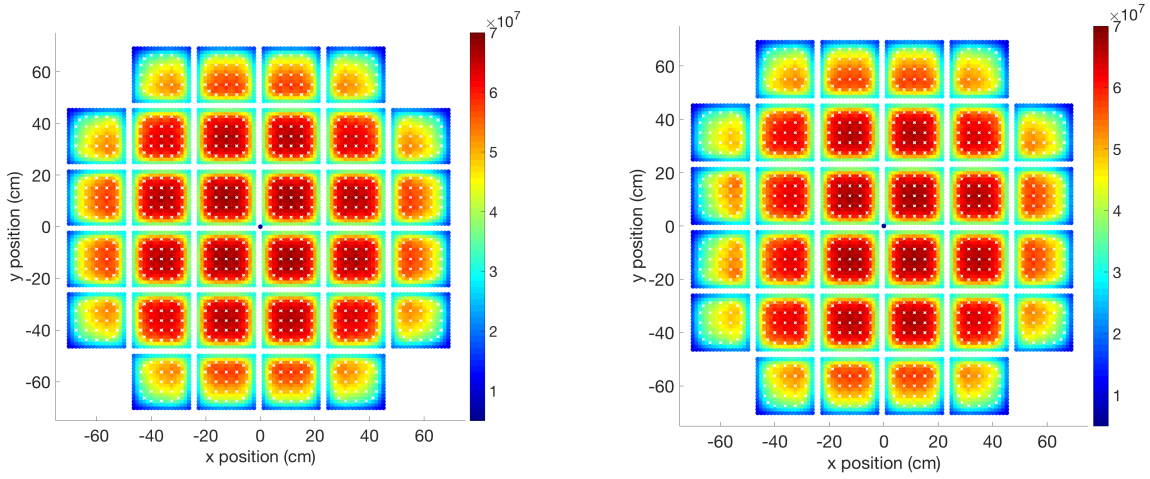

(a) Assembly Burnup Profile 1

(b) Assembly Burnup Profile 2

Figure 5.13 The 17^{th} Axial Level Pin-wised Fission Neutron Source (neutrons/sec)

higher than the profile 1. This is mainly because there are two assembly with lower burnup level. More fissile materials are presented in burnup profile 2 with more fission neutron multiplication.

5.6 ^{3}He Detector Response Calculations

To calculate the neutron detector response in a subcritical multiplication system, we will need to modify the Eq.(4.7) by

$$R_i = \sum_{j=1}^{N} \alpha_{i,j} S_j^{fiss} + \beta_{i,j} S_j^{ind} \tag{5.5}$$

where $\alpha_{i,j}$ and $\beta_{i,j}$ are the DRF coefficient for fission and independent neutron sources, the S_j^{fiss} and S_j^{ind} are the fission and independent neutron sources, respectively. Note that the neutron sources shown in the Figs. 5.12 and 5.13 are S_j^{fiss}. Here, only the fission source is considered for the ^{3}He detector response calculations.

5.6.1 Benchmarking the 0-degree Axial 3 ^{3}He Detector Response Calculation

Table 5.2 shows the comparisons of the calculated detector responses between RAPID using the DRF methodology and MCNP5+CADIS for the burnup profile 1.

Table 5.2 Burnup Profile 1 ^{3}He Detector Response Comparison for 0-degree Axial Level 3

Code/Approach	Detector Response (neutrons/sec)	Differences in %
RAPID/DRF (2 FAs)	5339.68	-3.50%
RAPID/DRF (5 FAs)	5551.40	0.33%
MCNP+CADIS (5 FAs)	5533.36±58.64	Reference

The results show that excellent agreement is observed. The detector response shows a 0.33% differences comparing with the MCNP5 reference calculation if the 5 assemblies in the Fig. 5.7 are all included. If only the purple assemblies are included, -2.62% of difference is observed, which has verified the FOV prediction in the section 5.3.3. The calculation wall-clock time comparisons are shown in the Table 5.3. Note that the RAPID DRF methodology calculations include the computation time for fission neutron source calculations.

Table 5.3 Burnup Profile 1 with 0-degree Axial Level 3 Detector Calculation Wall-clock Times

Code/Approach	Calculation Time	Number of Processors	Speedup
RAPID/DRF (2 FAs)	40.32 seconds	1	465.40
RAPID/DRF (5 FAs)	40.32 seconds	1	465.40
MCNP+CADIS (5 FAs)	312.75 minutes	8	Reference

Significant speedup on the detector response calculations is observed. The reference calculation is actually taking advantage from the RAPID code system by using the detailed pin-wised fission source distribution. The computation time will be more than what is shown here if traditional Monte Carlo subcritical multiplication calculation is performed.

5.6.2 Sensitivity of ^{3}He Detector DRF Coefficient to Burnup Level

As mentioned in the section 5.4, it is assumed that ^{3}He Detector DRF coefficients are not sensitive to the burnup levels. Thus far, the results show an excellent agreement, which indirectly verify the validity of the assumption. However, it is worthy to further verify the assumption by actually performing DRF coefficient calculations using burned fuel composition and spectrum. Table 5.4 shows the calculated detector responses using DRF coefficients

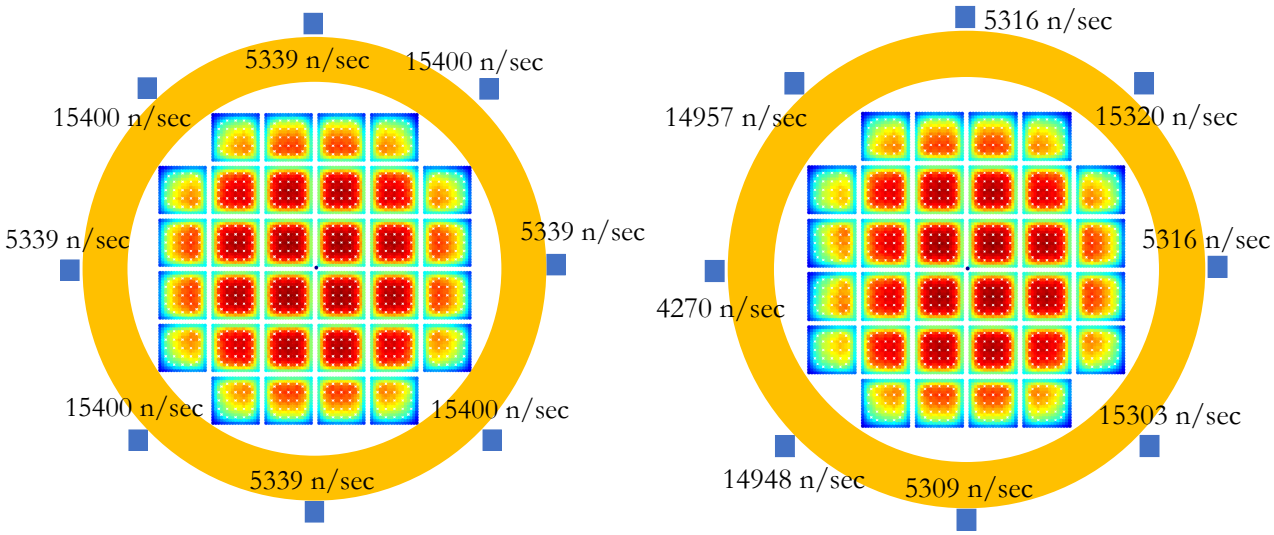

(a) Assembly Burnup Profile 1 **(b)** Assembly Burnup Profile 2

Figure 5.14 ^{3}He Detector Responses for Axial Level 3

calculated from fresh fuel and 50 GWd/MTHM burned fuel spectrum and material compositions.

Table 5.4 ^{3}He Detector Response Assembly Burnup Level Sensitivity Study

Code/Approach	DRF Coefficients	Det. Res. (neutrons/sec)	Diff. in %
RAPID/DRF (2 FAs)	Fresh Fuel	5339.68	-3.50%
RAPID/DRF (2 FAs)	50 GWd/MTHM	5383.56	-2.71%
MCNP+CADIS (5 FAs)	-	5533.36±58.64	Reference

Nearly negligible effect from burnup level is observed for the ^{3}He detector DRF coefficients. Therefore, the ^{3}He detector DRF coefficients created in this benchmark problem can be applied to fuel assembly burnup range at least up to 50 GWd/MTHM. This is mainly because the ^{3}He detector is sensitive to thermal neutron. This may not be true if fast neutron sensitive detector is used. This will be further examined in the next few chapters with other benchmark problems.

5.6.3 Detector Responses for Multiple Detector Locations

By taking advantage from the geometry symmetry, the DRF coefficients can be mapped to other detector locations. Fig. 5.14 shows the calculated detector responses at various detector locations in axial level 3 (middle of fuel assembly axial location).

The results shows that a symmetry pattern of detector responses is observed for assembly

burnup profile 1 while it is tilted for burnup profile 2. Similar to the radial DRF coefficient translation, axial dependent detector responses can also be obtained by axially translating the DRF coefficients. Fig. 5.15 shows an example of axial dosimeter responses for 0-degree ^{3}He detector with burnup profile 1.

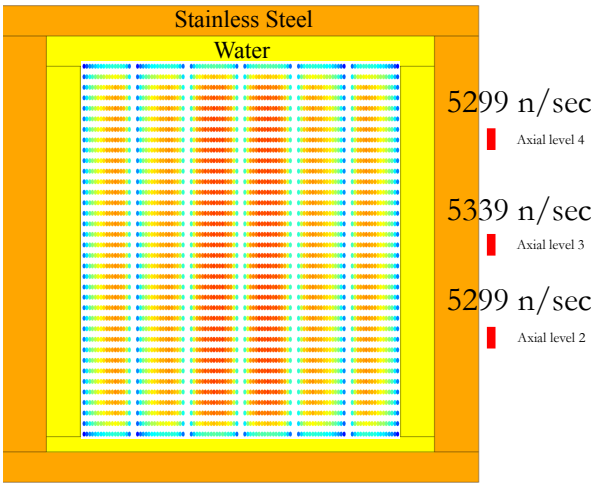

Figure 5.15 ^{3}He Detector Responses for 0-degree and Assembly Burnup Profile 1

The results show that the highest detector response is at mid-axial location. A symmetry behavior of detector response is observed since the fission source distribution is symmetry. Very little difference on detector responses at different axial location is observed. This is mainly because the assumption of axially uniform independent source distribution. The variation of axial fission neutron source distribution is driven by the independent neutron source. Note that all the detector responses shown in Fig. 5.14 and 5.15 are all within $\sim 1\%$ or lesser differences comparing with MCNP5 reference calculations.

5.6.4 Sensitivity of the DRF Coefficients and Detector Responses to the Boundary Structures

When moving the detector to the very top or bottom (axial locations 1 and 5 in Fig. 5.2), the axial DRF coefficients translation might be affected. To test the performance of the DRF methodology under such circumstance, detector responses at axial locations 1 and 5 are calculated using two different DRF coefficients: (1) DRF coefficients from axial translation; and (2) DRF coefficients calculated at boundaries. Table 5.5 shows the detector responses calculated by using different DRF coefficients.

Nearly negligible effect from the boundary structure is observed. The 1σ relative statistical uncertainty of MCNP reference calculation is $\sim$2.05%. Therefore, the DRF methodology calculated detector responses are all within 3σ relative statistical uncertainty ($\sim$99% confidence) of the reference calculation. This might be attributed to ^{3}He detector is only sensitive

Table 5.5 ^{3}He Detector Responses Comparison for 0-degree and Axial Level 5

Code/Approach	DRF Coefficients	Det. Res. (neutrons/sec)	Diff. in %
RAPID/DRF (2 FAs)	Axial Translation	3183.04	-2.70%
RAPID/DRF (2 FAs)	Real	3152.12	-3.65%
MCNP+CADIS (2 FAs)	-	3271.55±67.07	Reference

to thermal neutrons. Presence of water within the cask might be another reason for this observation. The bottom structures are very similar to the top structure. Therefore, it can be assumed that bottom structure has negligible effect on the DRF coefficients as well. However, if the detector is moved to the location above or below axial active fuel region (above axial location 5 or below axial location 1), different sets of DRF coefficients will have to be calculated separately. Here, the calculation time comparisons are also provided in the Table 5.6.

Table 5.6 Burnup Profile 1 with 0-degree Axial Level 5 Detector Calculation Wall-clock Times

Code/Approach	DRF Coefficients	Calculation Time	#Processors	Speedup
RAPID/DRF (2 FAs)	Axial Translation	40.32 seconds	1	1829.64
RAPID/DRF (2 FAs)	Real	40.32 seconds	1	1829.64
MCNP+CADIS (2 FAs)	-	20.492 hours	8	Reference

Note that the RAPID calculation times include the neutron source calculation time. Similarly, significant speedup is observed using the DRF methodology.

5.7 Summary of the Chapter

This chapter has utilized the GBC-32 SNF cask model with ^{3}He detectors to benchmark the DRF methodology. It is shown that accuracy of the DRF methodology for detector response calculation is excellent. The ^{3}He detector DRF coefficients for induced fission neutron source are not sensitive to the burnup level, and can be translated to various detector locations by the geometry symmetry and similarity. The DRF coefficients only need to be calculated once and can be reused. Real-time SNF cask shielding calculation can be achieved by the DRF methodology. This provide an excellent capability of online SNF cask monitoring.

Chapter 6

Benchmark of the DRF Methodology: VENUS-3 Problem

In this dissertation, one of the application of the DRF methodology is Reactor Pressure Vessel (RPV) neutron fluence calculations. The RPV fluence calculation is very important for reactor operation safety. To validate the new methodology, experimental benchmark is important. Since Virginia Tech does not have a research reactor, we use the VENUS-3 benchmark problem [11]. In this chapter, implementation of the DRF methodology to VENUS-3 RPV neutron fluence calculation will be discussed.

6.1 Problem Description

The word VENUS stands for Vulcan Experimental NUclear Study. The facility was originally built in 1963-1964. In 1967, it was adapted in order to study the Light Water Reactor (LWR) core designs and to provide experimental data validation. The facility was located at the SCK·CEN research institute at Belgium. Since then, there are VENUS-1, VENUS-2, and VENUS-3 experimental benchmark problems being performed [5]. Among all of them, the VENUS-3 is performed for studying the protection capability of Partial Length Shielded Assembly (PLSA) for RPV welding location. An additional purpose was to benchmark the accuracy of the existing computer codes used for RPV neutron fluence calculations. The VENUS-3 core was firstly critical on March 16^{th}, 1988. The experiment program started on March 29^{th}, 1988. Fig. 6.1 shows the core description of the VENUS-3 reactor [5]. About 14 independent benchmark calculations were performed by eight institutions. The numbers of dosimeter measurement location are ∼200 for ^{58}Ni(n,p), ∼100 for ^{115}In(n,n$'$), and ∼50 for ^{27}Al(n,α).

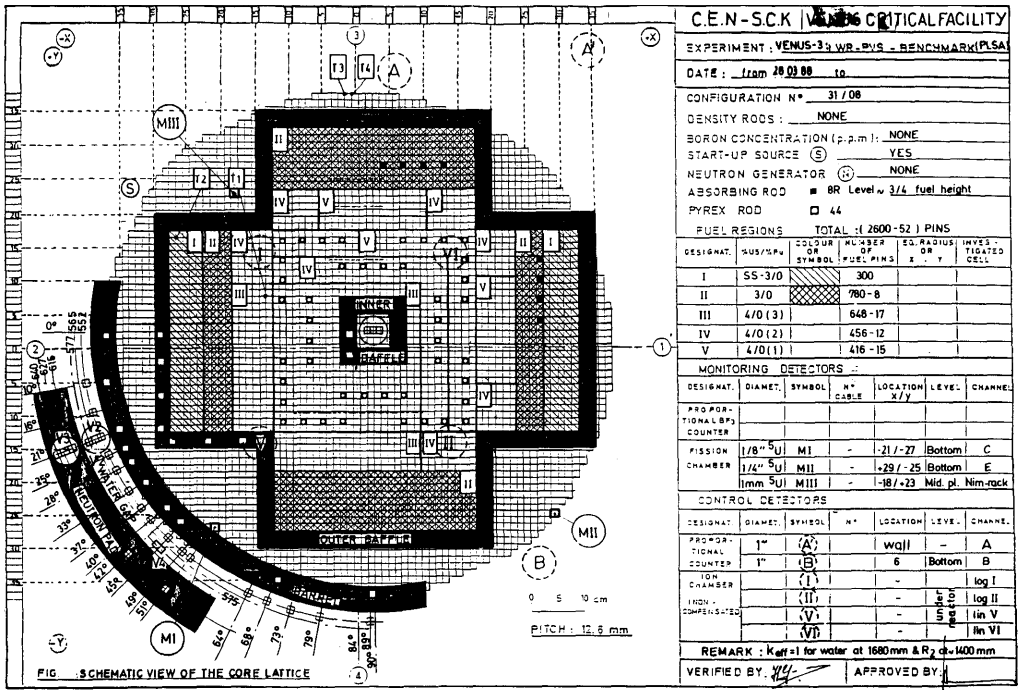

Figure 6.1 Core Description of the VENUS-3 Reactor [5]

6.2 MCNP5 Model

There are 4 types of rod in the VENUS-3 reactor: (1) 3wt% UO_2 rod; (2) 4wt% UO_2 rod; (3) Pyrex rod; and (4) Partial Length Shielded Assembly (PLSA) rod. There are 44 pyrex rod symmetrically distributed in the 4wt% UO_2 rod zone. Four boron control rod are paced at the II zone in the Fig. 6.1 for criticality control (small black boxes). The dimensions of the fuel, PLSA, and pyrex rods are listed in the Table 6.1.

Table 6.1 VENUS-3 Rod Dimensions

Item	Radius	Gap	Cladding	Length	Cell Pitch
$3wt\%$ fuel rod	0.4095 cm	0.0085 cm	0.058 cm	50 cm[a]	1.26 cm
$4wt\%$ fuel rod	0.4463 cm	0.0047 cm	0.038 cm	50 cm	1.26 cm
Pyrex rod	0.3020 cm (inner) 0.4524 cm (outter)	-	-	50 cm	1.26 cm
PLSA rod	0.4085 cm	-	-	25 cm	1.26 cm

[a] Part of the 3wt% fuel rod are 25 cm. The other 25 cm is the PLSA.

There are 60×60 rods in the core with missing 15×15 at the four corners, which gives a total of 2700 rods. Among all of them, 2652 of them are fuel rods, which consist 1456

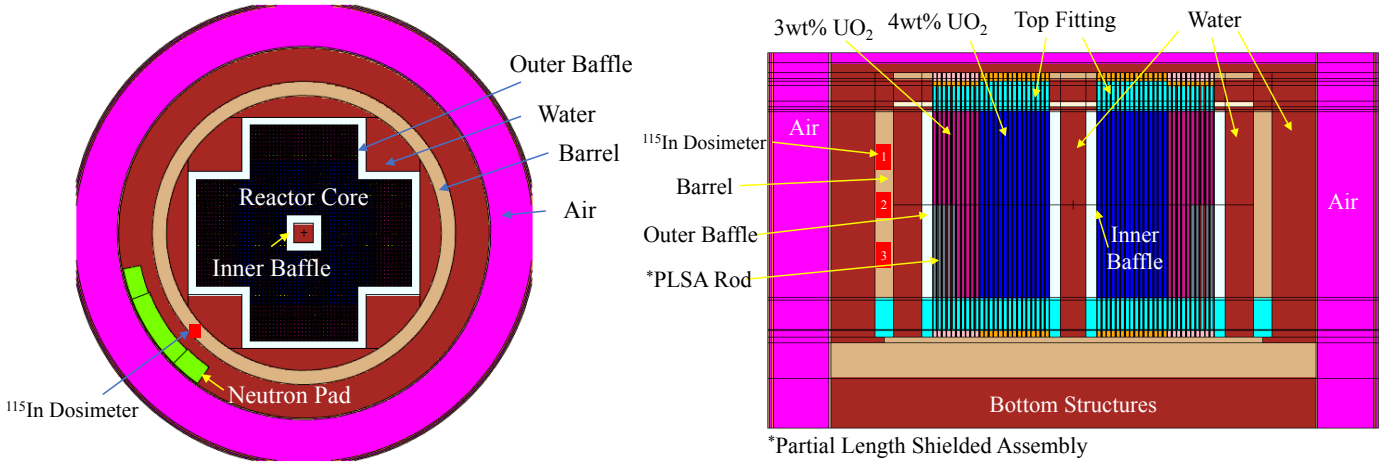

(a) Radial Projection **(b)** Axial Projection

Figure 6.2 VENUS-3 Detailed Core Geometry

4wt% fuel rods and 908 3wt% fuel rods. Part of the structure dimensions are listed in the Table 6.2.

Table 6.2 VENUS-3 Structure Dimensions

Item	Radius
Core Barrel Inner Radius	48.283 cm
Core Barrel Outter Radius	53.273 cm
Inner Jacket Wall Inner Radius	65.073 cm
Inner Jacket Wall Outer Radius	65.573 cm
Outer Jacket Wall Inner Radius	80.573 cm
Outer Jacket Wall Outer Radius	81.073 cm
Vessel Inner Radius	81.573 cm
Vessel Outer Radius	81.973 cm

The MCNP5 VENUS-3 model is shown in the Figs. 6.2 and 6.3. Here, three $^{115}\mathrm{In}(n,n')$ dosimeter locations (red cubes) are selected for study. The azimuthal location is 270-degree at the third core quadrant. The axial locations are z =114.5 cm, 131.5 cm, and 145.5 cm. Note that the active fuel segment is from 105 cm to 155 cm. The dosimeter sizes are all 1cm×1cm×1cm for convenience. The core water is slightly borated by 80 ppm for the reactivity control. Note that this will give a negative reactivity $\sim$ 700 pcm comparing with core without borated water.

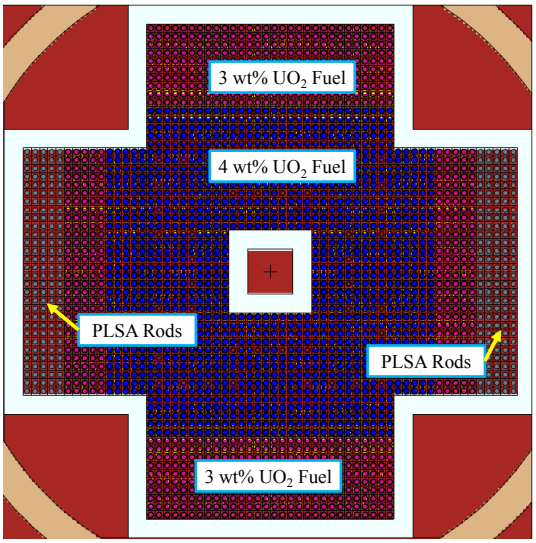

Figure 6.3 Core Configuration of the VENUS-3 Reactor

6.3 Importance Function Calculations and Field of View

To efficiently calculate the DRF coefficients, the importance functions have to be pre-calculated. The importance functions are calculated using the PENTRAN^{TM} code system. This section will discuss the importance function calculations, FOV and GC estimations, and lower weight window bounds calculations.

6.3.1 PENTRAN^{TM} Importance Model

Here, three models for the three $^{115}\text{In}(n,n')$ dosimeter locations are prepared. However, only the $^{115}\text{In}(n,n')$ dosimeter location at z =131.5 cm is shown here. The models and importance functions of other dosimeter locations can be found in the Appendix C. Fig. 6.4 shows the PENTRAN^{TM} importance model for $^{115}\text{In}(n,n')$ dosimeter located at 270-degree and $z = 131.5$ cm. The core material are homogenized using volume as weighting factor for simplicity.

The model size is 151.2cm×151.2cm×70cm. The mesh size of the importance model is from minimum 0.5 cm to maximum 8.5 cm. The anisotropic scattering Legendre expansion for differential scattering cross-section used is P3. The angular quadrature order selected is S8. The convergence criteria is 5×10^{-3} with maximum iteration number of 100. The cross-section library used is the BUGLE96 47 group neutron cross-section [62]. The $^{115}\text{In}(n,n')$ dosimeter macroscopic cross-section is used as the importance source. Fig. 6.5 shows the magnitude of multi-group microscopic $^{115}\text{In}(n,n')$ cross-section from the BUGLE96 library

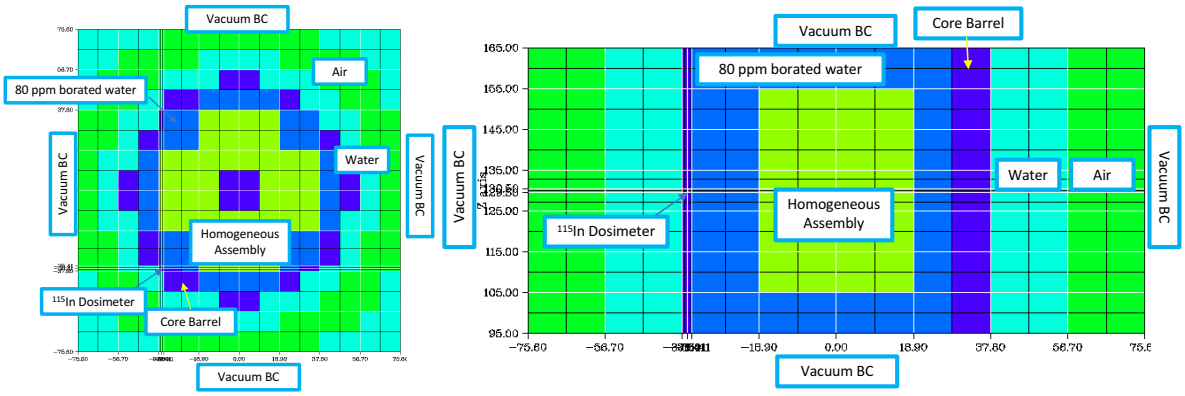

(a) Radial Projection **(b)** Axial Projection

Figure 6.4 PENTRAN^{TM} Importance Model: 270-degree $z = 131.5$ cm $^{115}\mathrm{In}(n,n^{'})$ dosimeter

[62].

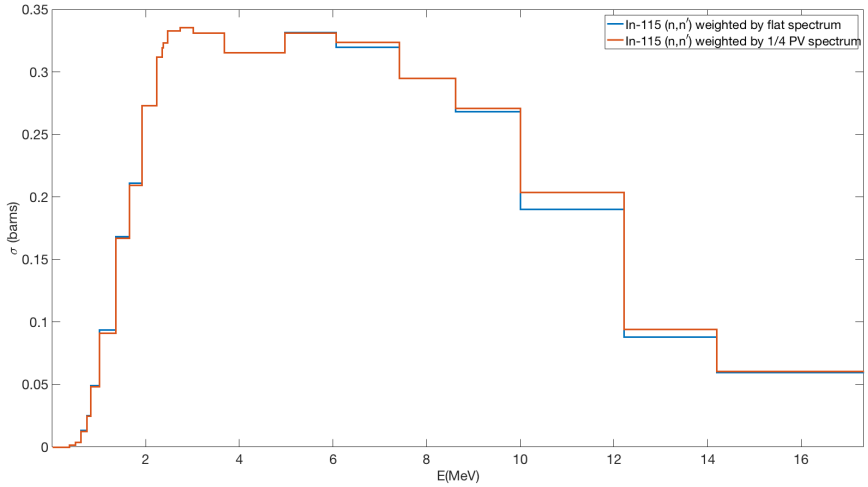

Figure 6.5 $^{115}\mathrm{In}(n,n^{'})$ Dosimeter Microscopic Cross-section

The cutoff energy for $^{115}\mathrm{In}(n,n^{'})$ in the BUGLE96 library is 0.3688 MeV. Therefore, only the first 24/47 groups are required for importance function calculations. Note that in the BUGLE96 library, there are two sets of $^{115}\mathrm{In}(n,n^{'})$ cross-sections: (1) Weighted using flat neutron spectrum; and (2) Weighted using a 1D pre-calculated 1/4 RPV neutron spectrum. In principle, the multi-group cross-section weighted by 1/4 RPV neutron spectrum is more appropriate since reaction rate conservation. However, the calculated importance function is only for FOV/GC estimation and acceleration of Monte Carlo fixed source calculations. Therefore, it is not very important which cross-section is used. In this study, the flat spectrum weighted cross-section is used.

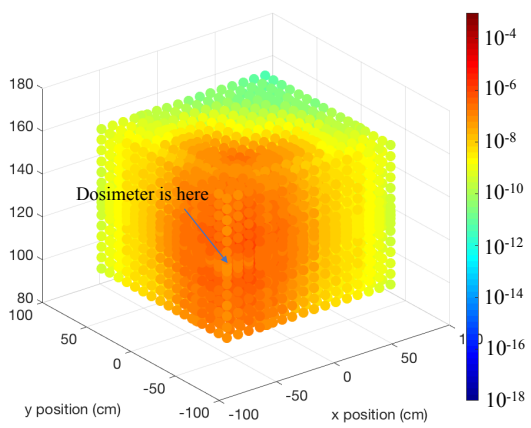

(a) Group 2: 12.2 MeV < E < 14.2 MeV

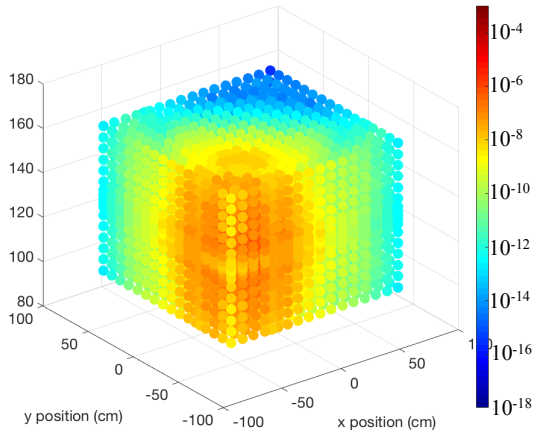

(b) Group 15: 1.92 MeV < E < 2.23 MeV

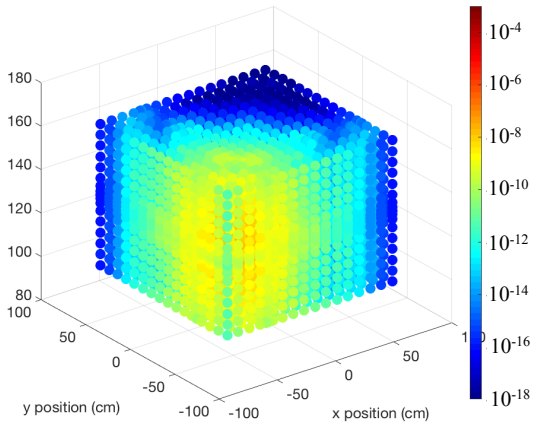

(c) Group 20: 0.82 MeV < E < 1.00 MeV

Figure 6.6 PENTRAN^{TM} Calculated Importance Functions: 270-degree $z = 131.5$ *cm* $^{115}\text{In}(n, n')$ dosimeter

6.3.2 PENTRAN^{TM} Calculated Importance Functions

Fig. 6.6 shows the selected three groups of calculated PENTRAN^{TM} importance functions for $^{115}\text{In}(n, n')$ dosimeter at 270-degree and z =131.5 cm. The importance functions for lower energy group drop much steeper than the fast group. This is mainly because neutron with higher energy have much greater probibility to penetrate through the structures and make contribution to the dosimeter responses, and therefore are more important. The importance function calculation requires $\sim$ 24.16 minutes on 2 processors.

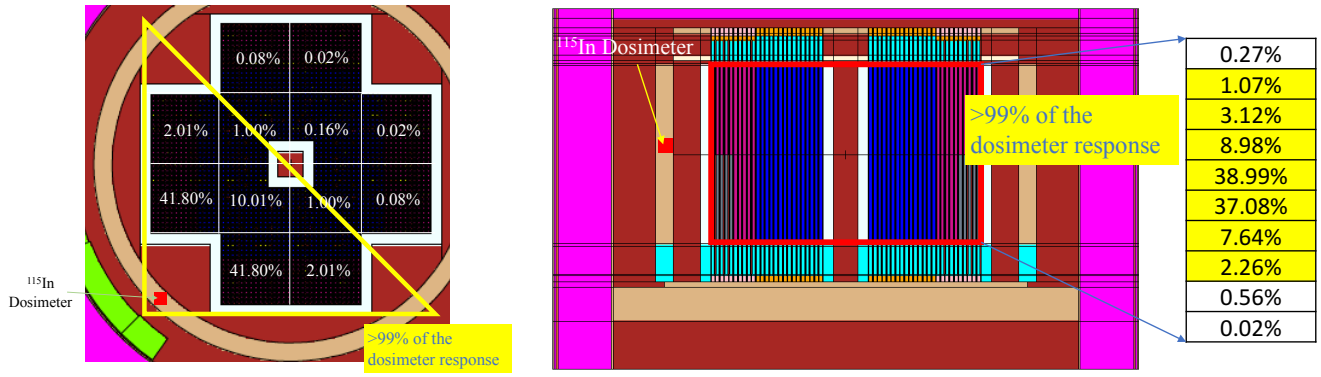

(a) Radial FOV **(b)** Axial FOV

Figure 6.7 Field of View: 270-degree $z = 131.5$ cm $^{115}\mathrm{In}(n, n^{'})$ dosimeter

6.3.3 Field of View Analysis by Importance Functions

Using the formulation from Eq. (5.4), we can calculate the FOV as *a priori* to determine how deep the $^{115}\mathrm{In}(n, n^{'})$ dosimeter "see" into the VENUS-3 core. Fig. 6.7 shows the FOV of the $^{115}\mathrm{In}(n, n^{'})$ dosimeter at 270-degree and z =131.5 cm. The axial segment for FOV study is via evenly dividing the 50 cm active fuel height.

The results show that more than $\sim$ 99% of the dosimeter responses are from the assembly segments with yellow frames. The contribution from the top axial half segment is slightly higher since presence of PLSA rods at lower half segment. The yellow frame will be the selected region for DRF coefficient calculations.

6.3.4 Group-wised Contribution Analysis by Importance Functions

Here, the GC is calculated to determine the energy group which dominate the dosimeter response contributions. Fig. 6.8 shows the GC for the $^{115}\mathrm{In}(n, n^{'})$ dosimeter at 270-degree and z =131.5 cm.

The result shows that negligible contribution is from the neutron energy lower than $\sim$ 0.6 MeV. Therefore, for the 270-degree $z = 131.5$ cm $^{115}\mathrm{In}(n, n^{'})$ dosimeter, the selected cutoff energy for DRF coefficient calculations can be 0.6 MeV. However, this may change with other dosimeter locations. More detailed results for other dosimeter locations can be found in the Appendix C. It is observed that cutoff energy of 0.6 MeV is sufficient for all the three selected $^{115}\mathrm{In}(n, n^{'})$ dosimeter locations.

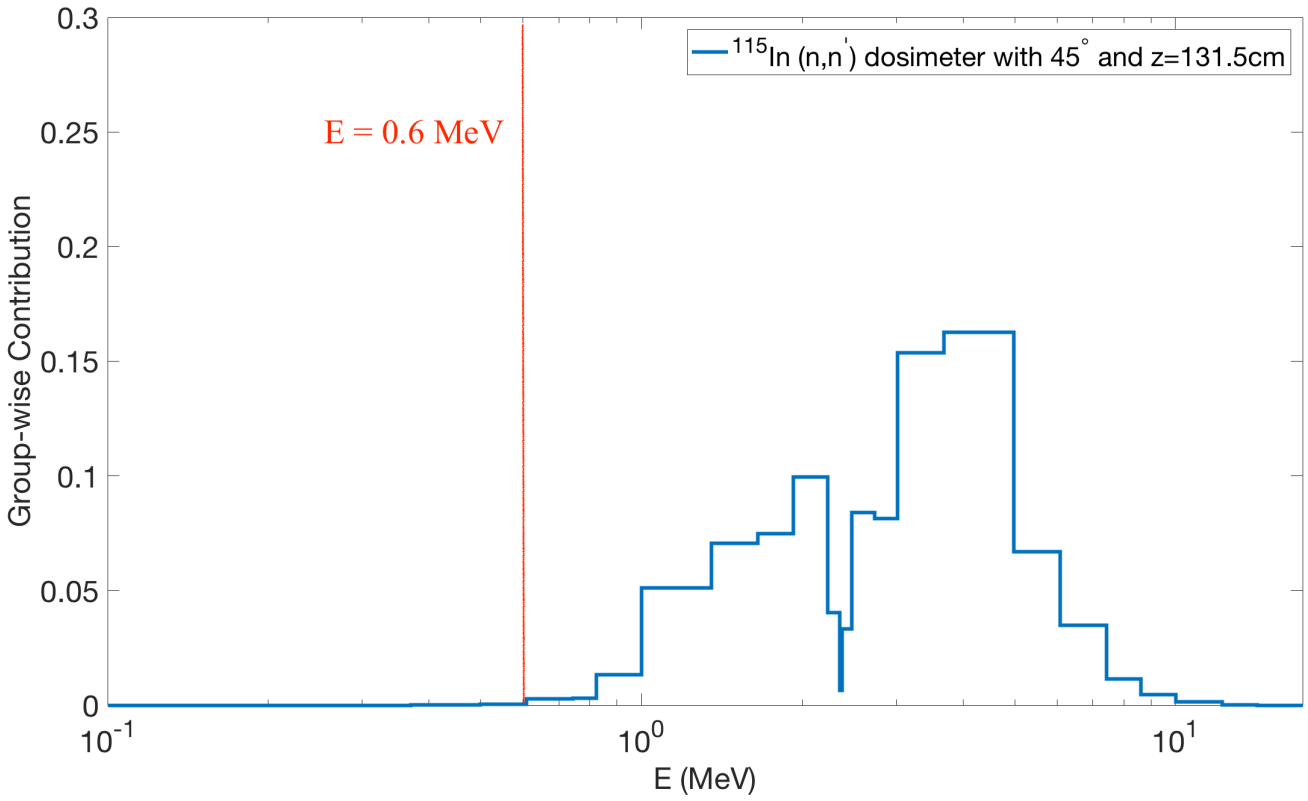

Figure 6.8 Group-wised Contribution: 270-degree $z = 131.5$ cm $^{115}\mathrm{In}(n, n^{'})$ dosimeter

6.3.5 Lower Weight Window Bounds Calculation

The lower weight windows are calculated using the Eq.(4.8) with $C_u = 5$. Fig. 6.9 shows the lower weight window bounds for $^{115}\mathrm{In}(n, n^{'})$ dosimeter at 270-degree and z =131.5 cm. The neutron born with relatively low energy far away from the dosimeter has a very high lower weight window bounds. This will result in a lot of Russian Roulette for relative lower energy neutrons, which will more likely be killed during the process. Lower energy neutron are less likely to penetrate through the structures and make contribution to dosimeter response. Therefore, terminating the "low contribution neutrons" can greatly enhance the calculation efficiency.

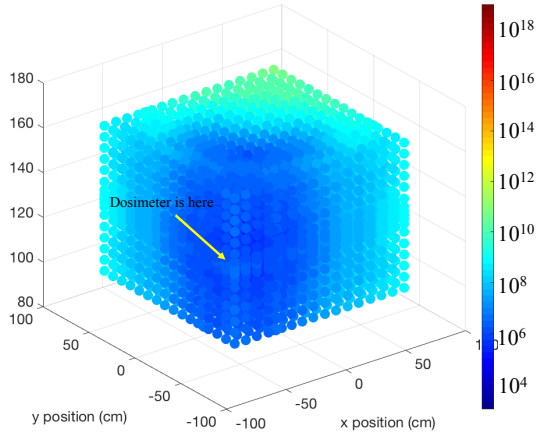

(a) Group 2: 12.2 MeV < E < 14.2 MeV

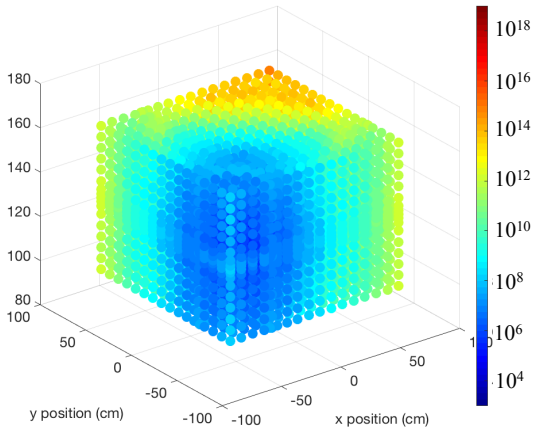

(b) Group 15: 1.92 MeV < E < 2.23 MeV

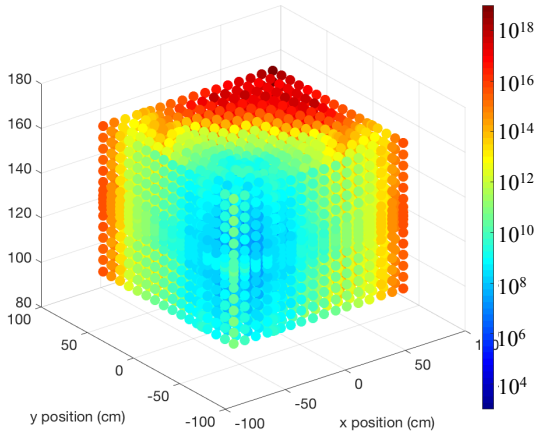

(c) Group 20: 0.82 MeV < E < 1.00 MeV

Figure 6.9 Lower Weight Window Bounds: 270-degree $z = 131.5\ cm$ $^{115}\mathrm{In}(n, n^{'})$ dosimeter

6.4 DRF Coefficient Calculations

The DRF coefficients are calculated using a series of Monte Carlo fixed-source calculations with the CADIS methodology by MCNP5. The DRF coefficients are calculated with non-uniform axial pitch. This arrangement is selected mainly because the axial heights of experimental source distribution are not uniform. In order to (1) keep consistency; and (2) for comparison, we have decided to use the axial height arrangement from the literature [105]. The possible reason for the original selection might be the difficulty of performing measurement in certain locations. The 14 axial heights are listed in the Table 6.3.

Table 6.3 Axial Heights for the DRF Coefficient Calculations

Axial Number	Height
14 (Top)	3.50 cm
13	4.00 cm
12	4.00 cm
11	4.00 cm
10	3.50 cm
9	3.00 cm
8	3.00 cm
7	3.00 cm
6	3.00 cm
5	3.00 cm
4	3.50 cm
3	4.00 cm
2	4.00 cm
1 (Bottom)	3.50 cm

The DRF Coefficient calculations for $^{115}\mathrm{In}(n,n^{'})$ dosimeter at 270-degree and $z = 131.5\ cm$ is performed at axial levels from 3/14 to 13/14, according to the FOV study from section 6.3.3. The number of particles used for the calculations are 2×10^7. Fig. 6.10 shows the calculated DRF coefficients for $\mathrm{In}(n,n^{'})$ dosimeter at 270-degree and $z = 131.5$ cm. Each DRF coefficient requires $\sim$ 1.5 minutes to calculate using 8 processors. There are 14265 DRF coefficients calculated using 56 processors. The total calculation time is $\sim$ 2.18 days.

The 1σ statistical uncertainties of the DRF coefficients are from $\sim$ 2% to $\sim$ 13% with a weighted value of $\sim$ 5.17%. The locations with $>$ 10% statistical uncertainties are mostly far away from the dosimeter and making negligible contributions. The weighting is performed by the following formulation:

$$Ave.\ 1\sigma = \frac{\sum_i DRF_i\ DRF1\sigma_i}{\sum_i DRF_i} \tag{6.1}$$

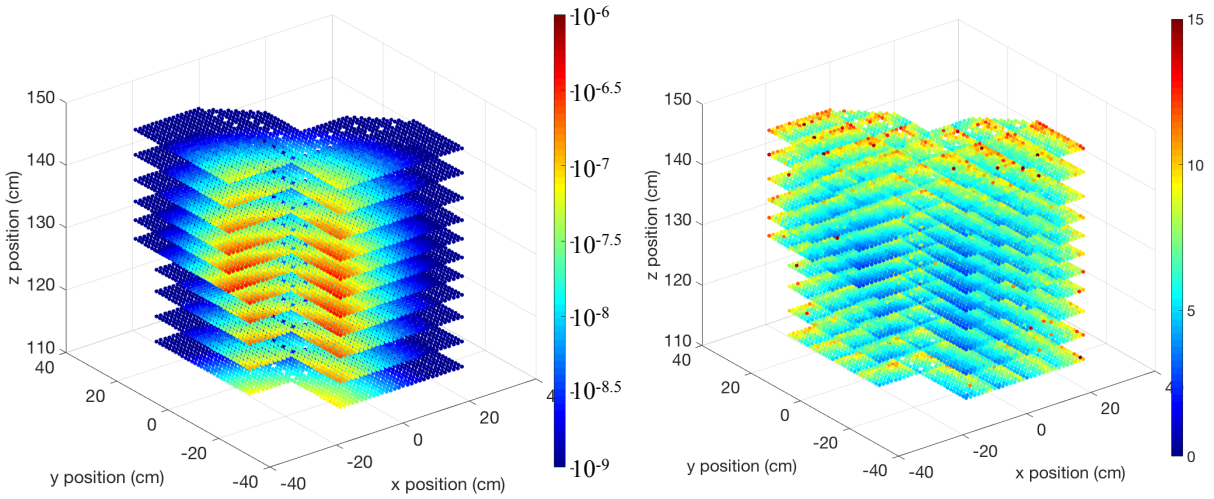

(a) DRF Coefficients

(b) 1σ Statistical Uncertainties in %

Figure 6.10 270-degree $z = 131.5\ cm$ $^{115}\mathrm{In}(n, n^{'})$ dosimeter

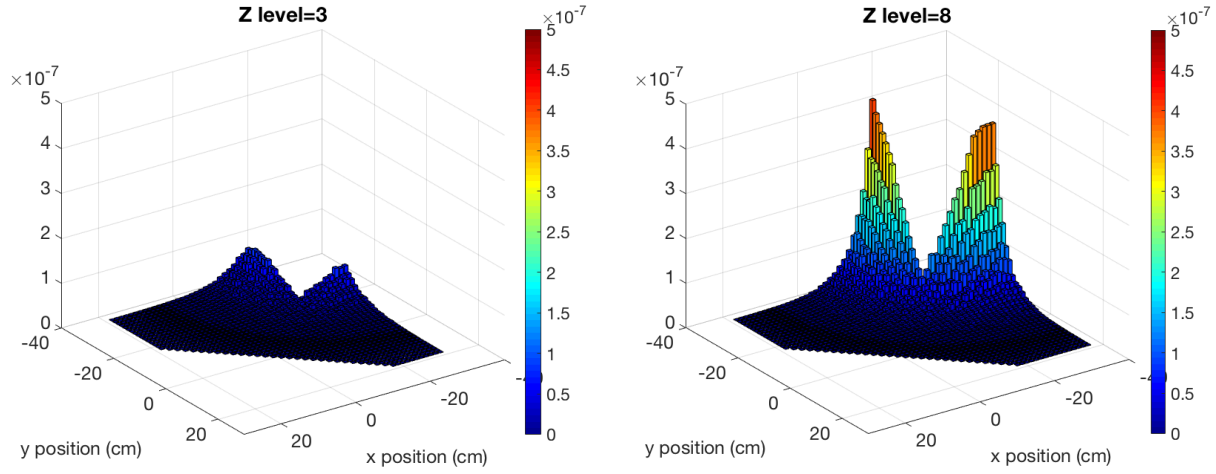

(a) Z Level 3

(b) Z Level 8

Figure 6.11 DRF Coefficients: 270-degree $z = 131.5\ cm$ $^{115}\mathrm{In}(n, n^{'})$ dosimeter

where DRF_i and $DRF1\sigma_i$ are the DRF coefficient and the 1σ statistical uncertainty at location i.

The DRF coefficients drops one order of magnitude radially for one assembly (15 fuel rods) away and one order of magnitude ~ 20 cm away axially. Note that the pyrex rod does not contain fuel, therefore no DRF coefficients are calculated for such locations. this can be seen in the Fig. 6.10a. To further show the slope of the DRF coefficients, Fig. 6.11 is provided. Discussion of the DRF coefficients for the other two axial locations can be found in the Appendix D.

6.5 Neutron Source Calculations

The neutron source distribution is calculated by the eigenvalue calculation using MCNP5 code system. The SINBAD library actually provides an experimental neutron source distribution [105]. However, only a quarter core of source distribution is given. For the purpose of this benchmark, it is necessary to have full 3D pin-wised whole core neutron source. Therefore, we choose to calculate the neutron source distribution independently. Note that the experimental neutron source distribution is obtained via interpolation technique. Therefore, a comparison of neutron source distribution between experiment and calculation is also provided in the Appendix E. Note that the heights of 14 axial are not uniform according to the experimental data [105] from the Table 6.3. To compare with experimental values, the axial height are selected consistently with the experimental fuel pellet axial height. The parameters for Monte Carlo eigenvalue calculations are: (1) 200 active cycles; (2) 200 skip cycles; and (1) 10^6 particles per cycle. There are total 33596 fission sources being tallied. Sensitivity study has been performed with combination of 10^5, 5×10^5, 10^6 particles and 50, 100, 150, and 200 skip cycles. Results show that the selected parameter is sufficient for a converged solution. Fig. 6.12 shows the 3D pin-wised fission neutron source distribution of the VENUS-3 core.

The calculated system eigenvalue (k_{eff}) is 1.00242 ± 0.00009 (3σ relative statistical uncertainty). The 1σ relative statistical uncertainties range are from 0.5% to $\sim$ 2%. The calculation time is ~ 22.86 hours using 32 processors.

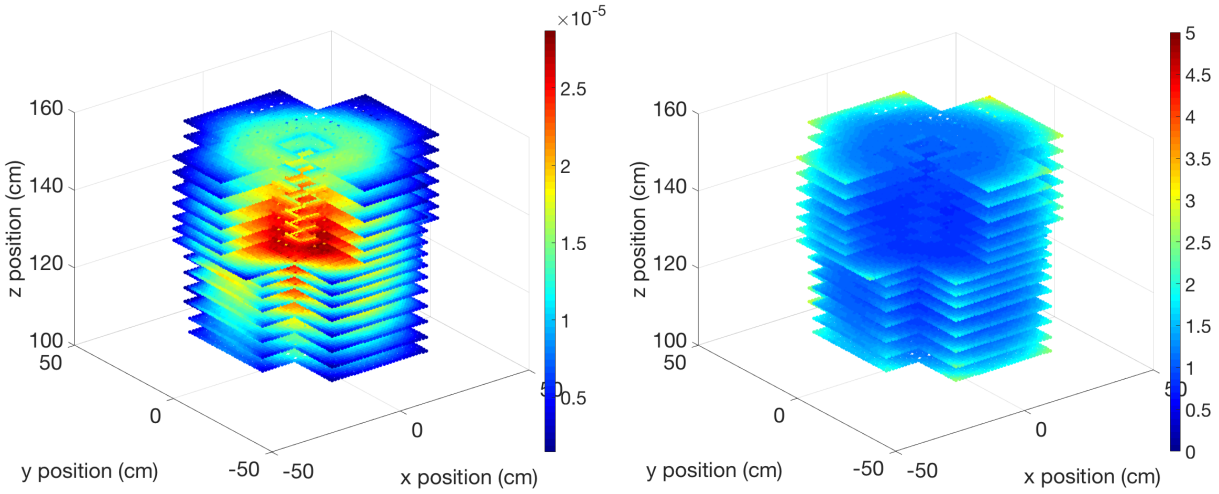

(a) Normalized Fission Neutron Source **(b)** 1σ Statistical Uncertainties in %

Figure 6.12 Normalized Neutron Source Distribution for VENUS-3 Core (14 Axial Levels)

6.6 Dosimeter Response Calculations

In this section, the dosimeter responses calculated by the DRF methodology and Monte Carlo Eigenvalue calculations will be compared to the experimental values. Detailed analysis on real FOV by coupling the neutron sources and DRF coefficients will also be presented.

6.6.1 Dosimeter Response Comparisons

Table 6.4 shows the dosimeter response comparisons for $^{115}\text{In}(n,n')$ dosimeter at 270-degree and $z = 131.5$ cm. Note that the calculated dosimeter responses are divided by an equivalent 1 group dosimeter macroscopic cross-section to obtain the neutron flux. The $^{115}\text{In}(n,n')$ 1 group equivalent macroscopic cross-section is 6.9324×10^{-3} cm^{-1}.

To provide one more reference, the eigenvalue Monte Carlo method is used for the dosimeter response calculation. The parameter used for eigenvalue Monte Carlo dosimeter response calculation is 200 active cycle, 200 skip cycle, and 5×10^6 particles per cycle. Note that no neutron source tallies are applied, therefore the calculation time will be faster. The results show that excellent agreement between MC/experiment and DRF methodology is observed. The DRF calculated dosimeter response falls in 1σ statistical uncertainty of the experimental result. The dosimeter responses for the other two dosimeter locations are shown in the Tables 6.5 and 6.6.

Similarly, excellent agreement between DRF methodology and experiment is observed. The calculation time comparisons are shown in the Table 6.7.

Table 6.4 $\mathrm{In}(n,n^{'})$ Dosimeter Response Comparisons: 270-degree $z = 131.5\ cm$

Code/Method	Axial Loc.	Param.[b]	Flux (ns/cm^2-sec)	1σ	C/E
RAPID / DRF	131.5 cm	2×10^7	4.43×10^7	-	0.96
MCNP5 / MC Eig.[c]	131.5 cm	$200/200/5 \times 10^6$	4.52×10^7	$\sim 3.87\%$	0.98
- / Experiment	131.5 cm	-	4.60×10^7	$\sim 4.00\%$	-

[b] Parameters are referring to the active/skip cycle and number of particle used for eigenvalue calculations or number of particle used for DRF coefficients fixed-source MC Calculations

[c] Monte Carlo Eigenvalue Calculation

Table 6.5 $\mathrm{In}(n,n^{'})$ Dosimeter Response Comparisons: 270-degree $z = 114.5\ cm$

Code/Method	Axial Loc.	Param.	Flux (ns/cm^2-sec)	1σ	C/E
RAPID / DRF	114.5 cm	5×10^6	3.16×10^7	-	0.99
MCNP5 / MC Eig.	114.5 cm	$200/200/5 \times 10^6$	3.18×10^7	$\sim 4.47\%$	~ 1.00
- / Experiment	114.5 cm	-	3.19×10^7	$\sim 4.00\%$	-

Table 6.6 $\mathrm{In}(n,n^{'})$ Dosimeter Response Comparisons: 270-degree $z = 145.5\ cm$

Code/Method	Axial Loc.	Param.	Flux (ns/cm^2-sec)	1σ	C/E
RAPID / DRF	145.5 cm	2×10^7	3.48×10^7	-	0.95
MCNP5 / MC Eig.	145.5 cm	$200/200/5 \times 10^6$	3.56×10^7	$\sim 4.47\%$	0.97
- / Experiment	145.5 cm	-	3.65×10^7	$\sim 4.00\%$	-

Table 6.7 Wallclock Time: $\mathrm{In}(n,n^{'})$ Dosimeter 270-degree $z = 114.5\ 131.5\ 145.5\ cm$

Code/Method	Calculation Time	Number of Processors	Speedup
RAPID / DRF	~ 3 second	1	15396
MCNP5 / MC Eigenvalue	739 minutes	32	-

The result shows that significant speedup using the DRF methodology is observed when comparing with the Eigenvalue Monte Carlo method.

6.6.2 Real FOV Analysis

In the section 6.3.3, the FOV analysis was performed using approximated importance function. Since we have detailed neutron source and DRF coefficients now, detailed and accurate FOV analysis can be performed. Fig. 6.13 shows different fraction of dosimeter responses with their corresponding contributions.

The results show that $\sim 90\%$ of the dosimeter responses are coming from the first nearby

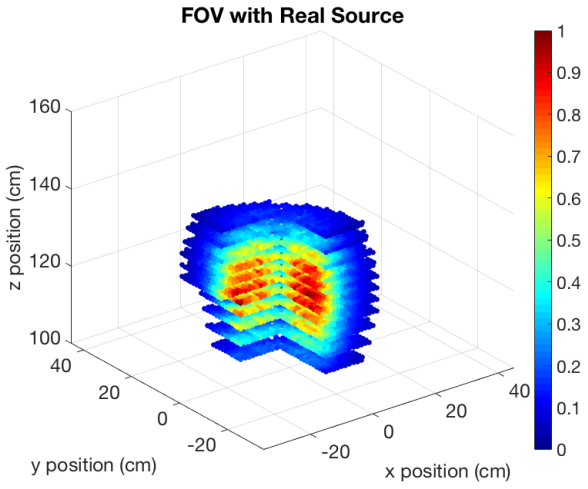

(a) 83.83% of Dosimeter Response

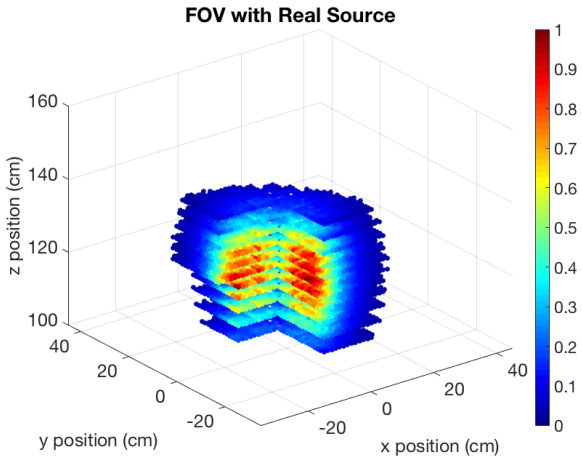

(b) 90.64% of Dosimeter Response

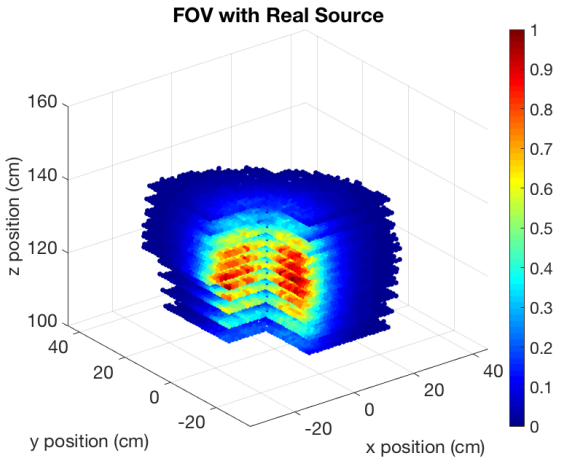

(c) 99.00% of Dosimeter Response

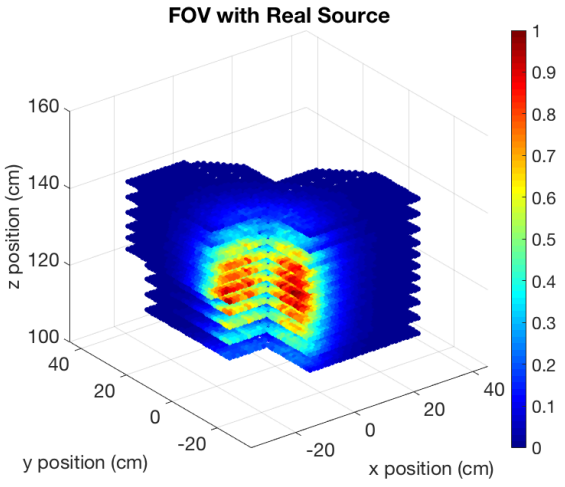

(d) 100.00% of Dosimeter Response

Figure 6.13 Real Field of View (Scaled the Maximum to 1): $\mathrm{In}(n, n^{'})$ Dosimeter 270-degree $z = 131.5\ cm$

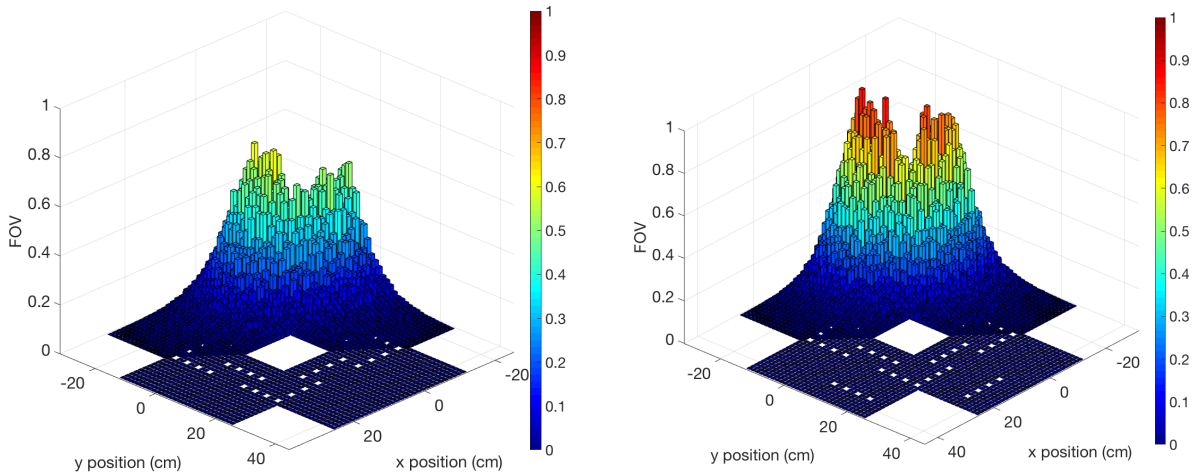

(a) Z Level 3 **(b)** Z Level 8

Figure 6.14 Real Field of View (Scaled the Maximum to 1): $\mathrm{In}(n, n^{'})$ Dosimeter 270-degree $z = 131.5$ cm (Rotated for 180°)

fuel assembly (15×15 fuel pellets). The dosimeters does not "see" into the system too much, even with such small system like VENUS-3 reactor. Fig. 6.14 further provides details of FOV axial level 3/14 and 8/14. Note that the dosimeter is located at axial level between 6/14 and 7/14. It further verified that only the closest 15×15 fuel rods are making significant dosimeter response contributions.

6.6.3 Verifying Flat Source Assumption for FOV Estimation

From the section 5.3.3 Eq. (5.4), we always assume the source distribution is flat for the FOV estimation. For a larger system such as SNF cask or commercial reactor, this might be a valid assumption. However, with such small system like VENUS-3 core, this assumption may not hold. To further verifying the statement: "the FOV may be underestimated by the flat source assumption", we have calculated the FOV using real and flat source distributions. Fig. 6.15 shows the two different FOV by using real and flat source distributions.

It is very obvious that the FOV calculated from the flat source assumption is smaller than the other one. To further quantify the differences, differences between Figs. 6.15a and 6.15b are shown in the Fig. 6.16.

Typically, the sign of differential from the slopes for DRF coefficient and neutron source distribution are opposite to each other. It makes perfect sense the neutron flux drops from the center of reactor core to the peripheral regions. Therefore, the statement "the FOV may be underestimated by the flat source assumption" will typically hold for most of the

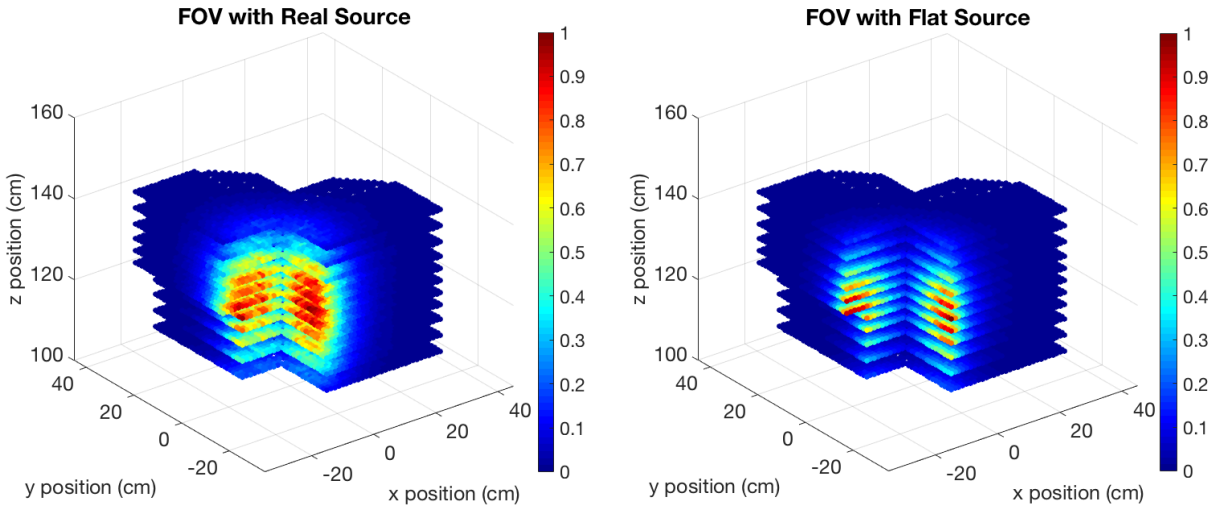

(a) Using Real Source **(b)** Using Flat Source

Figure 6.15 Real Field of View (Scaled the Maximum to 1): $\mathrm{In}(n, n^{'})$ Dosimeter 270-degree $z = 131.5\ cm$

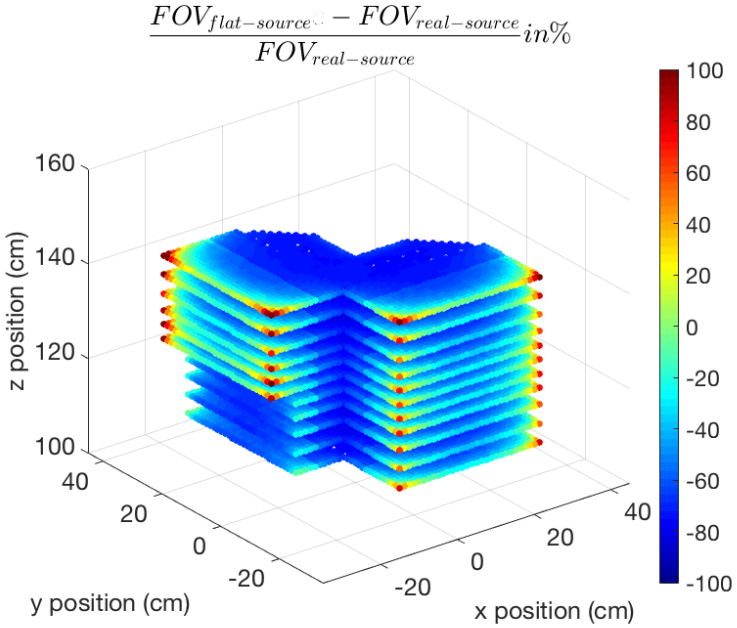

Figure 6.16 Differences of the FOV by Real/Flat Source Distributions in %

nuclear systems that require external shielding analysis. The statement might not hold for commercial Reactor in-core measurement.

6.7 Summary of the Chapter

In this chapter, we have successfully utilized the VENUS-3 experimental problem to benchmark the new DRF methodology. The experimental benchmark is very important to the confidence of a new methodology. The results show an excellent agreement between experimental value and the DRF methodology calculated dosimeter responses. All the dosimeter responses calculated by the DRF methodology are within 2σ relative statistical uncertainty of the experiments. Significant speed up using the DRF coefficients to calculate the responses are also observed.

However, since the VENUS-3 is a relative small reactor with less similarity in geometry, part of the DRF coefficients may have to be re-calculated if core configuration is changed. Fig. 6.17 shows an example of this. If the PLSA rods are replaced with fuel rods, the DRF coefficients from the yellow frame segment may have to be recalculated while the one in the gray frame may not need recalculations. This is mainly because there is a major material change through the penetration path of those neutron born in the yellow frame. But, if configuration changes are the UO_2 enrichment, dimension, and density of the fuel pellet, the DRF coefficients can still be re-used. This is because (1) No change on fission spectrum associated with enrichment if UO_2 is still used; and (2) The DRF coefficients are defined as per unit neutron source.

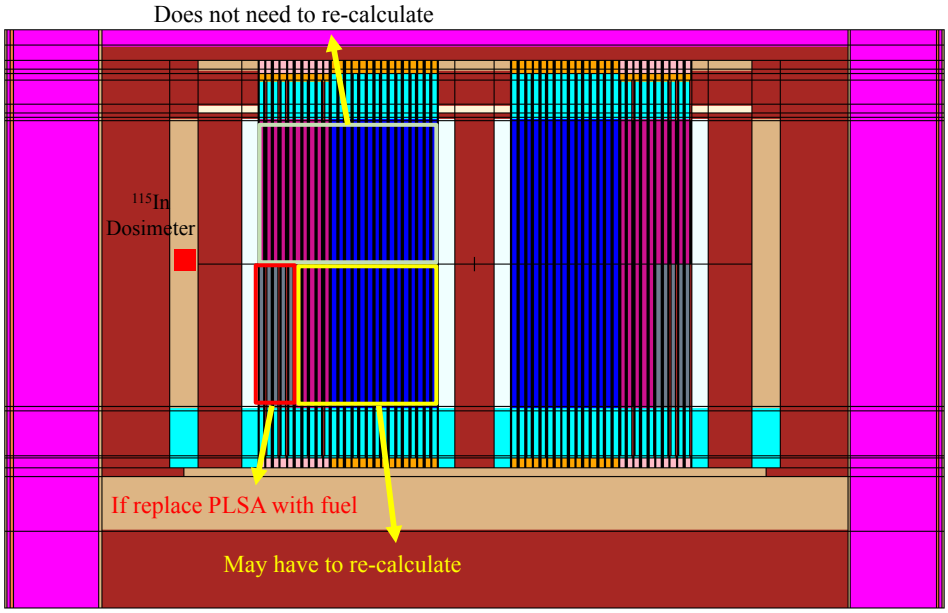

Figure 6.17 Example of Changing Core Configuration

The FOV estimation using flat source assumption may leads to underestimation for the control volume of DRF coefficient calculation. It is suggested to calculate slightly more DRF coefficients if flat source assumption is used for FOV estimation.

Chapter 7

Benchmark of the DRF Methodology: TMI-1 RPV Surveillance

In this chapter, the Three Mile Island Unit 1 (TMI-1) [106] will be used for Reactor Pressure Vessel (RPV) dosimetry benchmark calculations. Since there is no public data for detailed dimension of TMI-1 reactor core, the dimensions are mainly from one of the reference article [107]. Therefore, the model dimension and configuration are reasonable, but not very exact. However, analysis can still be performed with the amount of information we have.

7.1 Problem and Model Description

The TMI-1 reactor is a B&W Designed Lowered Loop Pressurized Water Reactor (PWR) with thermal power of 2568 MWt. The TMI Nuclear Power Plant (NPP) site is located at Dauphin County, Pennsylvania, U.S.A., near Harrisburg city. The TMI-1 fuel lattice size is 15x15, and contains 208 fuel rods, 16 guide tubes, and 1 centered irradiation tube. The reactor core contains 177 fuel assemblies. Here, two models are prepared: (a) A simplified 1D projected TMI-1 model; and (2) A full 3D TMI-1 model. The 1D model is prepared mainly for fast sensitivity study and uncertainty quantification. Note that part of the structure dimension and materials are from the OECD/NEA Monte Carlo Performance PWR Benchmark Problem [108].

7.1.1 MCNP5 1D Model

Fig. 7.1 shows the simplified 1D model. The dimensions and distance of the dosimeter from the RPV are listed in the figure. Only 5 fuel rods are considered in this model for sensitivity study and uncertainty quantification.

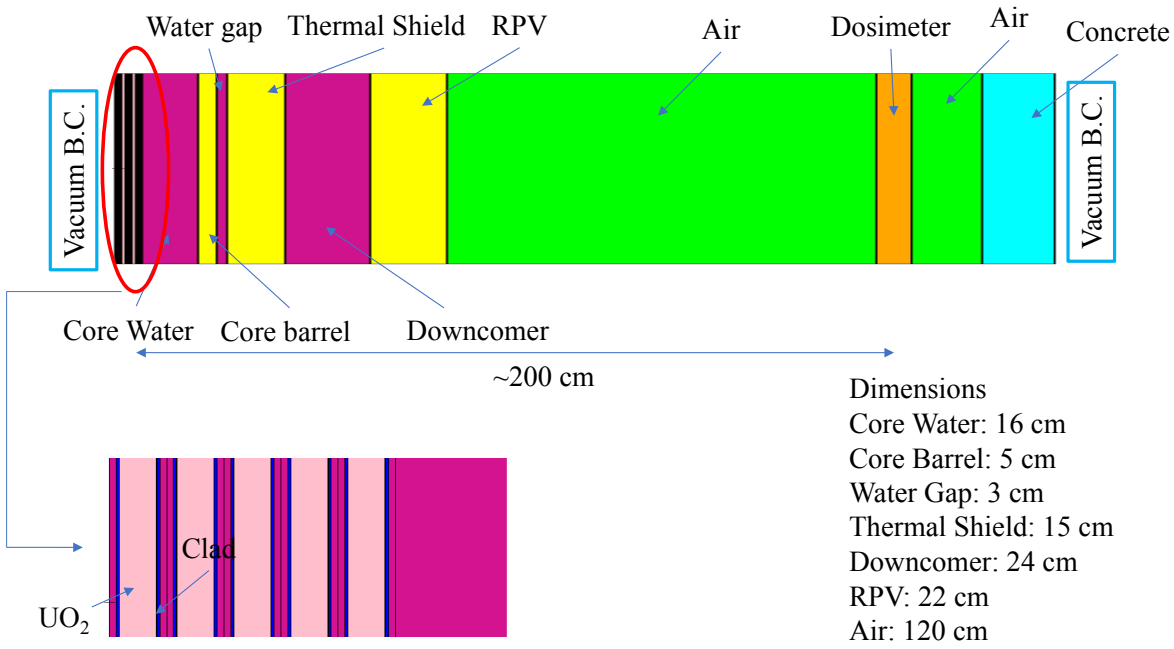

Figure 7.1 A 1D Projection TMI-1 Model

7.1.2 MCNP5 3D Model

Figs. 7.2 and 7.3 show the TMI-1 MCNP full 3D model and a radial projection of single fuel assembly. The dimensions of the model are:

- Fuel Pellet - 0.4680 in radius and 2.54 cm in height.
- Length of Fuel Rod - 360.68 cm (142 axial levels).
- Fuel Clad - Inner radius 0.4790 cm, Outer radius 0.5460 cm.
- Guide Tubes - Inner radius 0.63246 cm, Outer radius 0.67310 cm.
- Irradiation Tube - Inner radius 0.56007 cm, Outer radius 0.62611 cm.
- Fuel Rod Lattice Pitch - 1.44 cm.
- Fuel Assembly Lattice Pitch - 21.811 cm.

In the Fig. 7.3, the red and blue materials are UO_2 and water. The hole in the center is the irradiation tube while other holes are the guide tubes. Note that no boric acid is added in the water. The dimension of the structures are also listed below:

- Inner Radius of Core Barrel - 179 cm

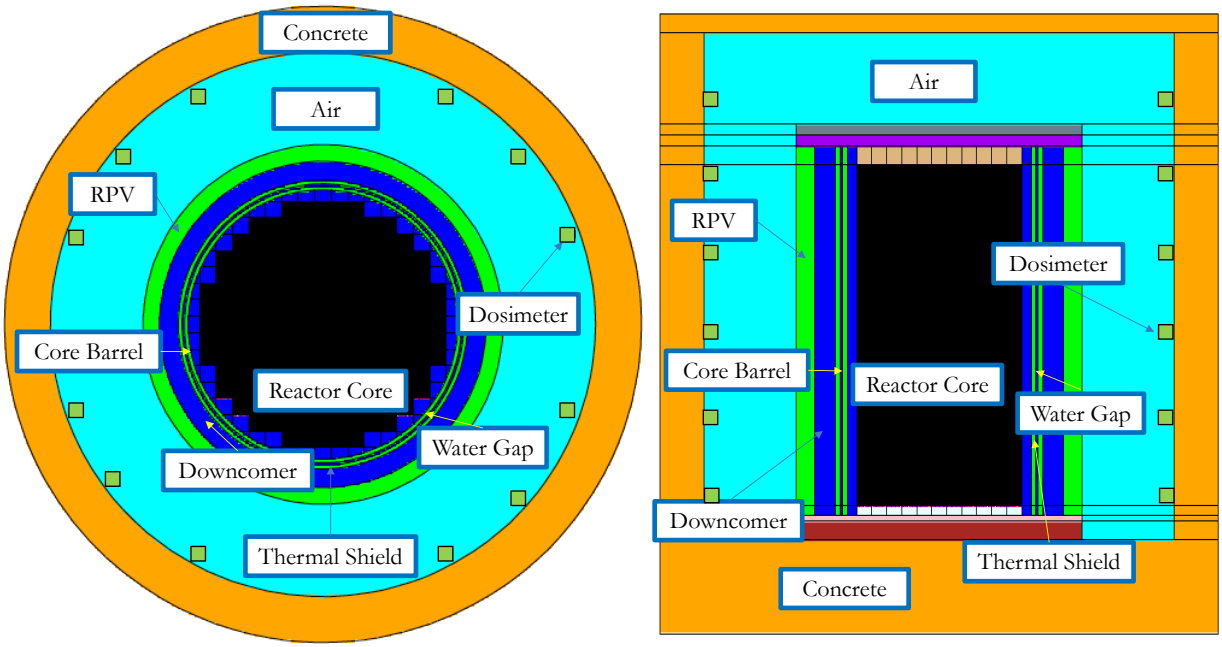

(a) Radial Projection **(b)** Axial Projection

Figure 7.2 TMI-1 3D Model

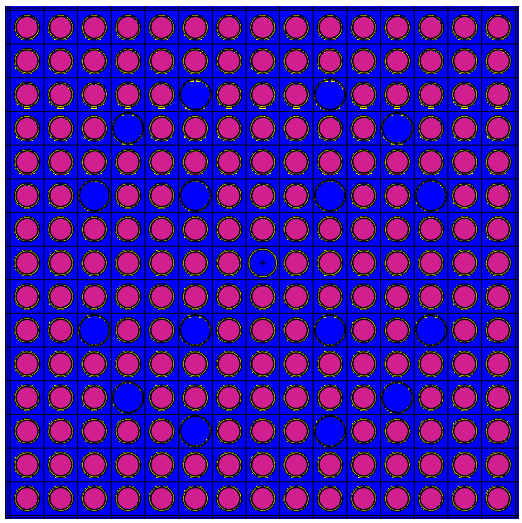

Figure 7.3 A Single Fuel Assembly Radial Projection

- Outer Radius of Core Barrel - 184 cm
- Water Gap Thickness - 3 cm
- Thermal Shield Thickness - 5 cm

- Downcomer Thickness - 25 cm
- RPV - 22 cm
- Distance from RPV to Concrete (Air) - 122.939 cm
- Thickness of Concrete - 60.8405 cm

7.2 Importance Function Calculations and Field of View

The importance function is calculated by the PENTRAN^{TM} code system. Both 1D and 3D model will require variance reduction for efficient DRF coefficient calculations. Therefore, importance function calculation for both of them will be discussed in this section.

7.2.1 Importance Source

To calculate the importance function, the importance source has to be selected first. Here, the dosimeter cross-section of four dosimeters are selected. Fig 7.4 shows the microscopic cross-sections of six dosimeter types.

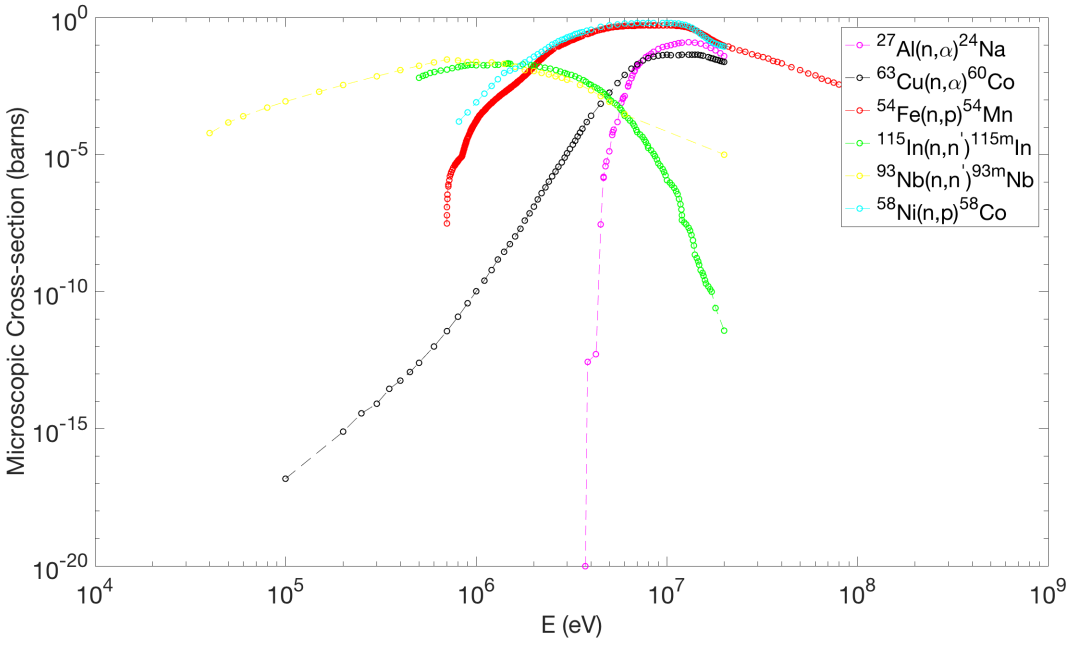

Figure 7.4 Microscopic Cross-section for Different Dosimeters

For RPV surveillance, the important energy range for most of the commercial PWR is E>1 MeV. Here, the four of them, with their corresponding threshold energy [109] presented, are used for benchmarking in this chapter:

- $^{27}\mathrm{Al}(n,\alpha)$ - 6.5 MeV
- $^{63}\mathrm{Cu}(n,\alpha)$ - 4.7 MeV
- $^{54}\mathrm{Fe}(n,p)$ - 2.3 MeV
- $^{115}\mathrm{In}(n,n^{'})$ - 0.95 MeV

Some literature [110] indicated that the $^{63}\mathrm{Cu}(n,\alpha)$ dosimeter threshold energy is 6.10 MeV.

To perform deterministic calculations, a multi-group importance source is required. Here, the multi-group dosimeter cross-section from the BUGLE96 data library [62] is used. Note that there are (1) 1/4 RPV neutron spectrum weighted; and (2) Flat spectrum weighted multi-group cross-section. Here, the flat spectrum weighted one is always used.

7.2.2 1D PENTRAN™ Importance Model

Fig 7.5 shows the mesh distribution and boundary conditions for the 1D PENTRAN™ importance model.

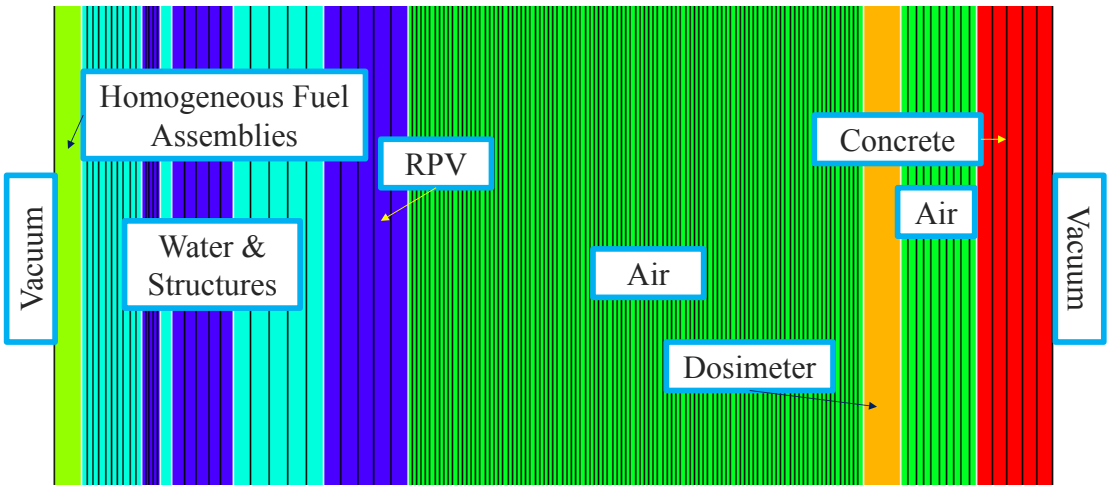

Figure 7.5 PENTRAN™ 1D Importance Model

The mesh distribution is used for all the dosimeter types. The details of water & structures can be found in the Fig. 7.1. Note that the fuel rods and core water are homogenized by volume weighting here for convenience. No detailed core geometry is used.

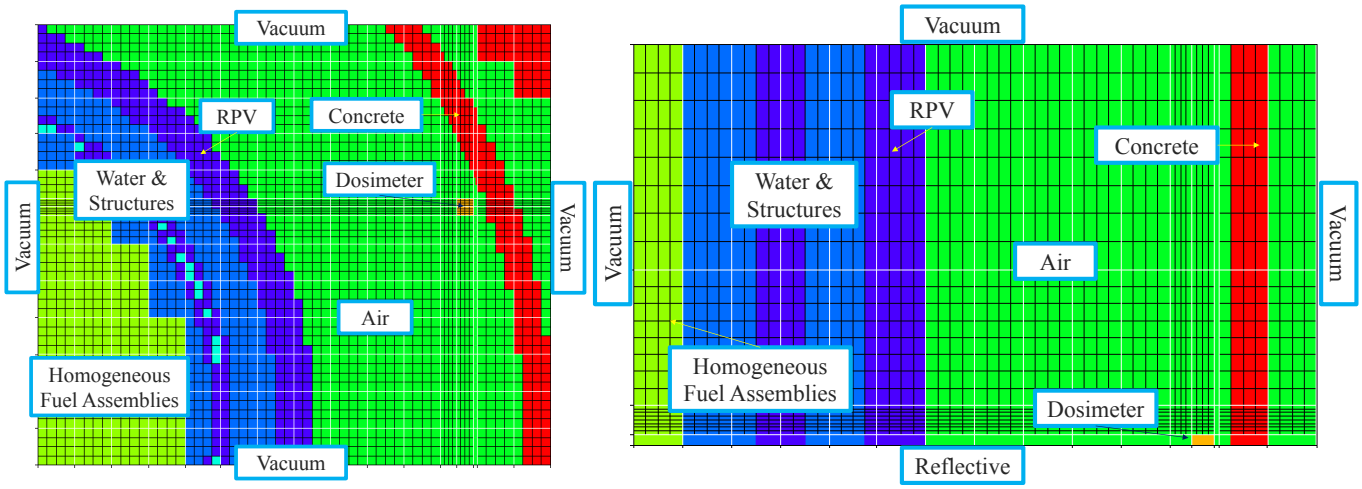

(a) Radial Projection **(b)** Axial Projection

Figure 7.6 TMI-1 Importance Model

7.2.3 3D PENTRAN^{TM} Importance Model

Fig. 7.6 shows the mesh distribution and the corresponding boundary condition of the 20-degree dosimeter 3D PENTRAN^{TM} importance model. The pre-selected control volume size is $303.079 \times 260.367 \times 180.34$ cm^3 with 4 assemblies in x-direction, 8 assemblies in y-direction, and 71 axial levels in z-direction. Note that one axial level is 2.54 cm.

Similar to the 1D model, the core structures are all homogenized by volume weighting for convenience. This is also a valid approximation since

- The dosimeter is very far away and will not "see" the details of the core geometry. In other word, the core geometry is very "fuzzy" to the dosimeter sitting outside of RPV.
- The importance function is only for acceleration of the DRF coefficient calculation, and therefore does not to be very accurate.

7.2.4 1D Importance Functions

The calculation parameters are: (1) Mesh size from minimum 0.05 cm to maximum 4.8 cm; (2) Legendre anisotropic scattering order of P3; (3) Quadrature order of S8; (4) Convergence criteria with 10^{-3} on scalar flux and maximum iteration of 100 per energy group. The calculations are performed using 1 processor with less than 5 minutes for all of them. Figs. 7.7 show the first six group of PENTRAN^{TM} calculated importance function for the $^{27}\mathrm{Al}(n,\alpha)$ dosimeter. The location of the structures are briefly indicated in the importance function plot.

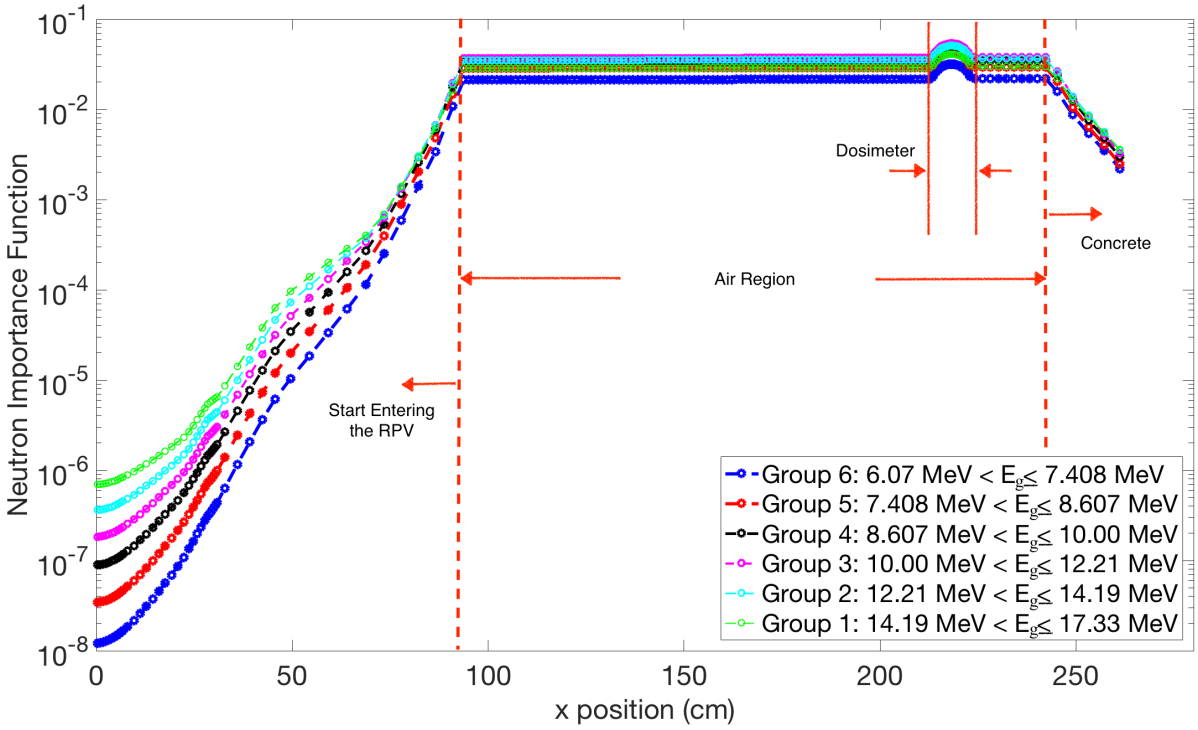

Figure 7.7 Importance Function: 1D Model with $^{27}\mathrm{Al}(n,\alpha)$ Dosimeter (Group 1 to 6)

The peak of the importance functions are obviously at the dosimeter location. The neutron born in the dosimeter has the highest probability to interact with the dosimeter and make contribution to the dosimeter response. In the air region, the neutrons rarely interact with the air due to very low concentration of atoms per unit volume. When entering into the RPV, the importance function drops significantly. The neutrons born from the core will encounter large amount of interaction with the structural materials. Consequently, they will be slowed down with lower energy, or even absorbed. Therefore, the neutron born further away from the dosimeter within the RPV are significantly less important.

The importance function for neutron with lower energy drops more significantly than the neutrons with higher energy. This is mainly because neutrons with higher energy carry larger kinetic energy, and will be more likely to penetrate through the structures. Therefore, they are more likely to make contribution to dosimeter response.

7.2.5 3D Importance Functions

The Calculation parameters are: (1) Mesh size from minimum 0.25 cm to maximum 12.5 cm; (2) Legendre anisotropic scattering order of P3; (3) Quadrature order of S8; (4) Convergence criteria with 5×10^{-3} on scalar flux and maximum iteration of 100 per energy group. The calculations are performed using 2 processor with $\sim$ 2 hours. Figs. 7.8 shows the PENTRAN$^{\text{TM}}$

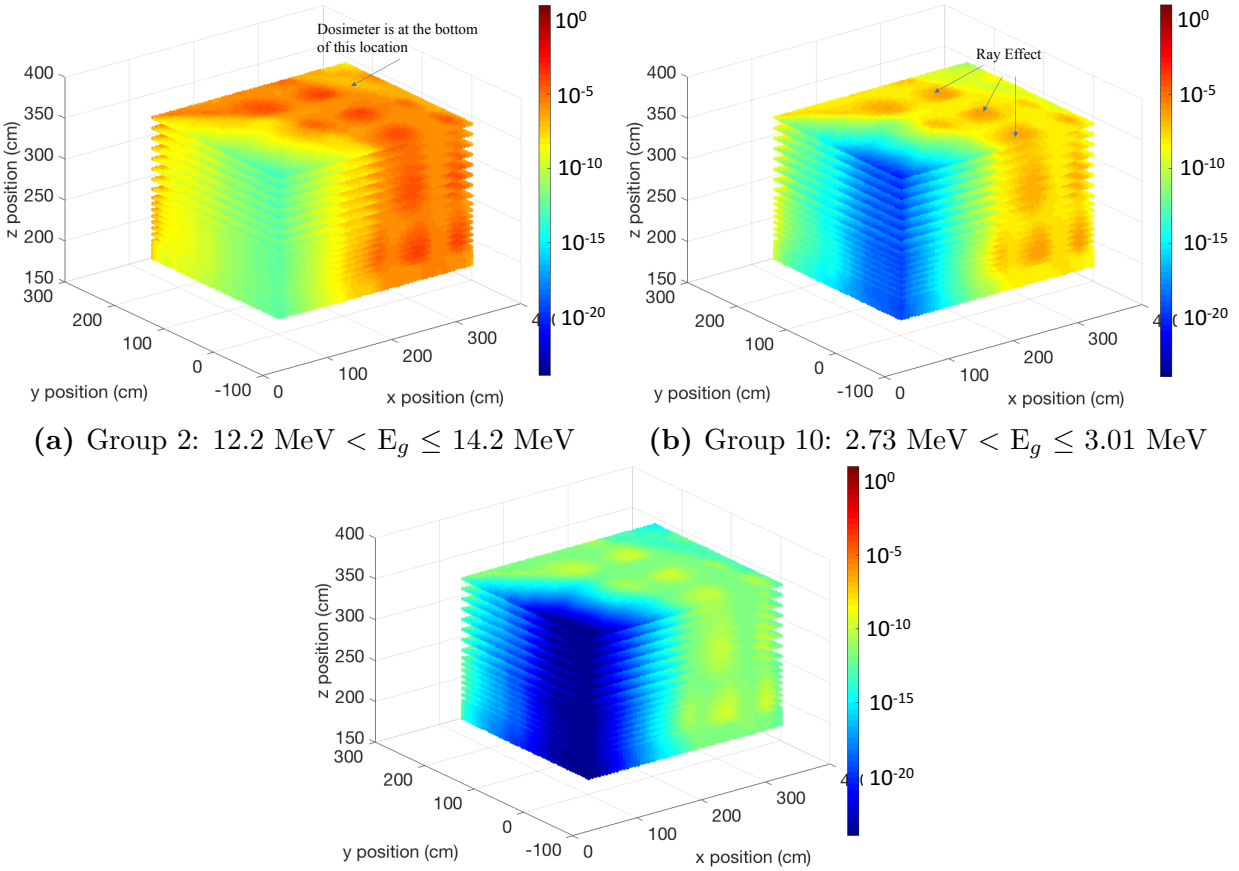

(a) Group 2: 12.2 MeV $< E_g \leq$ 14.2 MeV

(b) Group 10: 2.73 MeV $< E_g \leq$ 3.01 MeV

(c) Group 15: 1.92 MeV $< E_g \leq$ 2.23 MeV

Figure 7.8 PENTRAN^{TM} Calculated Importance Functions: 20-degree Middle Axial Plane ^{27}Al(n, α) Dosimeter

calculated importance function for the 20-degree middle axial plane ^{27}Al(n, α) dosimeter.

Similar to all the importance function we have seen in chapter 5 and 6, the importance function drops orders of magnitude away from the dosimeter. The importance function of neutrons with higher energy drops less significantly than the neutrons with lower energy. This is mainly because neutrons with higher energy are more likely to make contribution to the dosimeter response while the lower energy neutrons are opposite. Note that since the dosimeter is located at a region with large amount of air, the Ray effect [9] is clearly observed in Fig. 7.8.

7.2.5.1 3D Field of View Estimation

Figs. 7.9, 7.10, and 7.11 show the FOV for the 20-degree Middle Axial Plane ^{27}Al(n, α) Dosimeter.

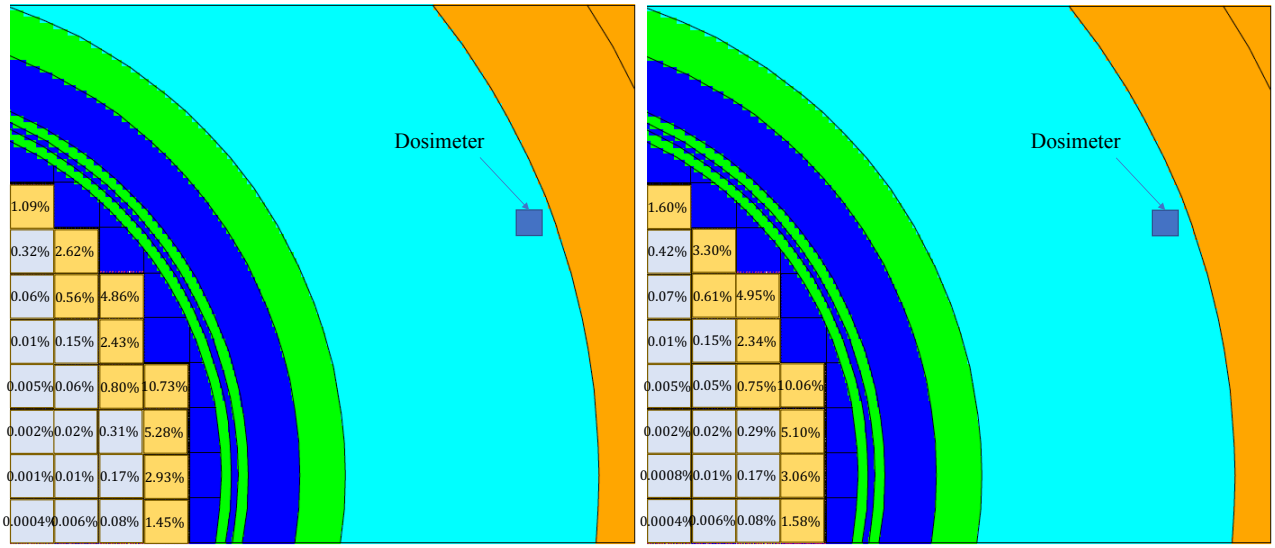

(a) Axial Level 1 **(b)** Axial Level 2

Figure 7.9 Field of View: 20-degree Middle Axial Plane $^{27}\mathrm{Al}(n,\alpha)$ Dosimeter

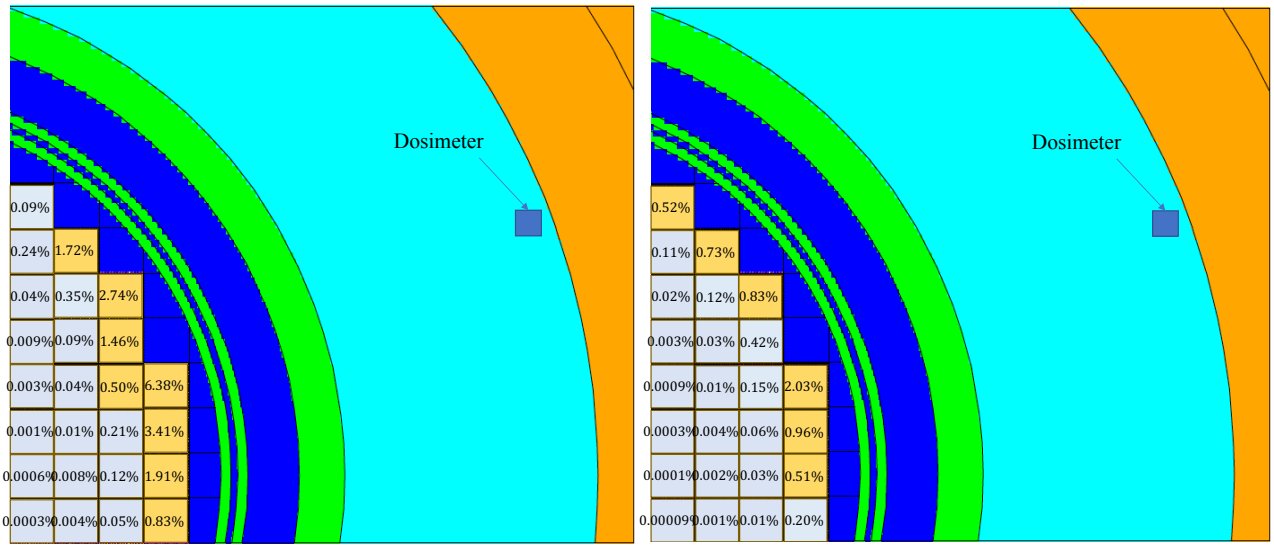

(a) Axial Level 3 **(b)** Axial Level 4

Figure 7.10 Field of View: 20-degree Middle Axial Plane $^{27}\mathrm{Al}(n,\alpha)$ Dosimeter

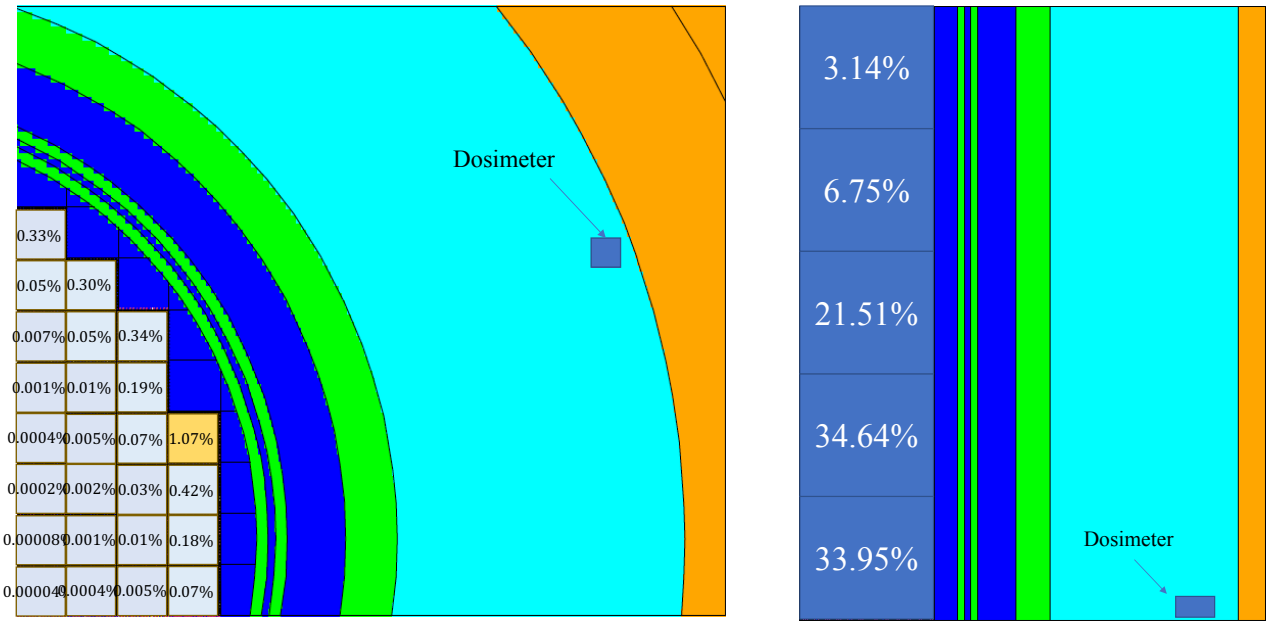

(a) Axial Level 5 **(b)** Axial FOV

Figure 7.11 Field of View: 20-degree Middle Axial Plane $^{27}\mathrm{Al}(n,\alpha)$ Dosimeter

Fig. 7.11b shows the axial FOV. Here, the fuel assemblies are evenly divided into five axial segments with 30.068 cm in length per segment. The lowest three axial segments contribute more than 90% of the $^{27}\mathrm{Al}(n,\alpha)$ dosimeter response. Figs. 7.9a, 7.9b, 7.10a, 7.10b, and 7.11a are the corresponding detailed assembly-wised FOV for the five axial segments. Here, we select a threshold assembly contribution of 0.5%.

The assemblies marked with light orange color are those with dosimeter response contribution more than 0.5%. The light yellow assemblies contribute $\sim$ 91.60% of the total dosimeter response. Therefore, only the DRF coefficient within these assembly need to be calculated. However, a little more assembly may be considered since we have concluded in chapter 6 that using flat source assumption may underestimate the FOV. Here, we assume cosine shape for axial source distribution while flat radial source distribution is still used for the FOV estimation.

Note that in Fig. 7.11b, the contribution from the lowest segment is slightly lesser than the one above it. This does not make sense in physics since the segment that is closer to the dosimeter should contribute more dosimeter response. However, this may be attributed to the Ray effect. The scalar importance function may not be very accurate due to presence of the Ray effect. Moreover, the importance function may not be fully converged. Again, the importance function is mainly for estimation of FOV and acceleration of DRF coefficient calculations, and thus does not need to be fully converged.

The FOV for other three dosimeters, $^{63}\mathrm{Cu}(n,\alpha)$, $^{54}\mathrm{Fe}(n,p)$, and $^{115}\mathrm{In}(n,n')$, the FOV are

very similar to each others. Therefore, only the ^{63}Cu(n,α) dosimeter with the same location is shown in the Appendix F for demonstration.

7.2.5.2 3D Group-wised Contribution

Fig. 7.12 shows the GC for the four dosimeter types. The ^{63}Cu(n,α) dosimeter has the highest cutoff energy ~ 6 MeV, mainly because the dosimeter cross-section is only 6 group. The ^{54}Fe(n,p) dosimeter has a second highest cutoff energy of ~ 2 MeV. The cutoff energy of other two dosimeters are ~ 1 MeV. These information provide us the input for PHYS card in the MCNP5 DRF coefficient calculations.

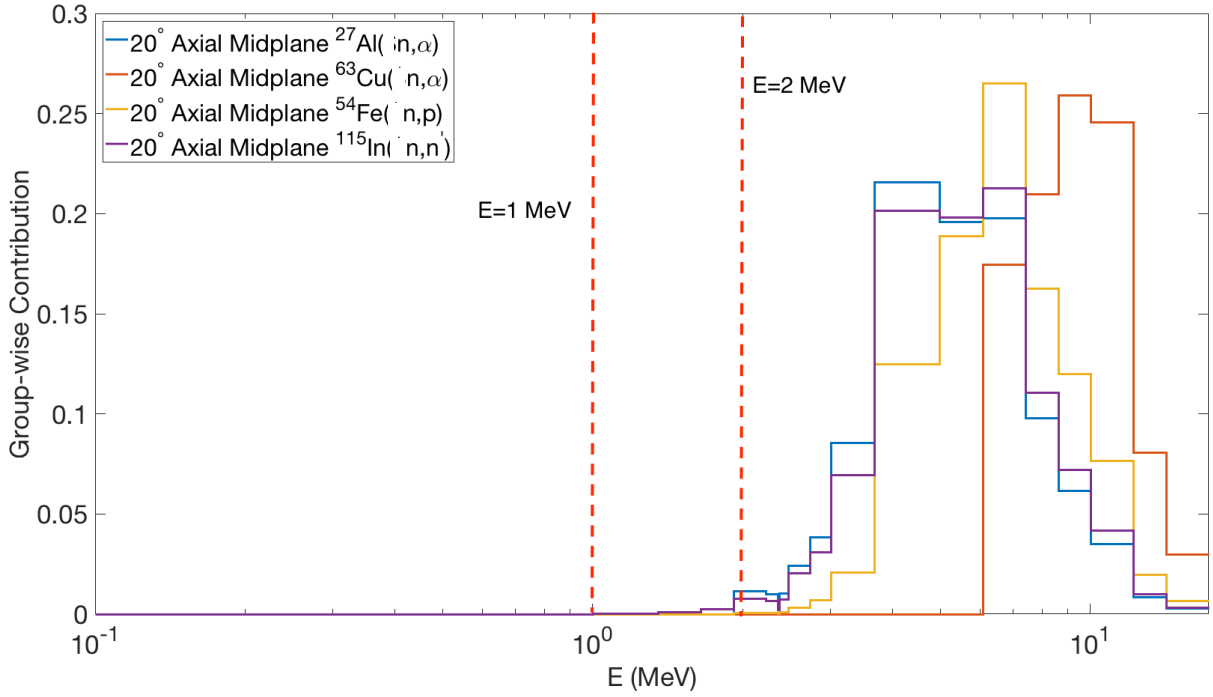

Figure 7.12 Group-wised Contribution for the Four Dosimeters: 20-degree Middle Axial Plane

7.2.5.3 3D Lower Weight Windows Calculations

Fig. 7.13 shows the calculated corresponding lower weight window bounds for 20-degree middle axial plane ^{27}Al(n,α) dosimeter using Eq. (4.8). The weight windows grow exponentially when location is far away from the dosimeter. This will cause more neutron being killed with the birth location far away from the dosimeter, which is reasonable. The neutrons born far away from the dosimeter are less likely penetrate through the complex structures and

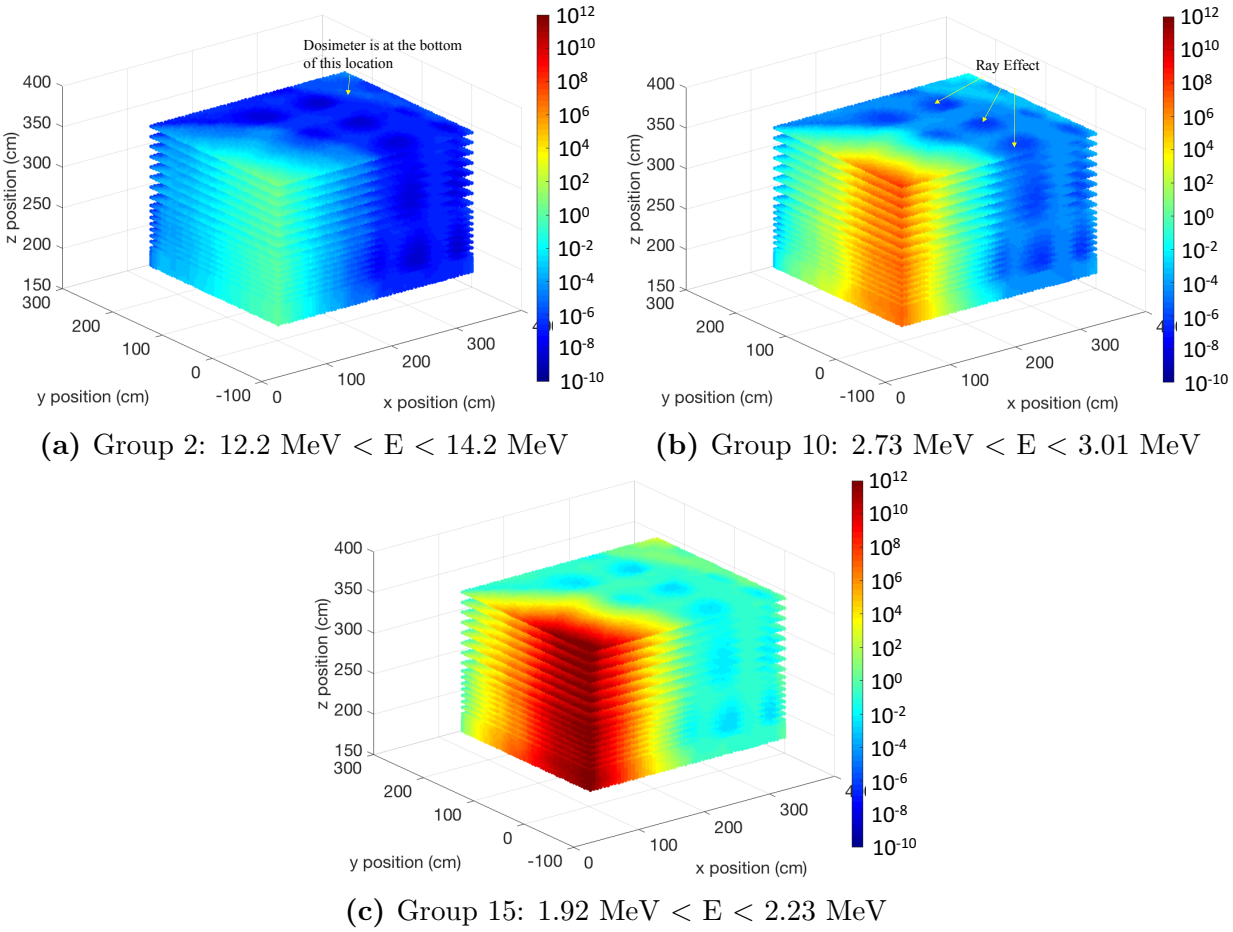

(a) Group 2: 12.2 MeV < E < 14.2 MeV

(b) Group 10: 2.73 MeV < E < 3.01 MeV

(c) Group 15: 1.92 MeV < E < 2.23 MeV

Figure 7.13 Lower Weight Window Bounds: 20-degree Middle Axial Plane $^{27}\mathrm{Al}(n,\alpha)$ Dosimeter

contribute to the dosimeter response. Note that the ray effect is still observed in the lower weight window bounds since they are calculated from the importance functions.

7.3 DRF Coefficient Sensitivity Study Using the 1D Model

In this section, the sensitivity study of the DRF coefficient to various parameters are performed. All the calculations are performed with number of particle from 10^8 to 2×10^9 in order to minimize the statistical noise, i.e., relative statistical uncertainty 1σ, to lower than 1%. The CADIS methodology is used for acceleration. The calculation time is from 5 minutes to 2 hours using 8 processors for one coefficient. The wide range of calculation time is mainly because the quality of importance function. Since 1D model is relatively faster to

calculate, quality on the importance function is not examined. Fig. 7.14 shows the selected fuel pellet for sensitivity study. It is assumed all the fuel pellets behave similarly on the sensitivity to different parameters.

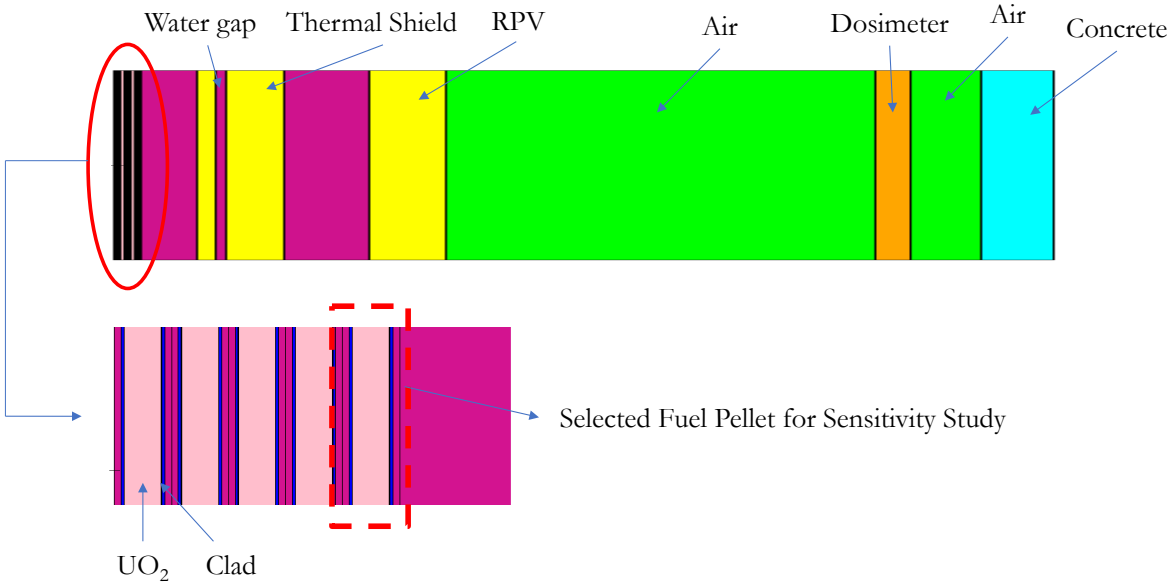

Figure 7.14 Selected Fuel Pellet for Sensitivity Study

7.3.1 ^{239}Pu to ^{238}U Ratio

In a PWR reactor, ^{239}Pu and ^{235}U are the nuclide which contribute to most of the fission. For the fuel assembly in a nuclear reactor, the two main things that affect the neutron behavior are (1) Fission Spectrum; and (2) Isotopic. The isotopic has been examined by placing pure UO_2 in the fuel pellet as material but using ^{239}Pu Watt fission spectrum for the DRF coefficient calculations. The result shows that less than 1% of change is observed when comparing with the DRF coefficient calculated by using pure ^{239}Pu Watt fission spectrum with PuO_2 material. Thus, the fission spectrum may be considered the main role for the DRF coefficient sensitivity. Here, sensitivtiy study is performed by placing different fraction of UO_2 and PuO_2 in all the fuel pellets in Fig. 7.14 using corresponding Watt fission spectrum constants from Eqs. (5.1), (5.2), and (5.3). The change of DRF coefficient is calculated using the following formula:

$$DRF\ Coefficient\ Change\ in\ \% = \frac{DRF_{concentration=i\%} - DRF_{concentration=0\%}}{DRF_{concentration=0\%}} \tag{7.1}$$

where i is a constant between 0 to 100.

Fig. 7.15 shows the sensitivity of the DRF coefficient calculated from Eq. (7.1) for different dosimeter. Here, the ^{239}Pu concentration is varied from 0% to 100%.

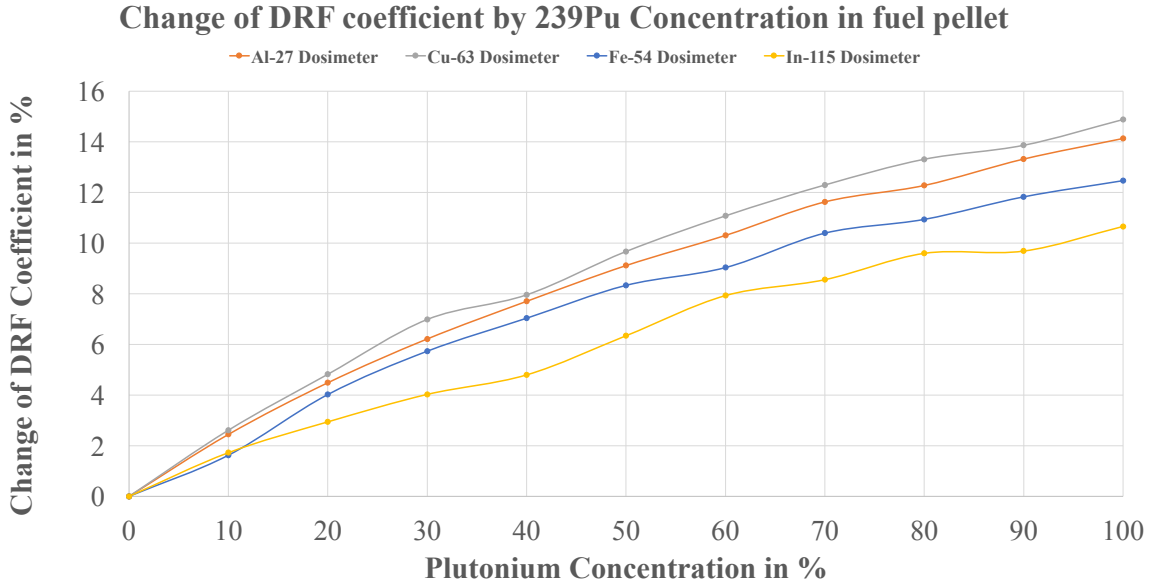

Figure 7.15 Sensitivity of the DRF Coefficient to ^{239}Pu to ^{238}U Ratio

The results show that maximum changes of 14.13%, 14.88%, 12.47%, and 10.66% are observed for $^{27}\mathrm{Al}(n,\alpha)$, $^{63}\mathrm{Cu}(n,\alpha)$, $^{54}\mathrm{Fe}(n,p)$, and $^{115}\mathrm{In}(n,n^{'})$ dosimeters, respectively. Current maximum averaged burnup level suggested by NUREG CR-6801 [111] is 40 GWd/MTHM with $4wt\%$ initial enrichment PWR fuel. With axial burnup profile, this value can be $\sim$ 50 GWd/MTHM. The corresponding ^{239}Pu/^{235}U ratio for such burnup level is $\sim 53:47$. From the results, the DRF coefficient is close to linearly dependent on burnup level with ^{239}Pu concentration range from 10% to 50%.

The dosimeter type will affect the sensitivity of DRF coefficient to ^{239}Pu/^{235}U ratio. Since the four dosimeters are sensitive to neutron in different energy range, it is expected that dosimeter with higher threshold energy is more sensitive to the ^{239}Pu/^{235}U ratio. This is mainly because the neutrons with higher energy penetrate through the RPV are more likely with free-flight process. More information will be carried out without collision process. The $^{27}\mathrm{Al}(n,\alpha)$ and $^{63}\mathrm{Cu}(n,\alpha)$ dosimeters have the highest threshold energy among all of them, and therefore have the maximum change on the DRF coefficients. The $^{115}\mathrm{In}(n,n^{'})$ dosimeter has a lowest 0.95 MeV threshold, and therefore scattered neutrons will be more likely to contribute to the dosimeter response. Therefore, the fuzziness through scattering process can yield smaller changes on the DRF coefficient.

Note that sensitivity study on fuel enrichment is also performed. The fuel enrichment does not affect the fission spectrum but only the concentration of ^{235}U. Therefore, the DRF coefficients are not sensitive to the fuel enrichment.

These results have been verified by the 3D model with different fuel assembly burnups at other locations. The results show that the 3D results are consistent with the 1D results.

7.3.2 Boron Concentration in Primary Coolant

The UO_2 4 wt% fresh fuel is used for the study. The boric acid are added into the PWR primary coolant for the purpose of reactivity control. Here, the sensitivity of the DRF coefficient to the boron concentration in water is examined. Fig. 7.16 shows the sensitivity of the DRF coefficients to the primary coolant boron concentration.

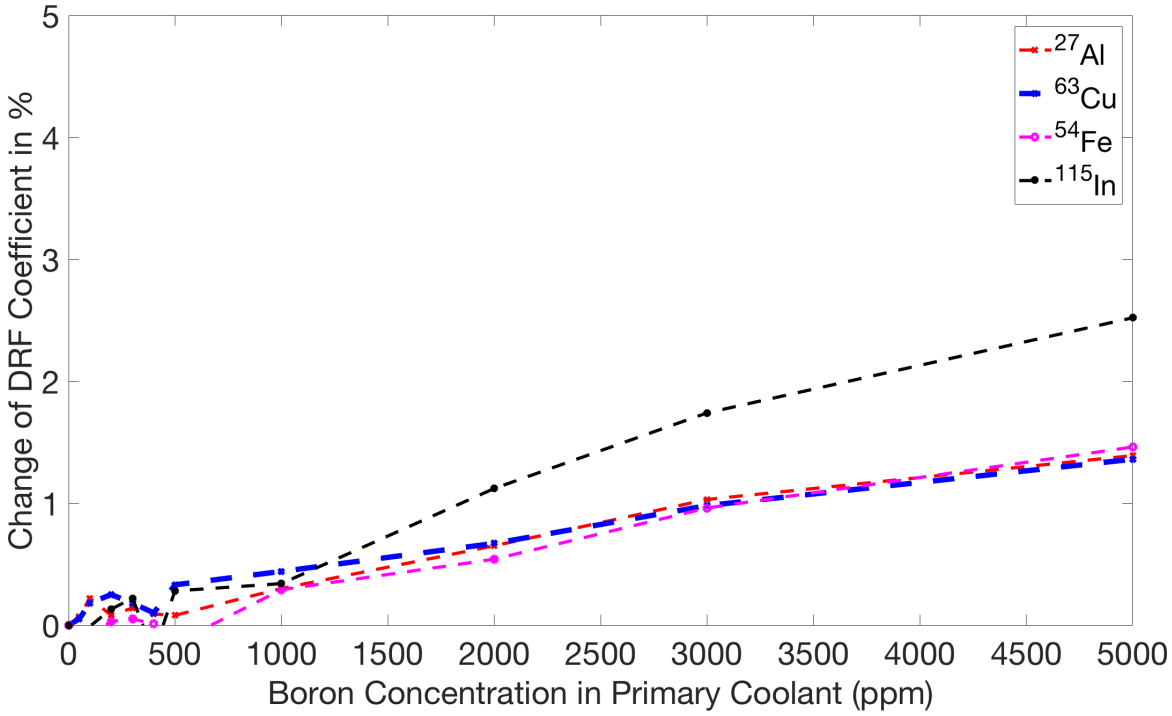

Figure 7.16 Sensitivity of the DRF Coefficient to Boron Concentration in the Primary Coolant

The results show that negligible changes on the primary coolant boron concentration lower than 1000 ppm are observed. Change of 1.39%, 1.36%, 1.46%, and 2.52% from boron concentration of 5000 ppm are observed for $^{27}\mathrm{Al}(n,\alpha)$, $^{63}\mathrm{Cu}(n,\alpha)$, $^{54}\mathrm{Fe}(n,p)$, and $^{115}\mathrm{In}(n,n')$ dosimeters, respectively. These changes are considered small mainly because boron mainly absorb thermal neutrons. The fast neutrons with E>1 MeV are more important for RPV neutron fluence calculations. However, larger changes for $^{115}\mathrm{In}(n,n')$ dosimeter is observed mainly because the lower threshold energy of 0.95 MeV.

7.3.3 Temperature Distribution

The UO_2 4 wt% fresh fuel is used for the study. Here, three temperature profiles are selected for study: (1) Fuel, cladding, and primary coolant temperatures are all 293 K; (2) Fuel: 900 K, primary coolant: 600 K, cladding: 600 K; and (3) Fuel: 1200 K, primary coolant: 600 K, cladding: 600 K. Here, the fist temperature profile (room temperature) is selected as the reference.

The results show that negligible change with order of 0.03% for all of the dosimeters are observed. For RPV neutron fluence calculations, only neutron with energy > 1 MeV are interested. The temperature will only affect the resonance shape, which the energy are all below 1 MeV for the importance nuclides. Fig. 7.17 shows the total microscopic cross-sections of the important heavy nuclides in the Light Water Reactors (LWRs).

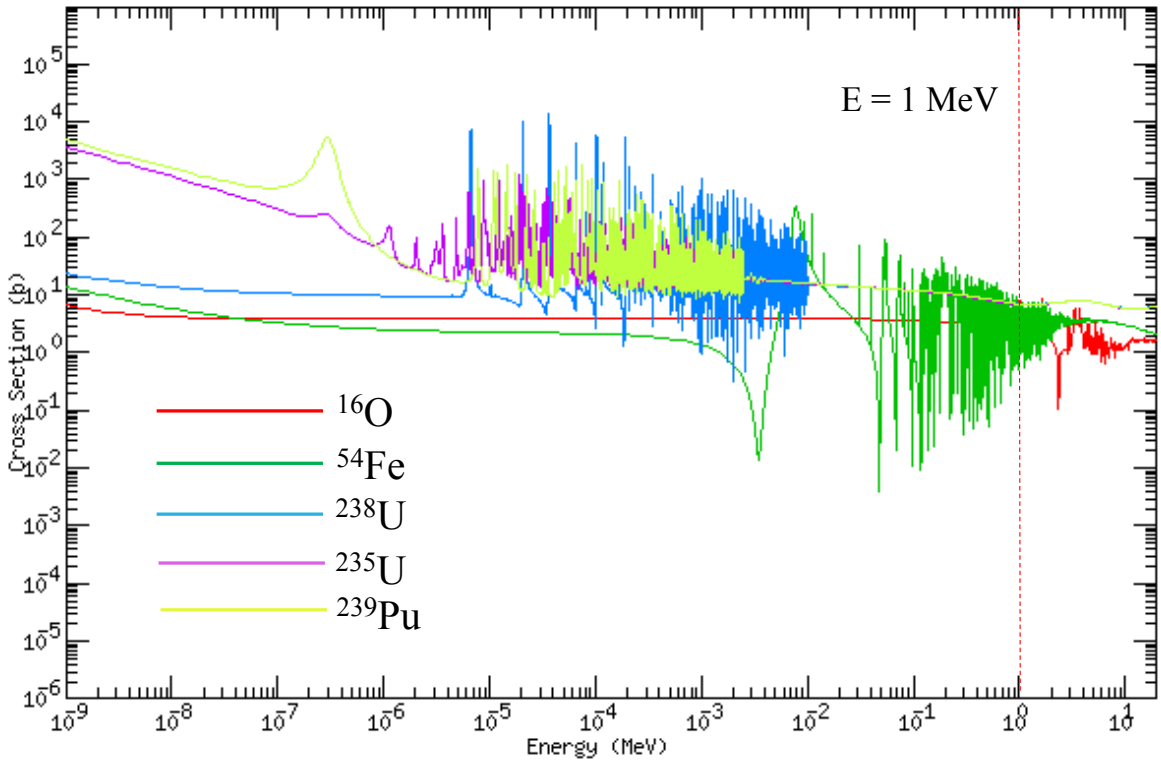

Figure 7.17 Microscopic Cross-section for the Important Nuclides in LWR [6]

Although the ^{54}Fe and ^{16}O have resonances for E > 1 MeV, the following reasons can make them become not important:

1. The amount of iron in reactor core are considered lesser than the other materials, and therefore will not affect the DRF coefficient significantly.

2. The resonance peak of ^{16}O is relatively much smaller than other peak for the heavy nuclides, and therefore the effect will be less significant.

3. Significant amount of ^{54}Fe is located at RPV. However, the temperature of the RPV will not be as high as it is in the reactor core. Therefore, it will have minimal effect.

7.3.4 Primary Coolant Density

Under reactor normal operating condition, the temperature of primary coolant is $\sim 300°$C, depending on the location of the core. With primary loop's pressure of $\sim$ 15 MPa, the density of water will be ~ 0.7g/cm^3. Here, the sensitivity of DRF coefficient by primary coolant density is studied. The primary coolant density is varied from 0.65 to 1.00 g/cm^3. Fig. 7.18 shows the sensitivity of the DRF coefficients to the primary coolant density.

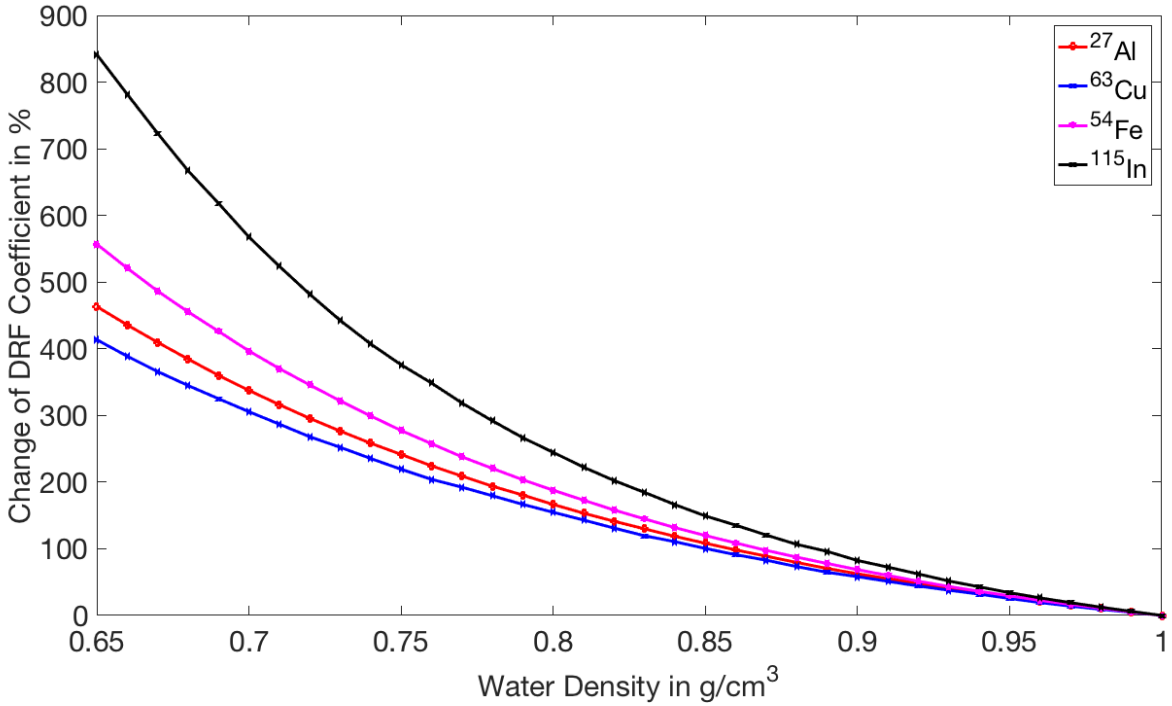

Figure 7.18 Sensitivity of the DRF Coefficient to Primary Coolant Density

Here, the DRF coefficients for primary coolant density of 1.00 g/cm^3 is considered the reference cases. The results show that maximum changes of $\sim$ 463%, $\sim$ 415%, $\sim$ 557%, and $\sim$ 841% with primary coolant density of 0.65 g/cm^3 for ^{27}Al(n,α), ^{63}Cu(n,α), ^{54}Fe(n,p), and ^{115}In$(n,n^{'})$ dosimeters, respectively. The neutrons will more likely to penetrate through the deep shield and contribute to the dosimeter response mainly because the lower density, which lower the number of collision. Therefore, the DRF coefficient will be depending on the primary coolant density.

7.3.5 Void Fraction

Under reactor transient condition, vapor may be formed from the two phase flow. Part of the primary coolant will become vapor under such condition. To study the sensitivity of the DRF coefficient by void fraction, the density of water is varied from 7.56×10^{-4} to 0.99 g/cm^3 to represent void fraction from 0 to 100%. The vapor and water densities are taken from the Pacific Northwest National Laboratory (PNNL) report - compendium of material composition data for radiation transport modeling [112]. Fig. 7.19 and 7.20 show the variation of the DRF coefficient and change of DRF coefficient in % by changing the void fraction. Note that the change of the DRF coefficient is calculated by selecting void fraction= 0 as reference case.

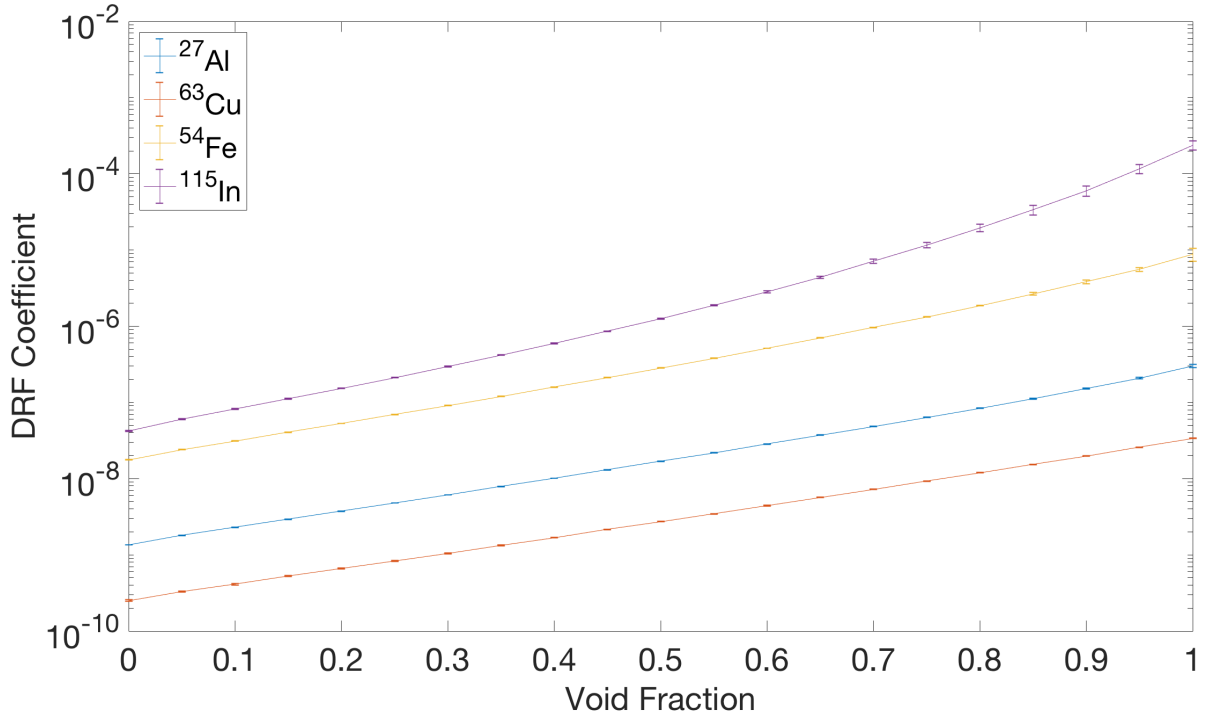

Figure 7.19 Variation of the DRF Coefficient by Void Fraction (with 3σ)

The results show that the DRF coefficient is very sensitive to the void fraction in primary coolant. Maximum changes of 2.22×10^4%, 1.33×10^4%, 4.98×10^4%, and 5.61×10^5% are observed for $^{27}\mathrm{Al}(n,\alpha)$, $^{63}\mathrm{Cu}(n,\alpha)$, $^{54}\mathrm{Fe}(n,p)$, and $^{115}\mathrm{In}(n,n')$ dosimeters, respectively. Two to four orders of magnitude differences are observed on the DRF coefficients. This is mainly because the significant increase on neutron penetration probability by increase of void fraction. The $^{115}\mathrm{In}(n,n')$ DRF coefficients show the largest change among all of them. This is because of the low threshold energy of 0.95 MeV. The penetration probability of low energy neutrons increase more significantly than the fast neutron. For this, dependency of void fraction on the DRF coefficient is necessary for transient scenarios.

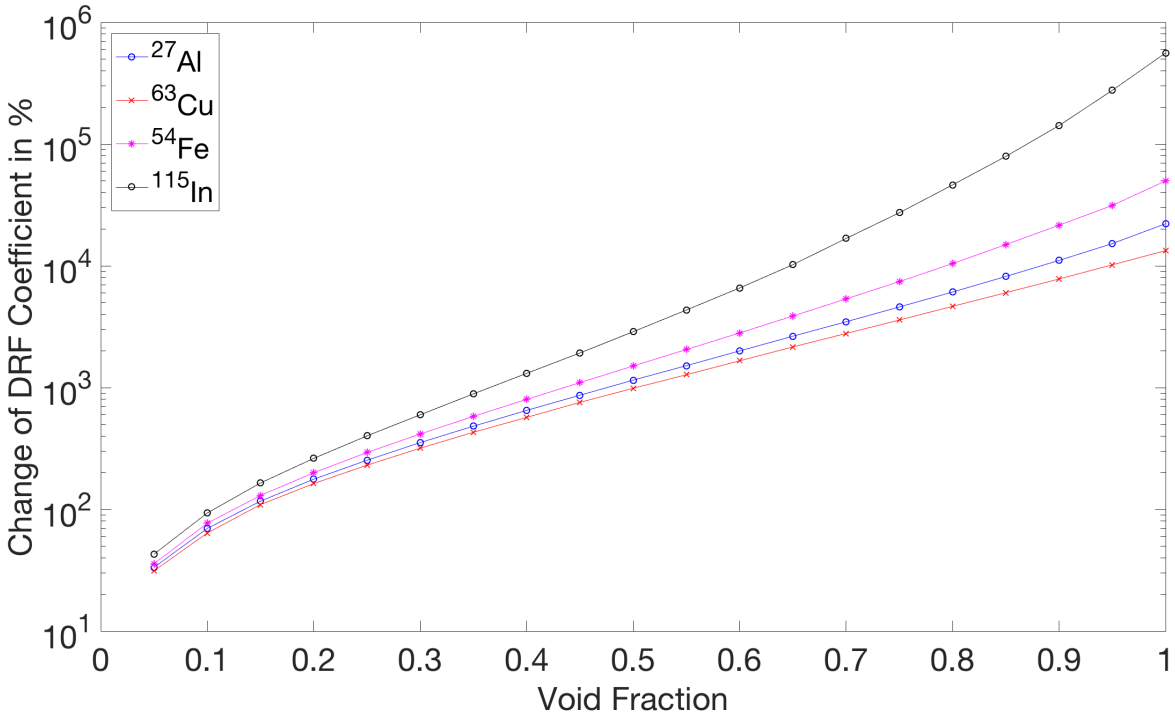

Figure 7.20 Cahnge of the DRF Coefficient by Void Fraction

7.3.6 Axial Boundary Structure

Due to limited computation resources and the size of TMI-1 RPV dosimetry problem, limited sensitivity study on axial boundary effect using the 3D model is performed. However, preliminary study using a few selected assemblies and $^{27}\mathrm{Al}(n,\alpha)$, $^{115}\mathrm{In}(n,n^{'})$ dosimeters at 20-degree and axial mid-pane is performed. The results show that range of $\sim -10\%$ to $\sim 10\%$ of changes on the $^{27}\mathrm{Al}(n,\alpha)$ DRF coefficients and $\sim 5\%$ change on dosimeter response is observed. For the $^{115}\mathrm{In}(n,n^{'})$ dosimeter, $\sim -30\%$ to $\sim 5\%$ of changes on the DRF coefficients with $\sim 8\%$ of change on dosimeter response is observed. The $^{115}\mathrm{In}(n,n^{'})$ dosimeter has a relative lower threshold energy. Therefore, more dosimeter response are from collided neutrons. In contrast, the dosimeter response of $^{27}\mathrm{Al}(n,\alpha)$ is mainly from free-flight neutrons. Therefore, the boundary structure has relatively small effect.

The sensitivity study of this part is performed with an axial boundary homogeneous structure material, which is mixture of water and steel. Sensitivity study of axial structure effect can be further performed using a more detailed Monte Carlo TMI-1 model. The most difficult part of this is the access to the detailed reactor structure geometry and material, which are proprietary of the vendors.

7.4 DRF Coefficient Uncertainty Quantification Using the 1D Model

In this section, the uncertainties mainly from the dimensions will be studied. From one of the reference article [113], the TMI-1 reactor dimension uncertainties with 3σ confidence range are:

1. Fuel density $\pm 0.17\ g/cm^3$
2. Fuel pellet diameter $\pm 0.013\ mm$
3. Gap thickness $\pm 0.024\ mm$
4. Clad thickness $\pm 0.025\ mm$
5. ^{235}U concentration $\pm 0.00224\ w/o$

Among all of them, the ^{235}U concentration has been studied and proven to be not sensitive to the DRF coefficient in the section 7.3.1. Note that all the uncertainties are estimated by assuming normal distribution.

7.4.1 Uncertainty from Fuel Density and Dimension

Figs 7.21 and 7.22 show the changes of the DRF coefficient by uncertainties from fuel pellet density and dimension.

The results show that less than 2% of differences are observed with such range of UO_2 density variation. Negligible variation of DRF coefficients from density variation of ± 0.17 g/cm^3 is expected. This is mainly because the DRF coefficients are defined as per unit neutron source.

Fig. 7.22 shows the changes of DRF coefficient by varying the fuel pellet dimension. Note that the reference fuel pellet diameter is 0.936 cm. Here, the range of diameter variation is from -0.4 to 0.01 cm. The upper limit does not increase more since the diameter of fuel pellet is restricted by the size of cladding.

The results show that less than 1% of changes are observed with diameter variation more than the value of ± 0.013 mm. The uncertainty of fuel pellet dimension and density are thus not important. This is also mainly because the DRF coefficients are defined as per unit neutron source. With such small change on the fuel pellet may impact the neutron source strength significantly, but negligible effect is observed for the DRF coefficients with the manufacturing uncertainty range.

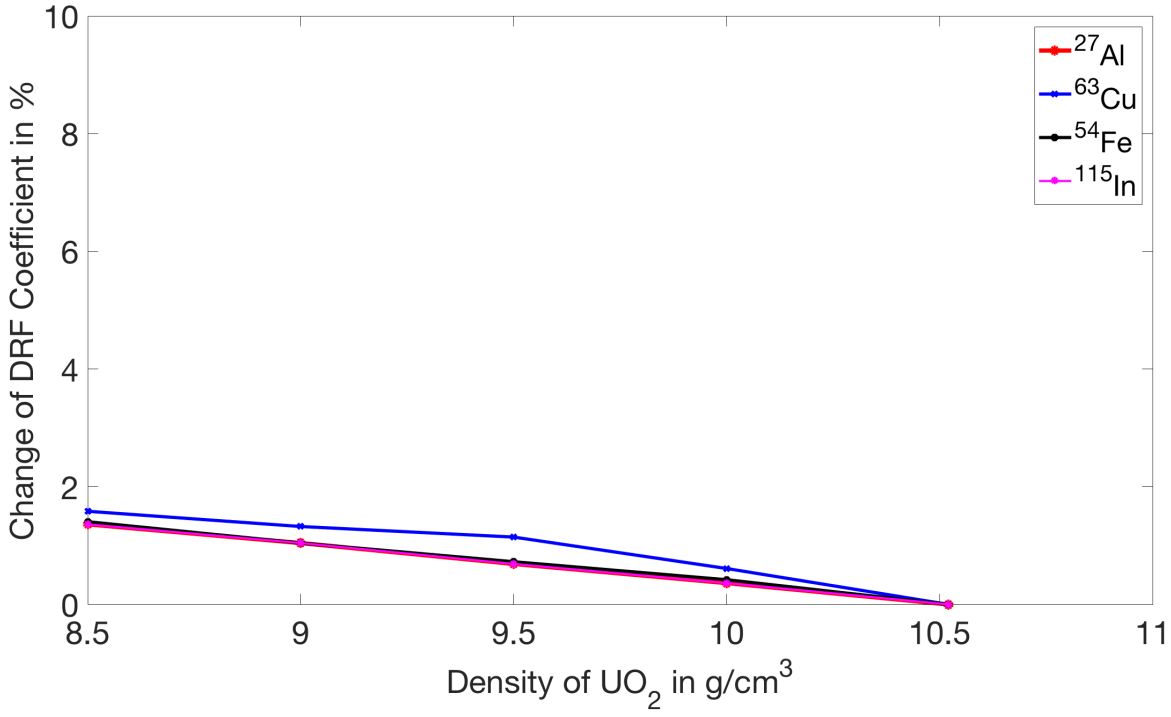

Figure 7.21 Cahnge of the DRF Coefficient by the UO_2 Fuel Density

7.4.2 Uncertainty from Fuel Clad and Gap Dimension

Uncertainty range of fuel cladding and gap thicknesses from -0.01 cm to 0.01 cm is selected for study. Note that the original cladding and gap thicknesses 400 are 0.0661 cm and 0.011 cm. The results show that less than 1% of changes on the DRF coefficients are observed from fuel cladding and gap thickness uncertainty. Therefore, negligible impact from the fuel cladding and gap thickness are observed.

7.4.3 Uncertainty from RPV Thickness

The standard RPV dimension of TMI-1 is 22 cm. Uncertainty of this number can occur from manufacturing side. For this, the uncertainty quantification is performed by varying the RPV dimension. Fig. 7.23 shows the changes of DRF coefficient by RPV dimension uncertainties. There is no public data available for the TMI-1 RPV dimension uncertainty. Therefore, the uncertainty range is from -2 to 4 cm, which corresponding to -10% to 20% changes of the RPV thickness are choosen. Note that $\sim$ 10% to 20% of dimension uncertainty is considered enormously large from the manufacturing side.

The results show that difference range from $\sim -50\%$ to $\sim 40\%$ of differences are observed. The change of $^{27}\mathrm{Al}(n,\alpha)$, $^{63}\mathrm{Cu}(n,\alpha)$, and $^{54}\mathrm{Fe}(n,p)$ dosimeter DRF coefficients are very

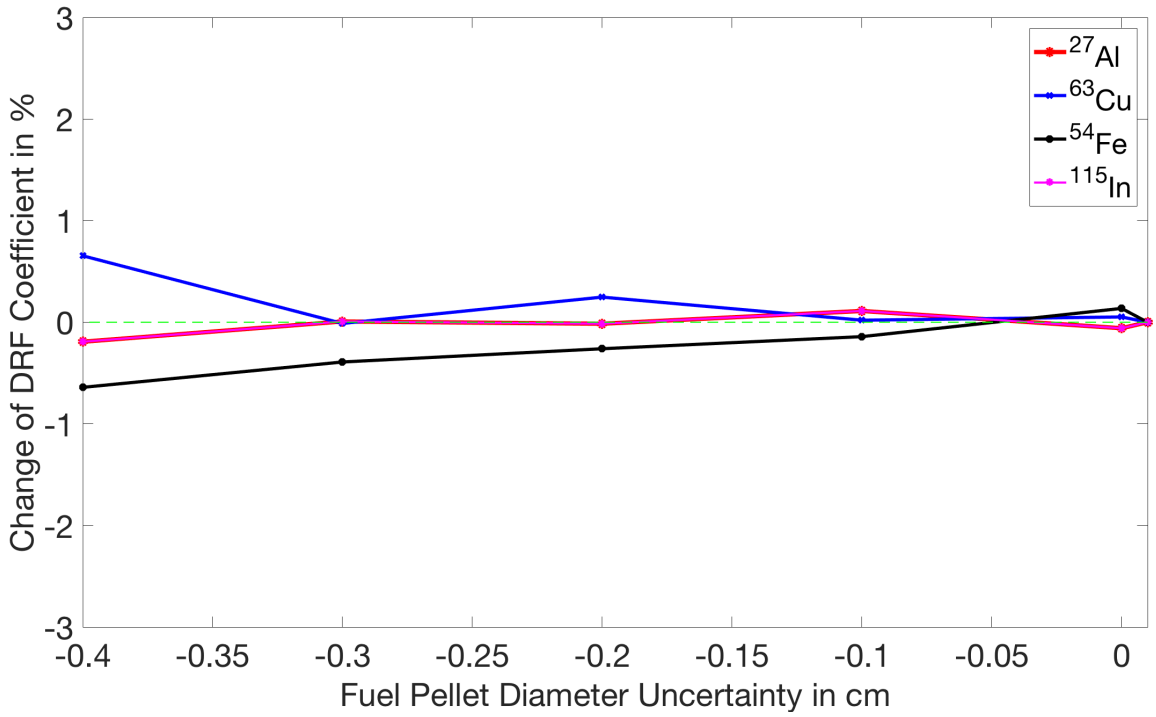

Figure 7.22 Cahnge of the DRF Coefficient by the UO_2 Fuel Pellet Dimension

close to each others. The $^{115}\text{In}(n, n^{'})$ dosimeter DRF coefficient is relatively less sensitive to the RPV thickness. The main reason is the lower threshold energy. A trend of exponential drop is shown in Fig. 7.23. Therefore, it is possible to perform extrapolation technique to determine the change of the DRF coefficient by the RPV thickness.

7.4.4 Uncertainty from Iron Cross-section of RPV

Literatures have indicated that iron cross-section at energy range from 5 to10 MeV have relative large uncertainty [114]. More than 65% of the composition of RPV are iron. The neutrons entering the RPV will encounter significant amount of scattering. Therefore, studying the impact of iron cross-section uncertainty is necessary. The macroscopic cross-section contains two component: (1) N - Number Density; and (2) $\tilde{\sigma}$ - microscopic cross-section. Here, we try to perturb the number density instead of microscopic cross-section. Fig. 7.24 shows the change of DRF coefficients by uncertainties from the macroscopic cross-section.

The results show that a consistent pattern is observed for all the dosimeter types. Changes of DRF coefficient from 55% to -40% are observed by uncertainties range of -7% to 8.5% from the macroscopic cross-section.

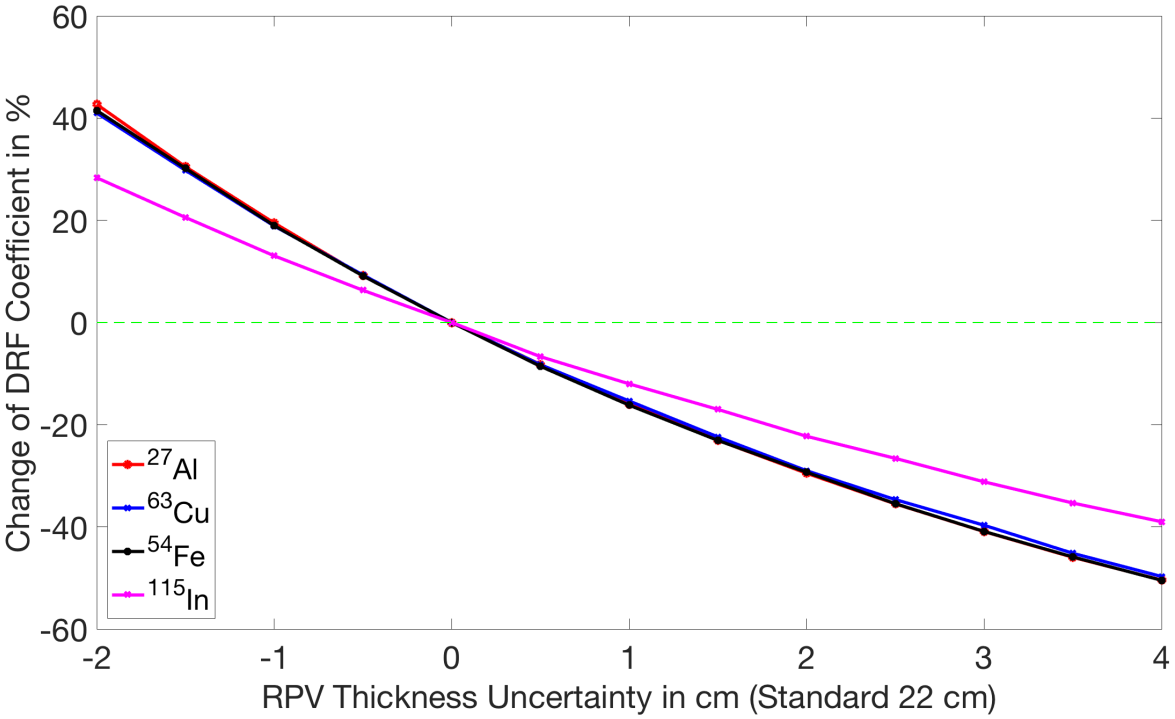

Figure 7.23 Cahnge of the DRF Coefficient by the RPV Dimension

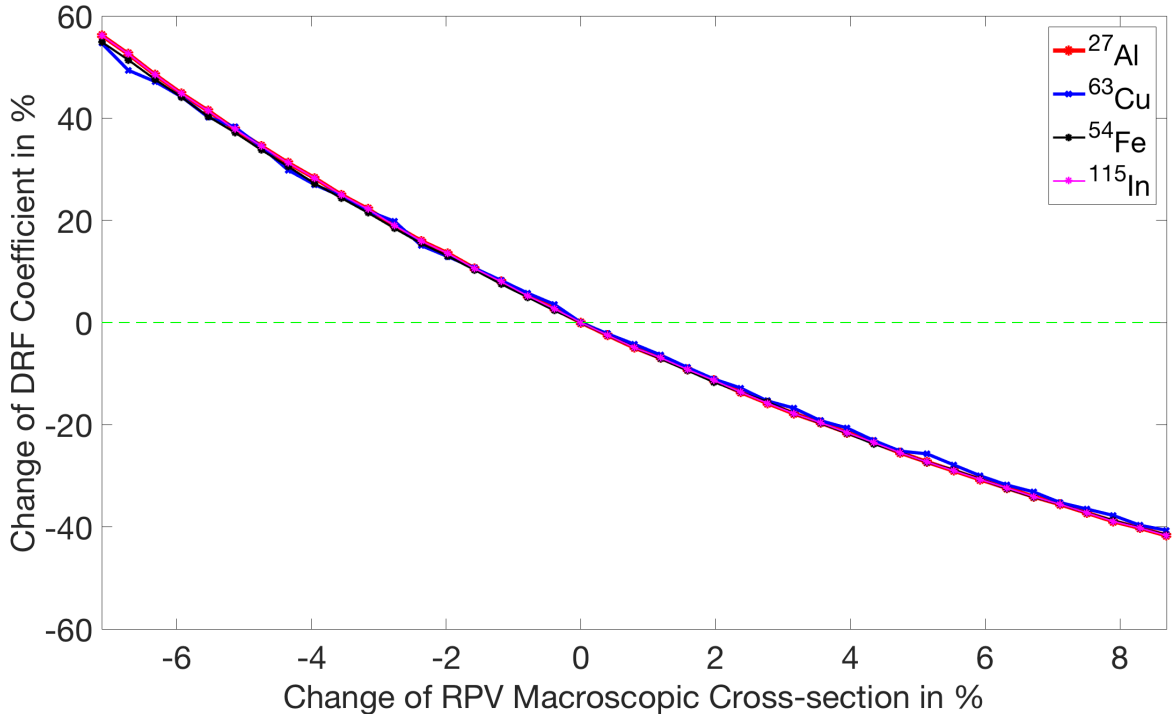

Figure 7.24 Cahnge of the DRF Coefficient by the Iron Cross-section of RPV

7.5 3D DRF Coefficient Calculations

The 3D DRF coefficient are calculated using the MCNP5 code system + the CADIS methodology. In this section, the approaches used to calculate the DRF coefficients and the behavior of them will be discussed.

7.5.1 Mesh of the Unit Neutron Source for DRF Coefficient Calculations

For the benchmark calculations we have performed in chapter 5 and 6, the FOV and model size are relatively small. Therefore, calculation of DRF coefficient within every fuel pellet is possible. However, the number of fuel pellet we will have to considered from the Figs. 7.9, 7.10, and 7.11 will be 35 assemblies $\times$ 208 $\times$ 5 fuel pellets (with axial pellet lumping) = 36400 DRF coefficients have to be calculated. This is considering an axial fuel pellet lumping scheme with $\sim$ 17 pellet lumping together axially. If we consider the 4 axial level lumping scheme in the chapter 5, there will be way much more DRF coefficient need to be calculated. In principle, this is still achievable if we have sufficient amount of processor, such as the TITAN cluster in Oak Ridge National Laboratory [115], which has 299,008 processors. However, it is typically impractical to spend effort trying to get access to such system, especially foreign national as the author of this dissertation.

However, if we think carefully, it is not hard to figure out that the slope of DRF coefficient may not be very steep in certain location, such as those assemblies making relatively smaller contributions. With the dosimeter locating at extremely far location from all the assemblies, the slope of the DRF coefficients may be less steeper than what we have seen so far as well. Fig. 7.25 shows an example of how the mesh can be arranged by the dosimeter location. The yellow lines between the fuel pellets are referring to the lumping scheme for unit source of DRF coefficient. This can be performed by the *Dp*RAPID utility code, which has been discussed in the section 3.1.

So far, we can see the DRF coefficients have the most steep drop for the fuel pellets that are the closest to the detector/dosimeter. They almost drop exponentially, therefore it is reasonable to have finer mesh at such locations as shown in the Fig. 7.25. With this arrangement, the number of DRF coefficients that have to be calculated can be greatly reduced. Similar lumping scheme can be applied axially as well.

7.5.2 Assumption for Mixing Assemblies with Different Burnup

In an operating commercial PWR, the burnup level of the fuel assemblies will be different from others. Based on the sensitivity study in the section 7.3.1, the DRF coefficients are

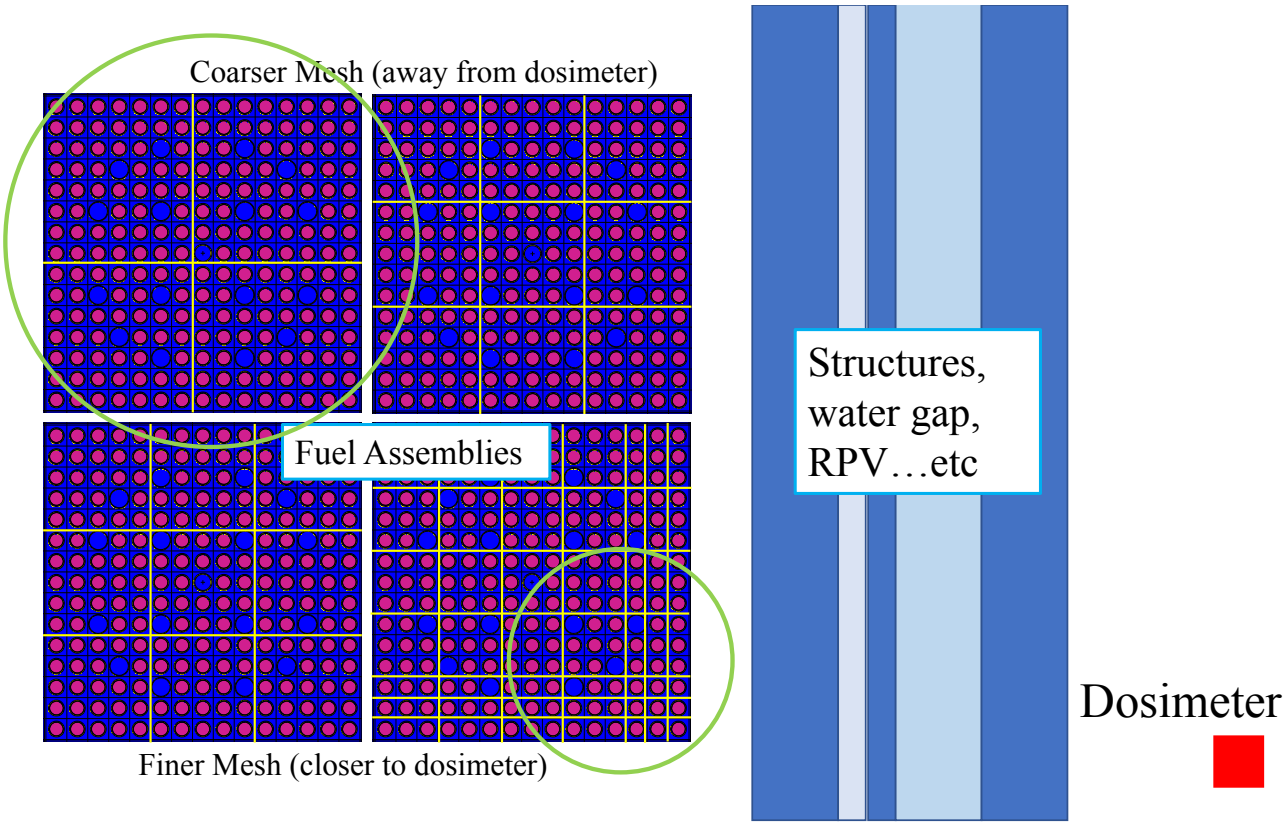

Figure 7.25 Example of Meshing Scheme for DRF Coefficient Calculations

way much sensitive to the fission neutron source spectrum than the isotopic. Furthermore, the isotopic change has almost no effect by UO_2 to PuO_2 ratio. For this, we can calculate the DRF coefficients using the approach shown in the Fig. 7.26.

The DRF coefficients for different burnup levels (or ^{239}Pu to ^{238}U ratio) are calculated with uniform burnup material composition in the reactor core. It is assumed that the fission spectrum is significantly much important than the material composition. This assumption holds for most of the case, except if there is a major change of materials, such as replacing fuel with air.

7.5.3 The 3D DRF Coefficients

In this section, the behavior of the calculated DRF coefficients will be discussed. Fig. 7.27 shows the calculated DRF coefficients for $^{27}\mathrm{Al}(n,\alpha)$ dosimeter located at 20-degree and axial mid-plane. The number of particles used for calculations varies from 10^8 to 2×10^9, depending on the meshing scheme and location.

Here, the fuel pellets are lumped axially with 4 of them together for the DRF coefficient

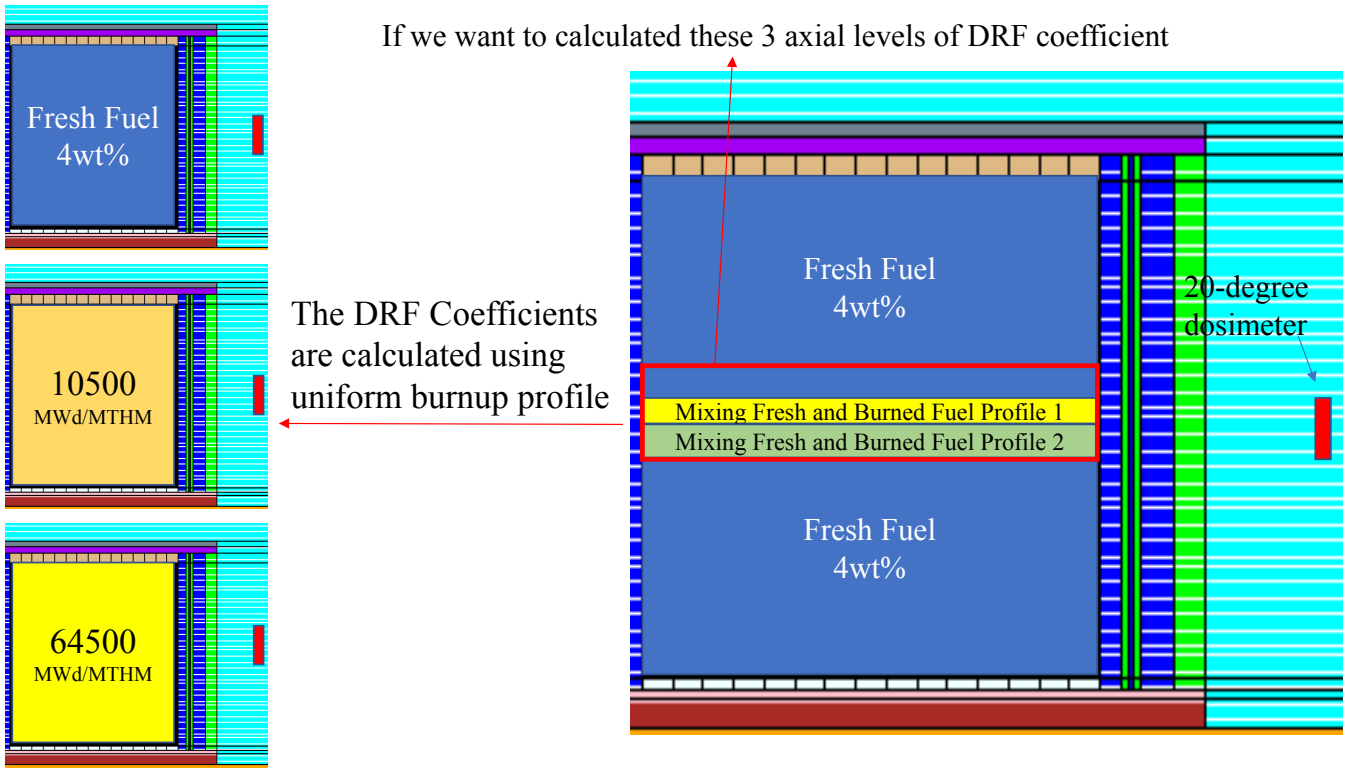

Figure 7.26 Approach to Calculate DRF Coefficients for RPV Sueveillance

calculations. One axial height is 2.54, which gives $2.54 \times 4 = 10.16$ cm axial level per DRF coefficient. The radial lumping scheme is used as well. The most closest fuel assemblies in every axial level are calculated pin-wised radially (1 fuel pellet radially for mesh). The mesh of other fuel assemblies are $3 \times 3 = 9$ fuel pellets. The unit coefficient calculation time is from 30 minutes to 13 hours using 8 processors. The total calculation time is about two weeks using 56 processors. Note that the long calculation time is because we are desiring 1σ statistical uncertainty $< 1\%$ for the assembly close to the dosimeter. In principle, lesser computation time can be tolerable with $\sim 3\%$ of 1σ statistical uncertainty.

The $^{27}\mathrm{Al}(n,\alpha)$ DRF coefficients drops 1 order of magnitude away for 1 assembly (~ 21.811 cm) radially. For axial distribution, it drops 1 order of magnitude for 13 axial levels (~ 132 cm) away. The axial FOV is larger than the radial FOV mainly because the neutron born at edge will be more likely to penetrate through the structures and contribute to dosimeter responses. With radial direction, the neutron born inside the fuel assemblies has more chance to be absorbed by fuel material after slowing down.

Fig. 7.28 shows the corresponding 1σ statistical uncertainties for the DRF coefficients in Fig. 7.27. The value varies from $\sim 0.8\%$ to $\sim 7\%$.

Note that the axial level numbers for calculated DRF coefficients here are from 19 to 31 (total 13 axial level). Further detailed DRF coefficients at different axial levels are shown in

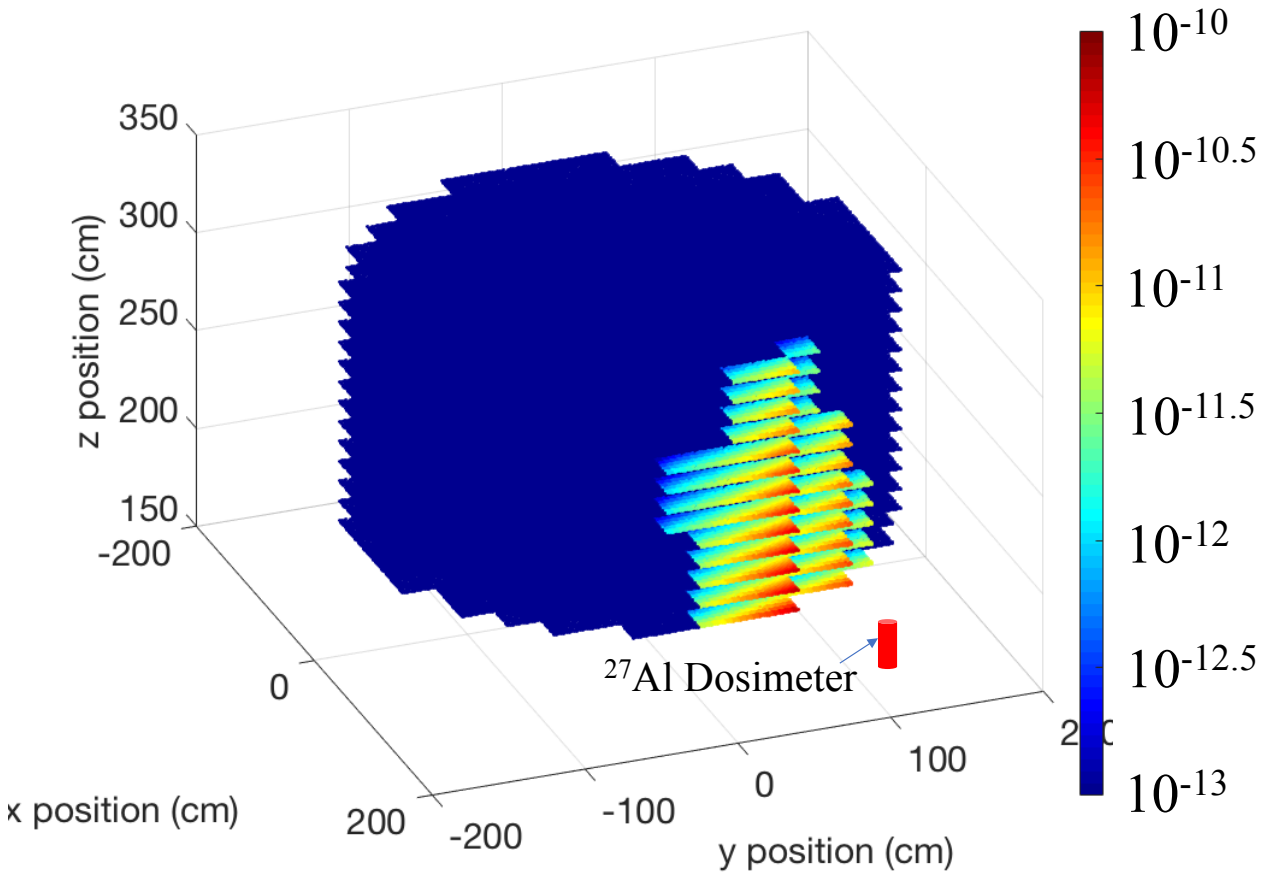

Figure 7.27 3D DRF Coefficients: $^{27}\mathrm{Al}(n,\alpha)$ at 20-degree Axial Mid-plane

the Fig. 7.29.

7.5.4 More 3D DRF Coefficients

In the previous section, we have calculated the DRF coefficients for $^{27}\mathrm{Al}(n,\alpha)$ dosimeter at 20-degree axial mid-plane with fresh fuel composition. We have calculated more DRF coefficients with another two sets of burnup levels: (1) 10500 MWd/MTHM; and (2) 64500 MWd/MTHM for both $^{27}\mathrm{Al}(n,\alpha)$ and $^{115}\mathrm{In}(n,n^{'})$ dosimeters. Note that only few selected fuel assembly locations are calculated due to the limited computation resources.

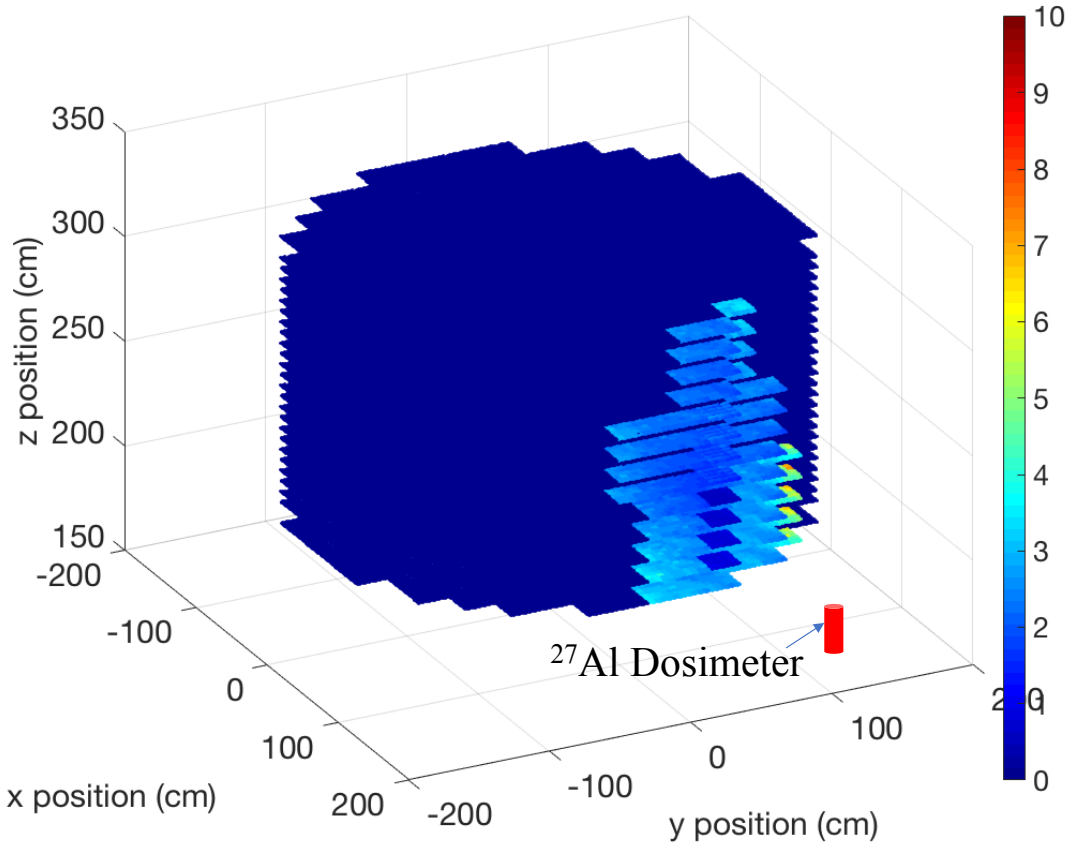

Figure 7.28 3D DRF Coefficients 1σ Statistical Uncertainty in %: $^{27}\mathrm{Al}(n,\alpha)$ at 20-degree Axial Mid-plane

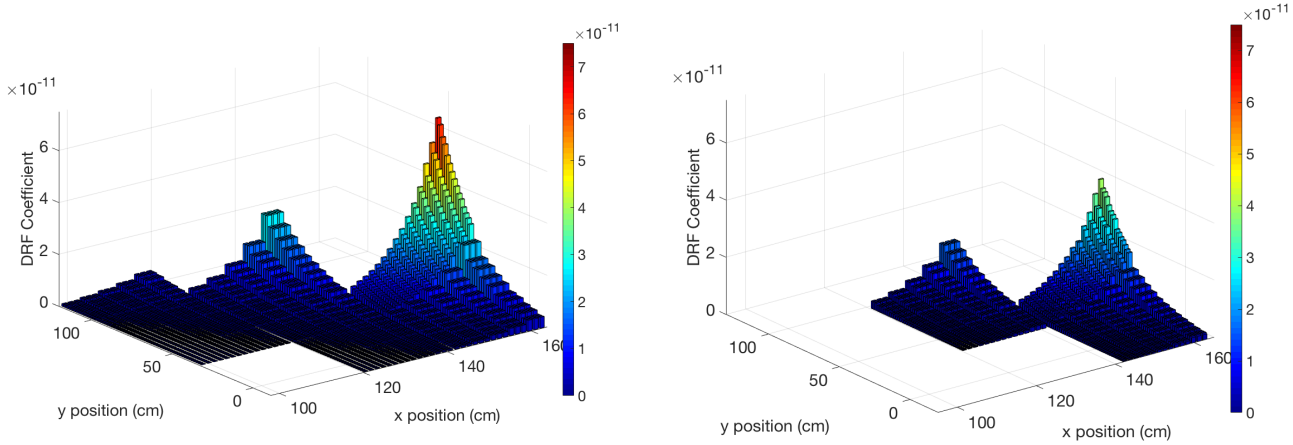

(a) Axial Level 20

(b) Axial Level 25

Figure 7.29 DRF Coefficients: 20-degree Middle Axial Plane $^{27}\mathrm{Al}(n,\alpha)$ Dosimeter (Rotated for 180-degree)

7.6 Neutron Source Calculations Using RAPID

The neutron source calculations are performed using the RAPID code system. Here, one fresh core configuration is used for testing the accuracy of the RAPID calculation result first. After that, two core configuration are used for benchmarking the DRF methodology.

7.6.1 FM Coefficient Calculations

To perform fission source calculations using the RAPID code system, the FM coefficient calculations have to be performed first. Here, 8 sets of coefficients are calculated:

1. 3 wt% initial enrichment - fresh fuel.
2. 4 wt% initial enrichment - fresh fuel and final burnup levels of 1500, 4500, 10500, 19500, 55500, 64500 MWd/MTHM with specific power of 30 MW/MTHM.

The model used for FM coefficient calculation is a radially infinite TMI-1 core lattice with axial length of 360.68 cm and axial vacuum boundary condition on the both sides. The neutron source is placed at axial location of 180.34 cm to 182.88 cm within the fuel pellets. The source location are then shuffling around an octant of fuel assembly. Therefore, there will be 45 coefficient calculated per burnup level. Note that the guide tube and irradiation tube does not have fuel in it, and thus the FM coefficients for such source locations will be filled by zero. The number of particles used are 10^6 for all the cases. Each coefficient requires $\sim$ 20 to 30 minutes using 8 processors to calculate. The total calculation time is $\sim$ 22 hours using 56 processors. An example of the FM coefficient and their corresponding 1σ relative statistical uncertainties are shown in the Figs. 7.30 and 7.30.

From the section 3.2.1, it is known that the FM coefficient control volume for PWR reactors is 3 assembly away. For verification purpose, the FM coefficient calculation here tallied 4 fuel assemblies away from the fuel assembly with neutron source. However, as it is shown in the Figs 7.30 and 7.31, the tally values from 4 fuel assemblies away are all zeros. The FM coefficients already drop 4 order of magnitude from 3 assembly away. Therefore, tallying 3 fuel assembly away is very sufficient.

7.6.2 Uniform Fresh Fuel Composition

First, the calculation result of RAPID should be verified with a standard Monte Carlo calculation. Here, uniform 3 wt% fresh fuel is used for The parameter used for RAPID calculations are:

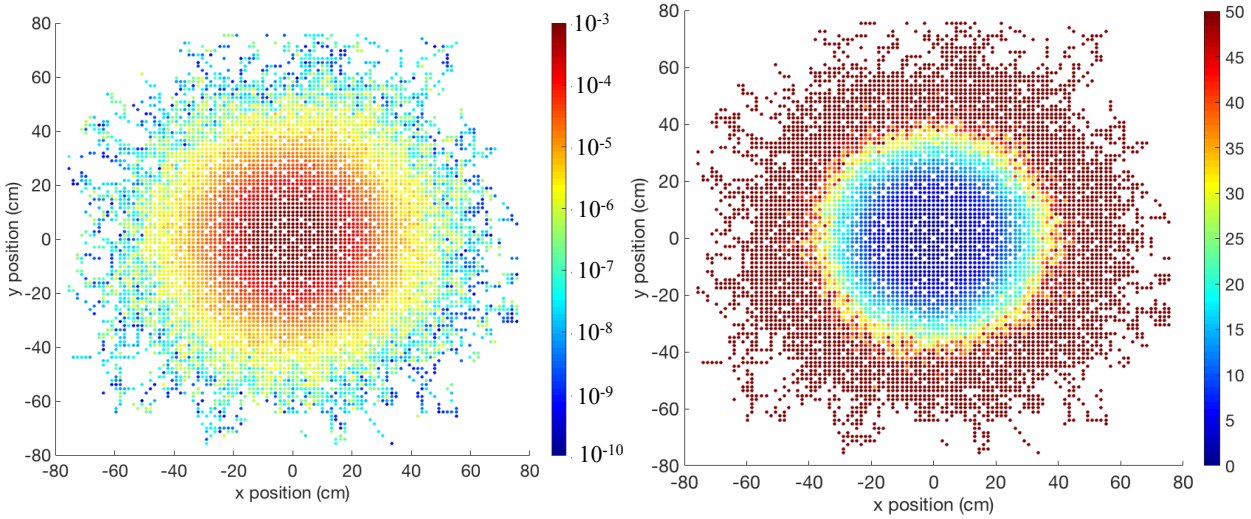

(a) FM Coefficients

(b) 1σ Relative Statistical Uncertainties in %

Figure 7.30 3 wt% Fresh Fuel Axial Level 0 from the Source Axial Location

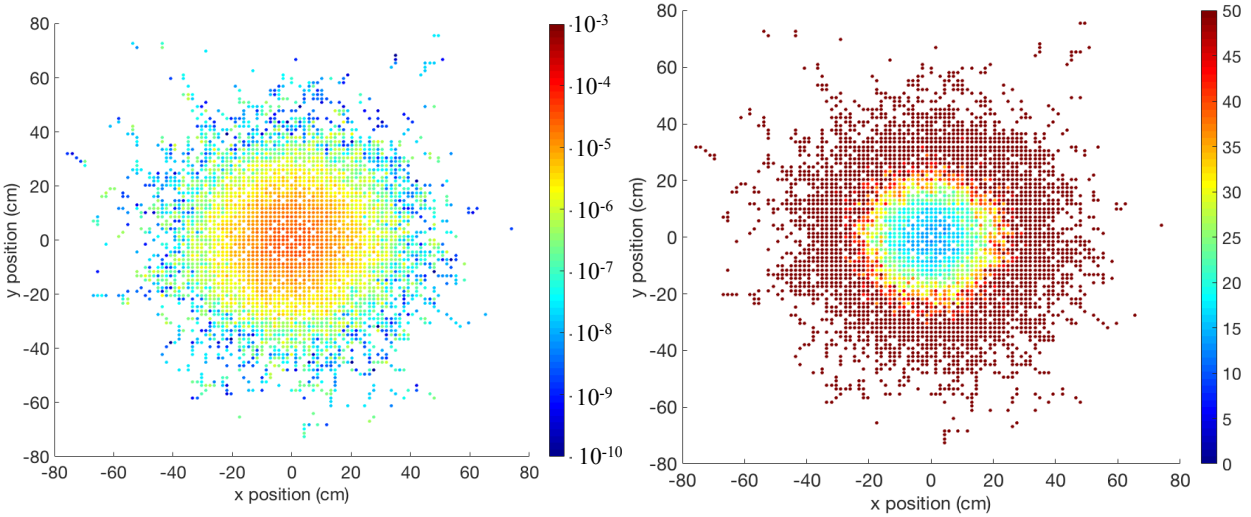

(a) FM Coefficients

(b) 1σ Relative Statistical Uncertainties in %

Figure 7.31 3 wt% Fresh Fuel Axial Level 9 from the Source Axial Location

- Radial single assembly FM coefficient collapsing scheme: 5 5 5 (summation=15, which is number of fuel pellets in x/y direction)
- Axial FM coefficient collapsing factor (NZC): 1 and 2 (two cases performed, total 142 fine axial level)
- fission source convergence tolerance: 10^{-5}
- Eigenvalue convergence tolerance: 10^{-7}
- Number of FM coefficient radial relative assembly: 3
- Number of FM coefficient relative axial level: 29
- No boundary corrections are applied

Here, two axial collapsing factor (NZC) is used for studying the balance between accuracy and calculation time. The calculated eigenvalue and comparisons with the MCNP5 reference calculation.

Table 7.1 Eigenvalue Comparison: 3wt% Fresh Fuel

Code/Approach	k_{eff}	3σ	NZC	Difference in pcm	Processor	Time
RAPID / FM Approach	1.39115	-	2	-79	1	2.63 hours.
RAPID / FM Approach	1.39503	-	1	309	1	36.39 min.
MCNP5 / Eigenvalue MC	1.39194	9	-	Ref.	16	217 min.

Table 7.2 Detailed RAPID Calculation Times (1 Processor)

Item	NZC=2	NZC=1
Input Read in	0.0567 seconds	0.0462seconds
Database Read and Collapse	0.6616 seconds	2.7351 seconds
Database Summary	0.1802 seconds	1.0352 seconds
Interpolating	0.0359 seconds	0.0710 seconds
FM Coefficient Filling	0.2170 seconds	0.4898 seconds
2D Slice Calculation	157.62 seconds	159.78 seconds
FM Coefficient Collapsing	36.78 seconds	75.35 seconds
Full 3D Calculations	2389.57 seconds	9190.01 seconds
Total Time	36.39 minutes	2.63 hours
Number of Iteration	306	318
Eigenvalue (k_{eff})	1.39503	1.39115

Note that no MCNP5 pin-wised fission source is provided here as reference. This is mainly because the difficulty of obtaining pin-wised fission source with acceptable relative statistical

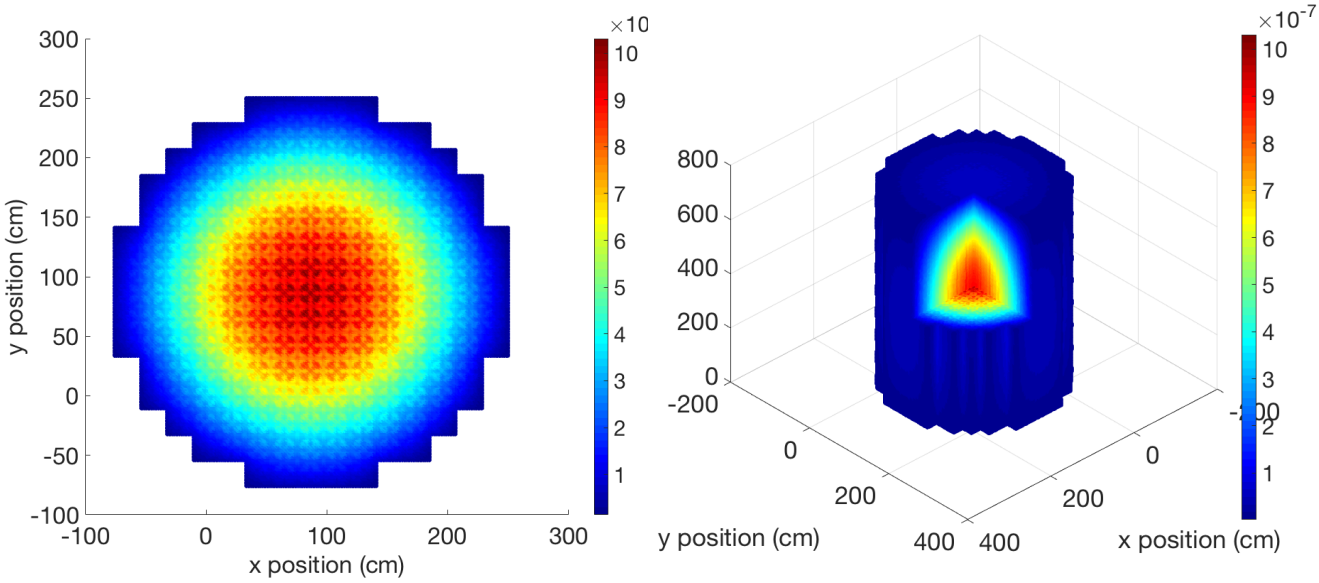

(a) Slice $72^{th}/142^{th}$

(b) 3D Pin-wised Fission Source

Figure 7.32 RAPID Calculated Normalized Pin-wised Fission Source Distribution (NZC=1): 3wt% Fresh Fuel

uncertainty. The results has demonstrated that the calculated eigenvalue is with an excellent agreement with the MCNP5 reference calculation if NZC=1 is selected. The precision of the eigenvalue will reduced by a difference of $\sim$ 300 pcm if NZC=2 is selected. This might be fixable using boundary correction factor. However, the main purpose of this dissertation is the DRF methodology. It is acceptable to use a source distribution with reasonable range of uncertainty since the DRF coefficients are completely separated from the source calculations.

The calculation time for the uniform 3 wt% fresh fuel core is $\sim$ 2.63 hours using 1 processors if NZC=2 while it can be reduced to $\sim$ 30 minutes if NZC=2 is selected.

7.6.3 Core Configuration 1

We have demonstrated that the FM coefficient are appropriately calculated and can be used on fission source calculation efficiently in the previous section. The first core configuration is prepared as shown in the Fig. 7.33 and 7.34. For faster calculation, only the centered 30 axial levels in the full model (142 axial levels) are prepared for the neutron source calculations.

Three types of fuel assemblies with different burnup levels are loaded in the core: (1) Fresh fuel; (2) 10500 MWd/MTHM; and (3) 64500 MWd/MTHM. Note that except the 3 selected axial levels, other 27 axial levels are all filled with 4 wt% fresh fuel assemblies. The RAPID calculated 3D pin-wised fission sources are shown in the Fig. 7.35.

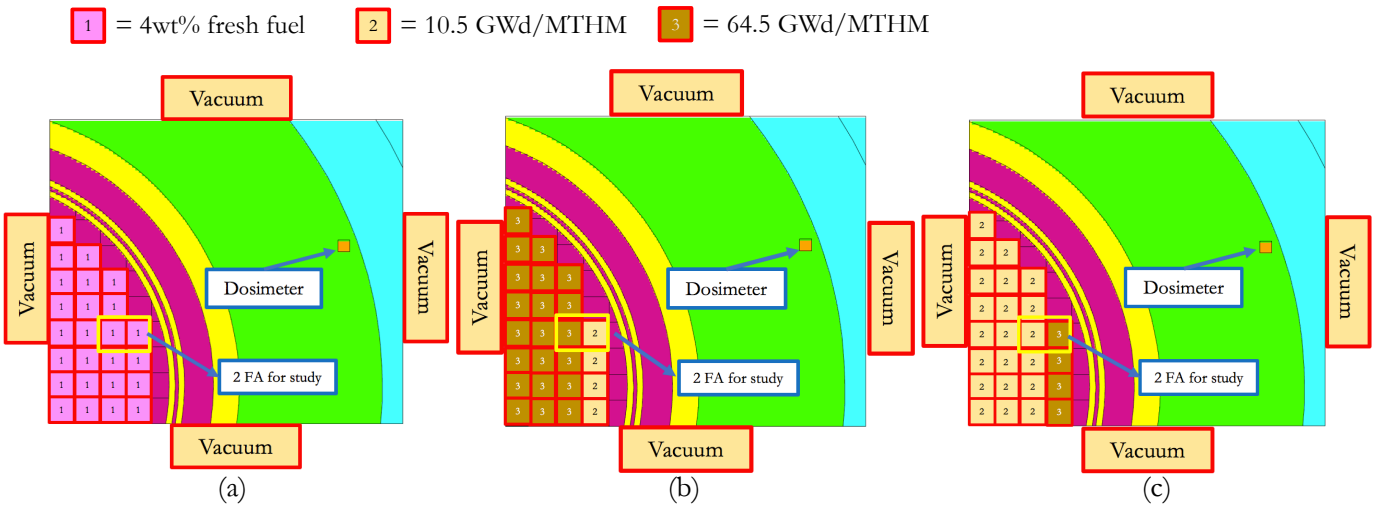

Figure 7.33 Core Configuration 1 - Radial Projection

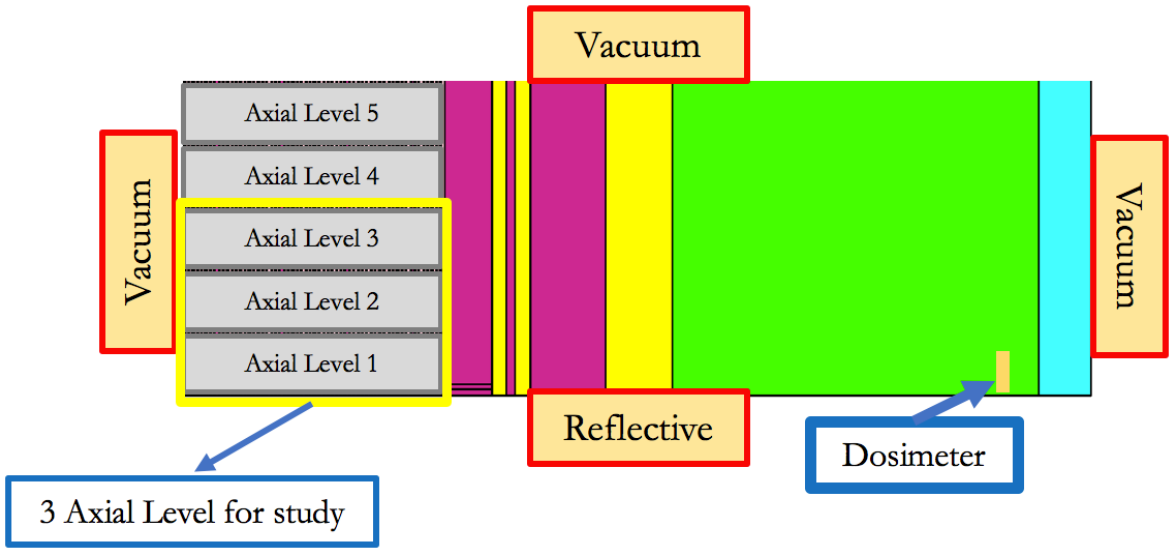

Figure 7.34 Core Configuration 1

The final k_{eff} of the core configuration 1 is 1.30833. Since 2 of the the 3 selected axial levels contain higher burnup, the the mid-axial locations show lower fission sources due to lesser fissile materials. The selected calculation parameters are all the same as section 7.6.2, except total axial level is 30 and NZC=1. The full 3D FM calculation for this configuration requires $\sim$ 16.20 minutes using 1 processor. Fig. 7.36 further shows the detailed pin-wised fission sources for the selected 3 axial level.

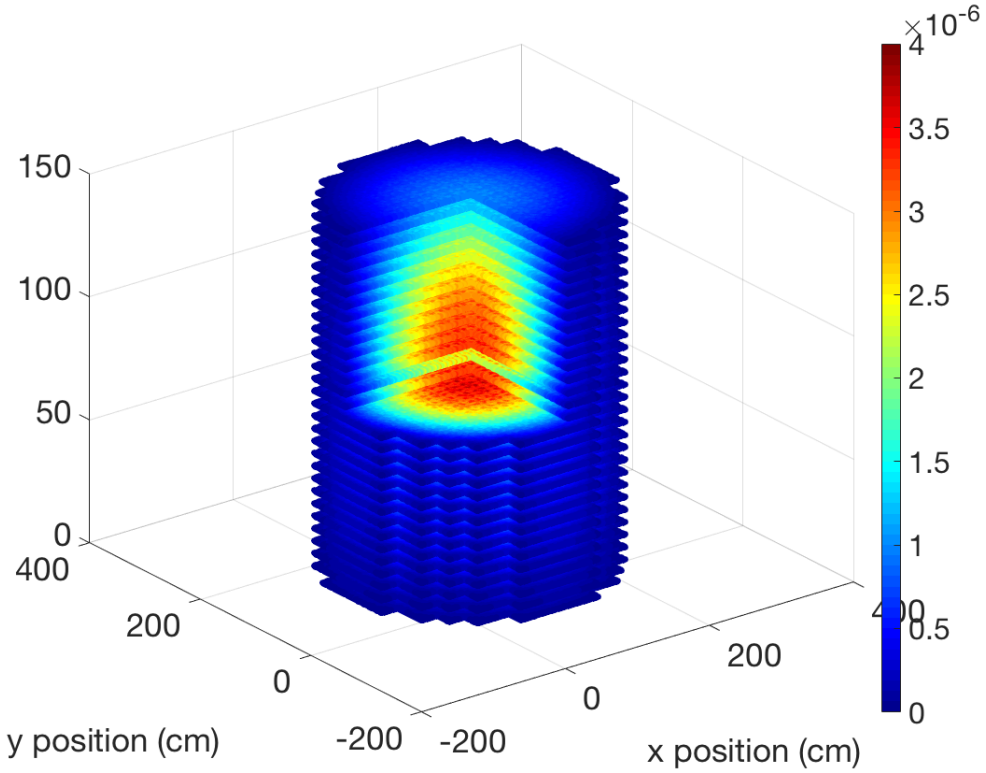

Figure 7.35 3D Pin-wised Normalized Fission Sources: Core Configuration 1

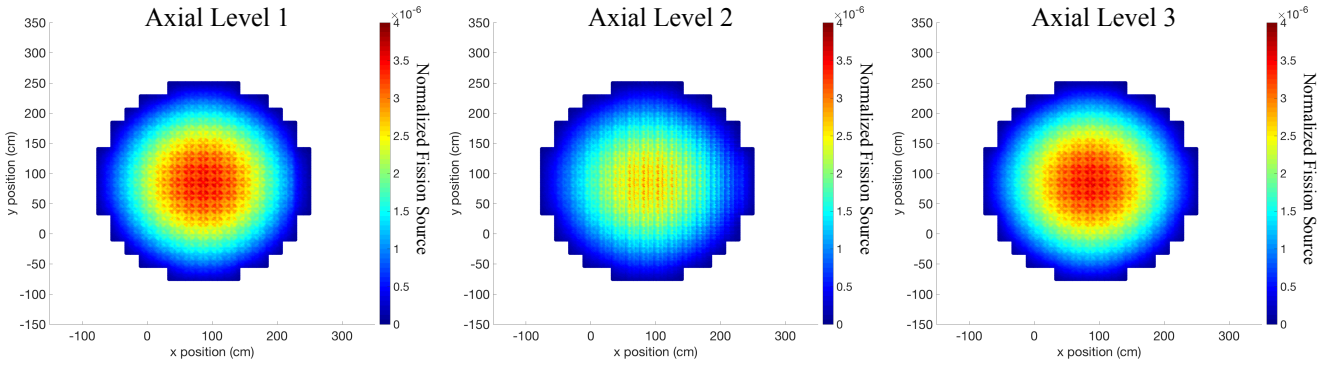

Figure 7.36 Normalized Pin-wised Fission Sources for Selected Axial Levels: Core Configuration 1

7.6.4 Core Configuration 2

The core configuration 2 is shown in the Fig. 7.37 with the same selected axial levels for study shown in the Fig. 7.34.

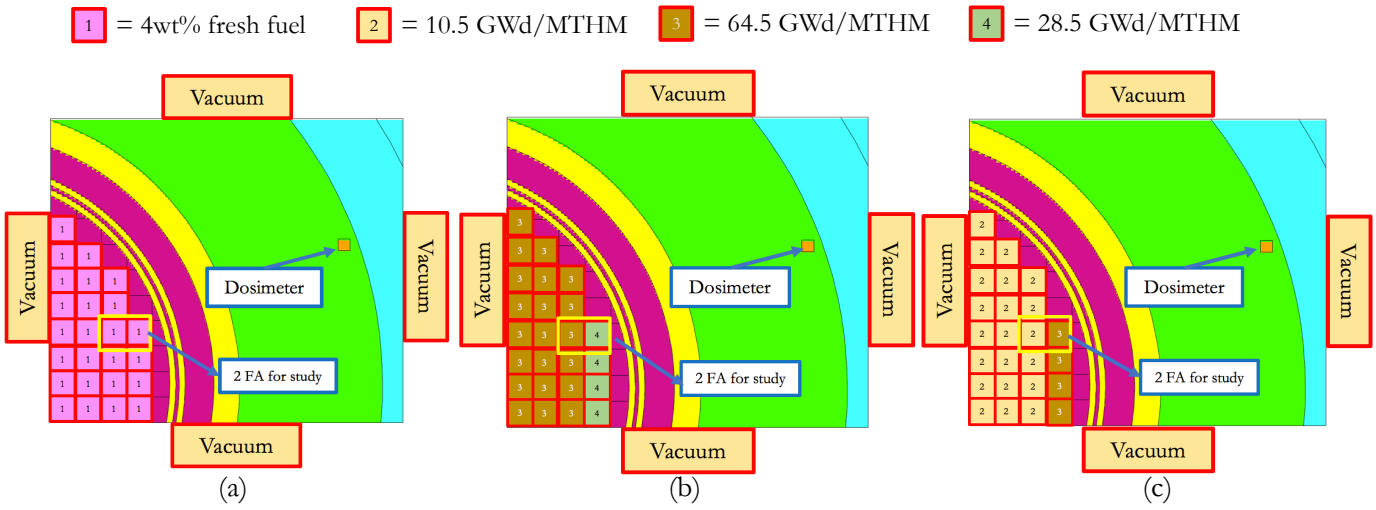

Figure 7.37 Core Configuration 2 - Radial Projection

In this configuration, we have one more fuel assembly burnup with 28500 MWd/MTHM. The FM coefficient of this burnup is linearly interpolated using the existing database from section 7.6.1. Fig. 7.38 and 7.39 show the RAPID calculated 3D pin-wised and the selected 3 assemblies' fission source distribution, respectively.

The final calculated system eigenvalue is 1.30742. The eigenvalue is lower than the configuration 1 mainly because more higher burnup fuel assemblies. Similar to the core configuration 1, the mid-axial levels show a lower fission source strength due to higher burnup levels. The RAPID parameter is same as core configuration 1. The full 3D FM calculation for this case is $\sim$ 18.69 minutes using 1 processor. Note that these neutron source distribution with mixing fuel assemblies might have bias. This is mainly because the fission source at assembly edges may be affected by the assumption made from section 3.2.4. He and Walters [87] has proposed a solution for this. However, this approach is not applied here.

Again, it is acceptable to use a fission source distribution with reasonable bias here since the main subject of this dissertation is the DRF methodology.

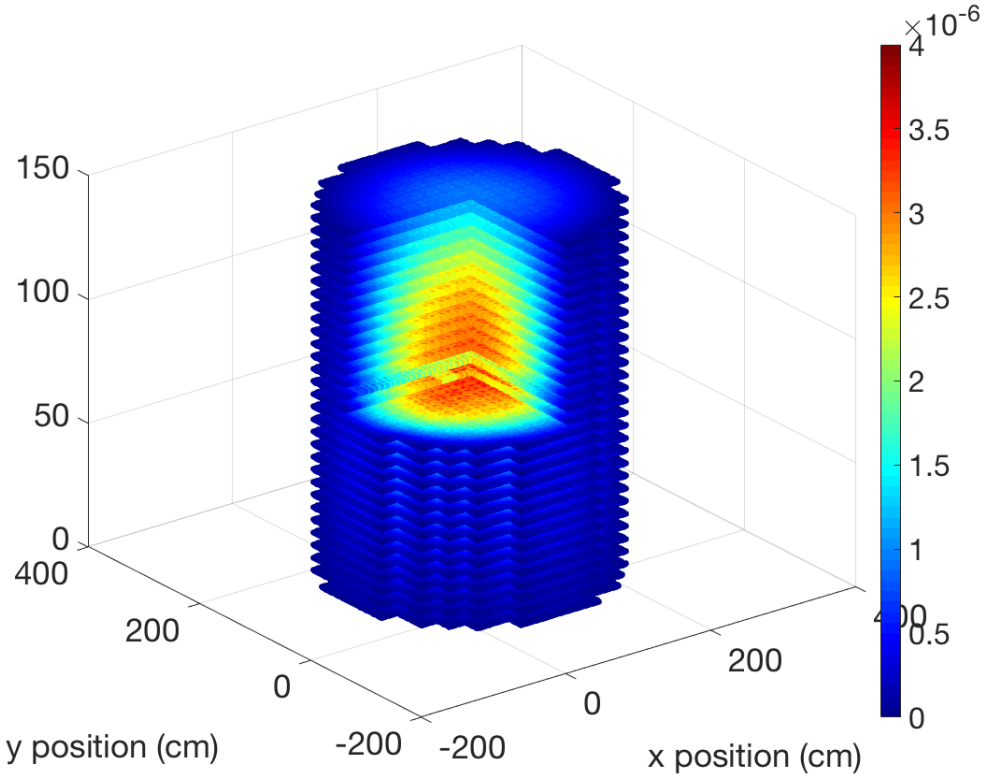

Figure 7.38 3D Pin-wised fission sources: Core Configuration 2

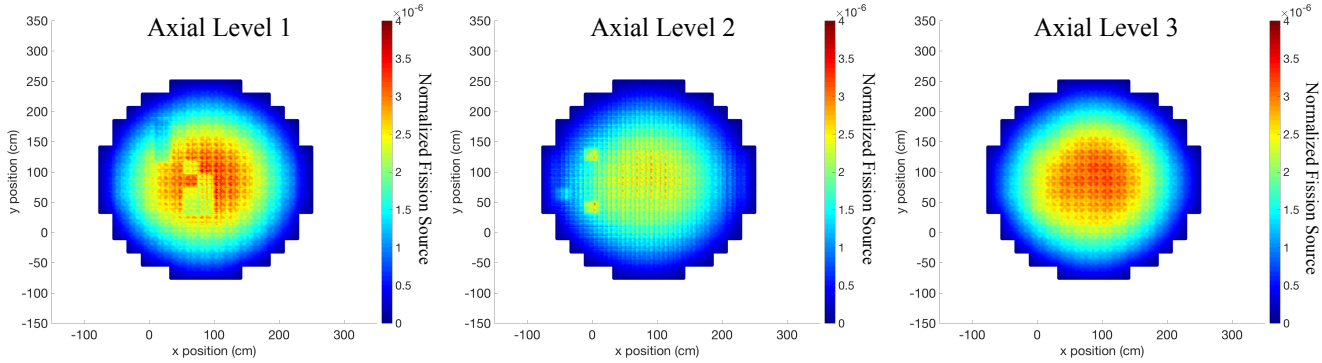

Figure 7.39 Pin-wised fission sources for Selected Axial Levels: Core Configuration 2

7.7 Dosimeter Response Calculations

In this section, the dosimeter response calculation will be presented. The FOV and part of the sensitivity study will be verified by the dosimeter response calculation using the 3D full model.

7.7.1 Verification of the FOV

The corresponding source distribution that within the FOV of the 20-degree axial mid-plane $^{27}\mathrm{Al}(n,\alpha)$ is shown in the Fig. 7.40. Note that the fission source shown here is recalculated using 144 axial level with NZC=4. The final eigenvalue is 1.39057, which requires $\sim$ 10 minutes to calculate using 1 processor. Other RAPID calculation parameters are same as section 7.6.2. The main reason of re-calculation of neutron source is for the 4 fuel pellet axial lumping scheme.

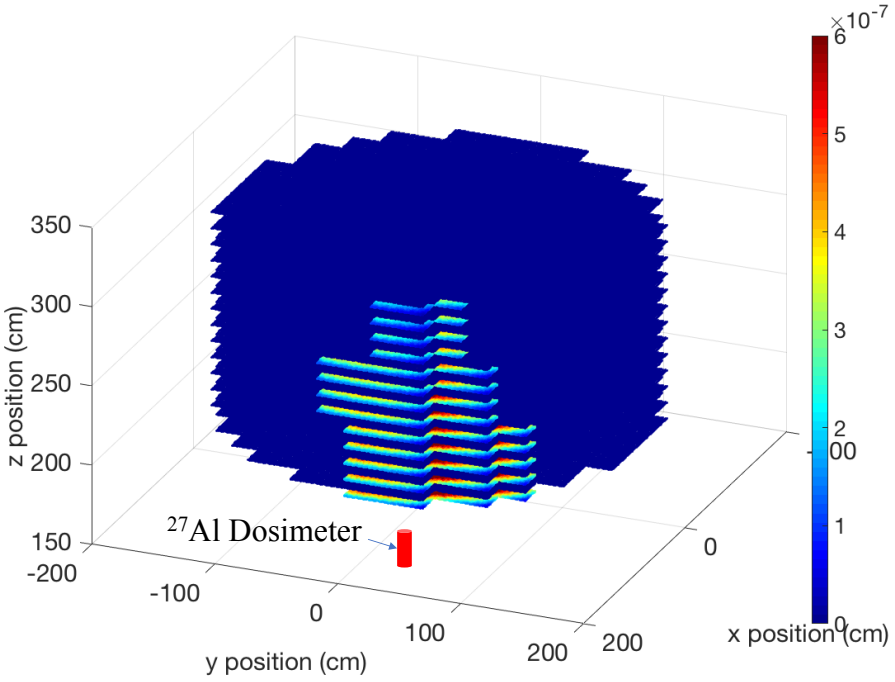

Figure 7.40 Normalized Neutron Source within the FOV: 20-degree Axial Mid-plane $^{27}\mathrm{Al}(n,\alpha)$ Dosimeter

By coupling the neutron sources with the DRF coefficients as shown in the Fig. 7.5.3, we can obtain the real FOV for the 20-degree axial mid-plane $^{27}\mathrm{Al}(n,\alpha)$ dosimeter shown in the Fig. 7.41.

The FOV values are scaled to maximum 1. The fuel assemblies contributing more than 0.6 are mostly at those close to the dosimeter with the first 5 axial levels. Again, the axial levels shown here are from 19 to 36. Detailed real FOV distribution for axial level 20 and 25 are further shown in the Fig. 7.42.

To further quantify the sufficiency of the selected FOV for the dosimeter response calculations, two reference MCNP5 calculations are prepared for comparison: (1) Including the assemblies in the FOV shown in Fig. 7.41; and (2) Including all the fuel assemblies in the model. The number of particles for the MCNP5 reference calculations are all 2×10^{10}.

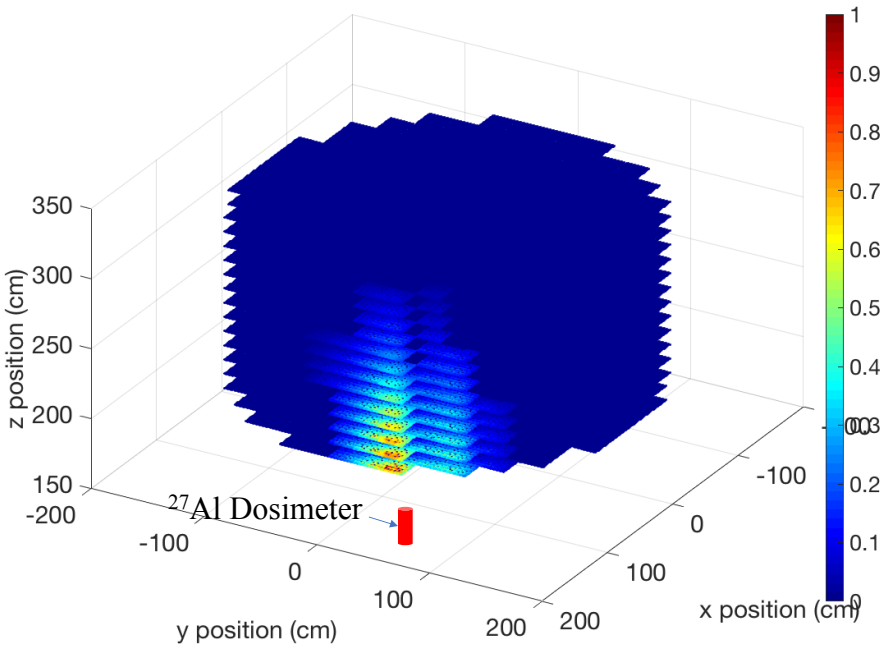

Figure 7.41 Real FOV (Scaled to Maximum 1): 20-degree Axial Mid-plane $^{27}\mathrm{Al}(n,\alpha)$ Dosimeter

Fig. 7.43 shows the neutron source for all the assemblies within the model for the MCNP5 reference calculation. Table 7.3 shows the comparisons of the calculated dosimeter responses.

Table 7.3 Dosimeter Response Comparison: 20-degree Middle Axial Plane $^{27}\mathrm{Al}(n,\alpha)$ Dosimeter

Code and Approach	Source Included	Dosimeter Response (n/sec)	1σ in %	Diff. in %
RAPID/DRF Method.	Within FOV	1.98×10^{-14}	-	-18.70%
MCNP5/Fixed-Src MC	Within FOV	1.98×10^{-14}	2.00%	-18.54%
MCNP5/Fixed-Src MC	All	2.43×10^{-14}	2.01%	Ref.

Here, we have verified two things:

1. The selected fuel pellet lumping scheme (mesh) is very appropriate. Only 0.17% of difference is observed between the RAPID and MCNP5+CADIS dosimeter response calculations.

2. The FOV estimation from the section 7.2.5.1 is underestimated by $\sim$ 10%, but still considered acceptable. The predicted FOV contains $\sim$ 91% of dosimeter response while $\sim$ 82% of dosimeter response is obtained here. This is mainly because the assumption of flat source distribution. Note that axial levels 32 to 36 are not calculated mainly

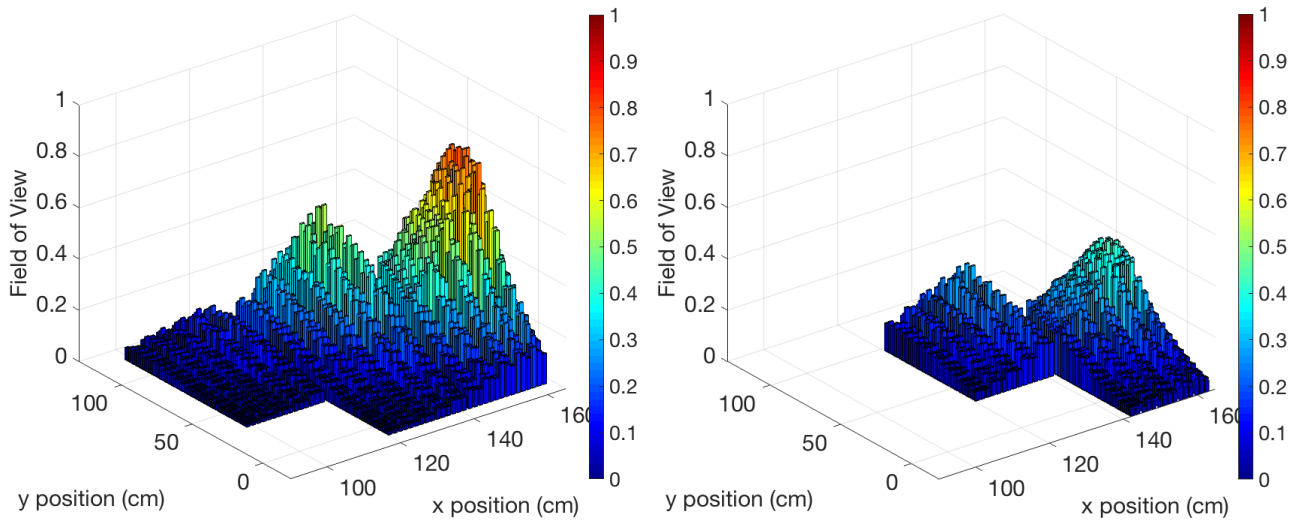

(a) Axial Level 20 **(b)** Axial Level 25

Figure 7.42 Real FOV (Scaled to Maximum 1): 20-degree Middle Axial Plane $^{27}\mathrm{Al}(n,\alpha)$ Dosimeter (Rotated for 180-degree)

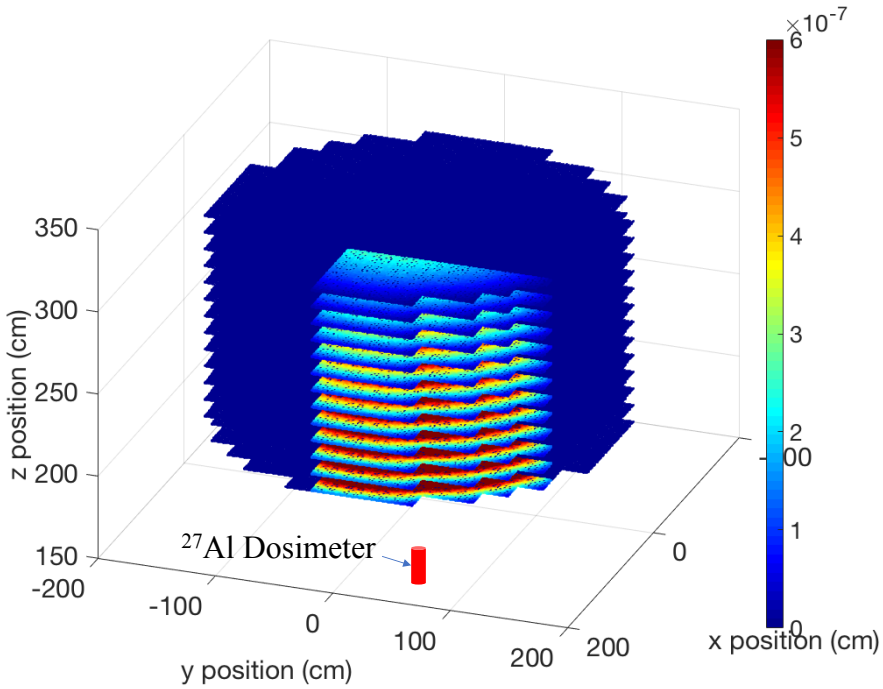

Figure 7.43 Normalized Neutron Source for All Assemblies: 20-degree Axial Mid-plane $^{27}\mathrm{Al}(n,\alpha)$ Dosimeter

because one order of magnitude drop on the DRF coefficient is already observed for axial level 31. This might be another reason for the observation of lower dosimeter response contribution.

The comparisons of wall-clock time for the calculations are shown in the Table 7.4.

Table 7.4 Wall-clock Time Comparison: 20-degree Middle Axial Plane $^{27}\mathrm{Al}(n,\alpha)$ Dosimeter

Code and Approach	Source Included	Wall-clock Time	Number of Processors	Speedup
RAPID/DRF Method.	Within FOV	1 second	1	17100
MCNP5/Fixed-Src MC	Within FOV	11.34 hours	4	-
MCNP5/Fixed-Src MC	All	4.75 hours	8	Ref.

The MCNP5 calculations require few hours using 8 processors while the RAPID calculation requires only a second. Significant speedup using the DRF methodology for dosimeter response calculation is observed.

7.7.2 Verification of the Sensitivity to Borated Primary Coolant

Here, the neutron source is assumed remaining unchanged with presence of boron. A few more cases with boron concentration from 500 to 5000 ppm are calculated using MCNP5+CADIS. Table 7.5 shows the comparison of the results. Note that the fuel assemblies included for dosimeter response calculations are those within the FOV.

Table 7.5 Dosimeter Response Comparison for Borated Primary Coolant Case: 20-degree Middle Axial Plane $^{27}\mathrm{Al}(n,\alpha)$ Dosimeter

Code and Approach	Boron Concentration	Dosimeter Response (n/sec)	1σ in %	Diff. in %
RAPID/DRF Method.	0 ppm	1.98×10^{-14}	-	0.19%
MCNP5/Fixed-Src MC	500 ppm	1.99×10^{-14}	2.00%	0.37%
MCNP5/Fixed-Src MC	1000 ppm	2.00×10^{-14}	2.00%	0.71%
MCNP5/Fixed-Src MC	1500 ppm	2.01×10^{-14}	1.99%	1.21%
MCNP5/Fixed-Src MC	2500 ppm	2.03×10^{-14}	1.96%	2.49%
MCNP5/Fixed-Src MC	5000 ppm	2.10×10^{-14}	1.92%	5.82%
MCNP5/Fixed-Src MC	0 ppm	1.98×10^{-14}	2.00%	Ref.

The results show that $\sim 1.21\%$, $\sim 2.49\%$, and $\sim 5.82\%$ of difference is introduced by 1500 ppm, 2500 ppm, and 5000 ppm of boron concentration in the primary coolant, respectively. Other concentrations shown in the table has very small effect. Therefore, it can be concluded

that boron concentration dependent DRF coefficient is not necessary if 1% of dosimeter response change is selected for tolerance with concentration lower than 1000 ppm. This can be flexible to the user defined tolerance level.

7.7.3 Verification of the Sensitivity to Temperature Profile

Table 7.6 shows the dosimeter response comparison by varying the fuel/primary coolant temperature.

Table 7.6 Dosimeter Response Comparison for Temperature Profile: 20-degree Middle Axial Plane $^{27}\mathrm{Al}(n,\alpha)$ Dosimeter

Code and Approach	Temperature (Kelvin)	Dosimeter Response (n/sec)	1σ in %	Diff. in %
RAPID/DRF Method.	All 300	1.98×10^{-14}	-	0.19%
MCNP5/Fixed-Src MC	Fuel 900 Water 600	1.98×10^{-14}	2.00%	0.19%
MCNP5/Fixed-Src MC	Fuel 1200 Water 900	1.98×10^{-14}	2.00%	0.19%
MCNP5/Fixed-Src MC	All 300	1.98×10^{-14}	2.00%	Ref.

The results show that almost no effect is observed on dosimeter response by temperature profile. This has verified the sensitivity study performed by the 1D model previously.

7.7.4 Verification of the Sensitivity to Primary Coolant Density

Table 7.7 shows the dosimeter response calculation by varying the primary coolant density.

Table 7.7 Dosimeter Response Comparison for Change on Primary Coolant Density: 20-degree Middle Axial Plane $^{27}\mathrm{Al}(n,\alpha)$ Dosimeter

Code and Approach	Primary Coolant Density (g/cm^3)	Dosimeter Response (n/sec)	1σ in %	Diff. in %
RAPID/DRF Method.	0.99	1.98×10^{-14}	-	0.19%
MCNP5/Fixed-Src MC	0.70	4.04×10^{-14}	1.47%	103.86%
MCNP5/Fixed-Src MC	0.99	1.98×10^{-14}	2.00%	Ref.

The results show that $\sim$ 2 times of dosimeter response is observed when decreasing the primary coolant density from 0.99 g/cm^3 to 0.70 g/cm^3. This is mainly because the neutron will be more likely to travel from fuel pellets to the dosimeter if density of primary coolant density is lower. Therefore, another sets of DRF coefficient has to be calculated by using different primary coolant density. Simply using the results from Fig. 7.18 to perform DRF

coefficient fix-up is not an appropriate approach due to ~ 4 times of change on DRF coefficient by decreasing the primary coolant density from 0.99 g/cm^3 to 0.70 g/cm^3 while only ~ 2 times of dosimeter response change is observed here.

7.7.5 Verification of the Sensitivity to Burnup Level (^{239}Pu to ^{238}U Ratio)

In this section, the sensitivity of the dosimeter response by fuel ^{239}Pu to ^{238}U ratio will be verified by the two core configuration introduced in the sections 7.6.3 and 7.6.4.

7.7.5.1 Core Configuration 1

The selected two assemblies shown in the Fig. 7.33 will be used for dosimeter response calculations. Table 7.8 shows the comparison of the calculated dosimeter response. The number of particles used for reference MCNP5 calculations are 10^9 with use of CADIS methodology.

Table 7.8 Dosimeter Response Comparison for Core Configuration 1

Dosimeter Type	MCNP5 Ref. (neutrons/sec)	MCNP 1σ (%)	DRF Method. (neutrons/sec)	DRF Coeff. Used	Difference (%)
$^{27}\mathrm{Al}(n,\alpha)$	2.45×10^{-15}	1.46	2.34×10^{-15}	Fresh Fuel	-4.36
$^{27}\mathrm{Al}(n,\alpha)$	2.45×10^{-15}	1.46	2.44×10^{-15}	Burnup Dependent	0.79
$^{115}\mathrm{ln}(n,n')$	6.17×10^{-14}	1.09	5.91×10^{-14}	Fresh Fuel	-4.26
$^{115}\mathrm{ln}(n,n')$	6.17×10^{-14}	1.09	6.08×10^{-14}	Burnup Dependent	-1.38

The results show that dosimeter response calculated using burnup dependent DRF coefficients is more accurate than directly using the fresh fuel DRF coefficients. Difference of $\sim 4\%$ is observed if using fresh fuel DRF coefficient to calculate the dosimeter responses. Since the burnup dependent DRF coefficients are calculated assuming uniform burned fuel composition, isotopic can yield bias as well. It is observed that $\sim 1\%$ of difference can be introduced by the uniform burned fuel composition assumption from DRF coefficient calculations. However, the bias from the uniform burned fuel composition assumption is very small. It can even be hidden from the statistical noise. The results show that the dosimeter responses calculated using burnup dependent DRF coefficients are all within 2σ relative statistical uncertainties of the MCNP5 reference calculations. The wall-clock time for all the calculations are shown in the Table 7.9.

Significant speedup is observed using the DRF methodology for the dosimeter response calculations.

Table 7.9 Wall-clock Time Comparison for Core Configuration 1

Dosimeter Type	MCNP5 Ref.	Number of Processors	DRF Method.	Number of Processor	Speedup
$^{27}\mathrm{Al}(n,\alpha)$	342 minutes	8	1 second	1	20520
$^{115}\mathrm{ln}(n,n^{'})$	223 minutes	8	1 second	1	13380

7.7.5.2 Core Configuration 2

For the core configuration 2, there is one more fuel burnup level - 28500 MWd/MTHM. Instead of creating one more DRF coefficient database, linear interpolation scheme is applied between 10500 MWd/MTHM and 64500 MWd/MTHM. The calculated dosimeter responses are shown in the Table 7.10.

Table 7.10 Dosimeter Response Comparison for Core Configuration 2

Dosimeter Type	MCNP5 Ref. (neutrons/sec)	MCNP 1σ (%)	DRF Method. (neutrons/sec)	DRF Coeff. Used	Difference (%)
$^{27}\mathrm{Al}(n,\alpha)$	2.96×10^{-15}	3.24	2.83×10^{-15}	Fresh Fuel	-4.25
$^{27}\mathrm{Al}(n,\alpha)$	2.96×10^{-15}	3.25	2.90×10^{-15}	Burnup Dependent	-1.78
$^{115}\mathrm{ln}(n,n^{'})$	6.46×10^{-14}	1.40	6.28×10^{-14}	Fresh Fuel	-2.78
$^{115}\mathrm{ln}(n,n^{'})$	6.46×10^{-14}	1.40	6.42×10^{-14}	Burnup Dependent	-0.58

Similarly, very good agreements are observed using burnuped dependent DRF coefficients. The differences of dosimeter responses using burnup dependent DRF coefficients are all within 1σ relative statistical uncertainties of the MCNP5 reference calculations.

Table 7.11 Wall-clock Time Comparison for Core Configuration 2

Dosimeter Type	MCNP5 Ref.	Number of Processors	DRF Method.	Number of Processor	Speedup
$^{27}\mathrm{Al}(n,\alpha)$	509 minutes	8	1 second	1	30540
$^{115}\mathrm{ln}(n,n^{'})$	335 minutes	8	1 second	1	20129

7.8 Summary of the Chapter

In this chapter, we have successively demonstrated the robustness of the DRF methodology on commercial PWR RPV dosimetry applications. Here, we can conclude that the DRF coefficient could have dependency on:

1. Dosimeter Type - This parameter will be necessary.

2. Neutron Source (Fuel Pellet) Location - This parameter will be necessary.
3. ^{235}U to ^{239}Pu ratio - This parameter will be necessary.
4. Primary Coolant Density - This parameter will be necessary.
5. Void Fraction - Mainly for transient scenario, not necessary for steady state operation.
6. Boron concentration - It may not be needed for boron concentration lower than $\sim$ 3000 ppm. However, commercial power reactor's boron concentration can be up to 8000 ppm. Under such condition, boron concentration dependency may be needed for dosimeter with higher energy threshold.

The axial boundary structure will potentially affect the dosimeter response calculation by 5% to 8% depending on the dosimeter type if direct DRF coefficient translation is used. However, this error tolerance can be user specified. If 5% to 8% of difference is not tolerable, different sets of DRF coefficient for axial boundaries will be necessary.

The uncertainties will be mainly from the RPV thickness and iron cross-section. Potentially, the RPV uncertainty can be determined by comparing calculation and experiment. For the iron cross-section uncertainty, more detailed and comprehensive uncertainty analysis can be performed using the nuclear covariance data. This can be a potential future work.

Chapter 8

Benchmark of the DRF Methodology: Dry Storage Cask External Dosimetry

In this chapter, the same GBC-32 cask from the chapter 5 will be used for benchmark again. However, we will replace the water with air to simulate the dry storage cask. For a dry storage cask, there are three main radiation sources: (1) Photon source; (2) Independent neutron source; and (3) Induced fission neutron source. Since we have the benchmark study from chapter 5 as *a priori*, it is reasonable to utilize some of the information, i.e. FOV and GC study, for this benchmark problem. This will be discussed with details in the following sections.

Note that only the neutron sources will be studied in this chapter. The photon transport is more complicated than the neutron transport, and therefore requires more effort. Some preliminary implementation of the DRF methodology to photon source external dosimetry for the same problem can be found in the Appendix G.

8.1 UNF-ST&DARD Code System

To analyze a dry storage SNF cask external dosimetry problem, the first task is obtaining the source spectrum and material composition of fuel assemblies. In this chapter, the UNF-ST&DARD Code System [7] is used. The UNF-ST&DARD (UNF-Storage, Transportation & Disposal Analysis Resource and Data System) Code System is developed by the Used Fuel System Group at Oak Ridge National Laboratory (ORNL). The purpose of the development on the code system was integration of database for SNF analysis. The SNF need to be analyzed at different storage, transportation, and disposal systems at various stages. Such analysis can be tedious, error-prone, and time consuming if no automative integrated database is available.

The UNF-ST&DARD code system provides the isotopic and multi-group neutron/photon spectrum and strength by commercial power reactor history in the U.S., potential extension to the country out of the U.S. is currently underway. It utilizes the ORIGAMI code system [116] to pre-calculate axial dependent fuel assembly burnup level by different combination of parameters. The parameters included are:

1. Initial enrichment of fuel assembly
2. Initial heavy metal weight
3. Specific power
4. Burnup level with interval of 3000 MWd/MTHM
5. Cooling time of the assembly with continuous interval
6. Axial Node for capturing axial burnup profile.

The isotopic for burnup level between data points can be interpolated by interpolating cross-section from the ORIGAMI data library. Since decay calculations are relatively fast, the cooling time dependent isotopic is calculated on the fly.

8.1.1 Current Status of the High Level Nuclear Waste in the U.S.

Fig. 8.1 shows the statistics of recent U.S. commercial discharged nuclear fuel assemblies. The figure is extracted from one of the reference article [7].

From the data sheet, it is shown that most of the US discharged fuel assemblies are with averaged burnup range from 30 to 50 MWd/MTHM and cooling time of 5 to 40 years.

In this study, burnup range from 4 wt% initial enrichment fresh fuel to 64500 MWd/MTHM with 0 to 20 years cooling time are selected for study. The selected specific power and initial heavy metal weight are 30 MW/MTHM and 459.9 kg.

8.1.2 Analysis of the Source Spectrum and Strength from the UNF-ST&DARD Code System

It is always important to study the variation of radiation source spectrum first, as we know that the radiation source spectrum is one of the most important variable in SNF system analysis. In the chapter 5, only the sensitivity of the ^{3}He detector DRF coefficients to the burnup level of induced fission neutron spectrum is performed. The problem was not a real problem, but just a demonstration of the approach. In this section, a comprehensive analysis on the source spectrum from the UNF-ST&DARD code system will be performed. Note that

Figure 8.1 Inventory of SNF discharged from U.S. commercial reactors through June 2013, from UDB (Unified Database), binned by burnup and cooling time. Cooling time was calculated on July 1, 2016 [7]

only neutron source will be analyzed here. The photon source analysis can be found in the Appendix G.

8.1.2.1 Independent Neutron Source

There are mainly three parts for the independent neutron source: (1) Spontaneous fission; (2) (α,n) reaction; and (3) delayed neutron. The contribution of the delayed neutron will reduced to almost zero within a very short time, i.e. less than few days. For the fuel assembly in the dry storage cask, typically they will be cooled and sitting in the SNF pool for $\sim$ 5 years. Therefore, the delayed neutron will not be discussed here.

To begin with, let's see what is the difference between spontaneous fission and (α,n) neutron spectrum. The two spectrum are calculated using the SORCE-4C code [103]. Figs. 8.2 and 8.3 show the comparison of the neutron spectrum from different neutron sources for UO_2 and $^{238}PuO_2$. Note that thermal neutron induced fission spectrum is also provided here for

comparison. the group structure selected here is the 238 group from the SCALE manual [117].

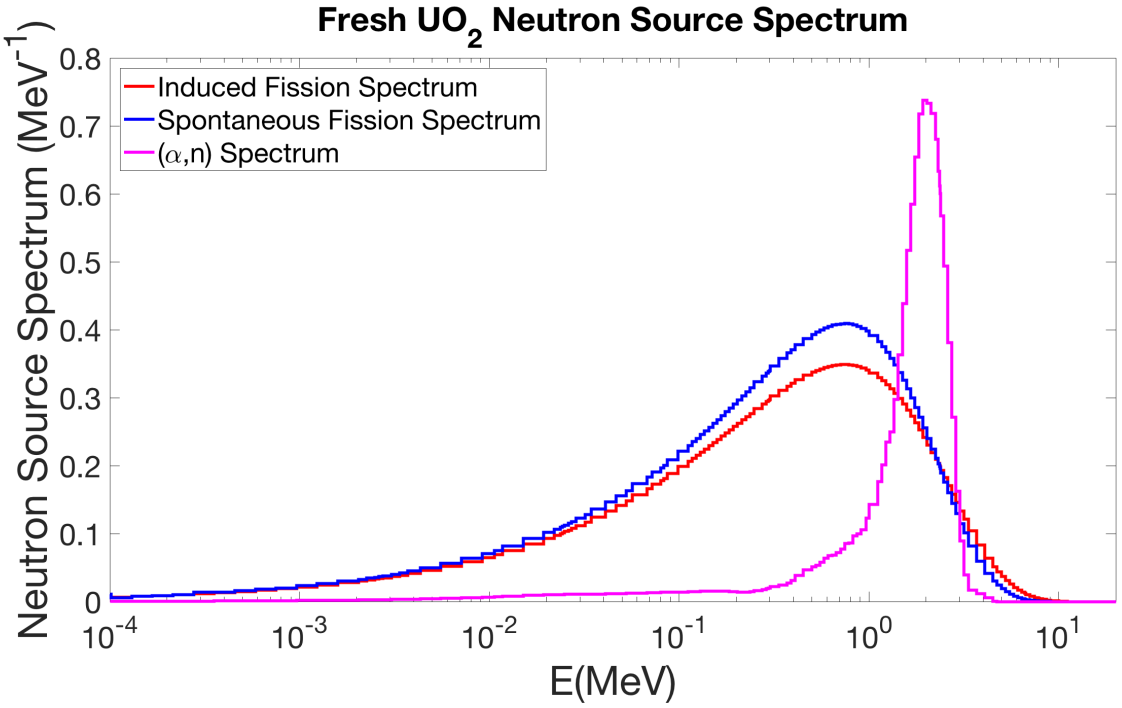

Figure 8.2 Independent Neutron Source Spectrum: UO_2

The results show that neutron spectrum of (α,n) reaction is significantly harder than the other two. This is mainly because the interaction probability of an α particle is typically more than 5 MeV for minimum [118]. With such high energy of α particle bombardment, relative higher energy neutron will emit out of the target nuclide. The strength of important nuclide for independent neutron source with their corresponding strength is also shown in the Fig. 8.4. In the calculation, the number of atoms for both transuranium nuclide and oxegen are always constant for all of the nuclide.

All these transuranium nuclides, except ^{241}Pu, are α emitters. In principle, the (α,n) neutron source should be order of magnitude larger than the spontaneous fission neutron source if there is enough target nuclide. However, the main neutron emitters from the (α,n) reaction are ^{17}O and ^{18}O. The abundances of ^{17}O and ^{18}O in natural oxygen are only 0.038% and 0.200%. Therefore, the α particle emitted from the transuranium nuclides does not have enough target to bombard and produce neutrons from the (α,n) reaction. Therefore, spontaneous fission neutron strength can be larger than the (α,n) neutron source under some circumstances.

The $^{252}CfO_2$ has extremely large spontaneous fission neutron source strength with fair amount of (α,n) neutron source with ~ 6 order of magnitude difference. However, the concentration of ^{252}Cf in SNF assemblies are considered extremely small, i.e. $\sim 10^9$ atoms/cm^3

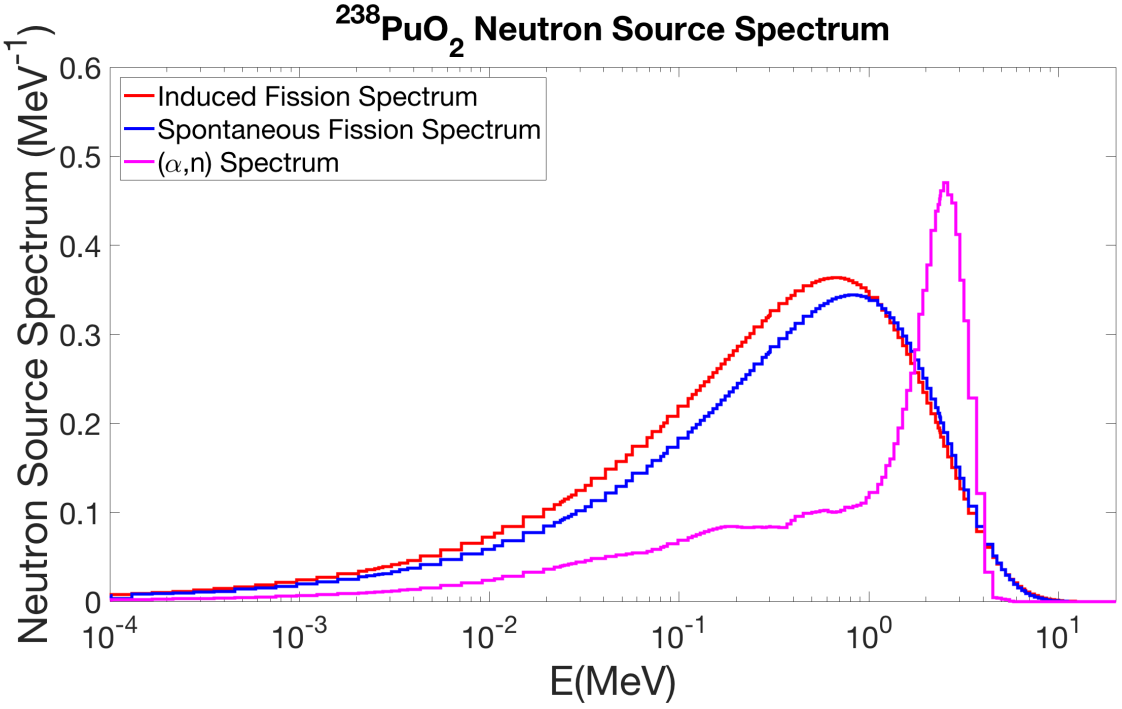

Figure 8.3 Independent Neutron Source Spectrum: $^{238}PuO_2$

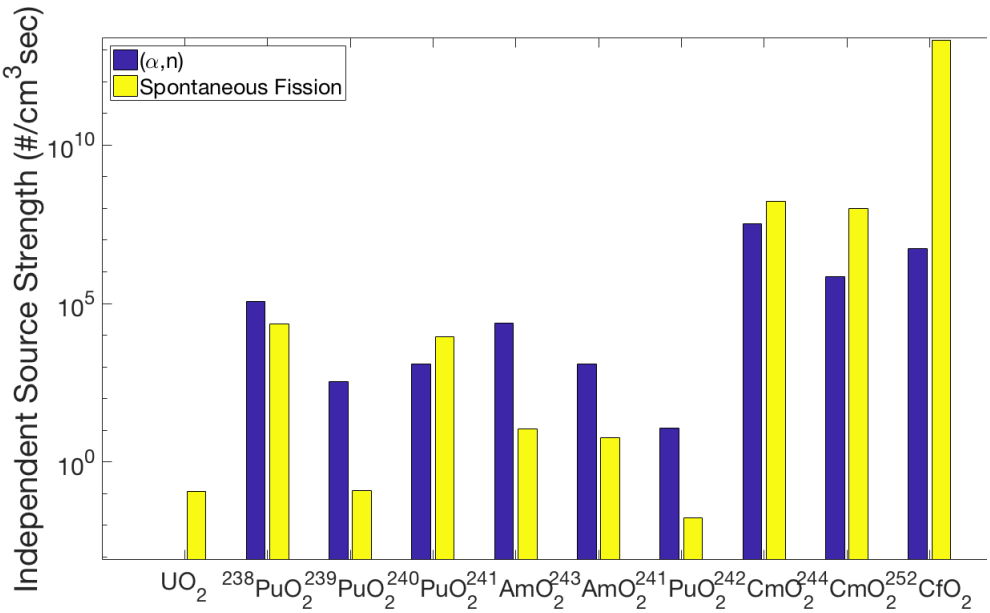

Figure 8.4 Independent Neutron Source Strength by Nuclides

for burnup level of 40000 MWd/MTHM (freshly discharged). Note that atom densities for other transuranium nuclide are at least $\sim$ 6 to 10 orders of magnitude larger than the ^{252}Cf.

Therefore, $^{252}CfO_2$ is typically not the most significant independent neutron source. The $^{242}CmO_2$ and $^{244}CmO_2$ are considered the main independent neutron source in the SNF. Comparing to other nuclides, except ^{238}Pu, the $^{242}CmO_2$ and $^{244}CmO_2$ will dominate the independent neutron spectrum for most of the time. The ^{238}Pu has some significant effect on the independent neutron spectrum for lower burnup. This is mainly because the relative short half-life of 87.7 years and the production rate of ^{238}Pu will reach saturation at certain burnup. The amount of other transuranium nuclides are increasing while the ^{238}Pu will not increase significantly at certain burnup level. This can be demonstrated by the Fig. 8.5, 8.6, and 8.7. Note that the spectrum here is obtained from the UNF-ST&DARD code system. The energy group is 200 with equal interval ranged from 10^{-11} to 20 MeV.

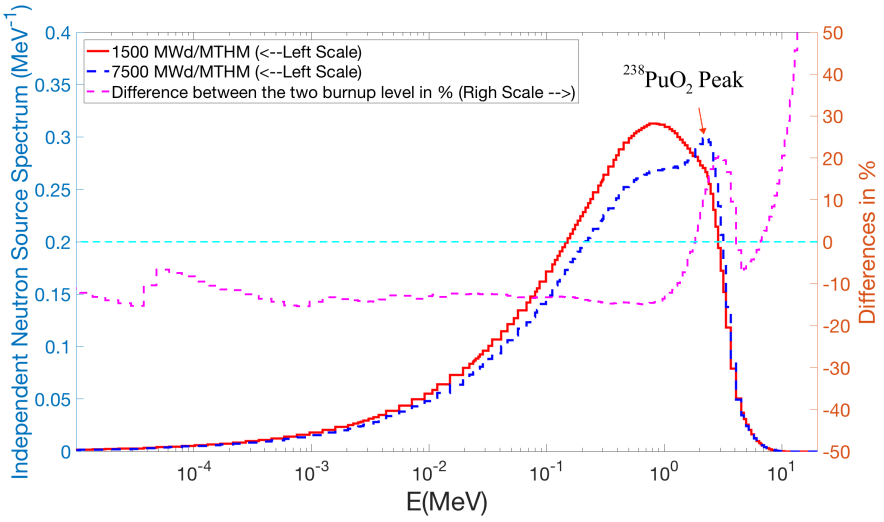

Figure 8.5 Independent Neutron Spectrum: Cooling Time 15 Years and Burnup of 7500 MWd/MTHM

Here, the neutron spectrum from burnup level of 1500 MWd/MTHM is selected as the reference. The differences between the selected burnup levels and the reference are also provided. For the neutron spectrum with burnup level of 7500 MWd/MTHM, there is an obvious peak from the $^{238}PuO_2$ (α,n) reaction. This is because the ^{242}Cm and ^{244}Cm have not been built up at this stage, the independent neutron spectrum is dominated by the $^{238}PuO_2$. After the burnup level become higher, the ^{242}Cm and ^{244}Cm are built up, therefore the independent neutron spectrum will be dominated by the spontaneous fission of these two nuclides. More details and analysis on the independent neutron source can be found in the Appendix I.

8.1.2.2 Thermal Neutron Induced Fission Neutron Source

In a subcritical multiplication system such as SNF cask, the thermal neutron induced fission neutron is another source of radiation. Fig. 8.8 shows the variation of the induced fission

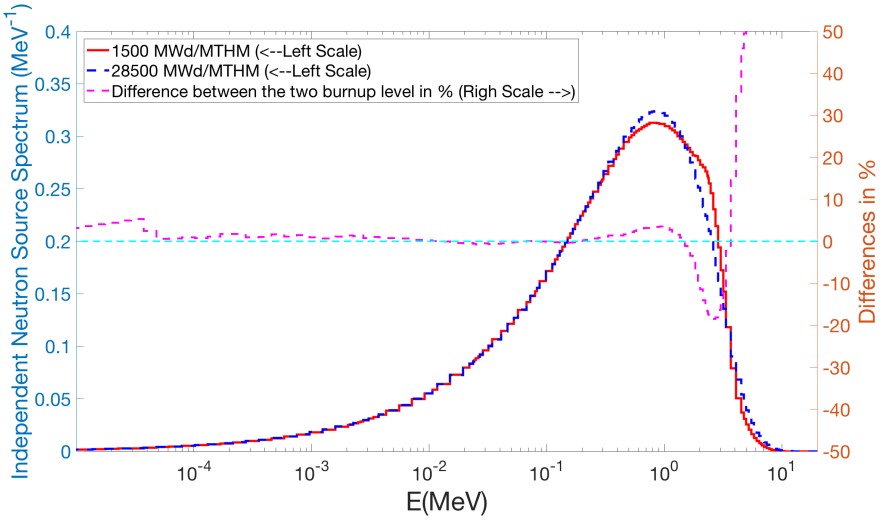

Figure 8.6 Independent Neutron Spectrum: Cooling Time 15 Years and Burnup of 28500 MWd/MTHM

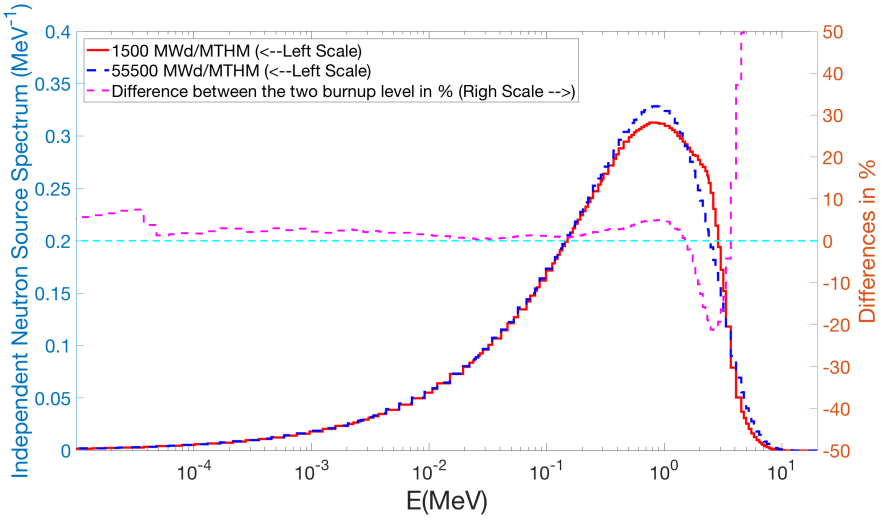

Figure 8.7 Independent Neutron Spectrum: Cooling Time 15 Years and Burnup of 55500 MWd/MTHM

neutron spectrum for averaged burnup level of 64500 MWd/MTHM and 15 years cooling time. Here, the different burnups from the 18 axial nodes are used for comparison. The Watt fission spectrum are obtained by using Eq. (5.1), (5.2), and (5.2).

The thermal neutron induced fission neutron spectrum does not vary as significant as the independent neutron spectrum do. However, it is still shown that the pure ^{235}U spectrum is softer than the ^{239}Pu spectrum.

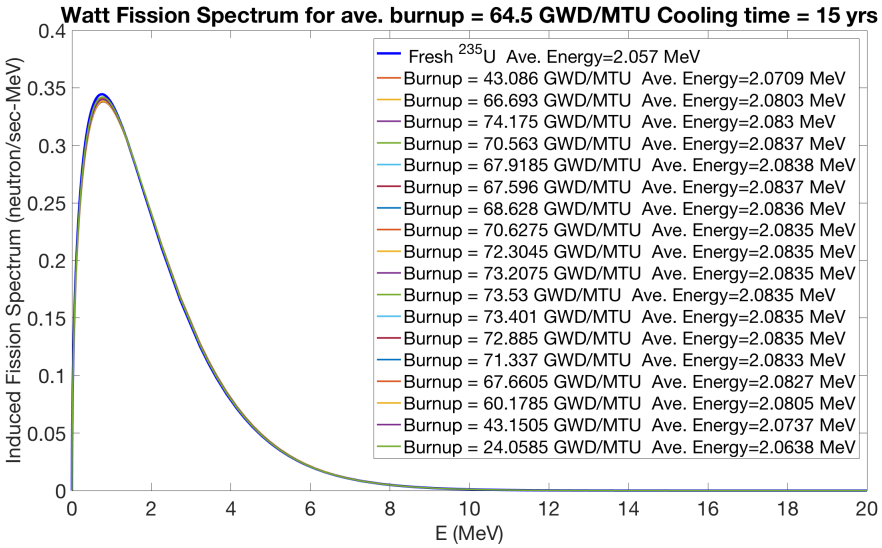

Figure 8.8 Thermal Neutron Induced Fission Neutron Spectrum

8.1.2.3 Summary of the Study for SNF Neutron Source Spectrum

Based on above discussions, we can conclude that:

1. The independent neutron spectrum varies with range of 0 to 10500 MWd/MTHM. It does not vary significantly with cooling time and burnup $\geq$ 10500 MWd/MTHM.
2. The thermal neutron induced fission neutron spectrum varies with burnup only, but in a less significant level comparing with the independent neutron source with burnup range 0 to 10500 MWd/MTHM.

These information are very important from the aspect of DRF coefficient generation. The source spectrum plays the major role on the DRF coefficient calculations. If the source spectrum does not change significantly within some range, i.e. burnup level $\geq$ 10500 MWd/MTHM for independent neutron source, same set of DRF coefficients can be reused and no re-calculation will be needed. However, these will need to be further demonstrated by actually performing the DRF coefficient calculation using the aforementioned source spectrum.

8.2 Problem Description

Here, two models are prepared: (1) The same 3D GBC-32 cask model from chapter 5, except replacing water with air; and (2) A 1D Model with similar dimension of the 3D GBC-32 model in radial direction. The 1D model is prepared mainly for the fast sensitivity analysis.

8.2.1 The 1D Spent Nuclear Fuel Cask Model with a Dosimeter

Fig. 8.9 shows the 1D dry storage cask model with dimensions and boundary conditions.

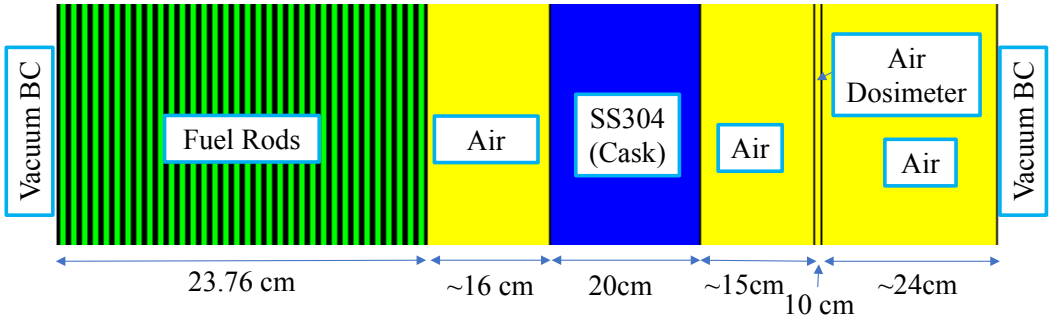

Figure 8.9 The 1D Dry Storage Cask Model

8.2.2 The 3D GBC-32 Dry Storage Cask model

The model of GBC-32 has been discussed in the chapter 8. For convenience, the model configuration is shown here again in the Figs. 8.10 and 8.11. Note that in this study, only dosimeter location of 0-degree and axial level 3 will be analyzed.

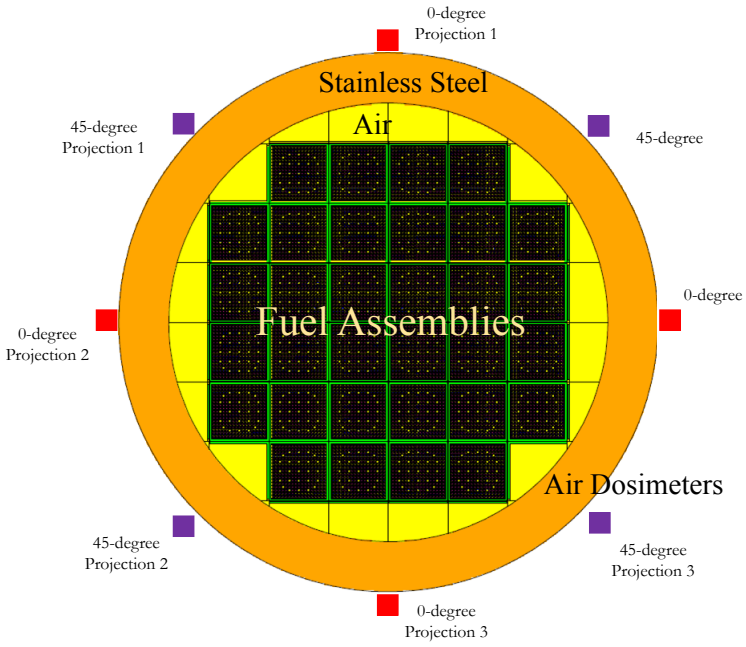

Figure 8.10 Dry GBC-32 SNF Cask with Air Dosimeters MCNP5 Model: Radial Projection

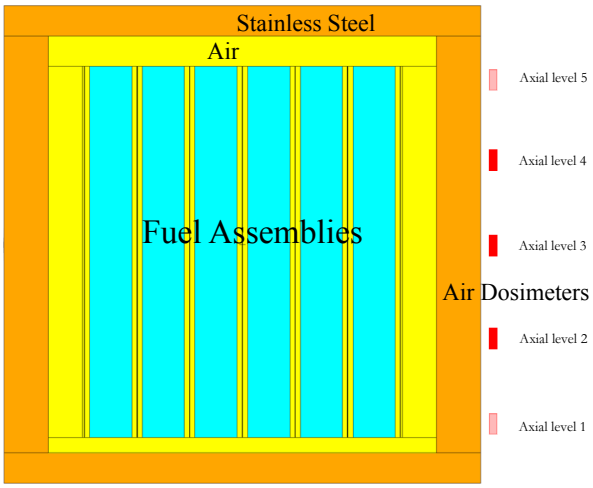

Figure 8.11 Dry GBC-32 SNF Cask with Air Dosimeters MCNP5 Model: Axial Projection

8.3 Importance Function Calculations and Field of View

In this section, the FOV and GC will be the main discussions. So far, we have discussed the importance function behavior and the lower weight windows bound in chapter 5, 6, and 7. We already have experience on the GBC-32 Cask external radiation detection. One question raised here: Can the FOV and GC being directly used for any detector or dosimeter? The answer is yes. Detailed reasons and analysis will be presented in this section.

8.3.1 Importance Source

Figs. 8.12 shows the ICRP and ANSI/ANS-6.1.1 flux to dose conversion factor for neutrons. The original group structure for ANSI/ANS-6.1.1 is 17 groups for neutrons while it is 14 group for the ICRP-21. The flux to dose conversion factor is interpolated to the BUGLE96 47 group structure for neutrons and used as importance source here. From the first glance, it is obvious that the flux to dose conversion factors are sensitive to the fast neutrons. The fast neutrons contribute a larger amount of dose by $\sim$ 2 order of magnitude comparing to the thermal neutrons.

8.3.2 Importance Models and Importance Functions

The importance function for both 1D and 3D GBC-32 model with an air dosimeter placed at 0-degree axial level 3 are calculate using the PENTRAN^{TM} code system. The calculation parameters are:

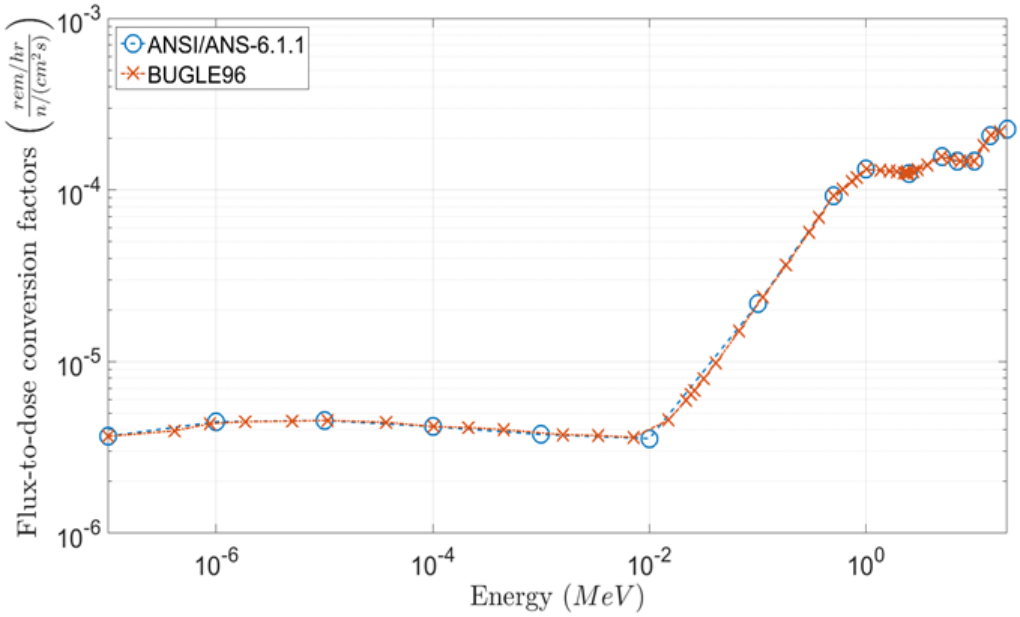

Figure 8.12 Neutron Flux to Dose Conversion Factor

- 1D Model - Mesh size from minimum 0.12 cm to maximum 1.29 cm. Legendre anisotropic scattering order of P3. Angular quadrature order S8. Convergence criteria 10^{-4} with maximum 200 iteration. The 47 group cross-section data library from the BUGLE96 is used.
- 3D Model - Mesh size from minimum 0.25 cm to maximum 5.00 cm. Legendre anisotropic scattering order of P3. Angular quadrature order S8. Convergence criteria 5×10^{-3} with maximum 100 iteration. The 47 group cross-section data library from the BUGLE96 is used.

Since we have discussed the behavior of neutron importance functions in chapter 5, 6, and 7, the detailed neutron importance function behavior will not be presented here. The importance function of neutrons are all very similar even with different dosimeter.

8.3.3 3D GBC-32 Model with Air Dosimeter Field of View Study

In principle, the FOV and GC from chapter 5 can be directly used here since we already have experience with the GBC-32 cask external detection for neutrons. However, it is always good to provide verification. In this section, FOV and GC analysis for the two neutron sources will be performed using the PENTRAN^{TM} calculated importance function.

8.3.3.1 Neutron Source

Since we already have experience with the GBC-32 external radiation detection from chapter 5, it is assumed the FOV for all neutron detector or dosimeters are very similar to each others. To provide an verification, the FOV for induce fission neutron source is shown in the Fig. 8.13. Note that here one axial level is 15 cm, which gives total pre-selected FOV of 2 assemblies away in x-direction, 3 assemblies away in y-direction, and 60 cm in axial (z) direction.

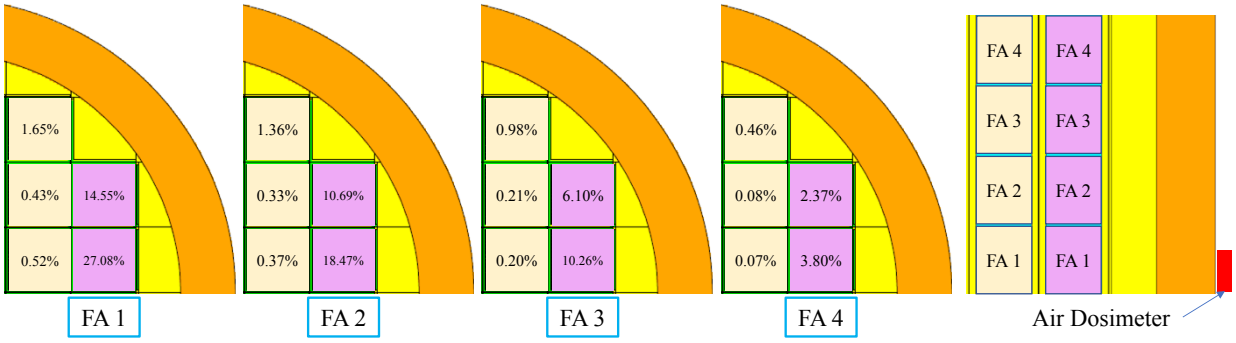

Figure 8.13 FOV of Fission Neutron Source: Zero-degree Air Dosimeter and Axial Level 3

If we compare Fig. 8.13 with Fig. 5.7 from chapter 5, it is observed that the FOV is very similar to each others. The two assemblies that are close to the dosimeter contribute $\sim 93\%$ of the dosimeter response. Therefore, it can be concluded that with a nuclear facility size determined, the FOV of any detector/dosimeter can be determined with 1 detector/dosimeter type, and apply to the others for induced fission neutron source. Note that this may hold if detector/dosimeter size does not change significantly, i.e. 1000 times of the volume size. Further demonstration for independent neutron source with burnup level 4500 MWd/MTHM and no cooling time is shown in the Fig. 8.14.

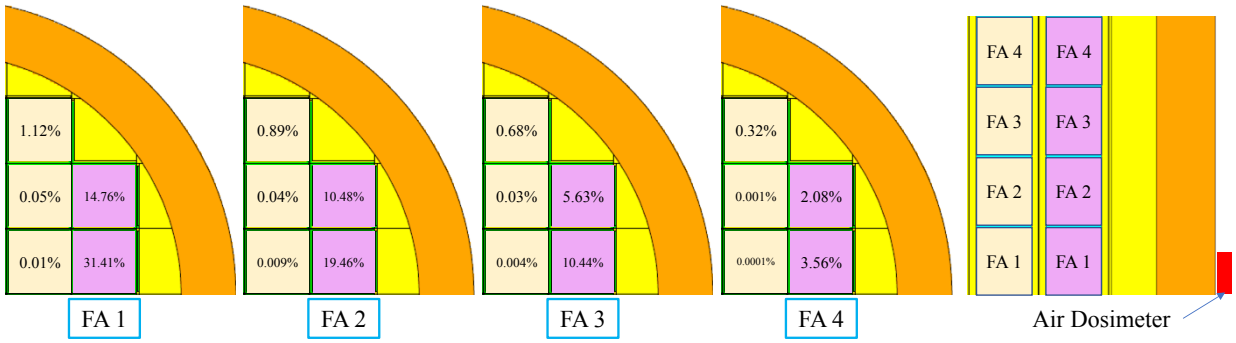

Figure 8.14 FOV of Independent Neutron Source (4500 MWd/MTHM No Cooling Time): Zero-degree Air Dosimeter and Axial Level 3

The reason for selection of such burnup is the large difference in the spectrum shape by the $^{238}PuO_2$ (α,n) source. The independent neutron source for higher burnup is very close to the spontaneous fission source of ^{242}Cm and ^{244}Cm, which is closer to the induced fission source spectrum. Therefore, the selected burnup level of 4500 MWd/MTHM is the better choice for extreme condition. Similarly, $\sim$ 98% of the dosimeter response form the independent neutron source are from the two closest fuel assemblies. The GC of the two neutron sources for the zero-degree axial mid-plane air dosimeter is shown in the Fig. G.6.

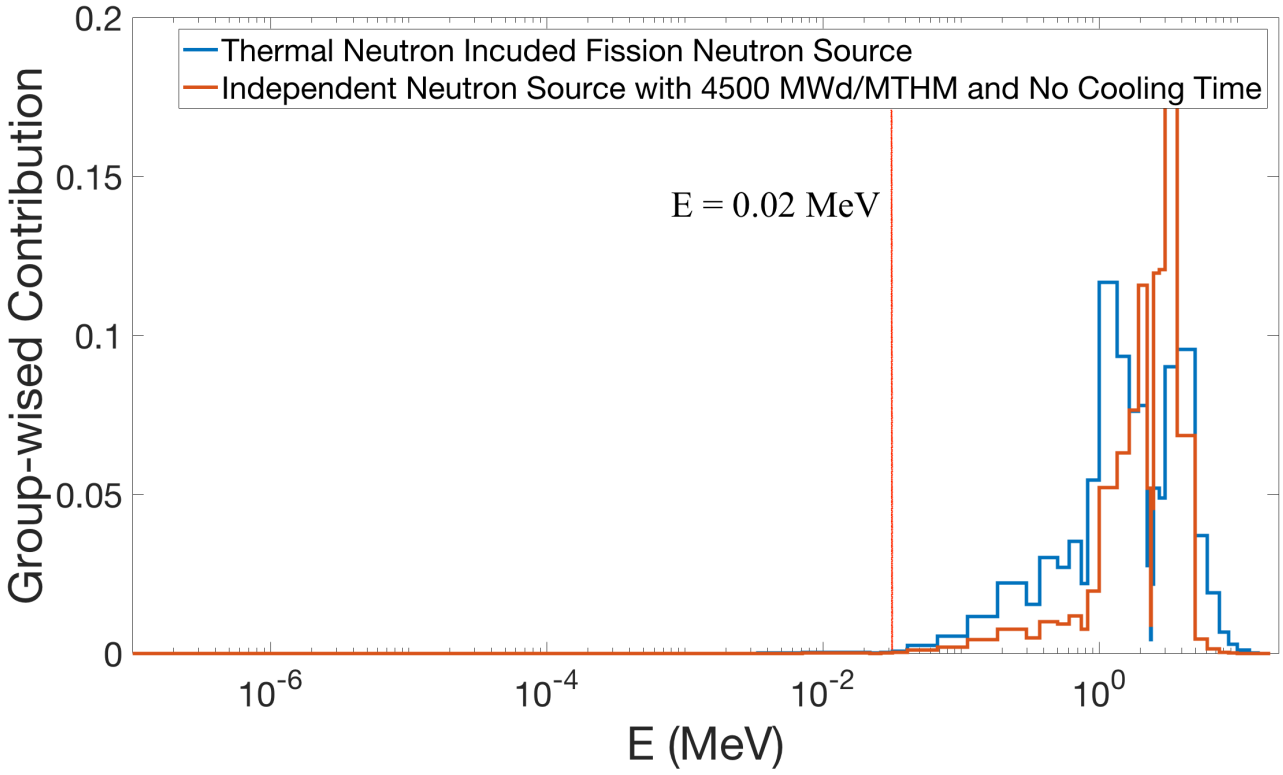

Figure 8.15 GC Neutron Sources: Zero-degree Air Dosimeter and Axial Level 3

The results show that the neutron energy more than 0.02 MeV are contributing to most of the dosimeter response. The GC shape is very similar to the result in Fig. 5.8, except the threshold energy is lower. This is mainly because the presence of water for Fig. 5.8 and presence of air for the model in this chapter. The presence of air can increase the probability of neutrons with relatively lower energy penetrating through the shield. However, with such large change in the material, i.e. replacing water with air, the threshold of GC is only shifted by less than 1 MeV. Therefore, it is further supporting the statement: "The FOV and GC can be performed once with one detector or dosimeter type for a specific SNF cask type, then the results can be applied to others directly for neutrons".

8.4 Sensitivity Study to the DRF coefficients

For a dry storage SNF cask, the most important variables are fuel assembly burnup and cooling time. Therefore, the sensitivity of the DRF coefficients to the burnup and cooling time will be performed against the two neutron sources in this section. The selected fuel pellet in the 1D model for study is shown in the Fig. 8.16.

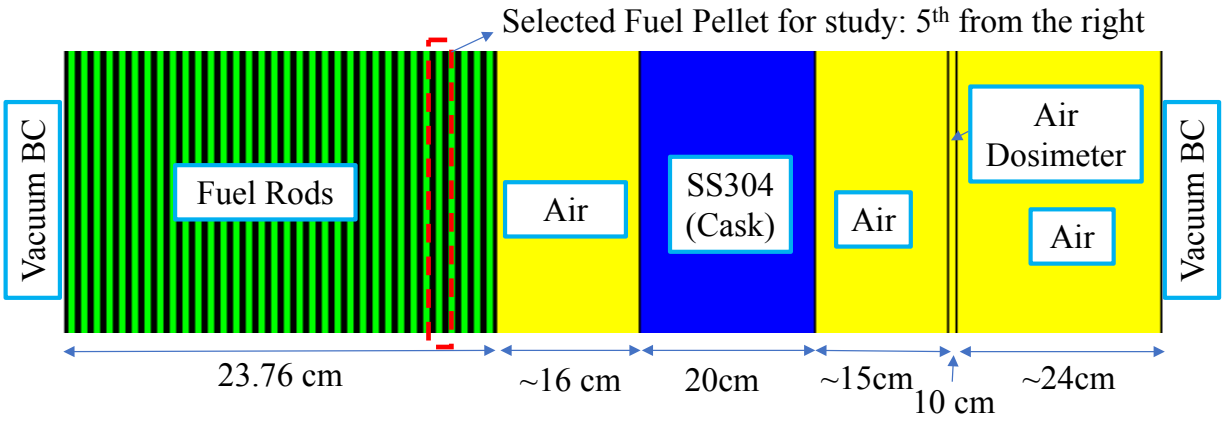

Figure 8.16 Selected Fuel Pellet for the DRF Coefficient Sensitivity Study

The 5^{th} fuel pellet from the right is selected for the sensitivity study. Similarly to the sensitivity study performed in the chapter 7, we assume the sensitivity of DRF coefficient to different parameters can be applied to all the fuel pellets. Here, we only examine the sensitivity of the DRF coefficients to fuel assembly burnup and cooling time. The MCNP5+CADIS methodology is used for all the DRF coefficient calculations. Note that the number of particle used for all the calculations are from 10^8 to 10^{10}. The neutron DRF coefficient usually takes < 20 minutes to achieve 1σ relative statistical uncertainty of 0.5%.

8.4.1 Independent Neutron Source

The sensitivity of independent neutron DRF coefficients for different burnup and cooling time is shown in the Fig. 8.17.

Here, the DRF coefficient of fresh fuel (UO_2) is selected as the reference case. For freshly discharged burned fuel assembly, the DRF coefficients are more sensitive mainly because presence of delayed neutron. The delayed neutron spectrum is much softer than the spontaneous fission and (α,n) neutron spectrum. Therefore, the value of DRF coefficients for freshly discharged fuel is lower. It is also observed that for burnup level more than $\sim$ 20000 MWd/MTHM, the independent neutron DRF coefficient does not change significantly. This is corresponding to the result we observed from section 8.1.2.1. Due to the dominance of $^{238}PuO_2$ at lower burnup level, the independent neutron spectrum is significantly different

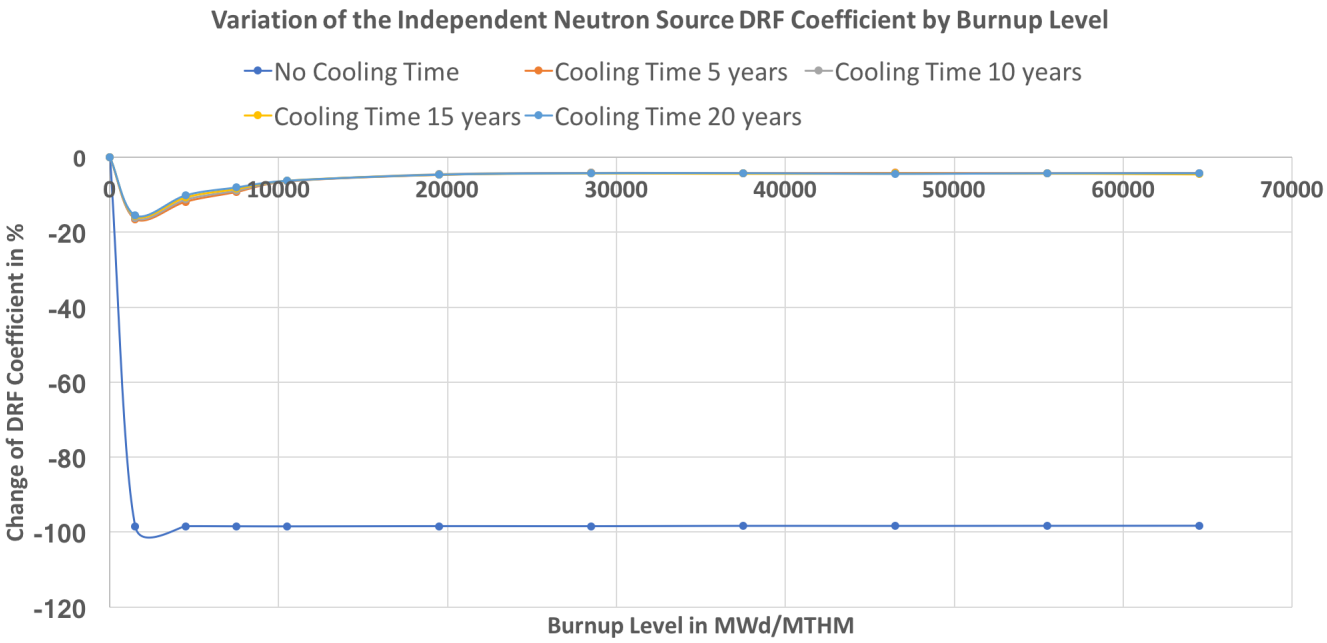

Figure 8.17 Sensitivity of the Independent Neutron Source DRF Coefficient to Burnup and Cooling Time - 1

from the higher burnup level. After the ^{242}Cm and ^{244}Cm dominate the source strength, the spectrum remain almost unchanged. Fig. 8.18 further re-plot it by looking into sensitivity of the independent neutron DRF coefficients to cooling time.

The results show that the DRF coefficient does not change significantly for cooling time of 5, 10, 15, and 20 years. This is mainly because no major nuclide transmutation is taking place by cooling time.

8.4.2 Fission Neutron Source

Fig. 8.19 shows the sensitivity of induced fission neutron DRF coefficients to the burnup and cooling time.

Here, the fresh fuel UO_2 DRF coefficient is selected as the reference case. The result shows that the DRF coefficient is nearly linear dependent on the burnup level. The fluctuation from 0 to 10000 MWd/MTHM may be mainly from the statistical noise. Fig. 8.20 further re-plot the Fig. 8.19 by looking into the sensitivity of DRF coefficient to the cooling time.

It is shown that the induced fission neutron DRF coefficients are not sensitive to the cooling time. This is mainly because no major change of fissile nuclide by cooling time. All the isotopic concentration for the heavy nuclide almost remain the same with increase of cooling time for a relatively short period of time, i.e. 20 years.

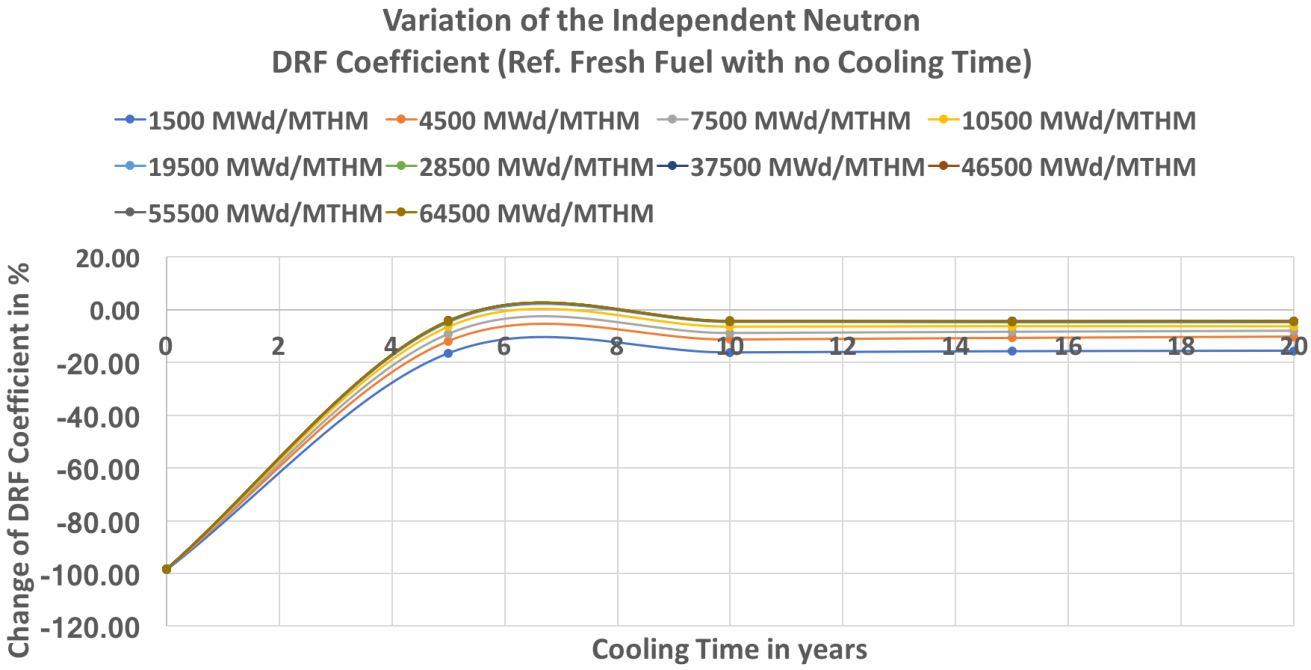

Figure 8.18 Sensitivity of the Independent Neutron Source DRF Coefficient to Burnup and Cooling Time - 2

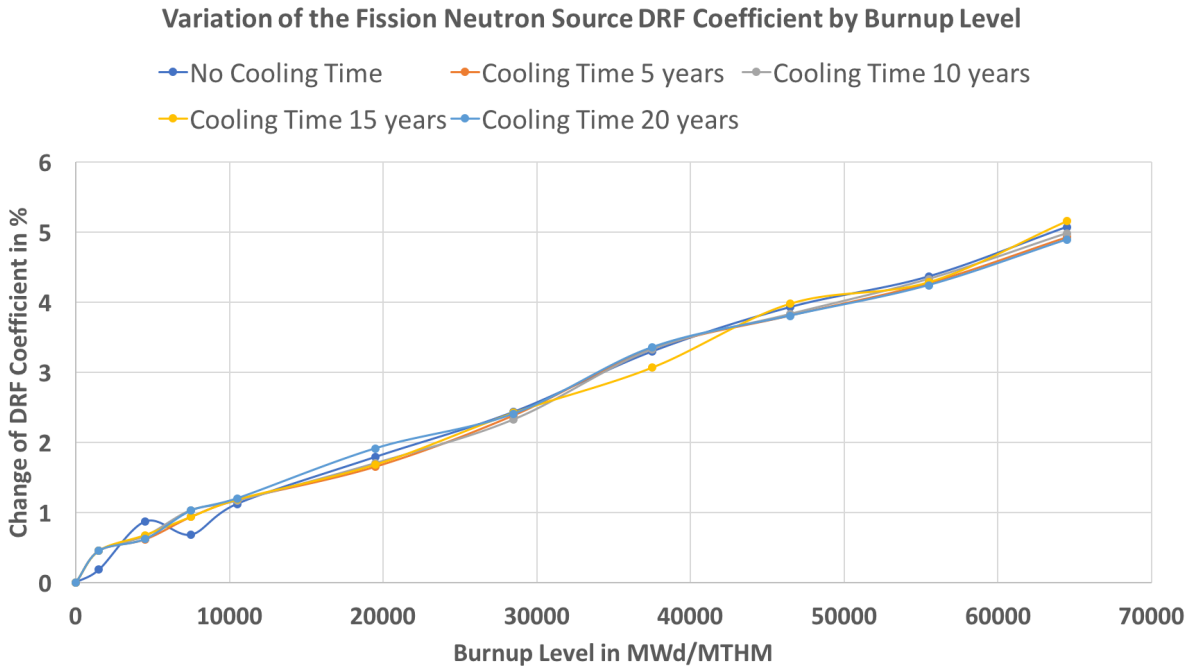

Figure 8.19 Sensitivity of the Fission Neutron Source DRF Coefficient to Burnup and Cooling Time - 1

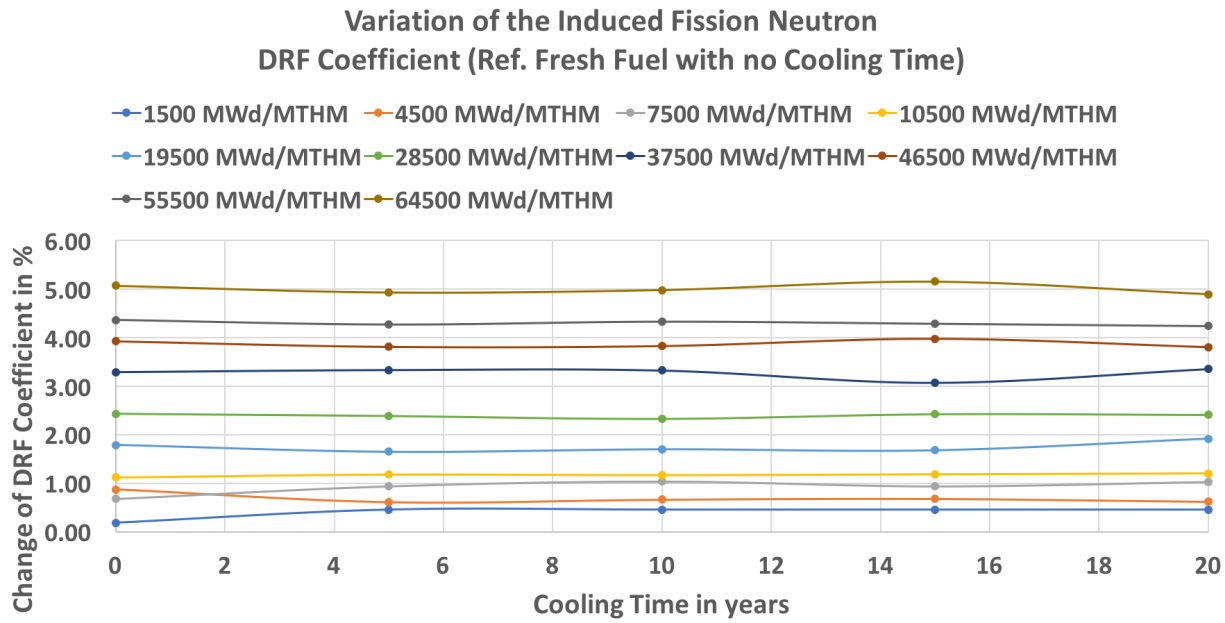

Figure 8.20 Sensitivity of the Fission Neutron Source DRF Coefficient to Burnup and Cooling Time - 2

8.4.3 Summary of the Neutron Source DRF Coefficient Sensitivity for Dry Storage Cask

All of the sensitivity studied for the two neutron sources are performed with presence of water and air within the cask. Very similar results are observed. Therefore, this can be generalized for SNF cask external dosimetry no mater there is presence of water or not. Here, we can conclude:

1. Independent Neutron Source DRF Coefficient - It is not sensitive to the burnup level if more than 20000 MWd/MTHM. It is also not sensitive to the cooling time, except freshly discharged fuel assemblies.

2. Fission Neutron Source DRF Coefficient - It is almost linearly dependent to the burnup level and not sensitive to the cooling time. Linear interpolation scheme can be applied for obtaining the burnup dependent DRF coefficient.

The most problematic part is the period within few days of freshly discharged fuel assemblies. The independent neutron spectrum change significantly within this period, mainly because the presence of delayed neutron source. Therefore, no pattern can be found for DRF coefficient. However, the SNF assemblies are typically placed in a SNF pool for more than 5 years before moving to dry storage cask. Therefore, this approach will still be applicable for dry storage cask.

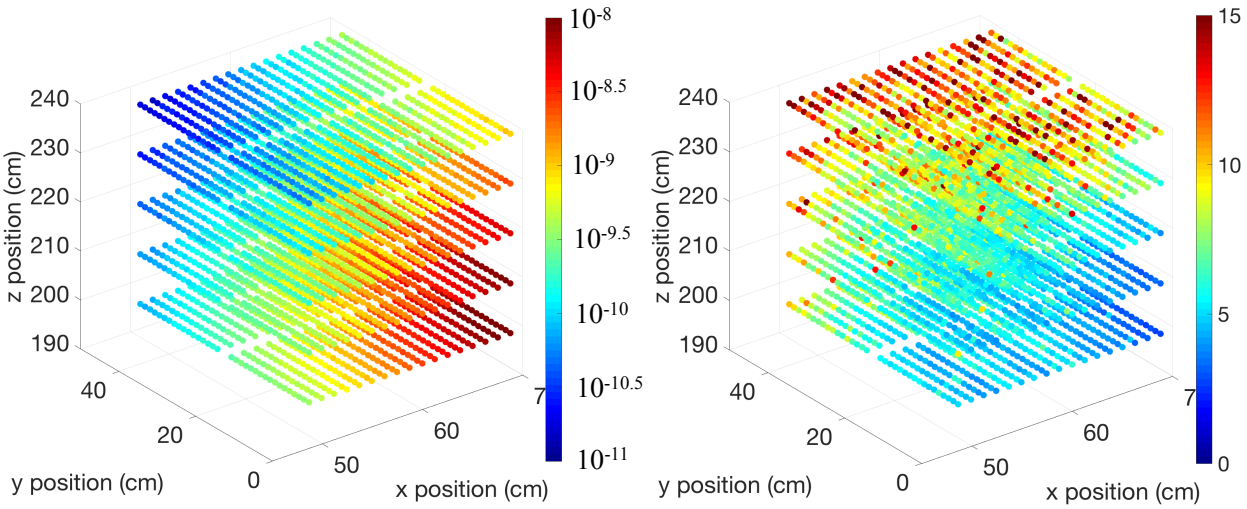

(a) DRF Coefficients

(b) 1σ Statistical Uncertainty in %

Figure 8.21 Independent Neutron Source DRF Coefficients: Burnup Level of 28500 MWd/MTHM and 5 Years Cooling Time

8.5 3D DRF Coefficient Calculations

The full 3D DRF coefficients for dosimeter location at 0-degree with the axial level 3 shown in the Fig. 8.10 are presented here. The DRF coefficient calculations are performed using the MCNP5 code system with the CADIS methodology. The lower weight widnow bounds for the use of CADIS methodology are obtained via the aforementioned importance function.

8.5.1 Independent Neutron Source DRF Coefficients

Fig. 8.21 shows the DRF coefficients for independent neutron source with burnup level of 28500 MWd/MTHM and 5 years cooling time. The unit DRF coefficient calculations requires $\sim$ 10 minutes using 8 processors. The number of particle used is 10^7. There are total 2890 DRF coefficients calculated using 56 processors, which requires $\sim$ 2.87 days of computation wall-clock time.

The independent neutron source DRF coefficients drops $\sim$ 2 orders of magnitude for 1 fuel assembly away ($\sim$ 23.76 cm) from the dosimeter radially, and $\sim$ 1 order of magnitude for $\sim$ 40 cm away from the dosimeter axially. More detailed trend of the DRF coefficients by 3D bar scatter plot are shown in the Fig. 8.22.

The dosimeter is located at the $19^{th}/36^{th}$ axial level in the model. Here, two selected axial levels are shown. It is further verified that the DRF coefficients drops significantly with 1 assembly away from the dosimeter radially. Almost a factor of 2 decrease on the DRF

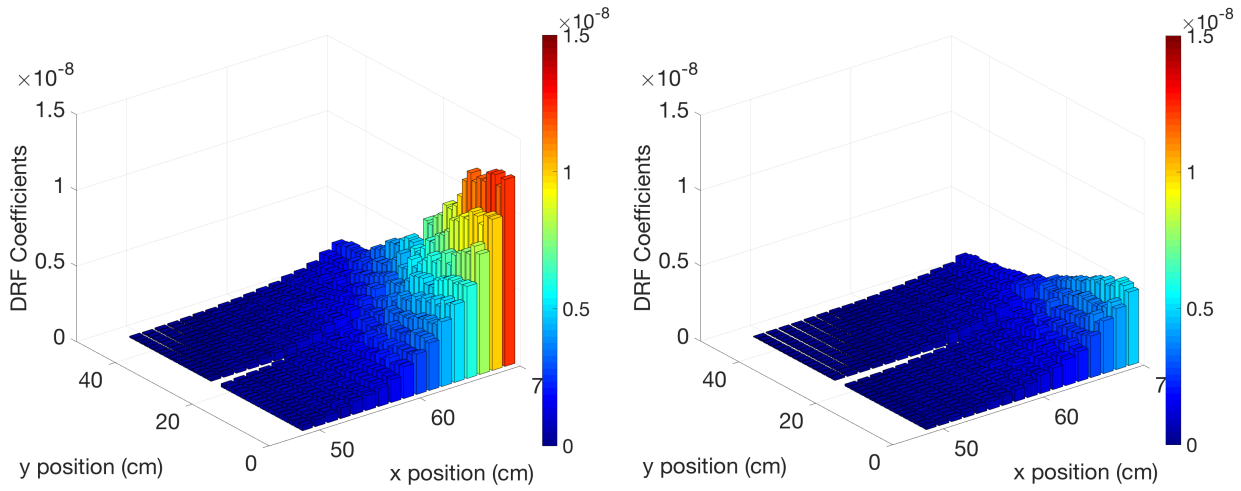

(a) Axial Level $19^{th}/36^{th}$ **(b)** Axial Level $21^{th}/36^{th}$

Figure 8.22 Independent Neutron Source DRF Coefficients: Burnup Level of 28500 MWd/MTHM and 5 Years Cooling Time (Dosimeter at Axial Level $19^{th}/36^{th}$)

coefficient is observed for 2 axial level away. Note that the length of 1 axial level is 10.16 cm.

8.5.2 Fission Neutron Source DRF Coefficients

Fig. 8.23 shows the induced fission neutron source DRF coefficients for burnup level of 28500 MWd/MTHM and 5 years cooling time. The unit DRF coefficient calculation requires ~ 1 to 2 minutes using 8 processors. The number of particle used for all the calculations are 10^7. There are total 3468 DRF coefficient calculated using 56 processors, which requires ~ 1 day of computation wall-clock time.

The induced fission neutron source DRF coefficients show a very similar behavior comparing with the independent neutron source DRF coefficients. It drops ~ 1.5 orders of magnitude for 1 assembly (~ 23.76 cm) away from the dosimeter radially, and ~ 1 order of magnitude for 40 cm away from the dosimeter axial plane. Fig. 8.24 further show the detailed DRF coefficients' behavior for the two selected axial planes.

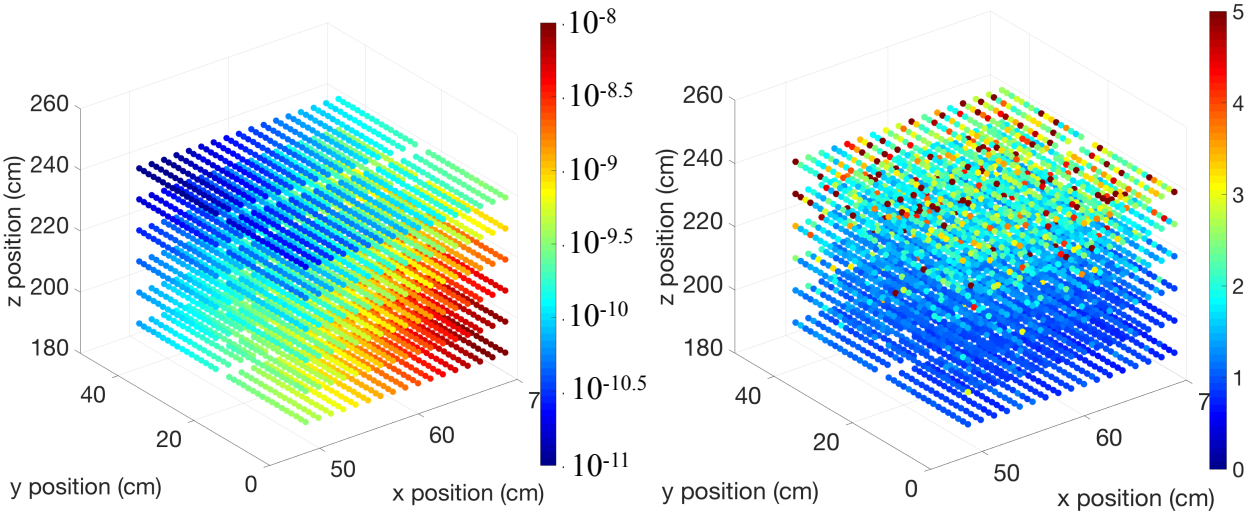

(a) DRF Coefficients **(b)** 1σ Statistical Uncertainty in %

Figure 8.23 Induced Fission Neutron DRF Coefficients: Burnup Level of 28500 MWd/MTHM and 5 Years Cooling Time

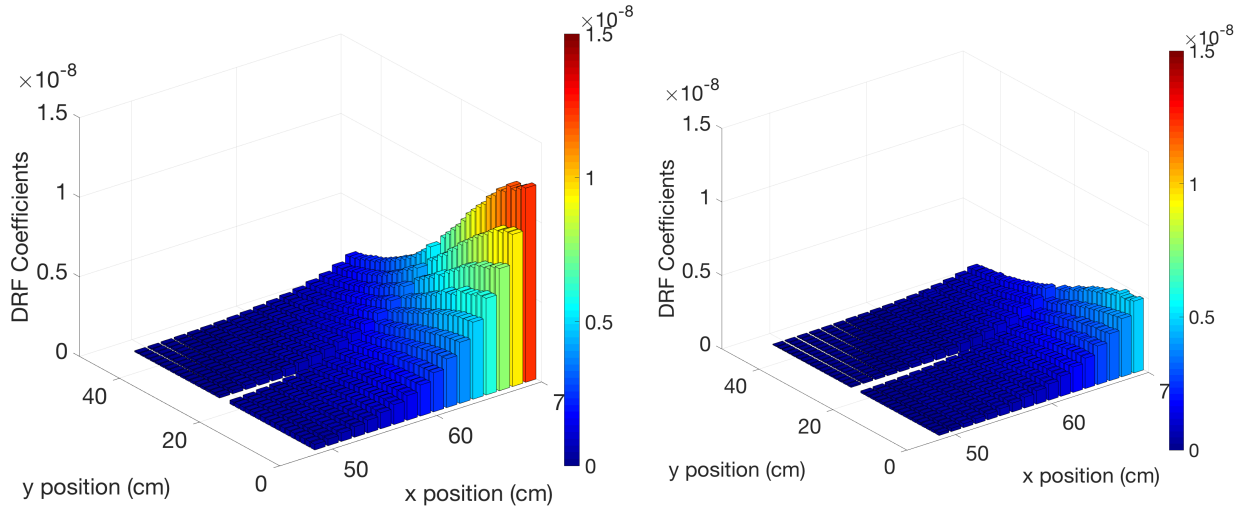

(a) Axial Level $19^{th}/36^{th}$ **(b)** Axial Level $21^{th}/36^{th}$

Figure 8.24 Induced Fission Neutron DRF Coefficients: Burnup Level of 28500 MWd/MTHM and 5 Years Cooling Time (Dosimeter at Axial Level $19^{th}/36^{th}$)

8.6 Neutron Source Calculations

To calculate the external dose value, the neutron sources have to be obtained first. The selected assembly burnup and cooling time profile is shown in the Fig. 8.25.

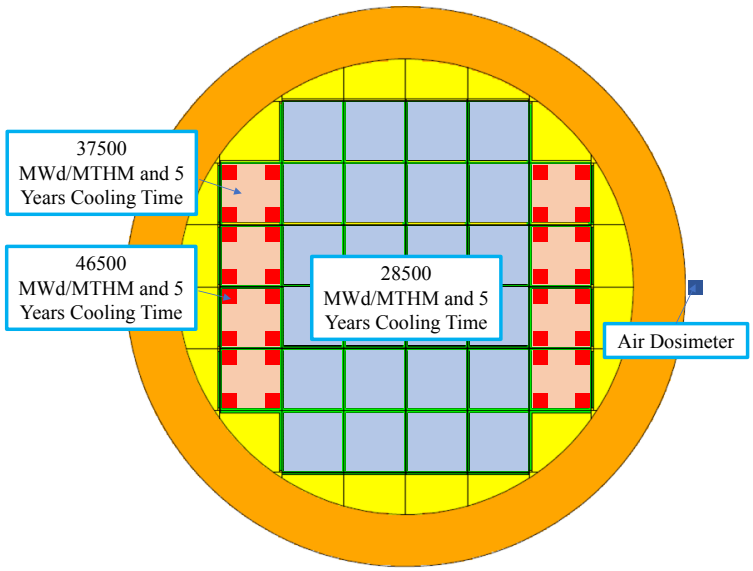

Figure 8.25 Assembly Burnup and Cooling Time Pattern

There are three types of fuel assemblies: (1) Burnup Level 28500 MWd/MTHM and 5 years cooling time; (2) Burnup Level 37500 MWd/MTHM and 5 years cooling time; and (3) Burnup Level 46500 MWd/MTHM and 5 years cooling time. The reason for the selected profile is to create mixing fuel burnup scenario. Note that burnup and cooling time profile are uniform in axial direction. The independent neutron source strength is obtained from the UND-ST&DARD code system.

8.6.1 Independent Neutron Source

Fig. 8.26 shows the pin-wised independent neutron source distribution for the selected core pattern.

The independent neutron source contains spontaneous fission, (α,n), and delayed neutron sources. The delayed neutron source for 5 years cooling time is almost zero, therefore we only have spontaneous fission and (α,n) sources here.

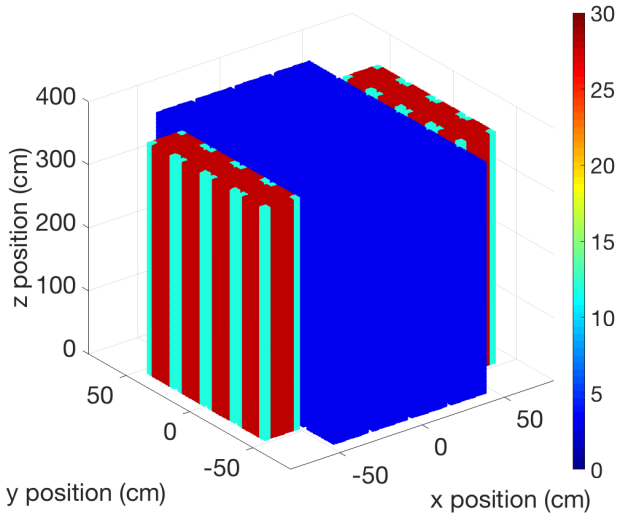

Figure 8.26 Pin-wised Independent Neutron Source (neutrons/sec)

8.6.2 Induced Fission Neuron Source

The induced fission neutron source is calculated using the MCNP5 subcritical multiplication mode, which turns off the NONU card when performing Monte Carlo fixed-source calculation. The number of particles tested for convergence study are 10^6, 10^7, and 1.5×10^7. The convergence test has shown that the solution has not completely converge even with 1.5×10^7 particles. However, the purpose of this study is the application of DRF methodology. It is acceptable to have an induced fission source distribution with certain level of accuracy, but not completely exact. Also, this is mainly because the limited computation resource. Three batches of calculation are perform independently for fuel rods with 28500, 37500, and 46500 MWd/MTHM and 5 years cooling time. This arrangement is mainly for convenience because the complexity of defining source spectrum and location with different burnup level in MCNP5. Fig. 8.27 show the calculated 3D pin-wised fission source distribution.

The results show that large uncertainty are still observed at the peripheral locations. This is mainly because the low sample at such locations. Larger fission neutron source are observed at fuel assemblies with 37500 and 46500 MWd/MTHM and 5 years cooling time. This is mainly because the magnitude of independent neutron source at such locations are larger, and thus inducing more fission reaction. Further detailed for axial slice fission source distribution and their corresponding 1σ statistical uncertainties are shown in the Figs. 8.28 and 8.29.

The fission source distribution at upper axial level, i.e. Fig. 8.29a, show a lower values. This is mainly because the location is close to the boundary with more leakage. Note that the induced fission source can be calculated using the RAPID code system. However, presence of air instead of water in the cask can create the following problems on FM coefficient

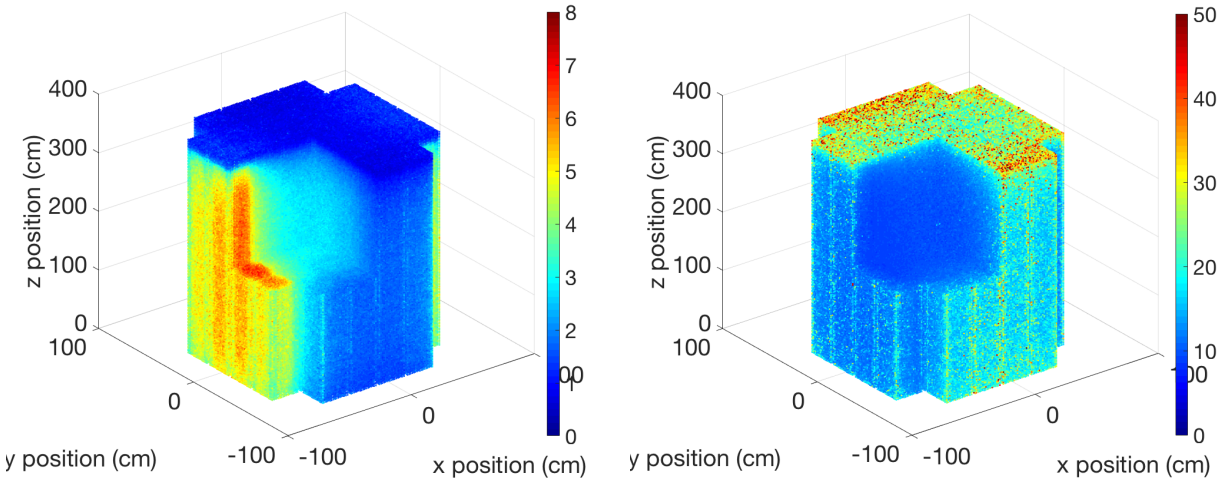

(a) Fission Source (neutrons/sec) **(b)** 1σ Statistical Uncertainty in %

Figure 8.27 Pin-wised Induced Fission Source

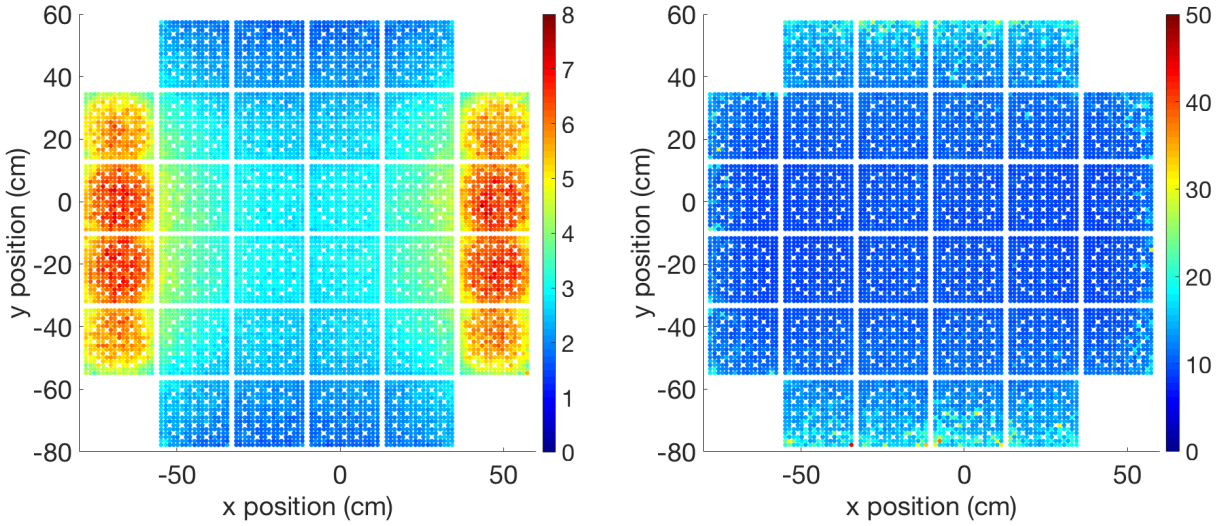

(a) Fission Source (neutrons/sec) **(b)** 1σ Statistical Uncertainty in %

Figure 8.28 Pin-wised Induced Fission Source: $73^{th}/144^{th}$ Axial Level

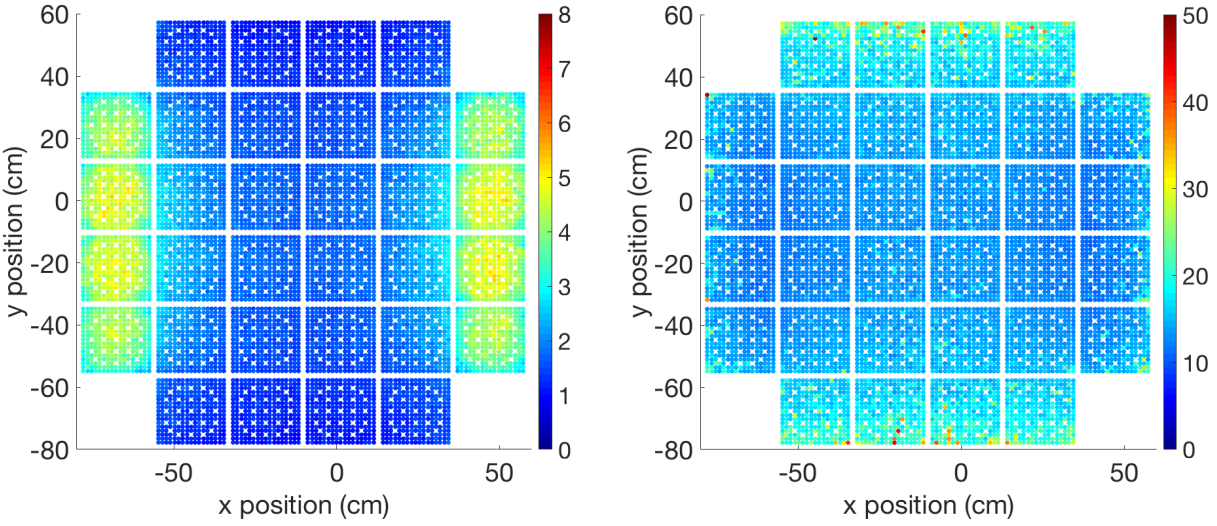

(a) Fission Source (neutrons/sec) **(b)** 1σ Statistical Uncertainty in %

Figure 8.29 Pin-wised Induced Fission Source: $135^{th}/144^{th}$ Axial Level

calculations:

1. The control volume will be significantly larger than the scenario flooded with water. This is mainly because the mean-free-path of neutrons will be significant larger with presence of air.
2. The neutrons will be highly directional with lower interaction rate. This will lead to a much longer calculation time for FM coefficient calculation.

The second problem may be solved by applying the CADIS methodology. However, the presence of air will lead to ray effect, which may create inappropriate lower weight window bounds that does not efficiently accelerate the calculation efficiency. Increasing quadrature order may help on solving this issue. However, more computation time may be needed for the importance function calculations.

8.7 External Dose Calculations

In this section, the external dose calculated from the two neutron sources are presented and discussed.

8.7.1 Dose from Independent Neutron Source

Table 8.1 shows the calculated doses from independent neutron source. A MCNP5 + CADIS reference calculation is also prepared for comparison. The number of particle used in the MCNP5 reference calculation is 10^8.

Table 8.1 Dose from the Independent Neutron Source

Code	Dose (mrem/hr)	1σ	Differences in %
RAPID / DRF Methodology	2.5992×10^{-4}	-	-1.17%
MCNP5 + CADIS	2.6300×10^{-4}	0.86%	Ref.

Note that one more axial level of source is added for the MCNP5 reference calculation to verify the FOV estimation. The result shows that the dose value calculated by RAPID is within 2σ relative statistical uncertainty of the MCNP5 reference calculation. Here, we have demonstrated that the FOV estimation is very accurate for independent neutron source. The additional axial level in the reference calculation almost has negligible contribution.

The DRF coefficients used for the dose calculation are with dependency of 28500 MWd/MTHM and 5 years cooling time. As we discussed in the section 8.4, the independent neutron source DRF coefficients are not sensitive to burnup level $>$ 20000 MWd/MTHM and cooling time $\geq$ 5 years. Therefore, we directly use the coefficients on all the dose calculation here. The result has demonstrated that this approach is very appropriate.

The calculation wall-clock time of MCNP5 is $\sim$ 11 minutes using 8 processors while the DRF methodology only requires less than a second using 1 processor.

8.7.2 Dose from Induced Fission Neutron Source

Table 8.2 shows the dose values calculated by RAPID and a MCNP5 reference case. The number of particle used in the MCNP5 reference calculation is 10^8.

Table 8.2 Dose from the Induced Fission Neutron Source

Code	DRF Coeff.	Dose (mrem/hr)	1σ	Differences in %
RAPID / DRF Method.	Real	5.9461×10^{-5}	-	-0.08%
RAPID / DRF Method.	Interpolation	5.9424×10^{-5}	-	-1.43%
MCNP5 + CADIS	-	5.9509×10^{-5}	0.86%	Ref.

Here, we obtained the DRF coefficient via two approaches: (1) Calculating the DRF coefficient with dependency to the corresponding burnup and cooling time; and (2) Interpolation. From the sensitivity study section, it is shown that the fission neutron DRF coefficients are almost linearly dependent on the burnup level with almost no dependency on cooling time.

Therefore, we obtained the DRF coefficient for burnup levels of 37500 MWd/MTHM and 46500 MWd/MTHM (5 year cooling time) by using two pre-calculated DRF coefficient: (1) 4 wt% fresh fuel; and (2) 64500 MWd/MTHM and 10 years cooling time.

The results show that this arrangement is very appropriate. The calculated dose value is within 2σ relative statistical uncertainty of the reference calculation if linear interpolation scheme is used to obtain the DRF coefficients.

8.7.3 Effect of Axial Structure

The boundary structure effect on the DRF coefficients and dose are also examined. Here, we examine the air dosimeter at 0-degree and axial level 5 shown in the Fig. 8.10. The dosimeter responses calculated using actual and translated DRF coefficients for dose from induced fission neutron source are shown in the Table 8.3. The number of particles used for the MCNP5 reference calculation is 10^7, which requires $\sim$ 5 minutes of computation wall-clock time using 16 processors.

Table 8.3 Effect of Top Structure on Induced Fission Neutron Dose: Dosimeter at 0-degree Axial Level 5

Code	DRF Coeff.	Dose (mrem/hr)	1σ	Differences in %
RAPID / DRF Method.	Real	4.7322×10^{-5}	-	2.31%
RAPID / DRF Method.	Translation	3.3153×10^{-5}	-	-28.32%
MCNP5 + CADIS	-	4.6254×10^{-5}	2.17%	Ref.

The results show that axial top structure will create $\sim$ 30% of difference on the dose value if directly using axial DRF coefficient translation. This is mainly because the decrease of neutron capture by the boundary structure. Smaller amount of fuel material are found at the axial boundary, and therefore decrease the capture rate of neutrons. This can be demonstrated by the smaller dose value using direct axial translation on the DRF coefficients.

From the chapter 5, we have observed that direct axial translation may works for SNF cask flooded with water using a ^{3}He detector. However, this is not valid with presence of air. This is mainly because the presence of water can create more neutron moderation. With presence of air, neutron are less moderated and thus will carry more information from the source.

For independent neutron source, the spectrum is harder than the induced fission neutron source. Therefore, it is expected that the dose value will be lower if using direct axial DRF coefficients translation. For the boundary structure at the bottom, it is also expected the DRF coefficients will be sensitive to it. This is mainly because the similar boundary structure material and dimension.

8.8 Summary of the Chapter

In this chapter, we have successively utilized a dry storage SNF cask external neutron dosimetry problem to benchmark the DRF methodology. Here, we can conclude the following items:

1. The FOV for a SNF cask can be generalized with any neutron detector/dosimeter type with and without presence of water.
2. The GC varies slightly with presence of air, but still can be generalized with any neutron detector/dosimeter type with a threshold energy ~ 0.01 MeV.
3. The dose rate from the independent neutron source can be calculated using same sets of DRF coefficient if burnup level is more than $\sim$ 20000 MWd/MTHM and cooling time greater or equal to 5 years.
4. The dose rate from the induced fission neutron source can be calculated using linear interpolation technique on the DRF coefficient. No cooling time dependency is required.
5. Different set of DRF coefficients for top and bottom boundaries are necessary.

Note that the bullets 3 and 4 may need to be re-studied with longer cooling time, i.e. more than 100 years or even 500 years. This is mainly because the half-life time of the ^{244}Cm is only 18.10 years. After this nuclide decay away, the ^{238}Pu or ^{241}Am may dominate the behavior of spectrum and sensitivity of DRF coefficients. However, most of the SNF cask are currently with cooling time range from 5 years to 40 years. These conclusion will be valid and sufficient for current application on SNF cask dosimetry.

Chapter 9

Summary and Guideline for the DRF Methodology

In this chapter, we will summarize the DRF methodology on the applications of RPV neutron fluence calculation and SNF cask external dosimetry. The DRF methodology has been demonstrated to be fast, accurate, and easy to implement on dose or detector/dosimeter response calculations, if neutron or photon source are appropriately prepared. Here, will give a general guideline for implementing the DRF methodology on radiation shielding analysis.

9.1 General Procedure of the DRF Methodology

To implement the DRF methodology to the deep penetration problems, we will need:

1. An LBE Deterministic Solver - To perform DRF coefficient calculation, use of the CADIS methodology is required. It will be impractical to perform DRF coefficient calculations without variance reduction technique.
2. A Monte Carlo particle transport code with fixed-source calculation capability - Currently, the Monte Carlo code is considered the most accurate approach in he community. Therefore, it is reasonable to use such code systems to perform the DRF coefficient calculations. Weight windows technique is also required for the selected Monte Carlo code.

Note that above requirements are picked for the users who want to generate the DRF coefficients by themselves. The DRF coefficients can be pre-built as a database for a specific facility. By doing so, no DRF coefficient pre-calculation will be required from the user side, i.e. industry applications.

The procedure of the DRF methodology are:

1. Prepare a Monte Carlo model and a Deterministic model with a initial guess of FOV. The detector can be selected arbitrarily.
2. Calculate the approximated importance function.
3. Estimate the FOV and GC by using the approximated importance functions.
4. Effectively trim down the Monte Carlo model to the effective range based on the FOV and GC from the last step. This FOV and GC can be applied to other detector or dosimeters if no major change on the facility dimension and materials.
5. Calculate the lower weight window bounds for the selected detector/dosimeter locations.
6. Perform Monte Carlo fixed source calculations using the lower weight window bounds from the last step for for the DRF coefficient calculations.
7. The DRF coefficients are stored as database.
8. Calculated the detector/dosimeter responses using the DRF coefficients.

Based on the study in this dissertation, the FOV and GC are not very sensitive to the detector/dosimeter types. The FOV is sensitive to the detector/dosimeter location while the GC is slightly depending on it. The detector/dosimeter FOV and GC can be determined once with a facility with fixed dimension and no major material changes. It is suggested that the FOV and GC only need to be estimated with one detector type and a few locations. The selection of location is depending on the distant between detector/dosimeter and the radiation source. At least two locations, which are the longest and shortest distances between detector/dosimeter, have to be selected.

9.2 Guideline of the DRF Methodology for PWR RPV Neutron Fluence Calculations

For the PWR RPV neutron fluence calculation, it is suggested that the DRF coefficients need to have dependency on:

1. Dosimeter type
2. Dosimeter location
3. Neutron source location

4. ^{235}U to ^{239}Pu ratio
5. Primary Coolant Density or Void fraction
6. Boron concentration of primary coolant

The axial boundary structures will potentially impact the dosimeter response by $\sim 5\%$ to $\sim 8\%$, depending on the dosimeter type. It is optional for the user to select the tolerance of error. Different sets of DRF coefficient for axial boundary may or may not needed.

9.3 Guideline of the DRF methodology for SNF Cask External Dosimetry

For the SNF cask external dosimetry within 100 years for steel cask, the only DRF coefficient need to be considered is the photon DRF coefficient. It is suggested the photon DRF coefficients need to have dependency on:

1. Dosimeter type
2. Dosimeter location
3. Neutron source location
4. Burnup Level
5. Cooling Time
6. Axial boundary structure

The dose from neutron source can be calculated efficiently as well, if user wants to calculate it. The size of photon source DRF coefficient database will be larger than the neutron source. This is mainly because the photon DRF coefficients are more dependent on the burnup and cooling time. More data point is required for capturing the non-linear trend of burnup and cooling tine dependency on DRF coefficients.

It is shown that the DRF coefficients will be affected by axial boundary structure with presence of air in a SNF cask. Therefore, different sets of DRF coefficients have to be prepared. Another potential approach is to prepare a "correction factor" for axial boundary dose calculation.

9.4 Current Limitation of the DRF Methodology

Currently, the DRF methodology is very robust for fast and accurate radiation shielding calculations if the source location is known. Scenario such as core melting, for example, the Fukushima Daiichi accident, has not yet being considered. However, this capability can be further developed.

Furthermore, some physical parameters such as impact of corrosion has not yet being considered in the sensitivity study and uncertainty quantification. The material corrosion mainly affects the chemical property, but not the interaction between neutron and nucleus. The interaction between neutron and nucleus will be changed only if there are nuclide transmutations. Therefore, the uncertainty from the corrosion will be mainly from the dimension and density of the fuel material for the application of DRF methodology. This study has been performed in chapter 7, but not from the material corrosion aspect. Further impact from the corrosion on the DRF methodology can be studied in the future.

Chapter 10

Conclusion

In this dissertation, the robustness of the DRF methodology on real-time radiation shielding calculations has been demonstrated. The DRF methodology is capable of performing radiation shielding calculations in order of seconds using 1 processor while the traditional approach, i.e. Monte Carlo + Deterministic method, requires hours or days using multiple processors. Excellent accuracy on the DRF methodology is also observed by both computational and experimental benchmark problems.

Identifying the non-sensitive parameters to the DRF coefficients is the aim point of this methodology. This is mainly because the low successive rate of radiation shielding problems. The detector/dosimeter located outside of nuclear system typically does not "see" into the system too far. Therefore, the radiation from the nuclear system penetrated through the shield will not carry too much information, and thus may not be sensitive to certain parameters. The study has shown that the three most important parameters are:

1. Detector/Dosimeter Type
2. Detector/Dosimeter Location
3. Radiation Source Spectrum

The pre-calculated DRF coefficient can be reused, translated, and interpolated to calculate accurate detector response/dosimeter response/dose value in order of seconds. Thus far, the DRF methodology has been applied on:

1. Commercial PWR RPV neutron fluence calculations
2. Experimental VENUS-3 RPV neutron fluence calculation benchmark problem
3. SNF Cask external dosimetry and detection

Excellent performances on both accuracy and calculation speed are observed using the DRF methodology. The DRF methodology is capable of calculating the dose value or detector/-dosimeter response with an order of seconds using 1 processor if the DRF coefficient database is appropriately prepared. Among all of the existing problems, the RPV neutron fluence calculation can be greatly benefited by the development of DRF methodology. Currently, most of U.S. commercial nuclear power plants are undergoing lifetime extension. For this, the neutron fluence calculation need to be performed at the structures other than the beltline region. The DRF methodology can accurately perform online prediction of the neutron fluence at RPV. In principle, the DRF methodology can be applied to any complex radiation shielding problem, such as medical radiation facilities.

Chapter 11

Future Work

I have identified some interesting potential topics for further research. Currently, the DRF methodology is very robust for neutron detection. Several works can be further performed to improve the photon detection. The DRF methodology can also further be used on solving inverse problem. This is very important from the nuclear non-proliferation aspect.

11.1 Photon Dosimetry

Due to the limited computation resources, the application of DRF methodology on photon source is performed with some approximations, such as grouping photon source for calculation of DRF coefficients. The following sections will identify the potential work for the application of DRF methodology on photon shielding problems.

11.1.1 Photon Source DRF Coefficients

According to the results from Appendix G, the resolution of photon DRF coefficients has to be further improved with finer mesh. This is mainly because the higher interaction rate of photons with material. Furthermore, the FOV and GC of the photon source are not yet well understood. This might be attributed to the significant ray effect on the photon importance function. A comprehensive and detailed study has to be performed.

11.1.2 Photon Source and Spectrum from Fuel Assemblies

Currently, the photon DRF coefficient sensitivity study is performed using spectrum and isotopic from a fixed specific power depletion calculation. Different combination of reac-

tor specific power and irradiation time can create different isotopic, and consequently have different photon spectrum. Therefore, investigation on this can be performed.

11.1.3 Photon Source from Structural Materials

From all the dose rate calculation in chapter 8, only the photons from the fuel pellets are considered. However, The photon source from the structure material, mainly ^{60}Co, is one of the importance source of photon dose. The ^{60}Co has a single photon emission peak at 1.173 MeV or 1.312 MeV. This can greatly reduce the complexity of implementation of the DRF methodology since no photon spectrum pre-calculation is needed. The main effort for this will be selection of unit photon source volume for the DRF coefficient calculations.

11.2 DRF Coefficient with No Detector/Dosimeter Type Dependency

Currently, the DRF coefficients are detector/dosimeter type dependent. However, the DRF coefficients can be obtained in a different form by

$$\alpha_{j,g} = \frac{\int_{V_d} dV \int_{E_g}^{E_{g-1}} dE \int_{4\pi} d\Omega \psi(\underline{r}, E, \hat{\Omega})}{\int_{V_j} dV' \int_0^{\infty} dE' \int_{4\pi} d\Omega' S(\underline{r}', E', \hat{\Omega}')} \tag{11.1}$$

where $\alpha_{j,g}$ is the DRF coefficient for energy group g with source location j, V_d is the detector/dosimeter volume, V_j is the radiation source volume, E_g and E_{g-1} are the lower and upper bounds of energy group g.

By doing this, the detector/dosimeter response can be calculated by

$$R_i = \sum_{j,g} \sigma_{i,g} \alpha_{j,g} S_j \tag{11.2}$$

where $\sigma_{i,g}$ is the detector/dosimeter cross-section of detector/dosimeter type i with energy group g, S_j is the radiation source at location j.

This approach has the benefit of reducing DRF coefficient database size by calculating them without dependency on detector/dosimeter type. However, longer computation time on the DRF coefficient will be required. This is mainly because the DRF coefficients are energy group dependent, and will require more number of sample for an acceptable statistical uncertainty. I have performed some preliminary study on the FOV and GC on this approach using the GBC-32 SNF cask. The results show that the FOV and GC for such arrangement are still very similar from what we have observed.

11.3 Automation of the FOV and GC Estimation

Currently, the FOV and GC calculations are semi-automated. User has to build the importance model for importance function calculations. The part that is automated currently is after importance functions are appropriately calculated. The FOV.f90 code in the *Dp*RAPID utility system is capable to calculate the FOV in the region of interest. It is flexible on determining the radiation source segment for identifying the detector/dosimeter contribution from it.

The part that need to be automated is building importance model. In principle, the user only need to prepare one Monte Carlo model for implementing the DRF methodology on the problem of interest. A utility code that convert the Monte Carlo model directly to importance model is needed for this. The A^{3}MCNP has this capability. However, the A^{3}MCNP is written based on MCNP4A and TORT code, and therefore is not appropriate for the current version of MCNP5 + PENTRAN^{TM}. The ADVANTG has the capability to generate MCNP5 readable weight window files. However, it is not very flexible from the user side to study certain things such as parameters for importance functions and lower weight window bounds. Therefore, development and investigation of this part can be performed.

11.4 Statistical Uncertainty Evaluation

Currently, all the DRF coefficients are obtained via statistical (Monte Carlo) approach. This means that a statistical uncertainty is calculated when obtaining a DRF coefficient. Moreover, the radiation source, mainly induced fission neutron source, are calculated using the FM approach. The FM coefficients are with their statistical uncertainty as well. Therefore, a comprehensive statistical uncertainty of dose or detector/dosimeter response calculated from the DRF methodology has to be evaluated. There is no direct solution on this. However, two possible approaches are:

1. Change the random seed for random number generator in a Monte Carlo code, and calculate a few sets of coefficient. A sample standard deviation for the calculated doses or detector/dosimeter responses can be calculated using different set of coefficients.

2. Using the statistical uncertainties of calculated coefficients to sample more sets of coefficient by assuming normal distribution.

The first approach will require significant computation resource while the second approach may not. However, it is still debatable if all the coefficients follow normal distribution. The second approach might be more affordable and conservative.

11.5 Iterative Scheme for SNF System Loading Pattern Search

Since the RAPID code system is currently capable of perform neutron source and detector/dosimeter response calculation rapidly, it is possible to utilize such powerful tool for determination of some information from SNF system. The primary purpose is for the nuclear nonproliferation.

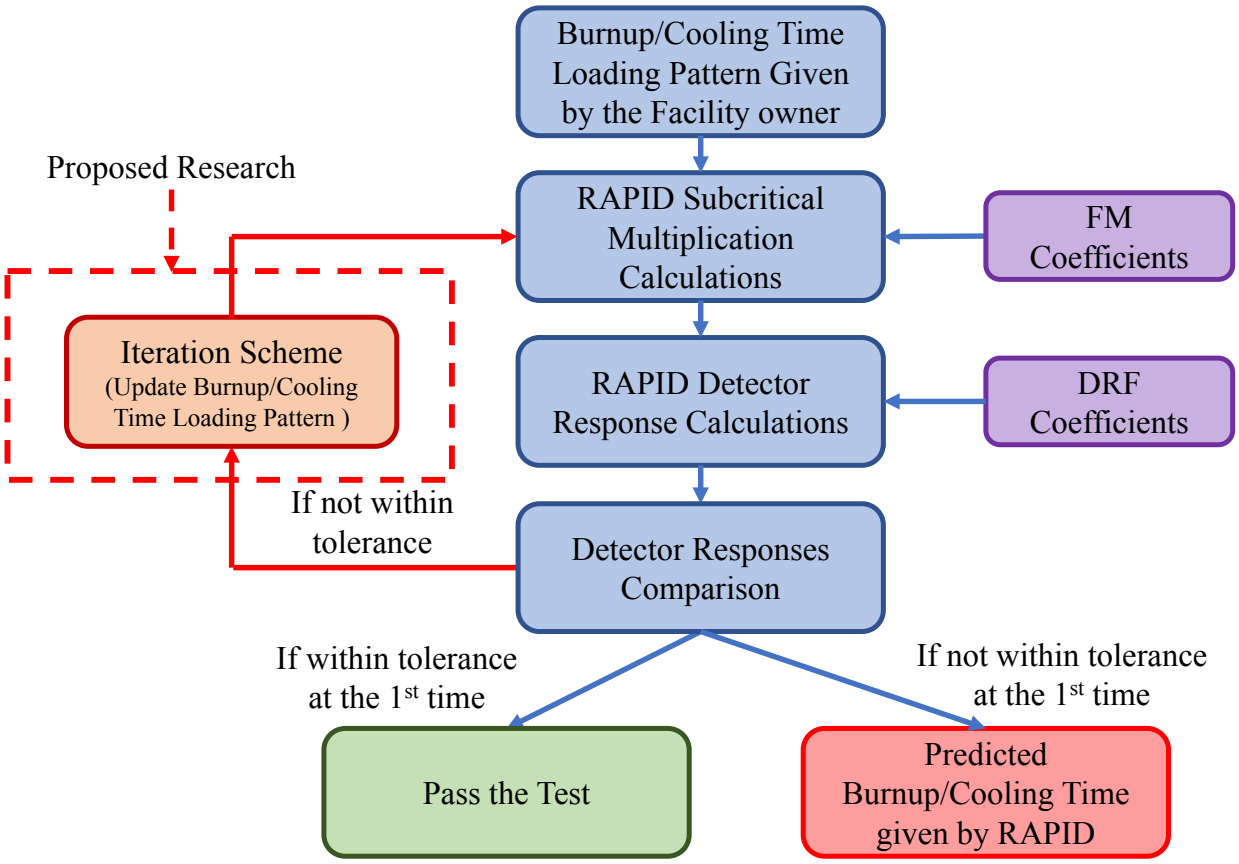

Figure 11.1 Potential Future Work: Iterative Scheme for SNF System Loading Pattern Search

With a relatively large system such as SNF pool or cask, it is almost impossible to use traditional Monte Carlo or deterministic approach to iteratively examine the burnup level and cooling time of every fuel assemblies. With current capability of the RAPID code system, I propose the procedure shown in the Fig. 11.1. The FM and DRF coefficients are pre-calculated and stored as database first. After that, we can compare the experimental detector/dosimeter response at multiple locations, and utilize techniques such as least square minimization to examine the results with RAPID calculated values. This can be performed

online currently. However, we can further develop an algorithm for iteratively searching the accurate burnup and cooling time values of each fuel assemblies. This will provide an excellent capability for organization such as International Atomic Energy Agency (IAEA) for the use of nuclear nonproliferation.

Bibliography

[1] S. Vidard, N. Jardin, and A. Donore. "EDF 3-Loop RPV Life Management Beyond 40 Years of Operation." `https://slideplayer.com/slide/13764096/` (2017).

[2] A. Haghighat. *Monte Carlo Methods for Particle Transport*. CRC Press (2016).

[3] N. Roskoff and W. Walters. *User Manual version 2: RAPID - Real Time Analysis for Particle Transport and In-situ Detection. Technical report*, Virginia Tech and Pennsylvania State University (2018).

[4] N. J. Roskoff. *Development of a Novel Fuel Burnup Methodology and Algorithm in RAPID and its Benchmarking and Automation*. Ph.D. thesis, Virginia Tech (2018).

[5] L. Leenders. *LWR-PVS Benchmark Experiment VENUS-3. Technical report*, FCP/VEN/01 Report (1988).

[6] "Table of Nuclides." `http://atom.kaeri.re.kr:8080/ton/index.html`. Accessed: 2019-06-18.

[7] R. Lefebvre *et al.* "Development of Streamlined Nuclear Safety Analysis Tool for Spent Nuclear Fuel Applications." *Nuclear Technology*, **199(3)**: pp. 227–244 (2017).

[8] A. International. *Annual Book of ASTM Standards: Nuclear, Solar and Geothermal Energy*. ASTM International (2002).

[9] E. E. Lewis and W. F. Miller. "Computational Methods of Neutron Transport." (1984).

[10] U. N. R. Commission *et al. Regulatory Guide 1.190: Calculational and Dosimetry Methods for Determining Pressure Vessel Neutron Fluence*. US Nuclear Regulatory Commission, Office of Nuclear Regulatory Research (2001).

[11] OECD/NEA. "Prediction of neutron Embrittlement in the Reactor Pressure Vessel: Venus-l and Venus-3 Benchmarks." (2000).

[12] W. W. Engle Jr. *A Users Manual for ANISN: A One Dimensional Discrete Ordinate Transport Code with Anisotropic Scattering. Technical report*, Oak Ridge Gaseous Diffusion Plant, Tennessee (1967).

[13] R. D. O'Dell, F. W. Brinkley Jr, and D. R. Marr. *User's manual for ONEDANT: A Code Package for One-dimensional, Diffusion-accelerated, Neutral-particle Transport. Technical report*, Los Alamos Scientific Laboratory (1982).

[14] T. Hill. *ONETRAN: A Discrete Ordinates Finite Element Code for the Solution of the One-dimensional Multigroup Transport Equation. Technical report*, Los Alamos Scientific Laboratory, New Mexico (USA) (1975).

[15] W. Rhoades and R. Childs. *Updated Version of the DOT 4 One- and Two-dimensional Neutron/Photon Transport Code. Technical report*, Oak Ridge National Lab., TN (USA) (1982).

[16] K. Lathrop and F. Brinkley. *TWOTRAN-II: An Interfaced, Exportable Version of the TWOTRAN Code for Two-dimensional Transport. Technical report*, Los Alamos Scientific Laboratory, New Mexico (USA) (1973).

[17] W. F. Walters, R. D. O'Dell, and F. W. Brinkley Jr. *THREETRAN (Hex, Z) Users' Manual. Technical report*, Los Alamos Scientific Laboratory (1979).

[18] W. A. Rhoades and D. Simpson. *The TORT Three-Dimensional Discrete Ordinates Neutron/Photon Transport Code (TORT version 3). Technical report*, Oak Ridge National Laboratory, TN (United States) (1997).

[19] R. E. Alcouffe *et al.* "PARTISN: A Time-dependent, Parallel Neutral Particle Transport Code System." *Los Alamos National Laboratory, LA-UR-05-3925 (May 2005)* (2005).

[20] C. Yi. *TITAN: A 3-D Deterministic Radiation Transport Code, TITAN User Manual Version 1.05.* Ph.D. thesis, University of Florida (2009).

[21] G. Sjoden and A. Haghighat. "PENTRAN: A Three-dimensional Scalable Transport Code with Complete Phase-space Decomposition." *Transactions of the American Nuclear Society*, **74**: pp. 181–183 (1996).

[22] T. M. Evans *et al.* "Denovo: A New Three-dimensional Parallel Discrete Ordinates Code in SCALE." *Nuclear Technology*, **171(2)**: pp. 171–200 (2010).

[23] R. E. Alcouffe. *THREEDANT: A Code to Perform Three-dimensional, Neutral Particle Transport Calculations. Technical report*, Los Alamos National Laboratory (1994).

[24] G. E. Sjoden. *PENTRAN: A Parallel 3-D S_N Transport Code with Complete Phase Space Decomposition, Adaptive Differencing, and Iterative Solution Methods.* Ph.D. thesis, The Pennsylvania State University (1998).

[25] K. Lathrop. "Spatial Differencing of the Transport Equation: Positivity vs. Accuracy." *Journal of Computational Physics*, **4(4)**: pp. 475–498 (1969).

[26] B. G. Petrović and A. Haghighat. "Effects of S_N Method Numerics on Pressure Vessel Neutron Fluence Calculations." *Nuclear Science and Engineering*, **122(2)**: pp. 167–193 (1996).

[27] B. Petrović. *Development of a Directional θ-weighted Sn Differencing Scheme for Shielding Applications*. Ph.D. thesis, Pennsylvania State University (1995).

[28] G. E. Sjoden and A. Haghighat. "The Exponential Directional Weighted (EDW) S_N Differencing Scheme in 3-D Cartesian Geometry." In: *Proc. Joint Int. Conf. on Mathematical Methods and Supercomputing for Nuclear Applications, Saratoga Springs, New York, Oct. 5-9, 1997*, volume 2, (p. 1267) (1997).

[29] G. E. Sjoden. "An Efficient Exponential Directional Iterative Differencing Scheme for Three-Dimensional S_N Computations in XYZ Geometry." *Nuclear Science and Engineering*, **155(2)**: pp. 179–189 (2007).

[30] W. Walters and A. Haghighat. "Development of The Adaptive Collision Source (ACS) Method for Discrete Ordinates." In: *International Conference on Mathematics and Computational Methods Applied to Nuclear Science and Engineering, M&C 2013*, (pp. 2339–2349) (2013).

[31] G. Longoni. *Advanced Quadrature Sets, Acceleration and Preconditioning Techniques for the Discrete Ordinates Method in Parallel Computing Environments*. Ph.D. thesis, University of Florida (2004).

[32] J. J. Jarrell. *An Adaptive Angular Discretization Method for Neutral-particle Transport in Three-dimensional Geometries*. Ph.D. thesis, Texas A&M University (2010).

[33] J. J. Duderstadt. *Nuclear Reactor Aanalysis*. John Wiley & Sons (1976).

[34] F. A. Alpan. *An Advanced Methodology for Generating Multigroup Cross-sections for Shielding Calculations*. Ph.D. thesis, Pennsylvania State University (2003).

[35] J. Mattingly *et al. Computationally Optimized Multi-group Cross-section Data Colapsing Using the YGROUP Code. Technical report*, Sandia National Laboratory (2009).

[36] C. Yi *et al.* "Computationally Optimized Multi-group Cross section Data Collapsing Using the YGROUP Code-087." (2010).

[37] J. C. Wagner and A. Haghighat. "Automated Variance Reduction of Monte Carlo Shielding Calculations Using the Discrete Ordinates Adjoint Function." *Nuclear Science and Engineering*, **128(2)**: pp. 186–208 (1998).

[38] H. Louvin. *Development of an adaptive variance reduction technique for Monte Carlo particle transport*. Ph.D. thesis, Université Paris-Saclay (2017).

[39] H. Louvin *et al.* "Adaptive Multilevel Splitting for Monte Carlo Particle Transport." In: *EPJ Web of Conferences*, volume 153, (p. 06006). EDP Sciences (2017).

[40] J. Leppänen. *Serpent – a Continuous-energy Monte Carlo Reactor Physics Burnup Calculation Code* (2015).

[41] X-5 Monte Carlo Team. "MCNP—A General N-Particle Transport Code, Version 5." (2003).

[42] P. Miller *et al.* "The Use of an Inbuilt Importance Generator for Acceleration of the Monte Carlo Code MCBEND." In: *The Physics of Reactors: Operation, Design and Computation. Volume 3* (1990).

[43] K. A. Van Riper, T. J. Urbatsch, and P. D. Soran. *AVATAR–Automatic variance reduction in Monte Carlo Calculations. Technical report*, Los Alamos National Laboratory (1997).

[44] A. Haghighat and J. C. Wagner. "Application of A^3 MCNP^{TM} to Radiation Shielding Problems." In: *Advanced Monte Carlo for Radiation Physics, Particle Transport Simulation and Applications*, (pp. 619–624). Springer (2001).

[45] A. Haghighat *et al.* "Performance of the Automated Adjoint Accelerated MCNP (A^3MCNP) for Simulation of a BWR Core Shroud Problem." In: *Proceedings of the International Conference on Mathematics and Computation, Reactor Physics, and Environmental Analysis in Nuclear Applications*, (p. 1381) (1999).

[46] Y. Miyake *et al.* "Improvement of Monte Carlo Code A^3MCNP for Large-Scale Shielding Problems." *Journal of Nuclear Science and Technology*, **41**: pp. 93–96 (2004).

[47] A. Haghighat, H. Hiruta, and B. Petrović. "Performance of A^3MCNP^{TM} for Calculation of 3-D Neutron Flux Distribution in a BWR Core Shroud." In: *Reactor Dosimetry: Radiation Metrology and Assessment*. ASTM International (2001).

[48] T. Booth, K. Kelley, and S. McCready. "Monte Carlo Variance Reduction Using Nested DXTRAN Spheres." *Nuclear Technology*, **168(3)**: pp. 765–767 (2009).

[49] S. W. Mosher *et al.* "ADVANTG: An Automated Variance Reduction Parameter Generator." *ORNL/TM-2013/416, Oak Ridge National Laboratory* (2013).

[50] J. C. Wagner, D. E. Peplow, and S. W. Mosher. "FW-CADIS method for Global and Regional Variance Reduction of Monte Carlo Radiation Transport Calculations." *Nuclear Science and Engineering*, **176(1)**: pp. 37–57 (2014).

[51] M. Munk and R. N. Slaybaugh. "Review of Hybrid Methods for Deep-Penetration Neutron Transport." *Nuclear Science and Engineering*, (pp. 1–35) (2019).

[52] M. Brovchenko *et al.* "On the use of Different Variance Reduction Techniques Within MCNP to Calculate the Flux on the Concrete Walls of a Pressurized Water Reactor." In: *International Conference on Mathematics and Computational Methods Applied to Nuclear Science and Engineering, M&C 2019* (2019).

[53] W. Walters *et al.* "Development of INSPECT-S for Inspection of Spent Fuel Pool." In: *Reactor Dosimetry: 14th International Symposium*. ASTM International (2012).

[54] A. Haghighat *et al.* "Development of AIMS Hybrid Tool for Active Interrogation." In: *INMM 54th Annual Meeting* (2010).

[55] A. Haghighat, K. Royston, and W. Walters. "MRT Methodologies for Real-time Simulation of Nonproliferation and Safeguards Problems." *Annals of Nuclear Energy (Oxford)*, **87(Part 1)**: pp. 61–67 (2016).

[56] W. J. Walters, N. J. Roskoff, and A. Haghighat. "The RAPID Fission Matrix Approach to Reactor Core Criticality Calculations." *Nuclear Science and Engineering*, **192(1)**: pp. 21–39 (2018).

[57] D. Zhang and F. Rahnema. "An Efficient Hybrid Stochastic/Deterministic Coarse Mesh Neutron Transport Method." *Annals of Nuclear Energy*, **41**: pp. 1–11 (2012).

[58] G. I. Bell and S. Glasstone. *Nuclear Reactor Theory. Technical report*, US Atomic Energy Commission, Washington, DC (United States) (1970).

[59] J. J. Duderstadt and W. R. Martin. *Transport Theory*. John Wiley & Sons (1979).

[60] O. Klein and Y. Nishina. "Über die Streuung von Strahlung durch freie Elektronen nach der neuen relativistischen Quantendynamik von Dirac." *Zeitschrift für Physik*, **52(11-12)**: pp. 853–868 (1929).

[61] R. Alcouffe and E. Larsen. *Review of Characteristic Methods Used to Solve the Linear Transport Equation. Technical report*, Los Alamos Scientific Laboratory, NM (USA) (1981).

[62] J. E. White *et al. BUGLE-96: A Revised Multigroup Cross-section Library for LWR Applications Based on ENDF/B-VI release 3. Technical report*, Oak Ridge National Laboratory (1996).

[63] J. Aull. *Stability of the Mesh-cornered Synthetic Method of Diffusion Acceleration of the DOT-IV Transport Code. Technical report*, Oak Ridge National Laboratory (1979).

[64] M. H. Kalos and P. A. Whitlock. *Monte Carlo Methods*. John Wiley & Sons (2009).

[65] J. Spanier and E. M. Gelbard. *Monte Carlo Principles and Neutron Transport Problems*. Courier Corporation (2008).

[66] B. T. Mervin *et al.* "Uncertainty Underprediction in Monte Carlo Eigenvalue Calculations." *Nuclear Science and Engineering*, **173(3)**: pp. 276–292 (2013).

[67] M. Wenner and A. Haghighat. "A Combined Diagnostic Approach for Monte Carlo Source Convergence Identification." (2009).

[68] M. T. Wenner. *Development of New Source Diagnostic Methods and Variance Reduction Techniques for Monte Carlo Eigenvalue Problems with a Focus on High Dominanceratio Problems*. Ph.D. thesis, University of Florida (2010).

[69] C. M. Perfetti, B. T. Rearden, and W. J. Marshall. "Diagnosing Undersampling Biases in Monte Carlo Eigenvalue and Flux Tally Estimates." *Nuclear Science and Engineering*, **185(1)**: pp. 139–158 (2017).

[70] M. Wenner and A. Haghighat. "A Fission Matrix Based Methodology for Achieving an Unbiased Solution for Eigenvalue Monte Carlo Simulations." *Progress in Nuclear Science and Technology*, **2**: pp. 886–892 (2011).

[71] K. Morton. *Criticality Calculations by Monte Carlo Methods. Technical report*, Great Britain Atomic Energy Research Establishment, Harwell, Berks, England (1956).

[72] G. Birkhoff and R. S. Varga. "Reactor Criticality and Nonnegative Matrices." *Journal of the Society for Industrial and Applied Mathematics*, **6(4)**: pp. 354–377 (1958).

[73] J. Hammersley and D. Handscomb. "Monte Carlo Methods, Methuen & CO." *Ltd., London*, **40** (1964).

[74] S. Carney *et al.* "Theory and Applications of the Fission Matrix Method for Continuous-energy Monte Carlo." *Annals of Nuclear Energy*, **73**: pp. 423–431 (2014).

[75] T. Kitada and T. Takeda. "Effective Convergence of Fission Source Distribution in Monte Carlo Simulation." *Journal of Nuclear Science and Technology*, **38(5)**: pp. 324–329 (2001).

[76] S. E. Carney *et al. Fission Matrix Capability for MCNP Monte Carlo. Technical report*, Los Alamos National Laboratory (LANL), Los Alamos, NM (United States) (2012).

[77] J. Dufek and W. Gudowski. "Fission Matrix Based Monte Carlo Criticality Calculations." *Annals of Nuclear Energy*, **36(8)**: pp. 1270–1275 (2009).

[78] W. Walters, N. Roskoff, and A. Haghighat. "A Fission Matrix Approach to Calculate Pin-wise 3D Fission Density Distribution." *Proceeding of Joint International Conference on Mathematics and Computation (M&C), Supercomputing in Nuclear Applications (SNA) and the Monte Carlo (MC) Method* (2015).

[79] N. Roskoff and A. Haghighat. "Development of A Novel Fuel Burnup Methodology Using the RAPID Practical Transport Code System." In: *Proceedings of PHYSOR* (2018).

[80] V. Mascolino and A. Haghighat. "Validation of the Transient Fission Matrix Code ^{t}RAPID Against the FLATTOP Benchmark." In: *International Conference on Mathematics and Computational Methods Applied to Nuclear Science and Engineering, M&C 2019* (2019).

[81] N. Roskoff, V. Mascolino, and A. Haghighat. "Accuracy of RAPID for Simulation of Pools with Diverse Spent Fuels." In: *Proceedings of PHYSOR* (2018).

[82] V. Mascolino, A. Haghighat, and N. J. Roskoff. "Evaluation of RAPID for A UNF Cask Benchmark Problem." In: *EPJ Web of Conferences*, volume 153, (p. 05025). EDP Sciences (2017).

[83] V. Mascolino, N. Roskoff, and A. Haghighat. "Benchmarking of the RAPID Code System Using the GBC-32 Cask with Variable Burnups." In: *Proceedings of PHYSOR* (2018).

[84] N. J. Roskoff *et al.* "Benchmarking of the RAPID Tool for a Subcritical Facility." *Proceeding of 57th INMM Annual Meeting*, (pp. 24–28) (2016).

[85] V. Mascolino *et al.* "Experimental and Computational Benchmarking of RAPID Using the JSI TRIGA Mark-II Reactor." In: *International Conference on Mathematics and Computational Methods Applied to Nuclear Science and Engineering, M&C 2019* (2019).

[86] S. Van Der Walt, S. C. Colbert, and G. Varoquaux. "The NumPy Array: A Structure for Efficient Numerical Computation." *Computing in Science & Engineering*, **13(2)**: p. 22 (2011).

[87] D. He and W. J. Walters. "A New Fission Matrix Correction Method to Estimate the Source Distribution in Nuclear Reactor Core." In: *Proceedings of PHYSOR* (2018).

[88] J. Butler. "Benchmarking of the RAPID Eigenvalue Algorithm Using the ICSBEP Handbook." (2019).

[89] S. Saito, T. Tanaka, and Y. Sudo. *Design of high temperature engineering test reactor (HTTR). Technical report*, Japan Atomic Energy Research Institution (1994).

[90] P. N. Haubenreich and J. Engel. "Experience with the Molten-salt Reactor Experiment." *Nuclear Applications and Technology*, **8(2)**: pp. 118–136 (1970).

[91] A. Koster, H. Matzner, and D. Nicholsi. "PBMR Design for the Future." *Nuclear Engineering and Design*, **222(2-3)**: pp. 231–245 (2003).

[92] N. Cerullo and G. Lomonaco IV. "Generation IV Reactor Designs, Operation and Fuel Cycle." *Nuclear Fuel Cycle Science and Engineering; Crossland, I., Ed.; Woodhead Publishing: Cambridge, UK*, (pp. 333–395) (2012).

[93] J. Bartel. "Development of 2D Pin-wise Burnup and Time Dependent Boundary Correction Algorithms in RAPID." (2019).

[94] K. O. Ott and R. J. Neuhold. *Introductory Nuclear Reactor Dynamics*. American Nuclear Society (1985).

[95] A. Laureau *et al.* "Transient Fission Matrix: Kinetic Calculation and Kinetic Parameters βeff and Λeff Calculation." *Annals of Nuclear Energy*, **85**: pp. 1035–1044 (2015).

[96] J. C. Wagner, A. Haghighat, and B. G. Petrović. "Monte Carlo Transport Calculations and Analysis for Reactor Pressure Vessel Neutron Fluence." *Nuclear technology*, **114(3)**: pp. 373–398 (1996).

[97] B. L. Broadhead *et al. Investigation of Nuclide Importance to Functional Requirements Related to Transport and Long-Term Storage of LWR Spent Fuel. Technical report*, Oak Ridge National Laboratory (1995).

[98] M.-J. Wang and A. Haghighat. "A Novel Detector Response Formulation for RAPID." In: *Proceedings of PHYSOR* (2018).

[99] J. Wagner. *Computational Benchmark for Estimation of Reactivity Margin from Fission Products and Minor Actinides in PWR Burnup Credit. Technical report*, Oak Ridge National Laboratory (2001).

[100] M. A. Jessee and M. DeHart. "Triton: A Multipurpose Transport, Depletion, and Sensitivity and Uncertainty Analysis Module." *Oak Ridge National Laboratory, ORNL/TM-2005/39 Version*, **6** (2011).

[101] M. Jessee and M. DeHart. "NEWT: A New Transport Algorithm for Two-dimensional Discrete-ordinates Analysis in Non-orthogonal Geometries." *Oak Ridge National Laboratory* (2011).

[102] I. Gauld. "ORIGEN-S: Depletion Module to Calculate Neutron Activation, Actinide Transmutation, Fission Product Generation, and Radiation Source Terms." *Oak Ridge National Laboratory, Oak Ridge, Tennessee*, (pp. 37831–36170) (2011).

[103] W. B. Wilson *et al.* "Sources: A Code for Calculating (α, n), Spontaneous Fission, and Delayed Neutron Sources and Spectra." *Radiation Protection Dosimetry*, **115(1-4)**: pp. 117–121 (2005).

[104] B. Watt. "Energy Spectrum of Neutrons from Thermal Fission of U^{235}." *Physical Review*, **87(6)**: p. 1037 (1952).

[105] I. Kodeli, E. Sartori, and B. Kirk. "SINBAD Shielding Benchmark Experiments Status and Planned Activities." In: *The American Nuclear Society's 14th Biennial Topical Meeting of the Radiation Protection and Shielding Division, Carlsbad New Mexico, USA*, (pp. 3–6). Citeseer (2006).

[106] US Nuclear Regulatory Commission. "Three mile island nuclear station, unit 1." `https://www.nrc.gov/info-finder/reactors/tmi1.html`.

[107] W. Weihermiller and G. Allison. *LWR Nuclear Fuel Bundle Data for Use in Fuel Bundle Handling. Technical report*, Battelle Pacific Northwest Labs., Richland, WA (USA) (1979).

[108] J. E. Hoogenboom, W. R. Martin, and B. Petrovic. "Monte Carlo Performance Benchmark for Detailed Power Density Calculation in a Full Size Reactor Core Benchmark Specifications." *Ann Arbor*, **1001**: pp. 48109–2104 (2010).

[109] R. Rulko. *Computing Radiation Dose to Reactor Pressure Vessel and Internals. Technical report*, NEA/NSC/DOC (96) 5, 1997, OECD-NEA (1997).

[110] C. English *et al.* "Approach and Methodology for Condition Assessment of Thermal Reactor Pressure Vessels." *International Journal of Pressure Vessels and Piping*, **54(1-2)**: pp. 49–87 (1993).

[111] US Nuclear Regulatory Commission and Others. *Recommendations for Addressing Axial Burnup in PWR Burnup Credit Analysis. Technical report*, NUREG/CR-6801.

[112] R. J. McConn *et al. Compendium of Material Composition Data for Radiation Transport Modeling. Technical report*, Pacific Northwest National Laboratory, Richland, WA (United States) (2011).

[113] K. Ivanov *et al. Benchmarks for Uncertainty Analysis in Modelling (UAM) for the Design, Operation and Safety Analysis of LWRs-Volume I: Specification and Support Data for Neutronics Cases (Phase I). Technical report*, Organisation for Economic Co-Operation and Development (2013).

[114] U. Fischer *et al. Monte Carlo Uncertainty Analysis for an Iron Shielding Benchmark Experiment. Technical report* (1999).

[115] Oak Ridge National Laboratory. "TITAN - Advancing the Era of Accelerated Computing." `https://www.olcf.ornl.gov/olcf-resources/compute-systems/titan/` (2019).

[116] W. A. Wieselquist *et al.* "ORIGAMI Automator Primer: Automated ORIGEN Source Terms and Spent Fuel Storage Pool Analysis." *ORNL/TM-2015/409, Oak Ridge National Laboratory* (2016).

[117] S. M. Bowman. "SCALE 6: Comprehensive Nuclear Safety Analysis Code System." *Nuclear technology*, **174(2)**: pp. 126–148 (2011).

[118] N. Soppera *et al.* "JANIS: NEA JAva-based Nuclear Data Information System." In: *EPJ Web of Conferences*, volume 146, (p. 07006). EDP Sciences (2017).

[119] A. Croff, R. Haese, and N. B. Gove. *Updated Decay and Photon Libraries for the ORIGEN Code. Technical report*, Oak Ridge National Laboratory (1979).

[120] J. B. Clarity *et al.* "As-Loaded Criticality Margin Assessment of Dual-Purpose Canisters Using UNF-ST&DARDS." *Nuclear Technology*, **199(3)**: pp. 245–275 (2017).

Appendices

Appendix A

Performance of the CADIS methodology by Importance Function Quality

In this section, three PENTRAN^{TM} importance function models with different levels of mesh refinement are used to calculate different level of importance function quality. Fig. A.1, A.2, and A.3 show the mesh distribution of the three models. Note that the purple materials are homogeneous UO_2 fuel and water , the green material is the stainless steel cask, the blue material is water the yellow material is air, the red material is ^{3}He detector. The mesh sizes of the meshes are minimal 1.25 cm and maximum 10 cm for model 1, minimal 0.625 cm and maximum 5 cm for model 2, minimal 0.3125 cm and maximum 2.5 cm for model 3, respectively. The cross-section and convergence criteria selected here are all the same as section 5.3.

The MCNP5 model prepared for DRF coefficients calculations are shown in the Fig. A.4. Only the fuel assembly 6 with FA segment 1 is selected for this study. The number of particles used for all the calculations are 10^6. The calculated DRF coefficients and their corresponding 1 statistical uncertainties (1σ) are shown in the Fig. A.5, A.6, and A.7.

By the first glance, it is obvious that the DRF coefficients of model 1 is much less smoother than model 2 and 3. Furthermore, the statistical uncertainties of model 1 is from 6% to 25% with an average of 6.8%. Therefore, it is clear that the DRF coefficients of model 1 has not converged due to lower quality of importance function.

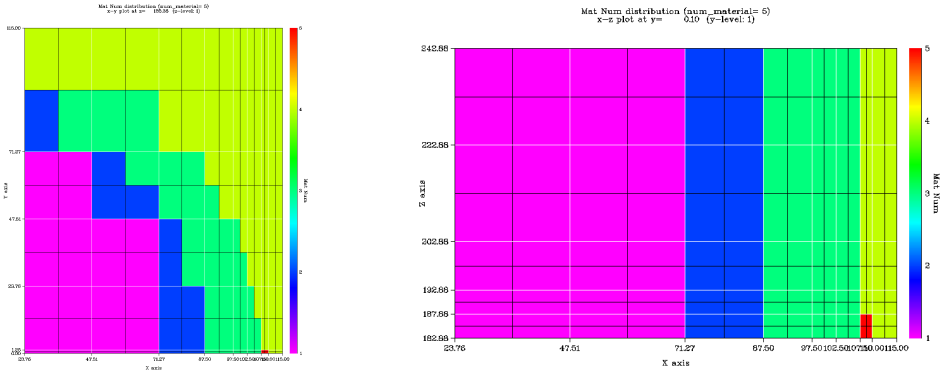

(a) Radial Projection **(b)** Axial Projection

Figure A.1 Model 1 Mesh Distribution

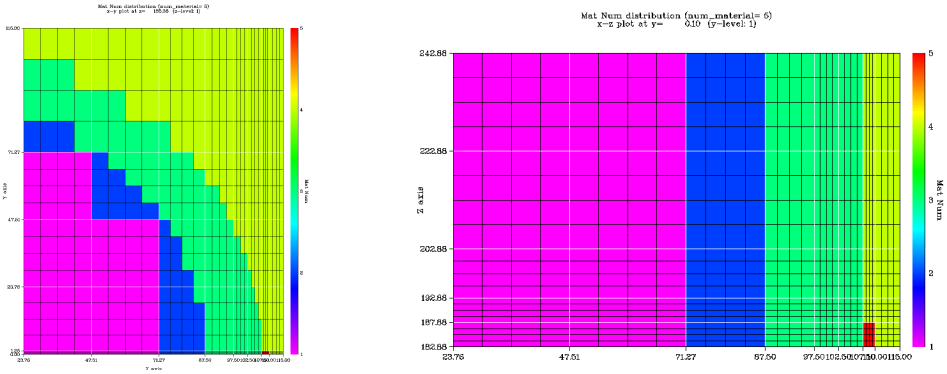

(a) Radial Projection **(b)** Axial Projection

Figure A.2 Model 2 Mesh Distribution

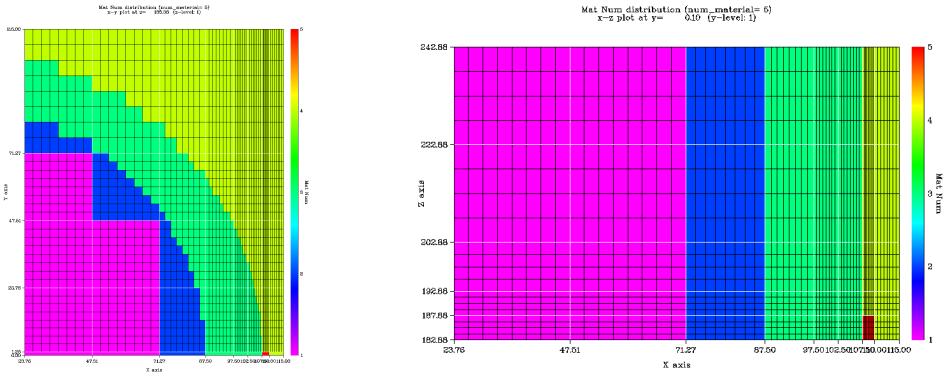

(a) Radial Projection **(b)** Axial Projection

Figure A.3 Model 3 Mesh Distribution

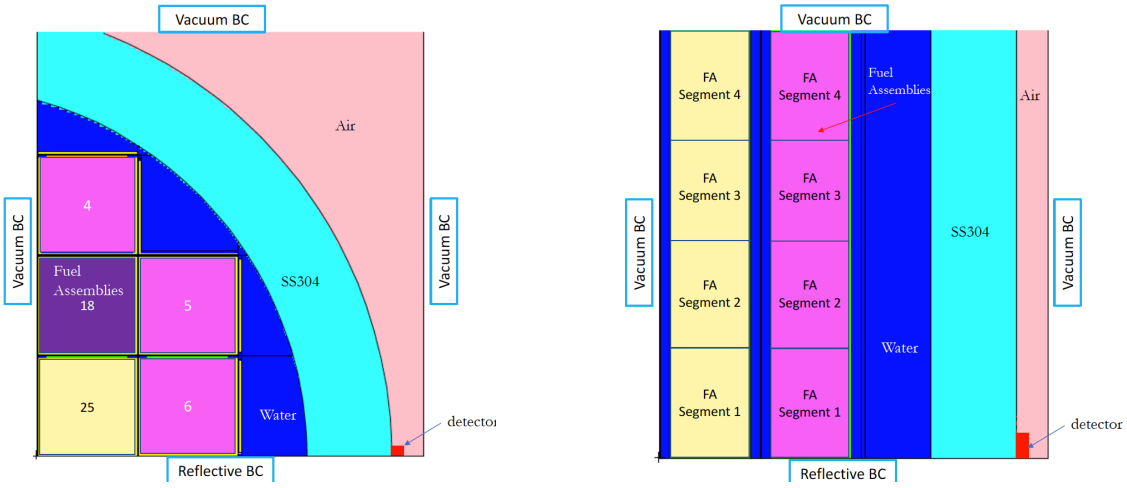

(a) Radial Projection **(b)** Axial Projection

Figure A.4 MCNP5 Model

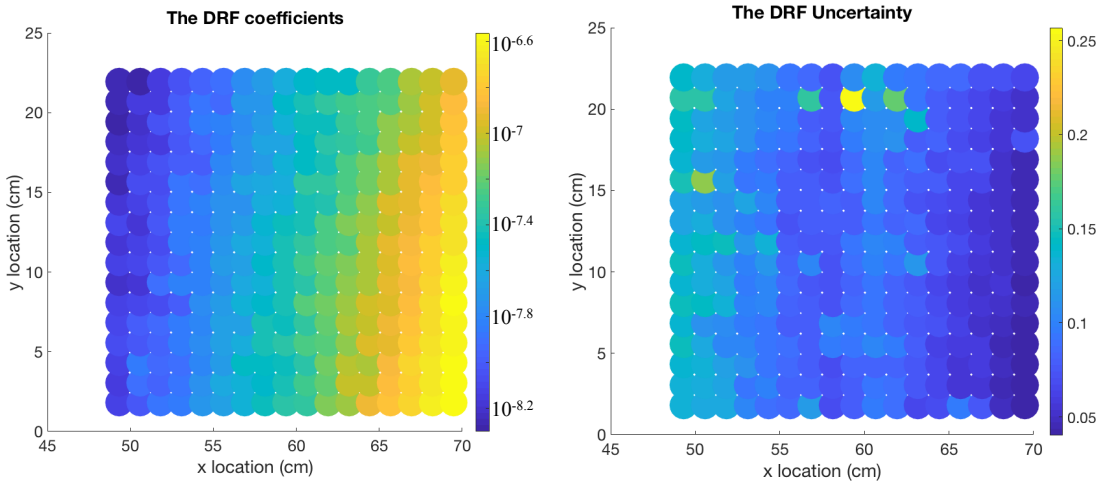

(a) DRF Coefficients **(b)** 1σ of DRF Coefficients

Figure A.5 Model 1

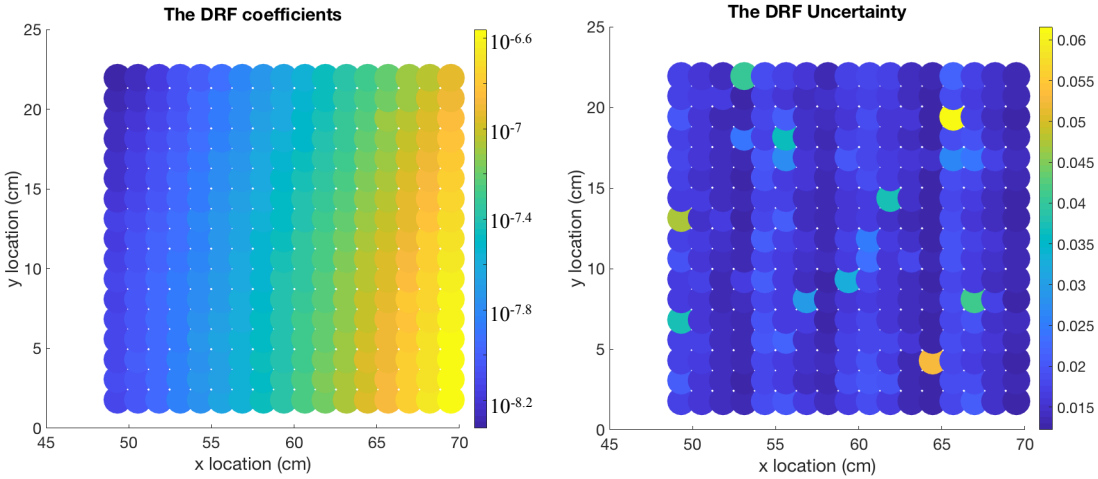

(a) DRF Coefficients **(b)** 1σ of DRF Coefficients

Figure A.6 Model 2

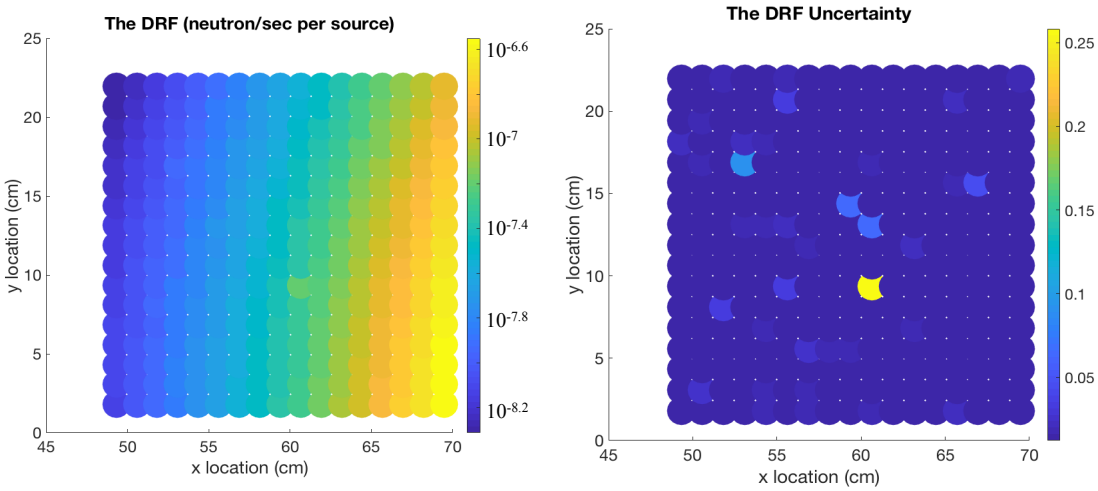

(a) DRF Coefficients **(b)** 1σ of DRF Coefficients

Figure A.7 Model 3

Appendix B

FOV and GC Study for ^{3}He Detector on the GBC-32 SNF Cask

In the chapter 5, the ^{3}He detector responses at two locations (azimuthal angle of 0° and 45°) are calculated using the DRF coefficients. However, sensitivity of ^{3}He detector locations and sizes on FOV and GC are not discussed. This investigation is important and necessary to effectively calculate the DRF coefficients. For convenience, the selected detector locations and their corresponding labels with assembly labels are shown in the Fig. B.1 and B.2. Note that the reference, case 1 and 2 are located at azimuthal angle of 0°. The case 5 and 6 are located at 45° while case 3 and 4 are located at 67.5°.

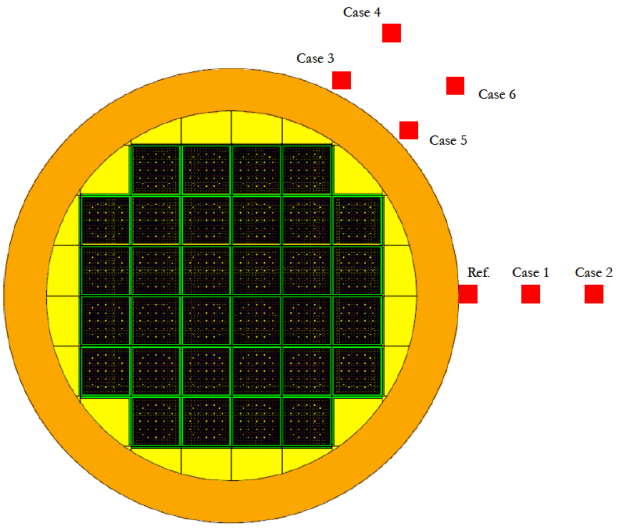

Figure B.1 Selected Detector Azimuthal Locations

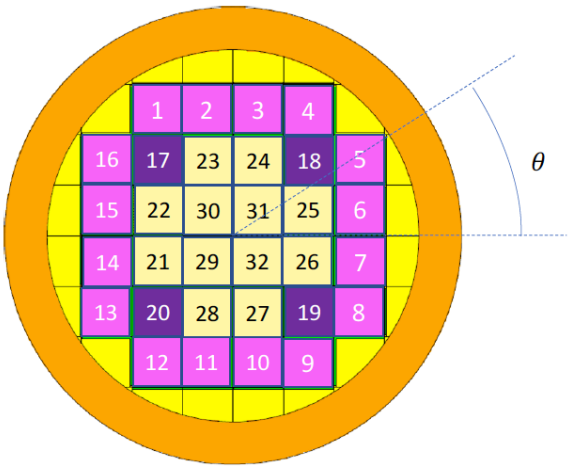

Figure B.2 Label of Fuel Assemblies

B.1 Field of View

By using the Eq.(5.4), the calculated FOV for the 7 detector locations are shown in the Table B.1.

Table B.1 Field of View for Different ^{3}He Detector Locations

Case	% of Detector Response	Fuel Assemblies Included (ID refer to Fig. B.2)
Reference	97.8	5 6 7 8
1	97.5	5 6 7 8
2	97.5	5 6 7 8
3	97.4	3 4 5 6
4	95.7	3 4 5 6
5	95.3	3 4 5 6
6	97.2	3 4 5 6 18

Note that the detector sizes are also varied from 2.5cm×2.5cm×10cm to 10cm×10cm×30cm. The changes are negligible if the detector location is the same. The results show that the ^{3}He detector FOV is :

- Not sensitive to the detector size.
- Not sensitive to the distance from the SNF cask surface if azimuthal location is fixed

B.2 Group-wised Contribution

Fig. B.3 shows the GC for different sizes of ^{3}He Detectors located at 0°.

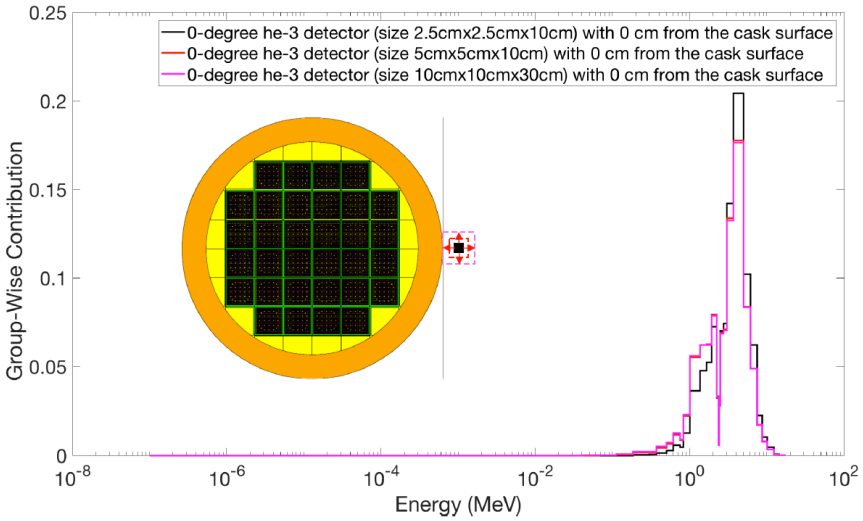

Figure B.3 GC for Different Sizes of ^{3}He Detectors

The results show that little change is observed when enlarging the detector size. Small increase from relative lower energy neutron if detector is enlarged. However, the cutoff energy is still around 0.5 MeV for all the cases with detector located at 0°. Fig. B.4 shows the GC for detector with different distances to the surface of the SNF cask.

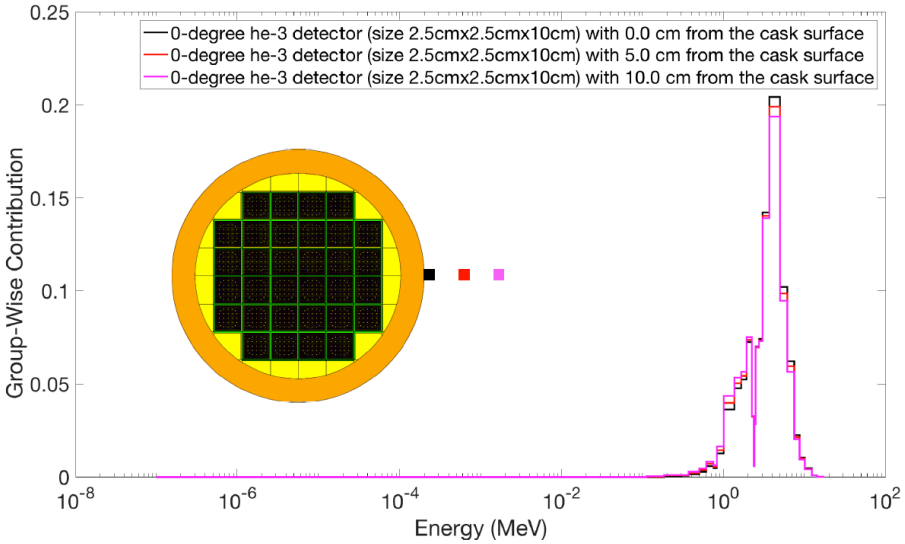

Figure B.4 GC for Different Distances to the Surface of SNF Cask of ^{3}He Detectors

Negligible effect is observed by different distances. This is mainly because the low interaction between neutron and air. Figs. B.5 and B.6 show the GC for different azimuthal detector locations.

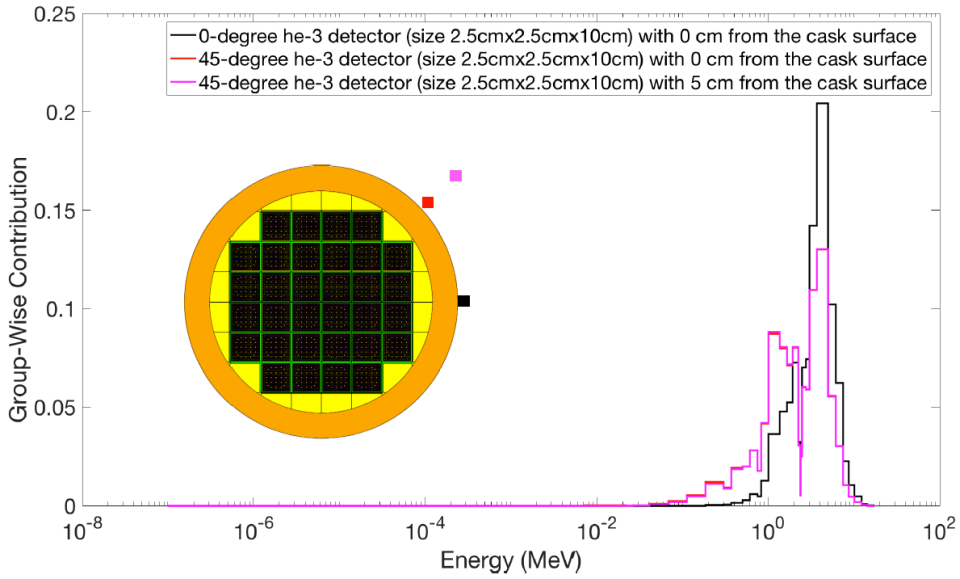

Figure B.5 GC for Different Angles of ^{3}He Detectors - 1

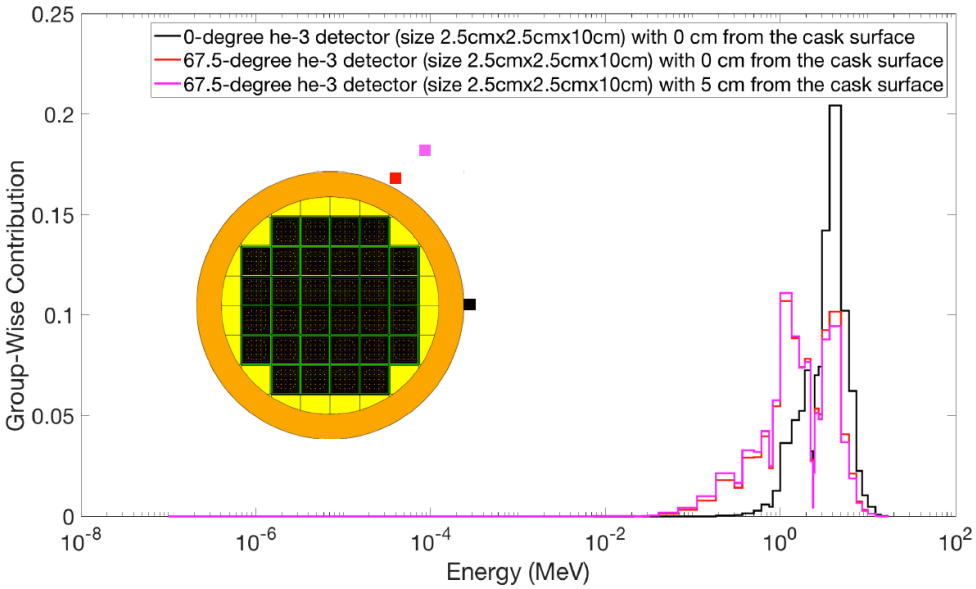

Figure B.6 GC for Different Angles of ^{3}He Detectors - 2

the results show that relative lower energy neutrons have more contribution for detector located at 45° and 67.5°. This is mainly because the detectors are closer to the fuel assemblies. Also, with thinner water gap between the detectors and fuel assemblies, neutron with lower

energy will be more likely to penetrate through shield and contribute to detector responses. The cutoff energy drops from 0.5 MeV to 0.02 MeV in this case. Therefore, with SNF flooded with water, the cutoff neutron energy for ^{3}He detector response calculation can be set at 0.02 MeV.

Appendix C

VENUS-3 Benchmark Problem: More Importance Functions

In the Chapter 6, we have discussed the importance function with FOV, GC, and lower weight window bounds calculation for the $^{115}\text{In}(n,n')$ dosimeter at z =131.5 cm. In this appendix, the other two locations will be discussed.

C.0.1 Importance Model and Meshes

For the radial mesh distributions, all of the three dosimeter locations are same as shown in the Fig. 6.4a. Fig. C.1 and C.2 show the axial projection for the PENTRAN^{TM} importance model with dosimeter location at z=114.5 and 145.5 cm, respectively.

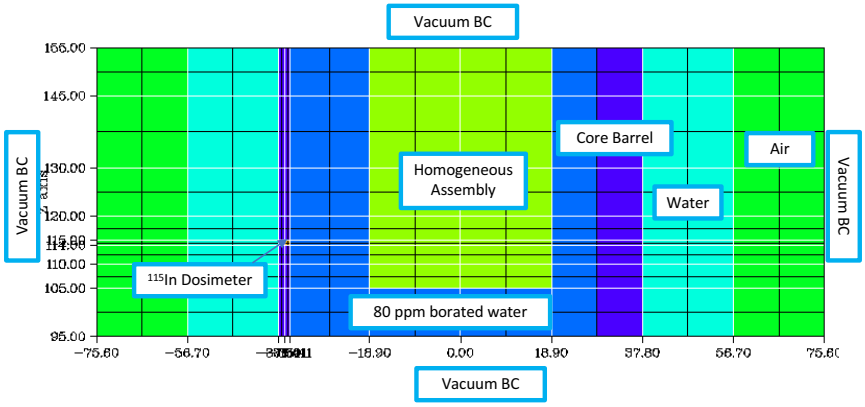

Figure C.1 PENTRAN^{TM} Importance Model z =114.5 cm: Axial Projection

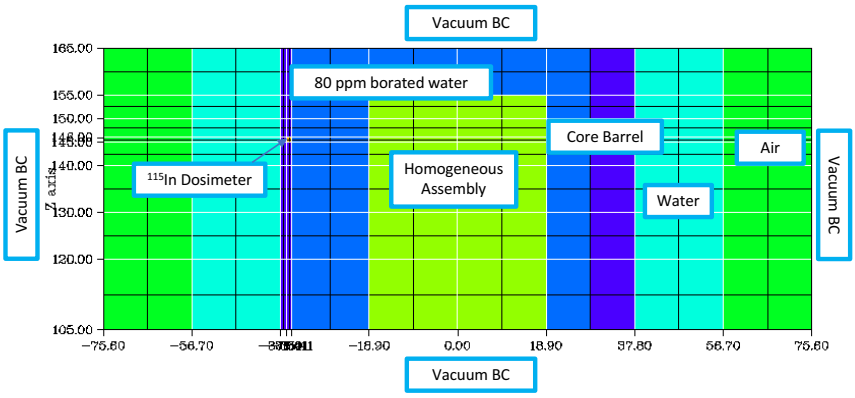

Figure C.2 PENTRAN^{TM} Importance Model z =145.5 cm: Axial Projection

C.0.2 Importance Functions

Figs. C.3 and C.4 show the PENTRAN^{TM} calculated importance functions for dosimeters at z =114.5 cm and 145.5 cm. Similar behaviors as shown in the Fig. 6.6 are observed. The neutron with higher energy are with higher importance away from the dosimeter while relative lower energy neutrons has much lower importance at the same region.

C.0.3 Field of View

The radial FOV for all of the three dosimeter locations are about the same as Fig. 6.7a. Fig. C.5 shows the calculated FOV for dosimeter locatio at z =114.5 cm and 145.5 cm. For the dosimeter at z =114.5 cm, the axial level 1 to 12 contribute $>$ 99% of the dosimeter responses. For the dosimeter at z =145.5 cm, the axial level 3 to 14 contribute $>$ 97% of the dosimeter response.

C.0.4 Group-wised Contribution

Fig. C.6 shows the GC for the three dosimeter locations. The results show that dosimeter at z =114.5 cm and 131.5 cm have very similar behavior while the dosimeter at z =145.5 cm has a greater contribution from the fast neutrons. The dosimeter at z =114.5 cm and 131.5 cm are closer to the PLSA rod, therefore more neutrons are undergoing scattering reactions. Relative lower energy neutrons are more likely to make contribution to the dosimeter response. The dosimeter at z =145.5 cm is closer to the fuel assembly and not next to the PLSA rod. Therefore, fast neutron born from fission process will be more likely to directly penetrate through the structures and contribute to dosimeter response.

C.0.5 Lower Weight Window Bounds

Figs. C.7 and C.8 show the corresponding lower weight window bounds.

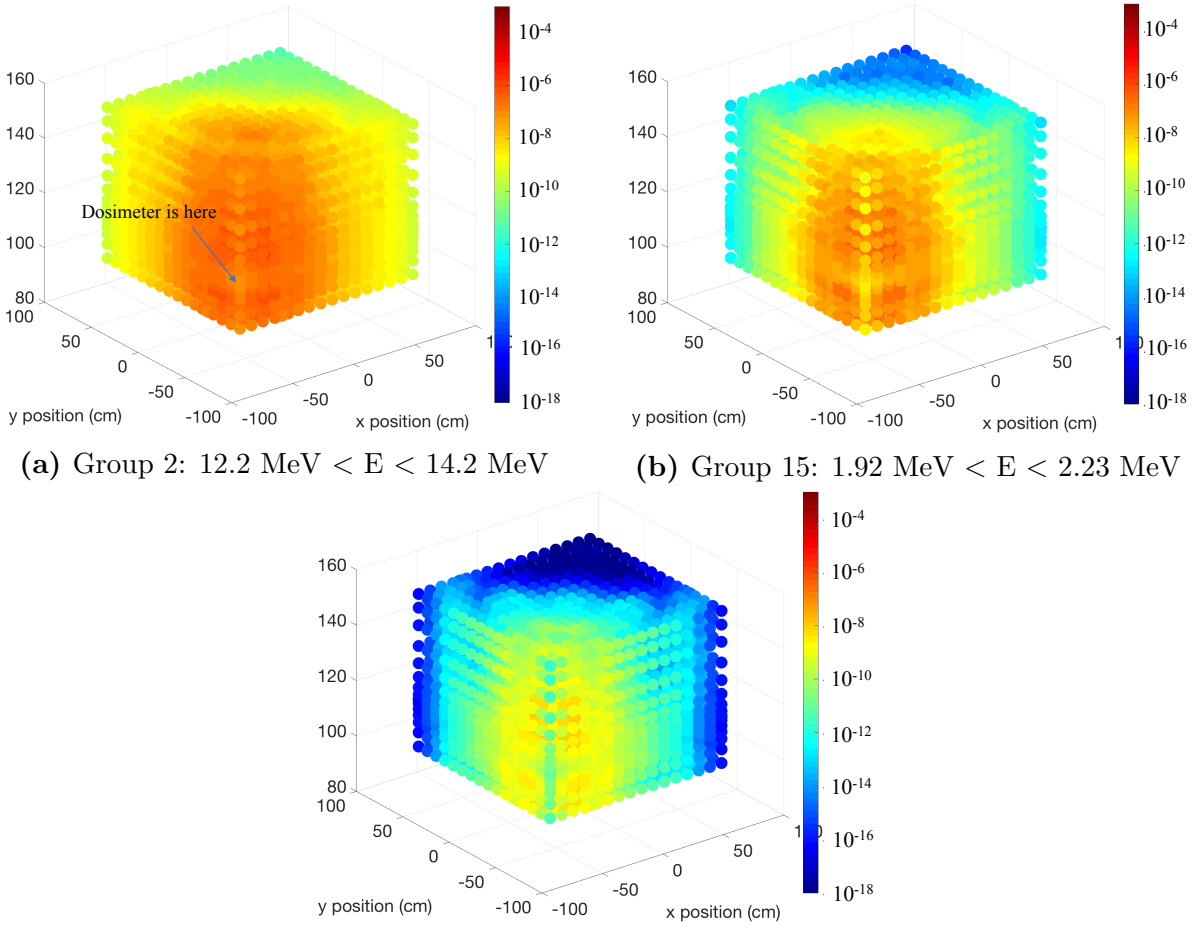

(a) Group 2: 12.2 MeV < E < 14.2 MeV

(b) Group 15: 1.92 MeV < E < 2.23 MeV

(c) Group 20: 0.82 MeV < E < 1.00 MeV

Figure C.3 PENTRAN^{TM} Importance Functions: 270° $z = 114.5\ cm$ $^{115}\mathrm{In}(n, n')$ dosimeter

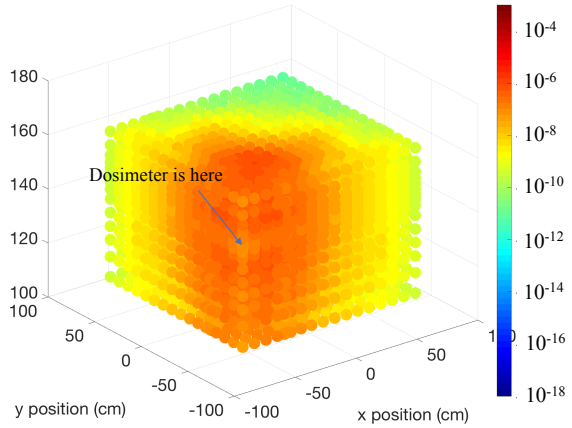

(a) Group 2: 12.2 MeV < E < 14.2 MeV

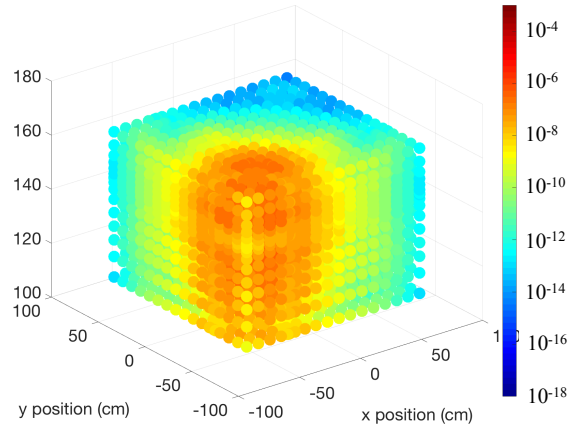

(b) Group 15: 1.92 MeV < E < 2.23 MeV

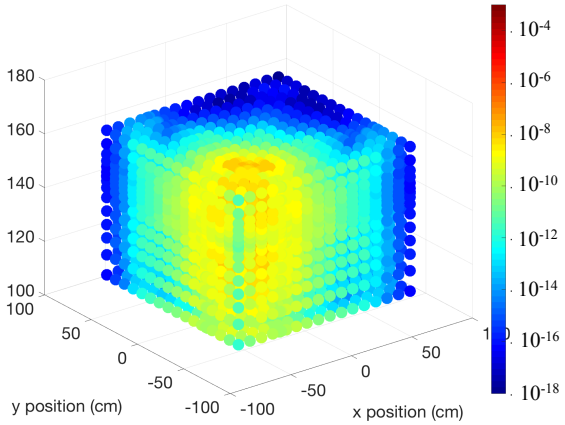

(c) Group 20: 0.82 MeV < E < 1.00 MeV

Figure C.4 PENTRAN^{TM} Importance Functions: 270° $z = 145.5\ cm$ $^{115}\mathrm{In}(n, n')$ dosimeter

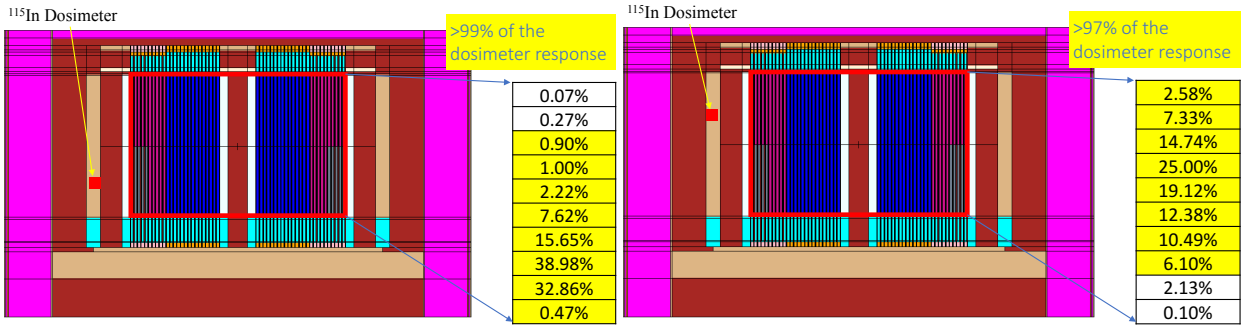

(a) z =114.5 cm **(b)** z =145.5 cm

Figure C.5 Field of View: 270° $^{115}\mathrm{In}(n, n')$ dosimeter

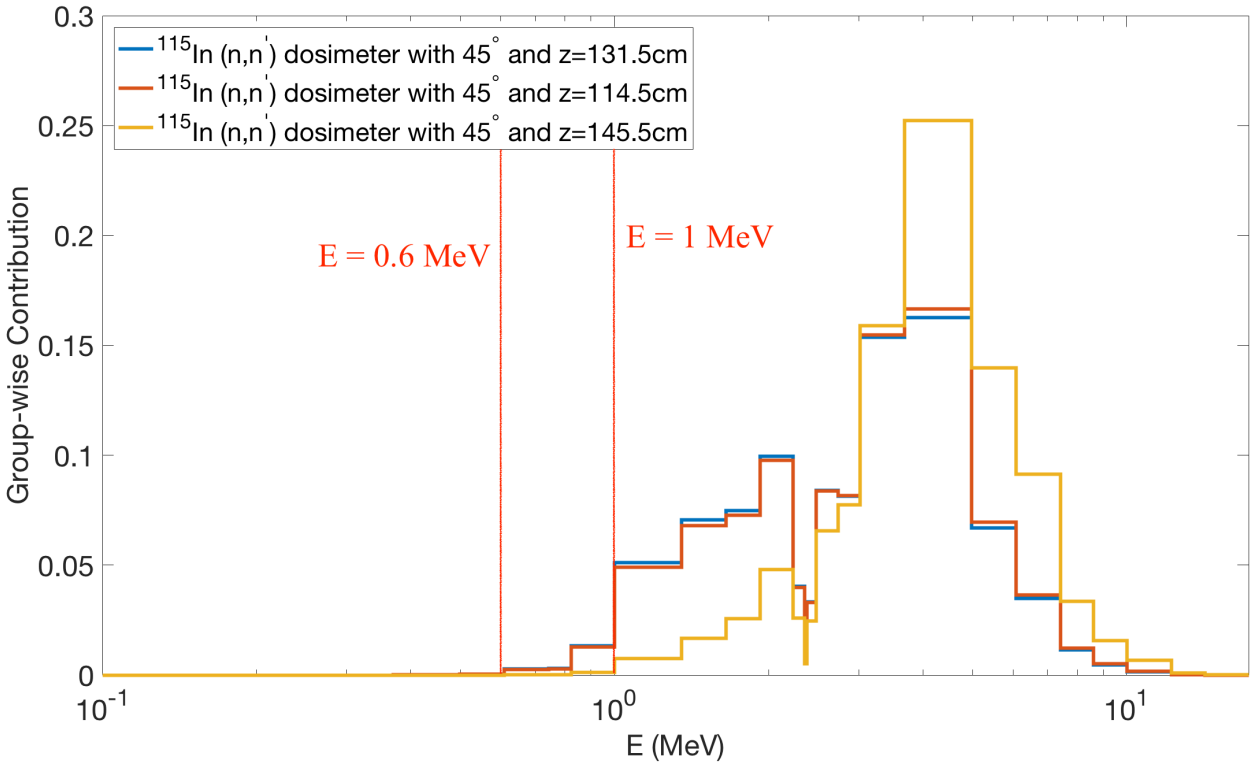

Figure C.6 $^{115}\mathrm{In}(n, n')$ Dosimeter Group-wised Contribution

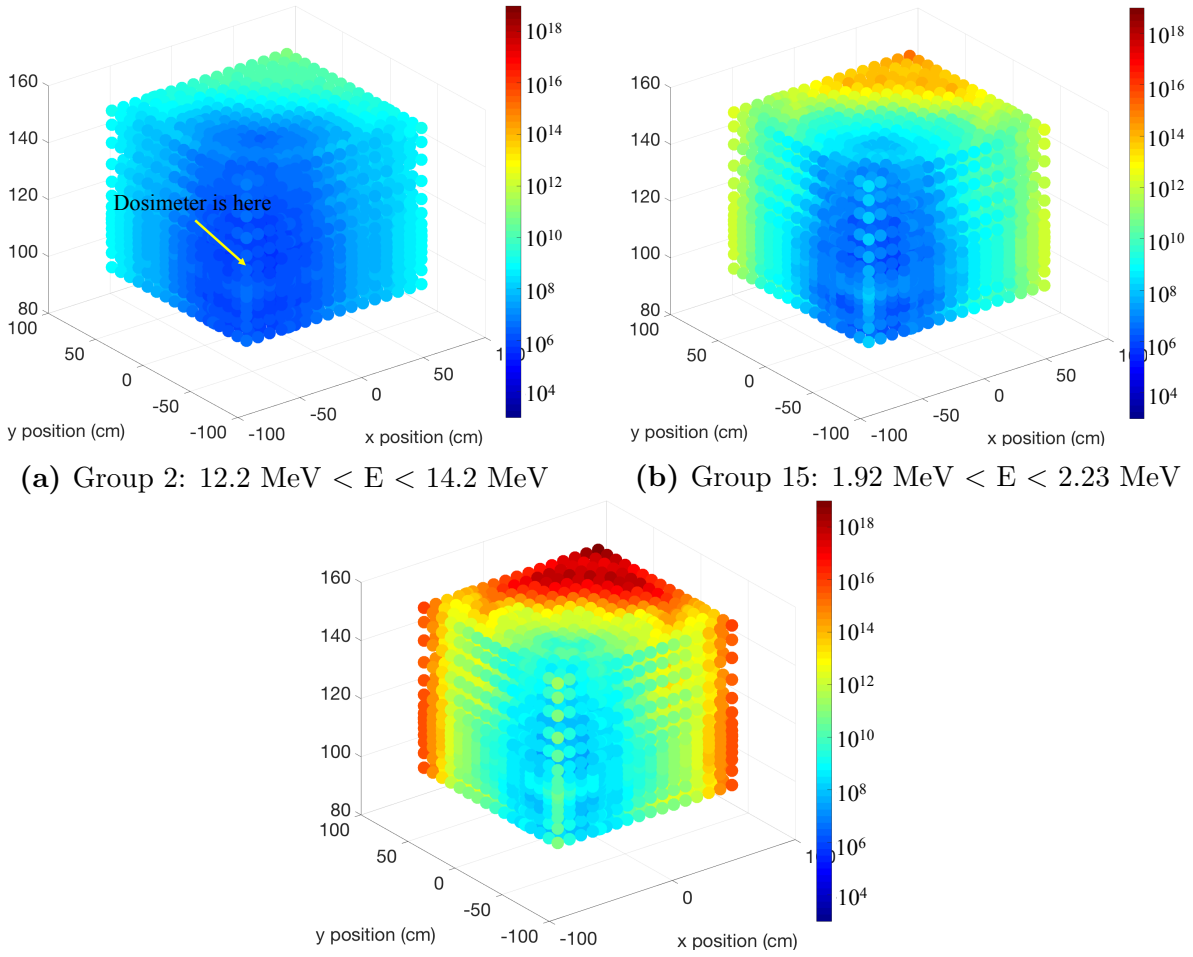

(a) Group 2: 12.2 MeV < E < 14.2 MeV

(b) Group 15: 1.92 MeV < E < 2.23 MeV

(c) Group 20: 0.82 MeV < E < 1.00 MeV

Figure C.7 Lower Weight Window Bounds: 270° $z = 114.5\ cm$ $^{115}\mathrm{In}(n, n')$ dosimeter

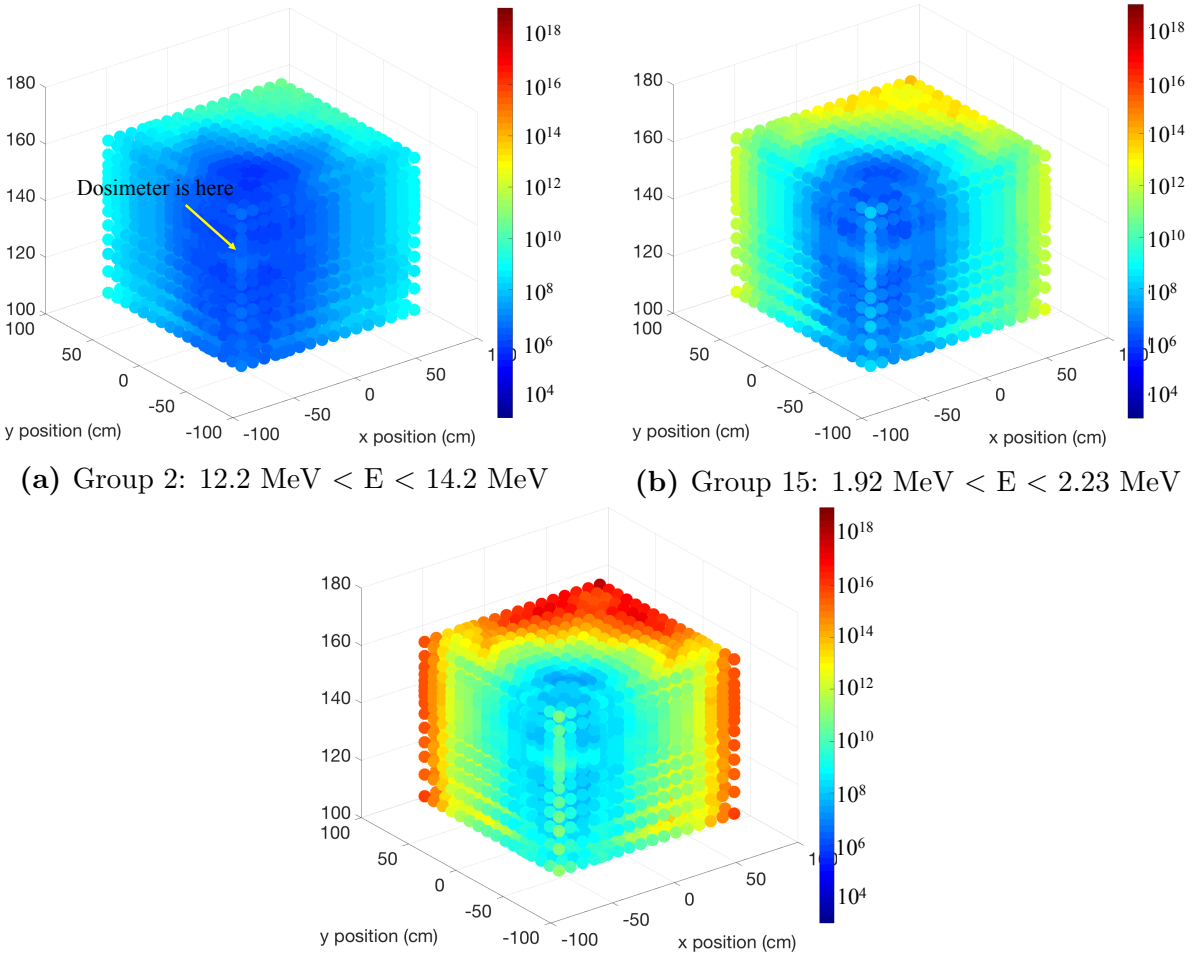

(a) Group 2: 12.2 MeV < E < 14.2 MeV

(b) Group 15: 1.92 MeV < E < 2.23 MeV

(c) Group 20: 0.82 MeV < E < 1.00 MeV

Figure C.8 Lower Weight Window bounds: 270° $z = 145.5$ cm $^{115}\mathrm{In}(n, n^{'})$ dosimeter

Appendix D

VENUS-3 Benchmark Problem: More DRF Coefficient Calculations

To calculate the DRF coefficients, the unit source volume has to be defined. In Fig. D.1, the VENUS-3 reactor core are divided to 14 axial levels (non-uniform axial heights). The three columns from the right show the definitions of unit source volume of the three dosimeter locations.

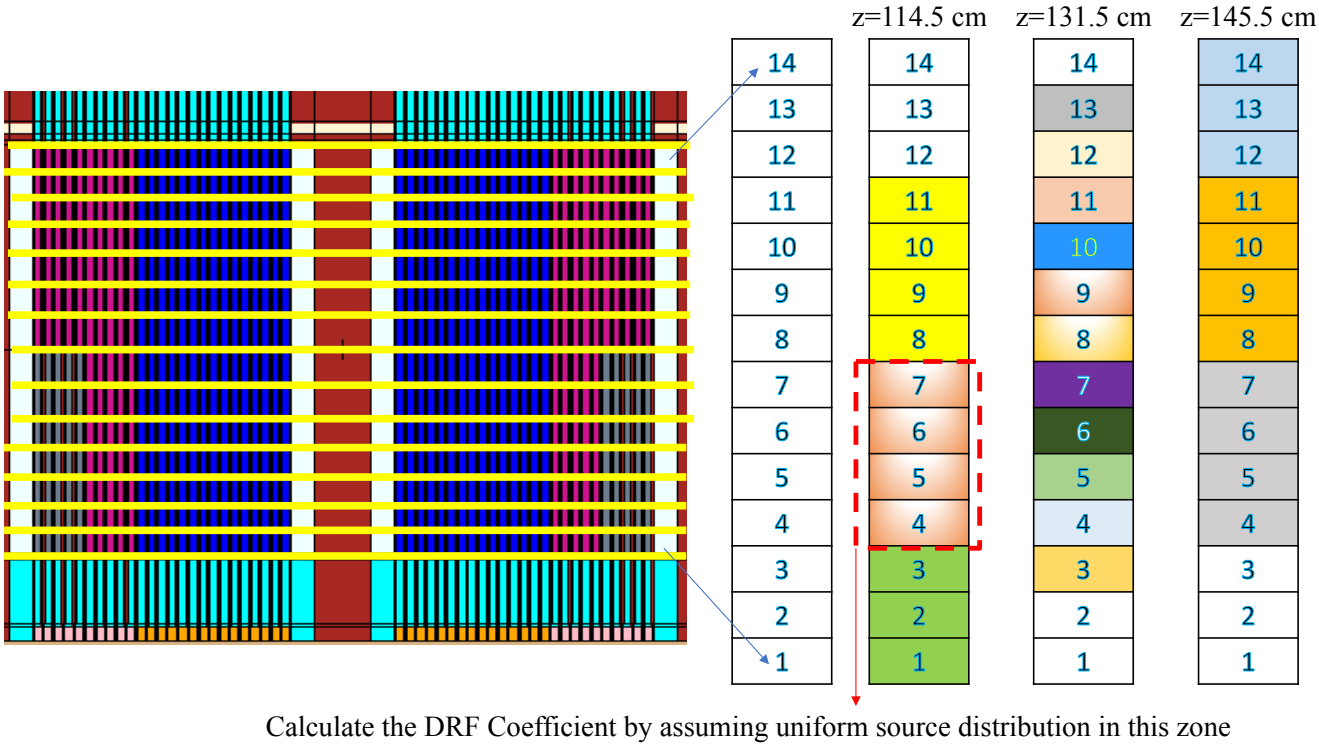

Figure D.1 Unit Source Volume Selections for the Three $^{115}\mathrm{In}(n,n^{'})$ dosimeter

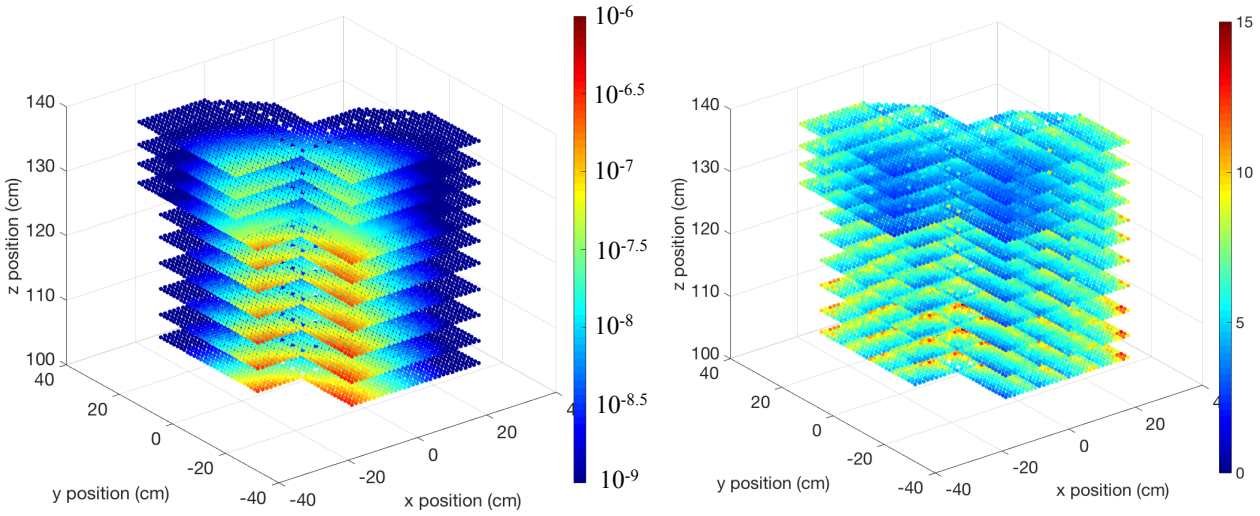

(a) DRF Coefficients

(b) 1σ Statistical Uncertainties

Figure D.2 DRF Coefficients: 270° $z = 114.5\ cm$ $^{115}\mathrm{In}(n, n')$ dosimeter

Among all of them, only dosimeter location at z =131.5 cm has no approximation on the unit source volume. The same colors with adjacent boxes represent that they are considered one unit source volume for the DRF coefficient calculations. In principle, the selection of unit source volume has to be studied, which is similar to deterministic calculation mesh size selection study. However, due to the limited computation resource, we simply select the unit source volume for two of the $^{115}\mathrm{In}(n, n')$ dosimeter locations based on experience. Fig. D.2 and D.3 show the DRF coefficients for $^{115}\mathrm{In}(n, n')$ dosimeters at z =114.5 cm and z = 145.5 cm, respectively.

Since the neutron source distribution are calculated with the 14 axial levels, the fuel pellet within the larger unit source volumes will have the same DRF coefficients. From the Table 6.6, it is obvious that difference of the dosimeter response is larger than the other two locations. This might be attributed to the unit source volume selection. The FOV for the dosimeter locations z =114.5 cm and 145.5 cm are also provided in Fig. D.4.

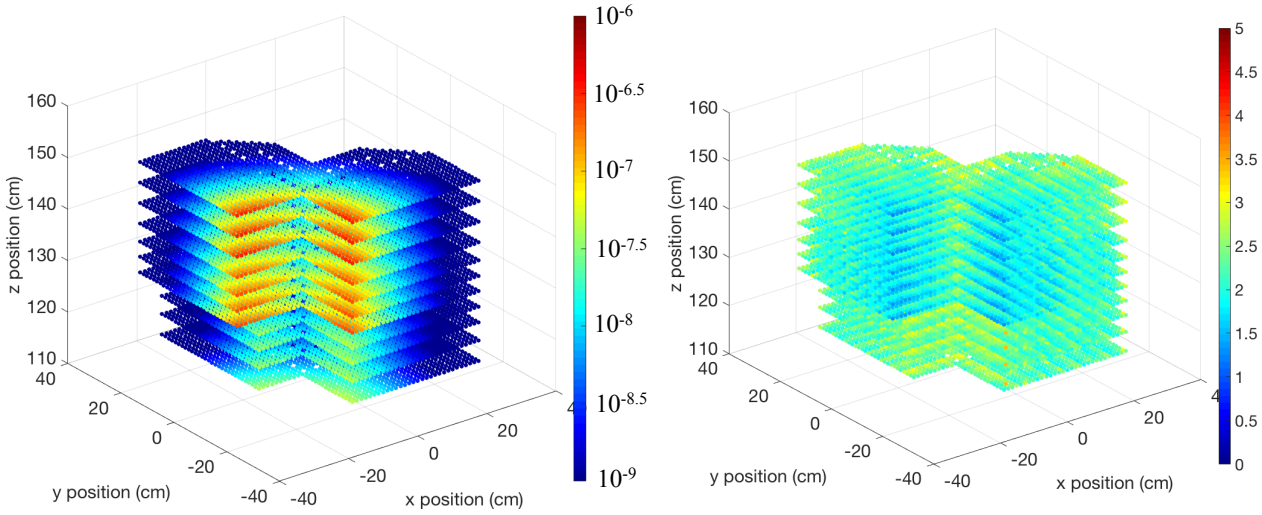

(a) DRF Coefficients

(b) 1σ Statistical Uncertainties

Figure D.3 DRF Coefficients: 270° $z = 145.5\ cm$ $^{115}\mathrm{In}(n, n')$ dosimeter

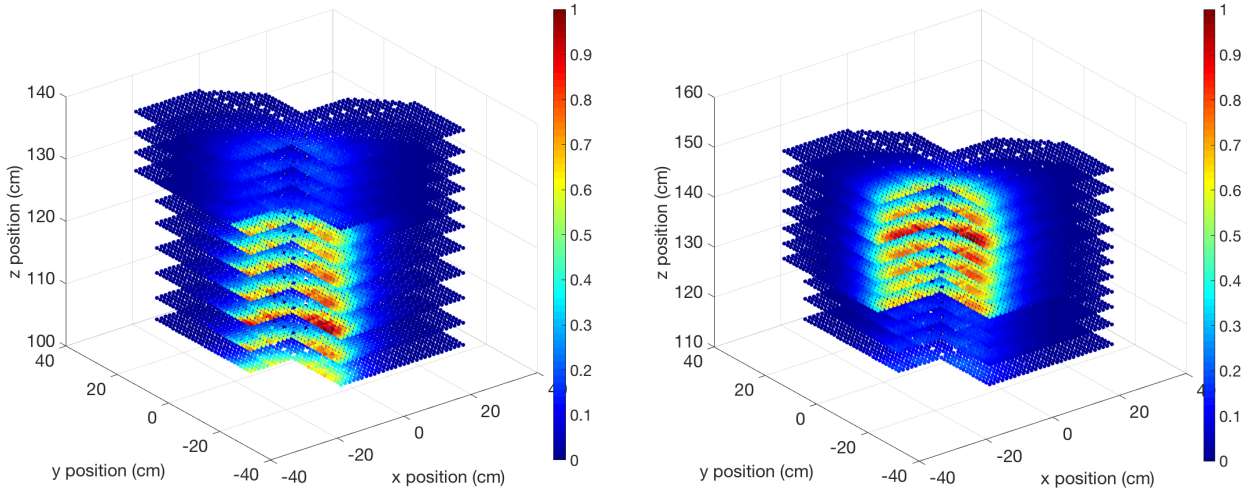

(a) $z = 114.5\ cm$

(b) $z = 145.5\ cm$

Figure D.4 Field of View: 270° $^{115}\mathrm{In}(n, n')$ dosimeter

Appendix E

VENUS-3 Benchmark Problem: Comparison of Experimental and Computational Source Distribution

In this appendix, the comparison of neutron source distribution of VENUS-3 core between experiment and calculation using MCNP5 will be presented. Fig E.1 shows the quarter core normalized neutron source distributions from experiment and MCNP5 calculations. By the first glance, it is obvious that there are some differences. To quantify the differences, Fig E.2 is provided. Here, the experimental source is used as reference.

The results show that differences up to $\sim 20\%$ are observed at the position close to structures with a lot of iron (inner baffle and PLSA rods). Some literature [114] has indicated that iron cross-section has larger uncertainties from the range of 5$\sim$10 MeV. This might be the main reason for the large differences. Further investigation on this can be performed.

Fig. E.3 shows a 100 axial (0.5 cm for height) pin-wised fission source distribution. This figure is provided for observation of fission source distribution. The fission source distribution shown in the Fig. 6.12 is calculated by non-uniform axial height, which might be misleading. The calculation parameter for this case is 200 active cycle with 200 skip cycle and 5×10^6 particles per cycle.

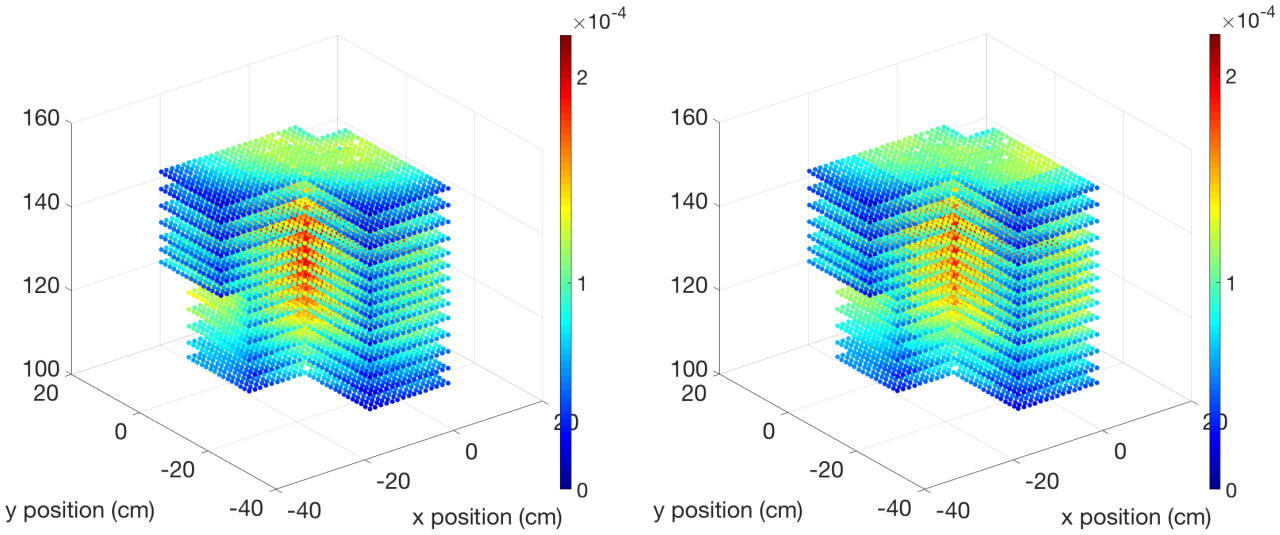

(a) MCNP5 Calculation **(b)** Experiment

Figure E.1 VENUES-3 Neutron Source Comparison Between computation and Experiment

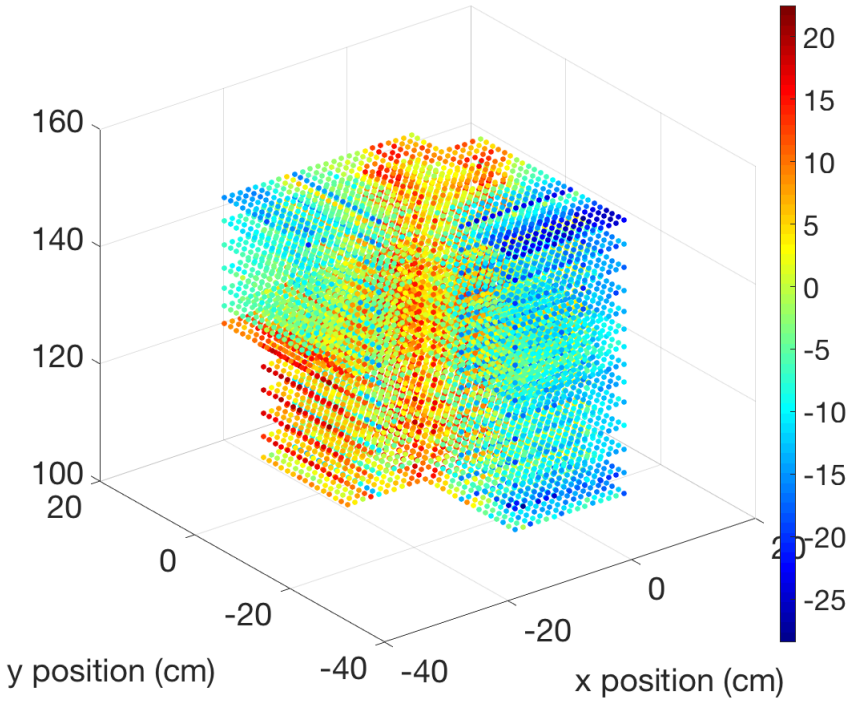

Figure E.2 Computation and Experiment Differences of VENUS-3 Neutron Source in %

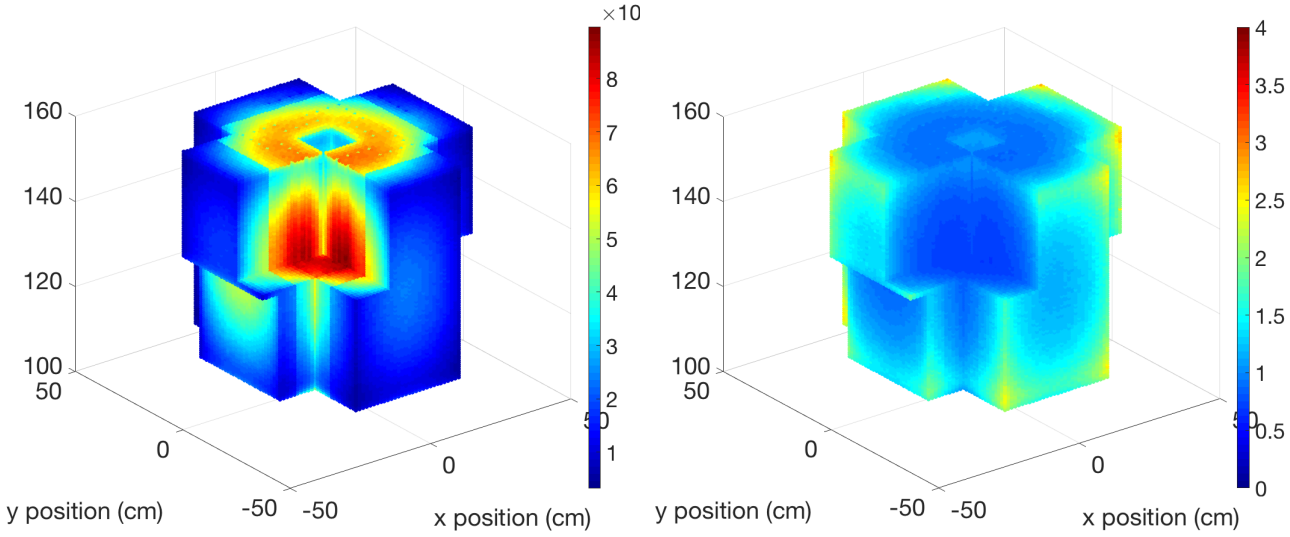

(a) Normalized Fission Source **(b)** 1σ Relative Statistical Uncertainties (%)

Figure E.3 VENUES-3 Neutron Source with 100 Axial Level (0.5 cm per Segment)

Appendix F

TMI-1 RPV Dosimetry: More FOV for Other Dosimeters

The 20-degree axial mid-plane $^{63}\mathrm{Cu}(n,\alpha)$ dosimeter FOV is shown in the Figs. F.1, F.2, and F.3. The FOV of $^{63}\mathrm{Cu}(n,\alpha)$ dosimeter is very similar to the $^{27}\mathrm{Al}(n,\alpha)$ shown in the section 7.2.5.1. Similarly, the light yellow frame are the assemblies with $> 0.5\%$ of the dosimeter contribution. The total contribution of the yellow frames are $\sim 87.08\%$.

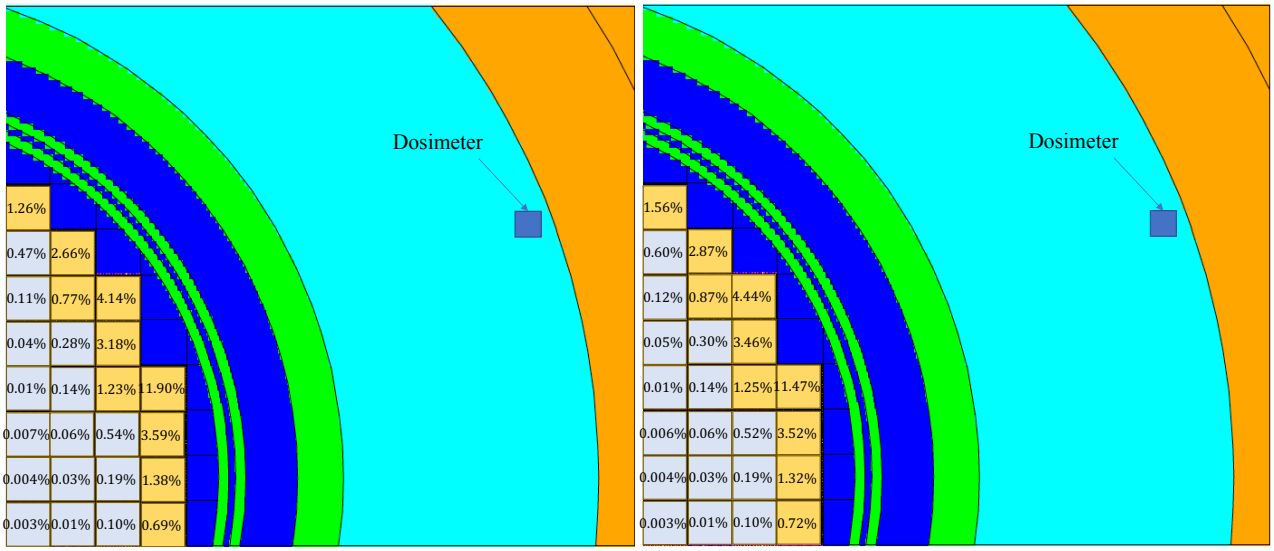

(a) Axial Level 1 **(b)** Axial Level 2

Figure F.1 Field of View: 20-degree Middle Axial Plane $^{63}\mathrm{Cu}(n,\alpha)$ Dosimeter

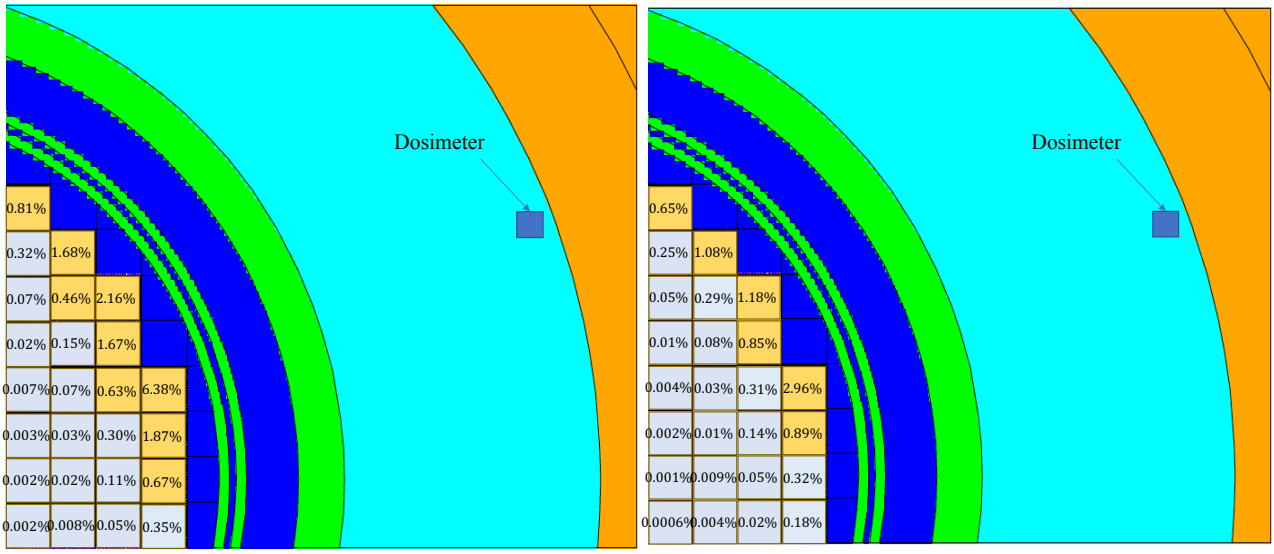

(a) Axial Level 3 **(b)** Axial Level 4

Figure F.2 Field of View: 20-degree Middle Axial Plane $^{63}\mathrm{Cu}(n,\alpha)$ Dosimeter

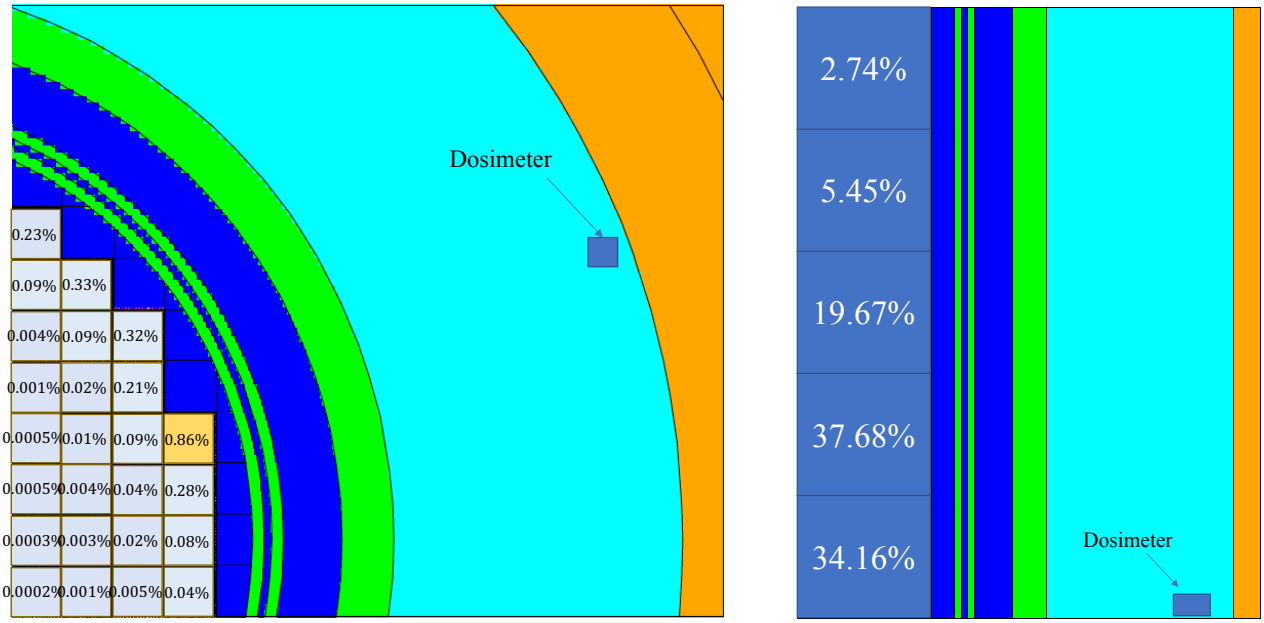

(a) Axial Level 5 **(b)** Axial FOV

Figure F.3 Field of View: 20-degree Middle Axial Plane $^{63}\mathrm{Cu}(n,\alpha)$ Dosimeter

Appendix G

Preliminary Study of the Implementation of DRF Methodology on Photon External Dosimetry for a Dry Storage Cask

In this appendix, a preliminary study for the photon external dosimetry for the same dry storage cask from chapter 8 is performed using the DRF methodology.

G.1 Analysis of Photon Source from the UNF-ST&DARD Code System

According to the ORIGEN-S manual [102], the photon source considered in the calculation are

1. X-rays
2. Gamma rays
3. Bremstrahlung
4. Spontaneous fission gamma rays
5. Gamma rays accompanying with the (α,n) reaction

The X-ray and Gamma ray emitted from the unstable nuclides for all decay modes are stored in the gamma library as line-energy and intensity data. The Gamma rays accompanying with

the (α,n) reaction is currently only from experimental data fitting [119]. The measurement is performed on $^{238}PuO_2$ source, which might not be applicable to other (α,n) source. I have personally contacted Mr. Ian Gauld, and he has agreed this might not be a good assumption for other (α,n) source. Note that Mr. Ian Gauld was the main person of contact and developer for the ORIGEN-S code. The spontaneous fission gamma rays are assumed to be similar for most of fissile nuclide, and directly using ^{235}U for all of them. The continuum spectra from bremsstrahlung, spontaneous fission, and (α,n) interactions are represented as binned pseudo-line data in the ORIGEN-S code [102].

Fig. G.1 shows the normalized photon spectrum for burnup level 10500 MWd/MTHM. Note that for PWR SNF analysis, typically the axial level selected is 18. The axial power factor of each node can be found in one of the reference article [120]. The The axial node selected for analysis is 12/18.

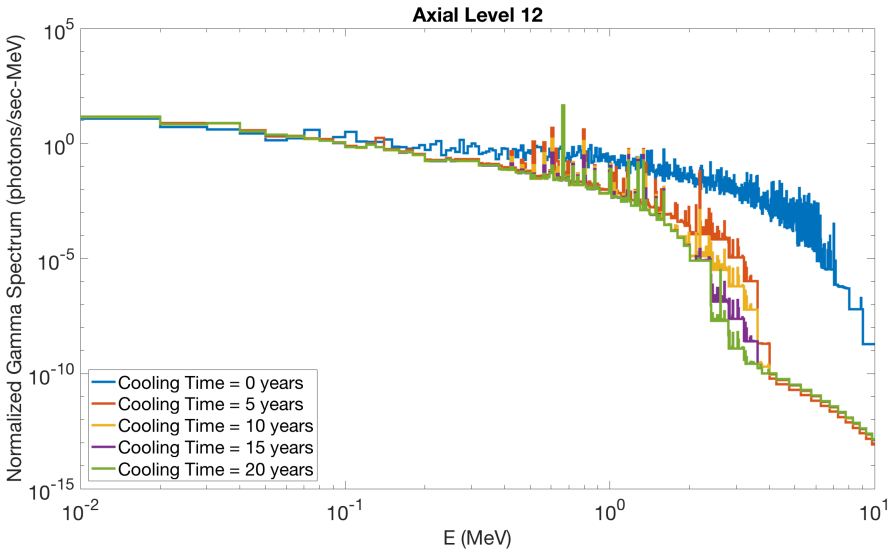

Figure G.1 Normalized Photon Spectrum: 10500 MWd/MTHM Axial Level 12

The energy group selected here for photon is 1000 with equal interval ranged from 0.01 to 10 MeV. It is shown that the photon spectrum for freshly discharge fuel assembly is significantly harder than the others. This is mainly because the extremely short living radioactive nuclides with relatively high energy photon emission. With more cooling time, the photon spectrum become softer. The photon strength at faster energy group, i.e. ≥ 5 MeV is ~ 10 orders of magnitude smaller than the lower energy photons, i.e. ~ 0.1 MeV.

Fig. G.2 shows the corresponding photon source strength for burnup level 10500 MWd/MTHM and axial node of 12. In this figure, the freshly discharged photon source strength is not plotted. This is mainly because the photon source strength with such condition is extremely large, which is $\sim 10^{17}$ photons/sec per metric ton of heavy metal. The source strength of other cooling time will be unobservable if we plot them together. This can be further

demonstrated by the photon spectrum with source strength shown in the Fig. G.3. For other burnup level and axial node, similar behavior is observed. This can be found in the Appendix I.

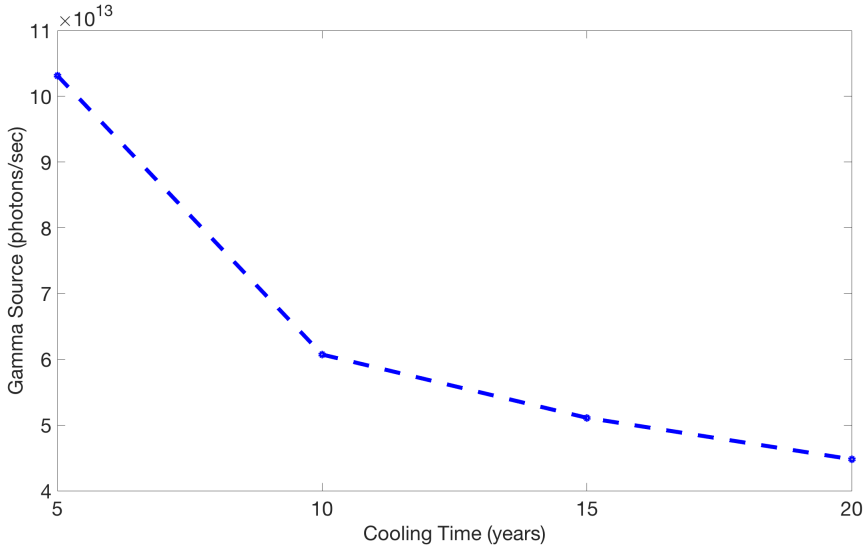

Figure G.2 Photon Source Strength: 10500 MWd/MTHM Axial Node 12/18 (Normalized to per Metric Ton Heavy Metal)

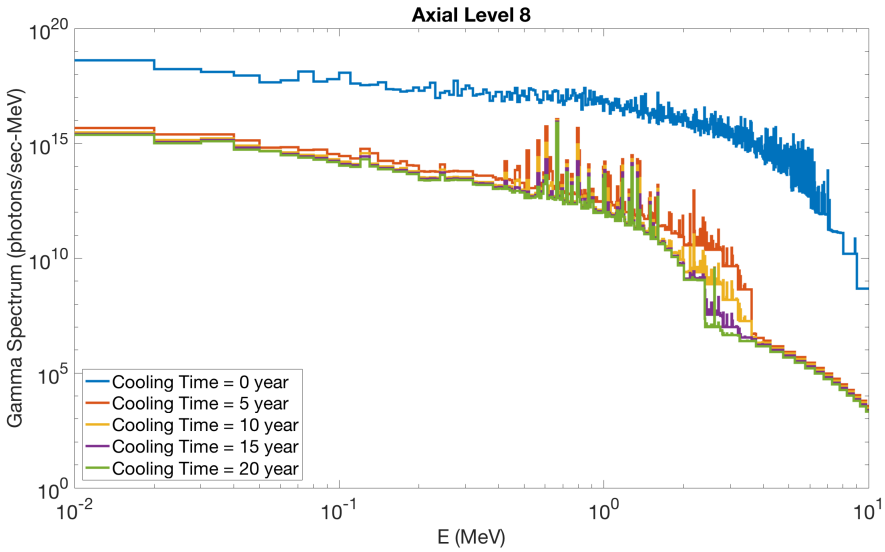

Figure G.3 Photon Spectrum: 10500 MWd/MTHM Axial Level 12 (Normalized to per Metric Ton Heavy Metal)

From the results, it is obvious that the photon spectrum varies by both burnup and cooling times.

G.2 Importance Source and Importance Function for Photon External Dose

Fig. G.4 shows the ICRP and ANSI/ANS-6.1.1 flux to dose conversion factor for photons. The original group structure for ANSI/ANS-6.1.1 is 38 group for photons while it is 20 group for the the ICRP-21. Since the ANSI/ANS-6.1.1 has a wider range of energy, the flux to dose conversion factor is interpolated to the BUGLE96 20 photon group structure and used as importance source here. From the first glance, it is obvious that the flux to dose conversion factors are sensitive to the fast photons.

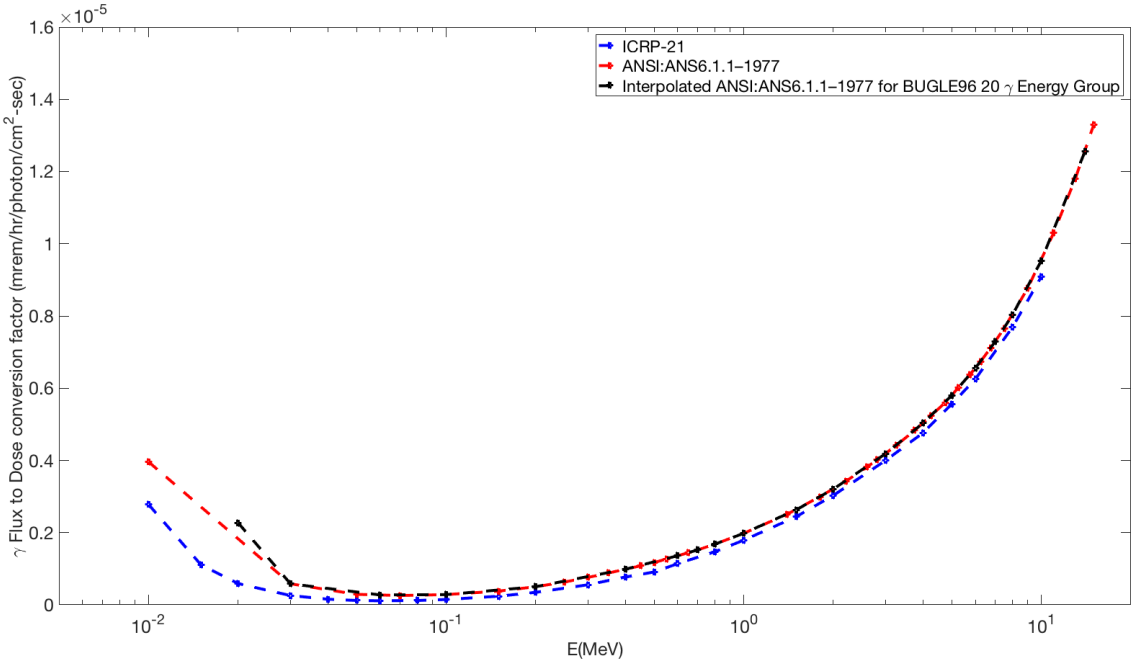

Figure G.4 Photon Flux to Dose Conversion Factor

The photon importance function drops more order of magnitude than the neutron mainly because the higher interaction rate. The behavior of photon importance function can be found in the Appendix H.

It is also verified that the FOV estimation for the fission neutron source is appropriate for the dose calculation. The Legendre anisotropic scattering order used here is all P3 for both neutron and photons. This arrangement is sufficient for neutrons while P5 is typically required for photons. However, the importance functions are calculated for acceleration of Monte Carlo fixed-source calculations. Therefore, it is acceptable for a lower precision of importance function. Moreover, I have tested the level of CADIS acceleration using both P3 and P5. The result shows that no significant speedup is observed in this case. This might also be attributed to the ray effect.

The 1D importance function calculation is relatively fast, which requires $\sim$ 5 minutes for photons, and $\sim$ 10 minutes for neutrons on 1 processor. The 3D importance function calculation requires $\sim$ 20 minutes for photons, and $\sim$ 35 minutes for neutrons on 2 processors.

G.3 FOV and GC for Photon Source

For FOV of neutron dosimeter/detector, we already have plenty of experience. However, the photon transport is quiet different from the neutron transport, and therefore the FOV might be different. Here, the same burnup and cooling time for fuel assemblies as the independent neutron source is selected for demonstration. Fig. G.5 shows the FOV for the photon source.

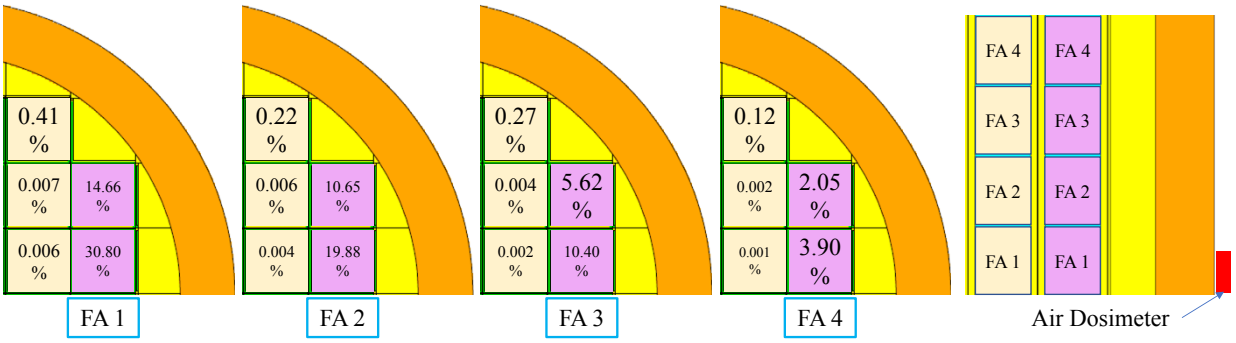

Figure G.5 FOV of Photon Source (4500 MWd/MTHM No Cooling Time): Zero-degree Air Dosimeter and Axial Level 3

The result shows $\sim$ 99% of the photon dosimeter response are from the two closest fuel assemblies. The FOV is slightly different mainly comparing with the induced fission neutron source. There main reason is that the photon importance function drops more significantly than the neutron importance function when location is away from the dosimeter. Fig. G.6 shows the photon source GC for the fuel assemblies with burnup of 4500 MWd/MTHM and 10 years cooling time.

The result shows that $\sim$ 99% of the photon dosimeter response is from the lowest energy group. This is mainly because the spectrum of photon source dominates the GC shape. The photon spectrum is also provided here for comparison. The low energy photon source strength is $\sim$ 6 to 10 order of magnitude larger than the photon with higher energy, and therefore the GC shape somehow, but not completely, follows the photon spectrum.

However, since the quality of the photon source importance function is not yet studied, these results cannot be the final conclusion at this stage.

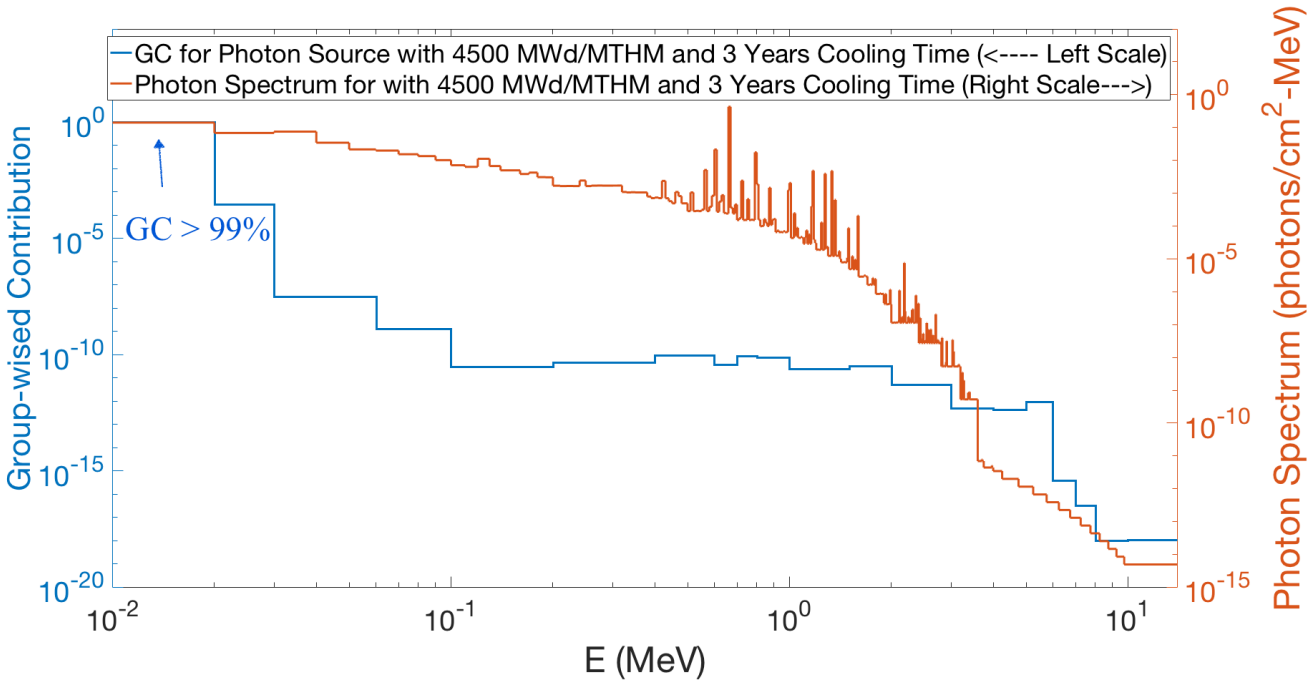

Figure G.6 GC Photon Sources: Zero-degree Air Dosimeter and Axial Level 3

G.4 Photon Source DRF Coefficient Sensitivity Study

In this section, the 1D model in Fig. 8.16 is used to perform photon source DRF coefficient sensitivity study. Fig. G.7 shows the sensitivity of photon source DRF coefficient to the fuel assembly burnup and cooling time.

Since fresh fuel has almost no photon source emission comparing with burned fuel, the freshly discharged photon source DRF coefficient of burnup level 1500 MWd/MTHM is selected as reference. The photon source DRF coefficient for freshly discharged assemblies are decreasing with fuel burnup level. This might mainly because with more heavy nuclide consumed, the photon spectrum will become softer. For the fuel assembly with longer cooling time, the photon source DRF coefficient increases with burnup levels. This might mainly because more activation with higher burnup level. Therefore, the photon spectrum will be harder with increase of burnup level. Fig. G.8 further re-plot the Fig. G.8 by looking into sensitivity to the cooling time.

Since it is known that the DRF coefficient for freshly discharged assembly is very different from the others, only the cooling time more than 5 years are compared here. The DRF coefficient for 5 years cooling time is taken as reference cases. The results show that the photon source DRF coefficients decrease with cooling time. This is mainly because the photon spectrum become softer with increase of cooling time. All the strong photon emitting nuclide decay away with longer cooling time. The trend is not exactly linear, but it is possible

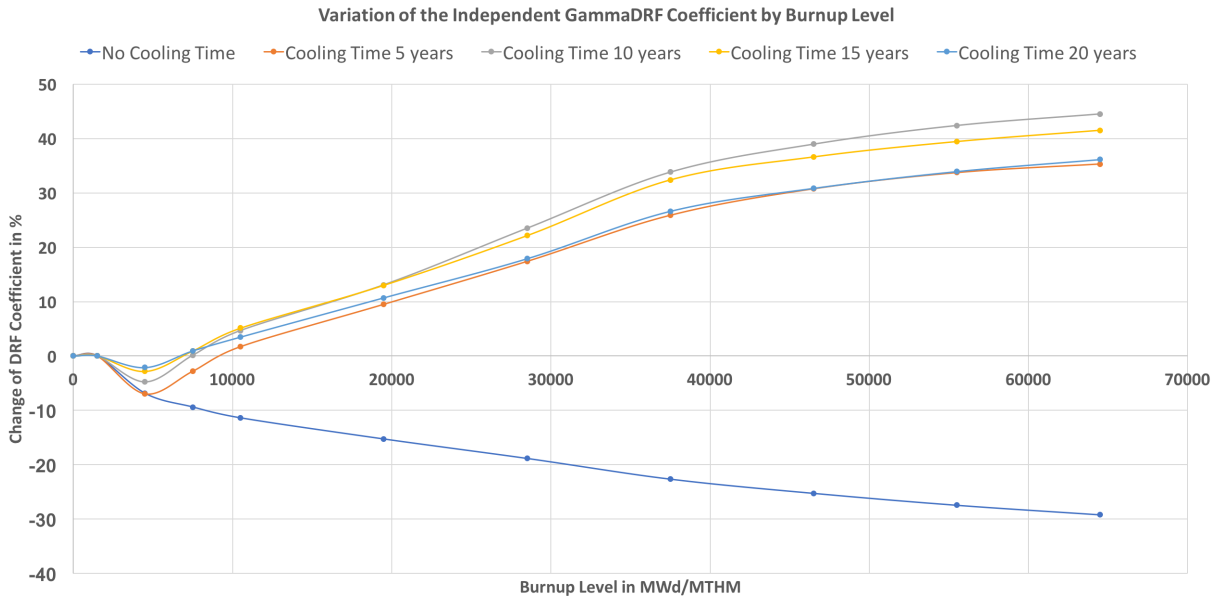

Figure G.7 Sensitivity of the Photon Source DRF Coefficient to Burnup and Cooling Time - 1

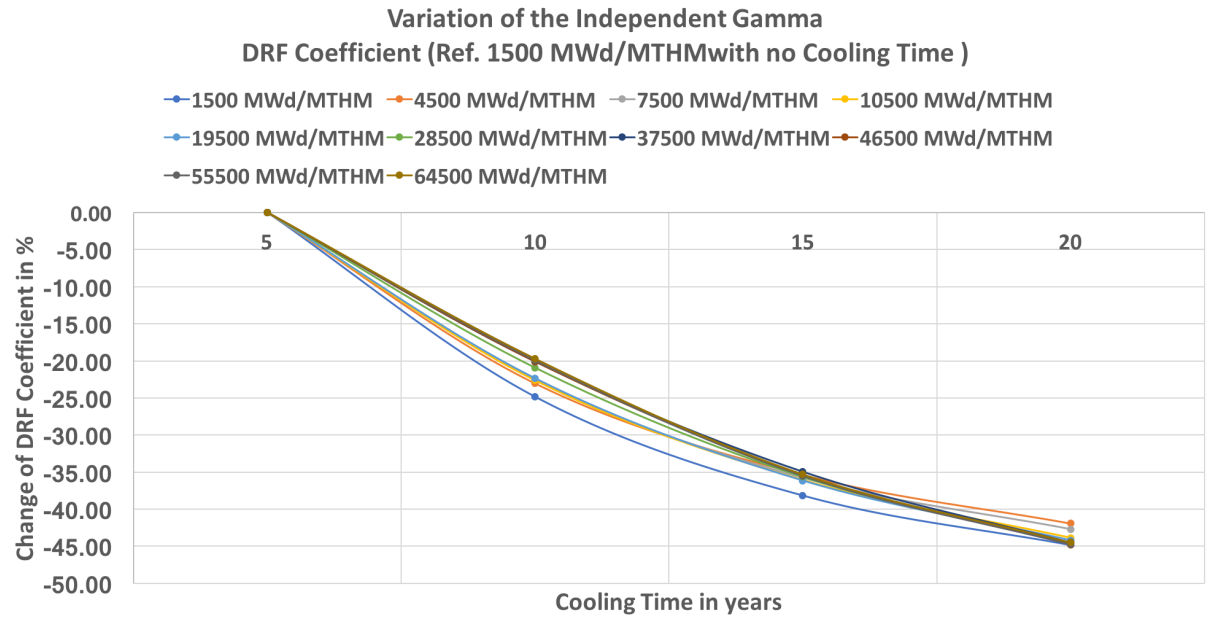

Figure G.8 Sensitivity of the Photon Source DRF Coefficient to Burnup and Cooling Time - 2

to utilize linear interpolation scheme to obtain the DRF coefficient with sufficient data points.

From the sensitivity study, it is demonstrated that the photon source DRF coefficients are sensitive to both burnup and cooling time.

G.5 3D Photon source DRF Coefficients

Fig. G.9 shows the small section of fuel rods that are selected for the photon source DRF coefficient calculations. The meshing scheme selected is also shown here. We use the lumping scheme shown in the Fig. G.9 and 4 pellet axially for one DRF coefficient calculations. Note that only 1 axial level is calculated. The main reason is the expected small control volume of photon source.

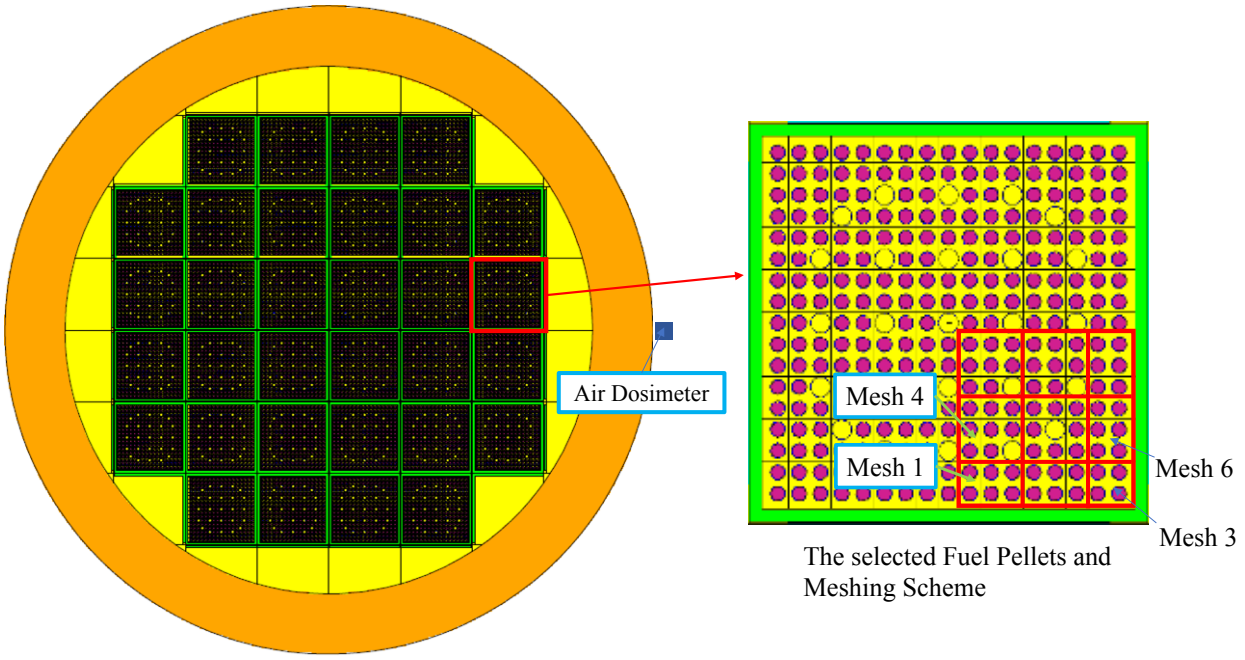

Figure G.9 Selected Fuel Pellet Locations for Photon DRF Coefficient Calculations

The photon DRF coefficient calculations require 10^{10} to 10^{11} particles to achieve a relative statistical uncertainty of $\sim$ 5%, depending on the location of photon source. The DRF coefficient with photon source further away from the dosimeter requires significant more computation time to achieve the same level of statistical uncertainty. However, the fuel pellet that are far away from the dosimeter are making negligible contribution, and thus are not necessary to be considered.

The photon DRF coefficients are $\sim$ 5 orders of magnitude smaller than the neutrons with same dosimeter and radiation source locations. This is mainly because the relatively high interaction rate of photons comparing with neutrons. It is also observed that the photon DRF coefficients almost drop 1 order of magnitude from the edge of assembly to about 6 fuel pellet into the assembly. With current computation capability we have, it is impractical to obtain pin-wised photon DRF coefficients. However, it is obvious that the segment of fuel assembly, i.e. fuel rods, that contributing to most of the dose value will be those at the surface. This is mainly because the high interaction rate of photons with materials.

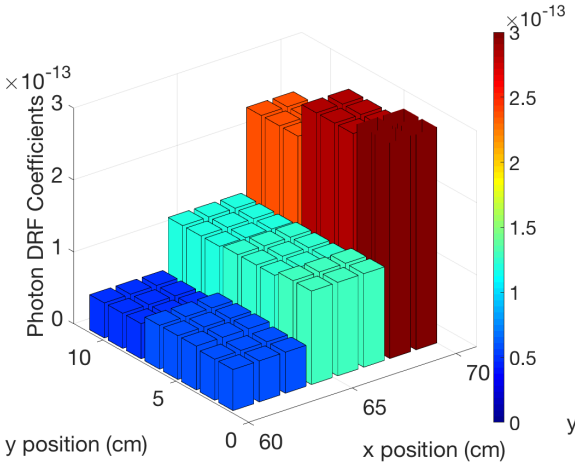

(a) DRF Coefficients

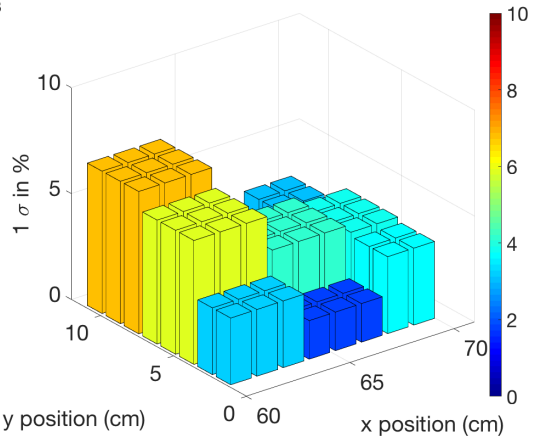

(b) 1σ Relative Statistical Uncertainties in %

Figure G.10 Photon DRF Coefficients: Burnup Level of 28500 MWd/MTHM and 5 Years Cooling Time

G.6 Photon Source Calculations

The burnup profile of the fuel assemblies are same as shown in the Fig. 8.25. The photon source strength is obtained from the UND-ST&DARD code system. Fig. G.11 shows the pin-wised photon source distribution for the selected core pattern.

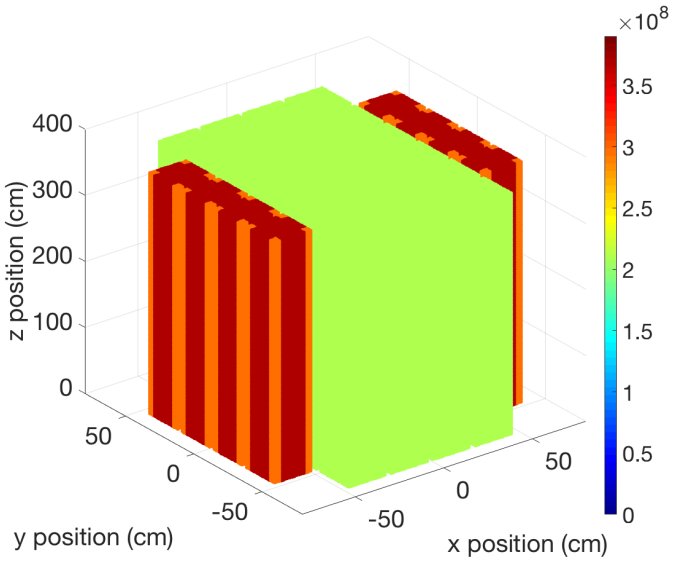

Figure G.11 Pin-wised Photon Source (photons/sec)

Since there are three different burnup with the same cooling time, there are three photon source strengths. The photon source strength of 46500 MWd/MTHM is roughly 2 times of 28500 MWd/MTHM.

G.7 Dose from Photon Source

In this section, the preliminary result of photon source dosimetry for the GBC-32 dry storage cask is discussed. Table G.1 shows the calculated dose values from photon source. Note that two MCNP5 cases are prepared: (1) Photon source within selected segment shown in the Fig. G.9; and (2) All the fuel assemblies within the estimated FOV. Table G.1 shows the photon doses calculated by the DRF methodology and the reference calculations. The number of particle for the MCNP5 reference calculations are 5×10^{10} and 2.5×10^{11} for the cases of selected and all fuel assemblies within the FOV, respectively.

Table G.1 Dose from the Independent Neutron Source

Code	FA incuded	Dose (mrem/hr)	1σ	Differences in %
RAPID / DRF Method.	Selected Segment	1.2763×10^{-2}	-	-69.04%
MCNP5 + CADIS	Selected Segment	1.4674×10^{-2}	4.15%	-64.19%
MCNP5 + CADIS	All within FOV	4.1229×10^{-2}	4.08%	Ref.

The results show that the dose calculated by DRF methodology for selected fuel assembly segment is $\sim$ 13% difference from the MCNP5 calculation. This can be attributed to the DRF coefficient fuel pellet lumping scheme. The selected fuel assembly segment has a $> 30\%$ of total dose from photons in this benchmark problem. The calculation wall-clock times for the two MCNP5 reference cases are $\sim$ 4.78 days and $\sim$ 2.75 weeks using 8 processors while the DRF methodology only requires a few second using 1 processor.

G.8 Overall External Dose

We have successfully calculate the dose rate of a dry storage SNF cask from the three main radiation sources. It is shown that the photons contribute most of of the total dose rate for the configuration of this benchmark problem, mixing fuel assembly burnup with 37500 and 46500 MWd/MTHM and 5 years cooling time. The contribution of the calculated dose from photons, independent neutrons, and induced fission neutrons for this benchmark problem is shown in the Table G.2. Note that the dose from photon source shown in this table is only a small segment of fuel assembly.

The results show that even with a small segment of fuel assembly, the photon source still contributes more than 97% of the dose rate for this benchmark problem. Further comparison

Table G.2 Dose from the Different Radiation Source 1: Air Dosimeter at 0-degree Axial Level 3

Radiation Source	Dose Rate (mrem/hr)	Percentage of Contribution
Photons (partial)	1.2763×10^{-2}	97.56%
Independent Neutrons	2.5992×10^{-4}	1.99%
Induced Fission Neutron	5.9461×10^{-5}	0.45%

using the photon dose rate with the full FOV is shown in the Table G.3. Note that the dose rate from photons are calculated by the MCNP5 here.

Table G.3 Dose from the Different Radiation Source 2: Air Dosimeter at 0-degree Axial Level 3

Radiation Source	Dose Rate (mrem/hr)	Percentage of Contribution
Photons	4.1229×10^{-2}	99.23%
Independent Neutrons	2.5992×10^{-4}	0.63%
Induced Fission Neutron	5.9461×10^{-5}	0.14%

The results show that more than 99% of the total dose rate of this benchmark problem is from the photon source. This has perfectly agreed with the literature's results [97].

Further verification of the FOV for both independent and fission neutron sources can be found in the Appendix J. Note that the photon source FOV will not be presented here since only a segment of model is used for demonstration. However, it is shown that the main contribution of photon dose are only from a few fuel pellets of the closest fuel assembly. This is mainly because the higher interaction rate of photons with materials. Relevant DRF coefficient sensitivity study to different photon source energy and location using the 1D model can be found in the Appendix K using the 1D model.

This appendix has performed a preliminary study on the implementation of DRF methodology to a photon shielding problem. However, more detailed studies has to be performed on: (1) The quality of photon importance function; and (2) The FOV and GC of the photon source.

Appendix H

Photon Importance Functions for Dry Storage Cask

Fig. H.1 shows the PENTRAN^{TM} 1D photon importance model with its corresponding boundary conditions. The model size is 124.8 cm.

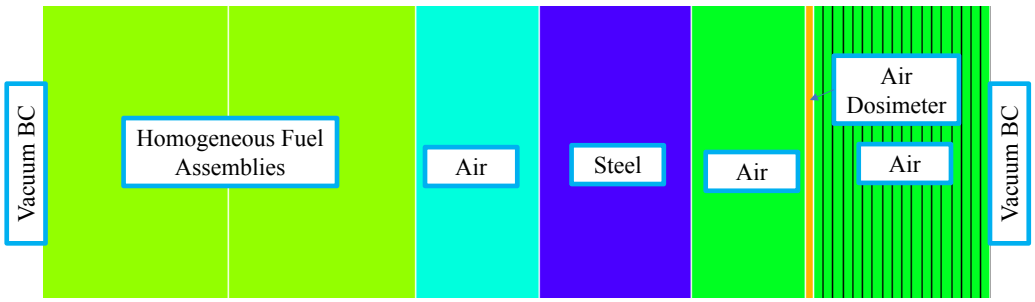

Figure H.1 PENTRAN^{TM} 1D Photon Importance Model

Fig. H.2 shows the importance functions of photon source. The importance function for low energy photons, i.e. 0.1 MeV $<$ E $\leq$ 0.2 MeV, drops significantly in the steel cask region. This is mainly because the high interaction rate of low energy photons. In the air region, the photons rarely encounter interaction. Therefore, a flat distribution with minimal drop of importance function is observed at such locations.

Fig. H.3 shows the radial and axial projection of the 3D photon importance model with air dosimeter located at 0-degree and axial mid-plane.

Figs. H.4 shows the photon importance function of ICRP air dosimeter. Note that the values lower than 10^{-37} are all adjusted to 10^{-40} here.

The photon importance function with low energy group drops drastically for location away

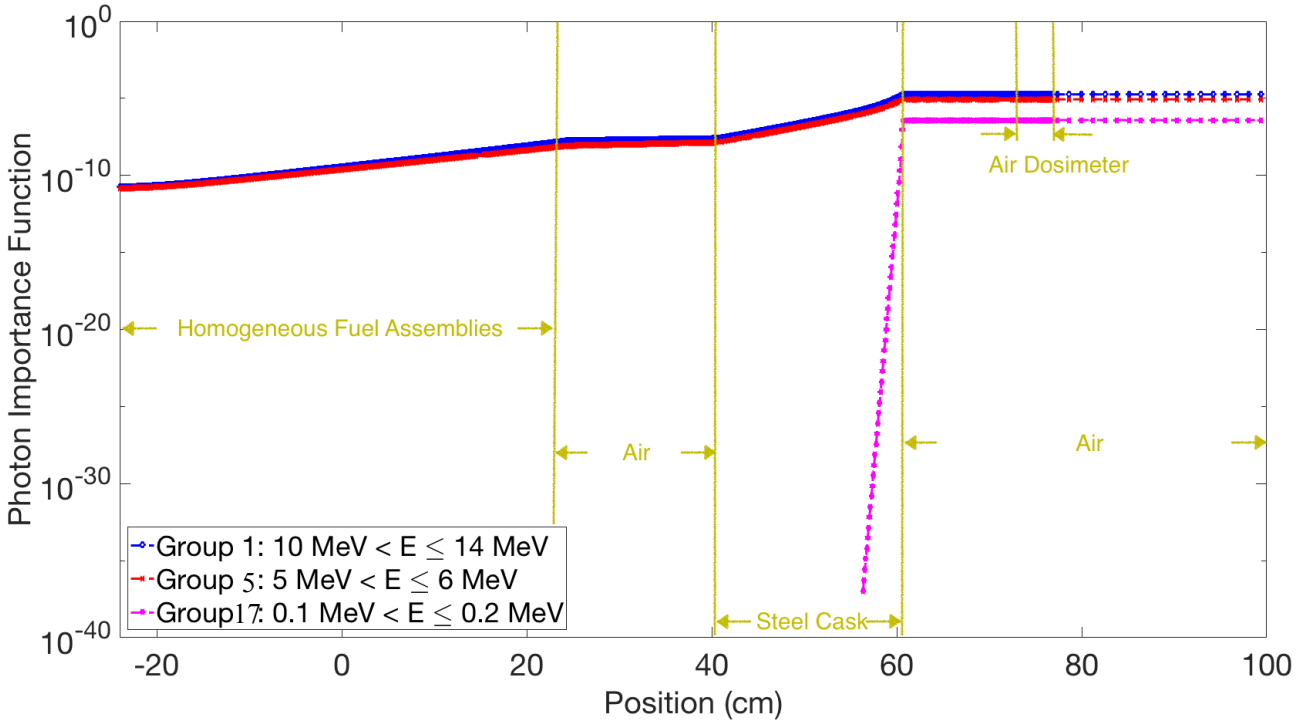

Figure H.2 PENTRAN™ 1D Photon Importance Function

from the dosimeter. Some of the importance function are zeros, mainly because computer is not able to process such small value.

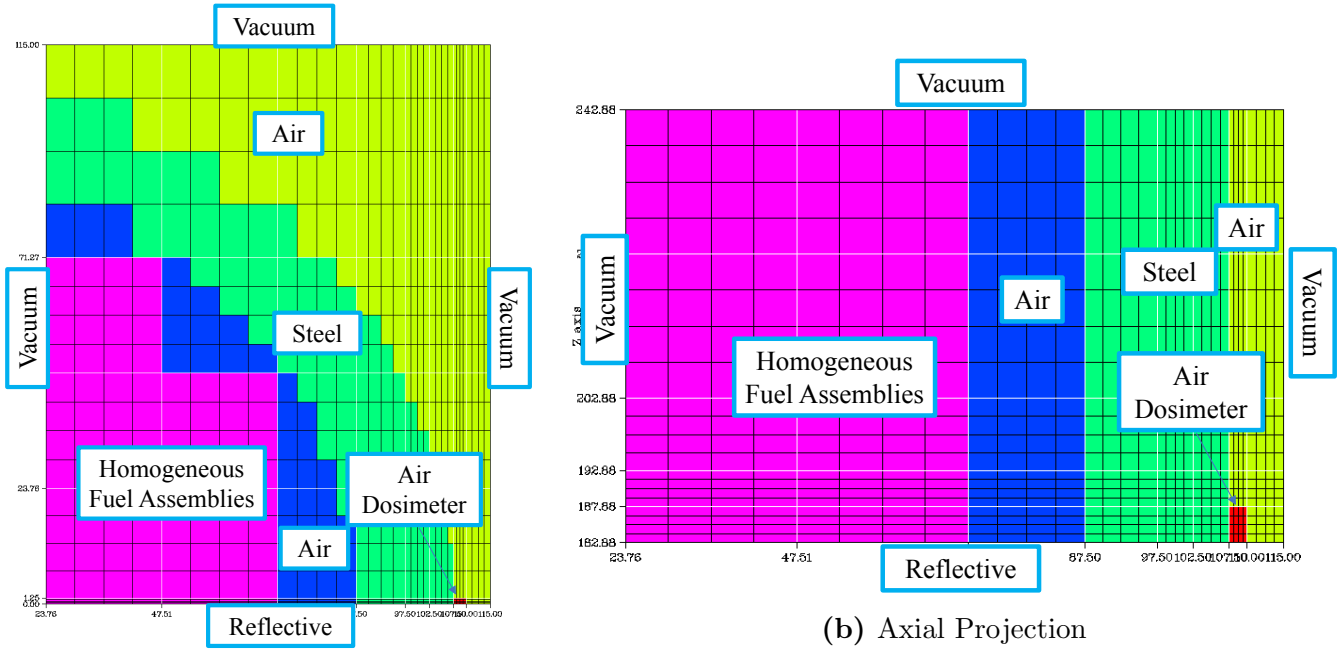

(a) Radial Projection

(b) Axial Projection

Figure H.3 Photon Importance Model for Air Dosimeter: 0-degree Axial Mid-plane

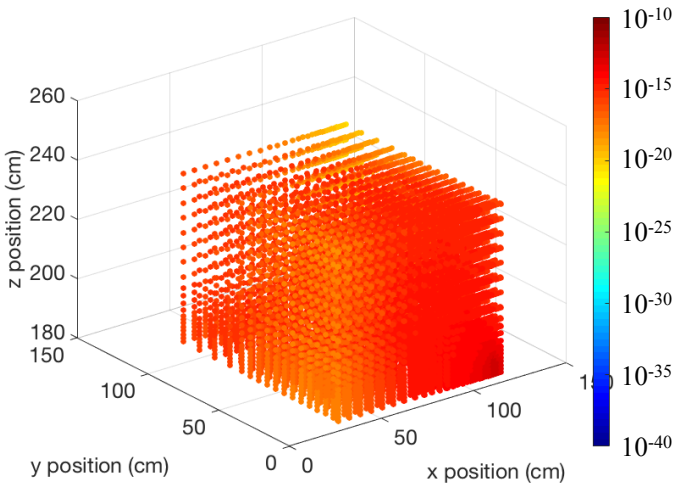

(a) Group 1: 10 MeV <E≤ 14 MeV

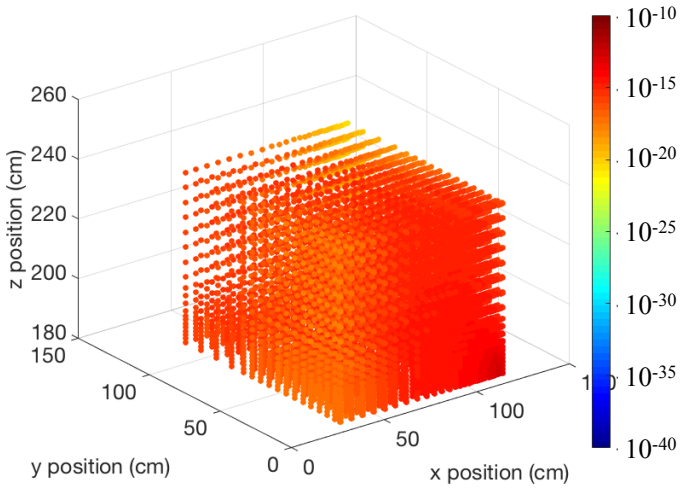

(b) Group 5: 6 MeV <E≤ 7 MeV

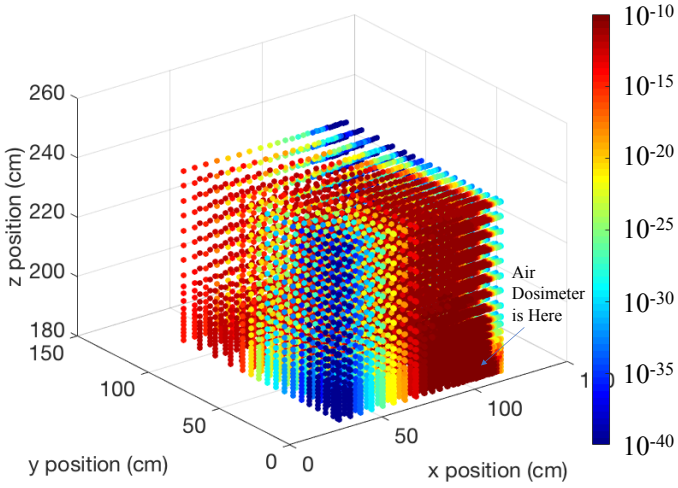

(c) Group 17: 0.1 MeV <E≤ 0.2 MeV

Figure H.4 Photon Importance Function for Air Dosimeter: 0-degree Axial Mid-plane

Appendix I

More Analysis on Radiation Source of SNF from UNF-ST&DARD

In this section, more analysis on the radiation source from the UNF-ST&DARD code system will be discussed.

I.1 Photon Source

The averaged photon source strength in a fuel pellet with various burnup and cooling time for PWR fuel assembly burnup axial level 3/18 is shown in the Fig. I.1. Note that the photon source strength shown here is an averaged value with each fuel pellet. There are 264 (radial) $\times$ 144 (axial) = 38106 fuel pellets. Therefore, the values in Fig. I.1 should be multiplied by 38106 if we wish to compare it with Fig. G.2.

The trend between cooling time of 0 and 5 years should not be linear but an exponential drop. Here, the linear trend is shown mainly because no data point is generated in between. The results show that $\sim$ 2 to 5 orders of magnitude drop on photon source strength after more than 5 years of cooling time comparing to a freshly discharged fuel assembly.

The photon source spectrum for various burnup level with 0 and 10 years cooling time are shown in the Figs. I.2 and I.3. Note that axial level selected here is 9/18.

The photon spectrum becomes slightly softer with increase of burnup with no cooling time. This has explained the decreasing trend of photon DRF coefficients shown in the section G.4. For SNF with more than 5 years of cooling time, the photon spectrum becomes harder with increase of burnup level. This has explained the increasing trend of the photon DRF coefficients in the section G.4. Figs. I.4 and I.5 further show the total photon source strength by various burnup levels with 0 and 10 years of cooling time.

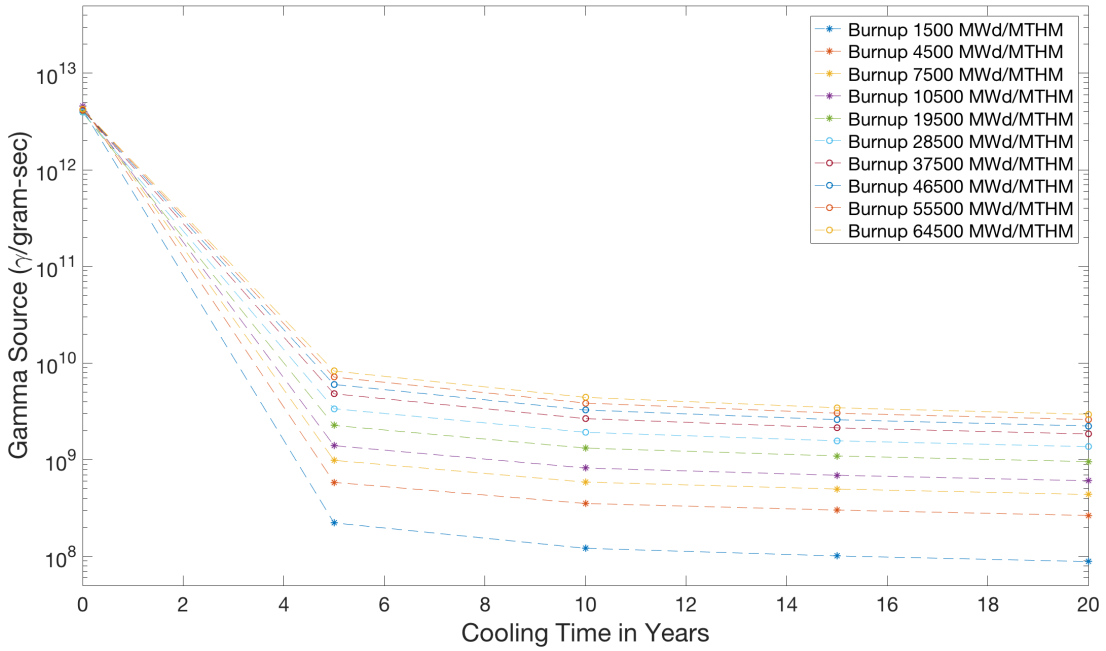

Figure I.1 Averaged Photon Source Strength with Various Burnup and Cooling Time in a Fuel Pellet (Axial Level 3)

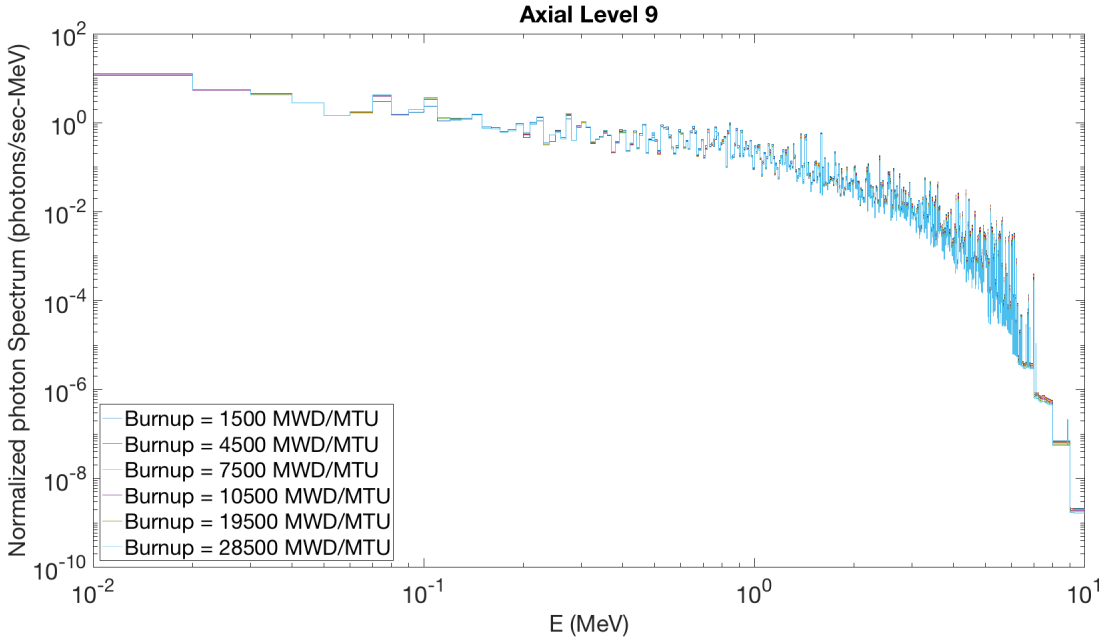

Figure I.2 Photon Spectrum with Various Burnup Level and No Cooling Time (Axial Level 9)

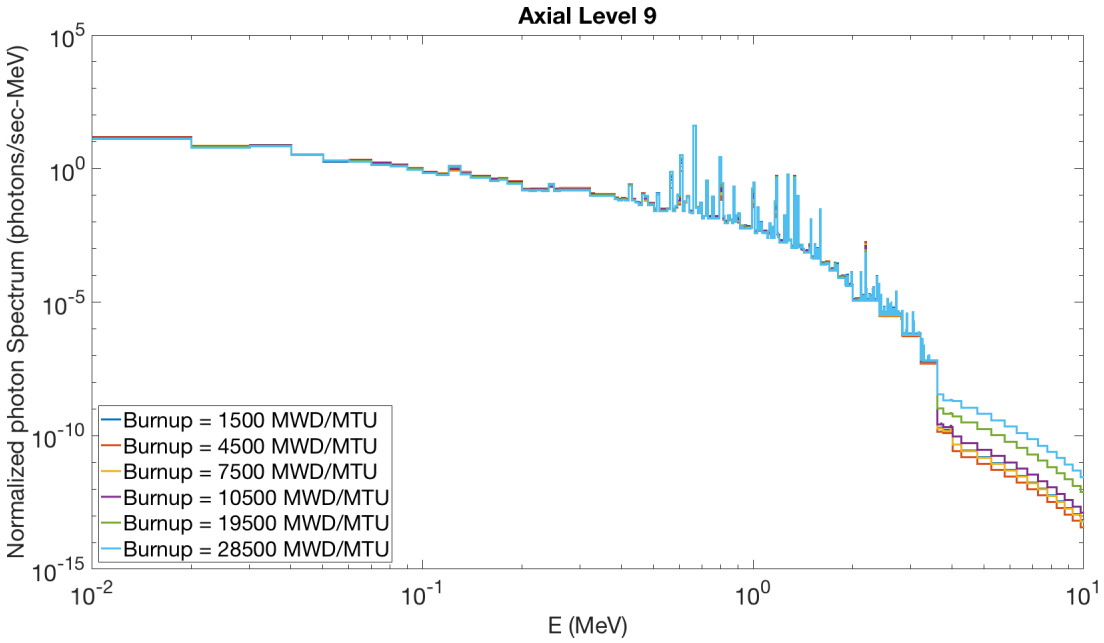

Figure I.3 Photon Spectrum with Various Burnup Level and 10 Years Cooling Time (Axial Level 9)

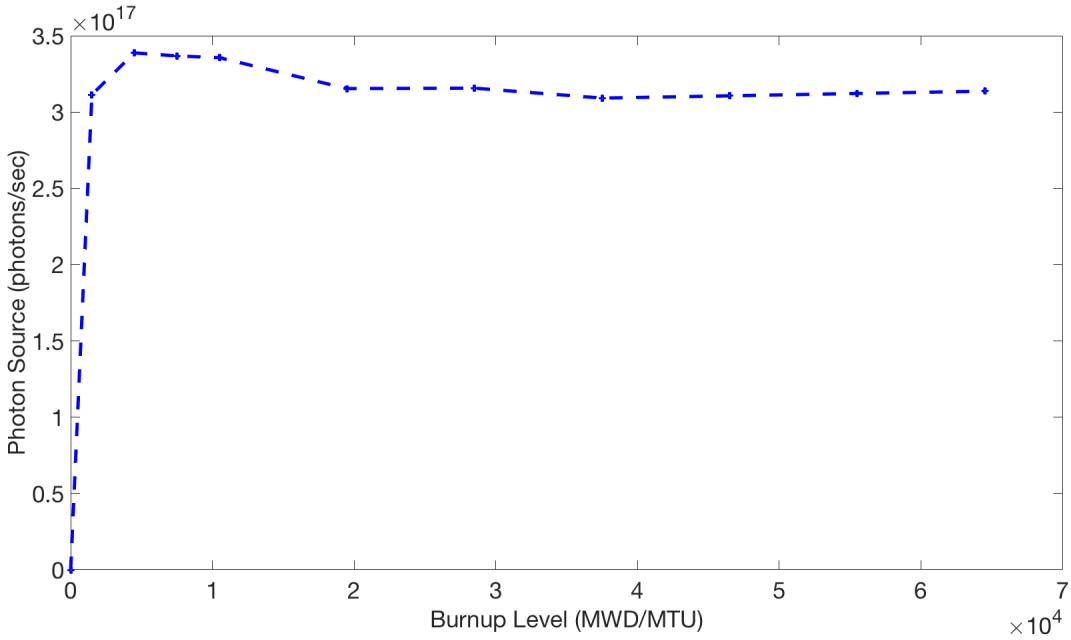

Figure I.4 Photon Source with Various Burnup Level and No Cooling Time (Axial Level 9)

The results show that the photon source strength for no cooling time grows exponentially with burnup level from 0 to 4500 MWd/MTHM, reaches a maximum around 7500 MWd/MTHM,

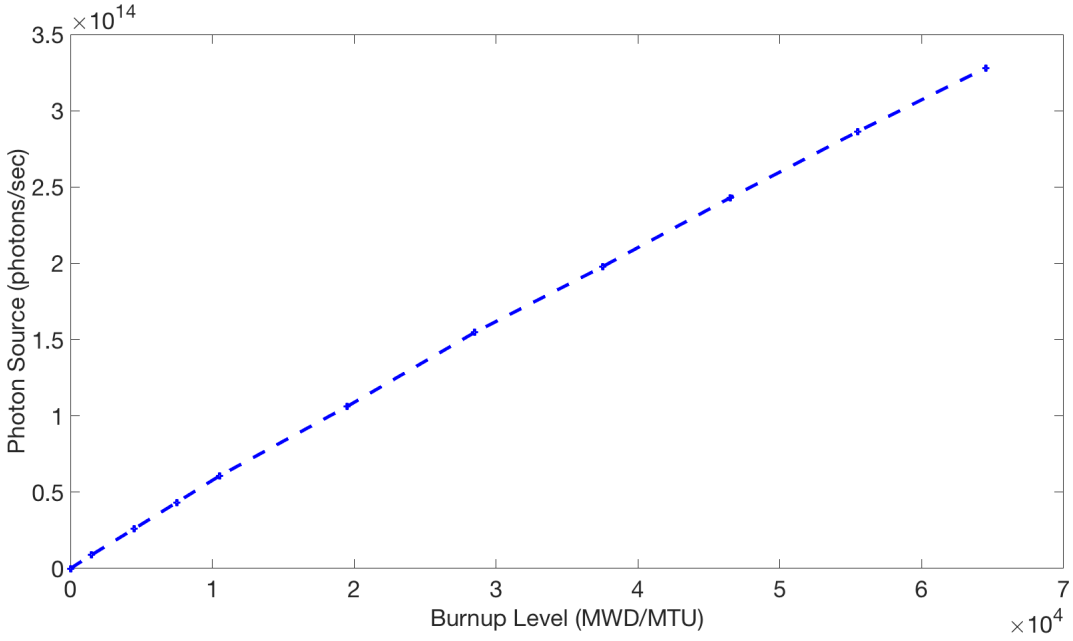

Figure I.5 Photon Source with Various Burnup Level and 10 Years Cooling Time (Axial Level 9)

and decrease slightly then remaining roughly the same for higher burnup values. This is mainly because the photon source generated from fuel activation reaches a steady state after certain burnup value. For the assembly with 10 years of coolingt time, the photon source strengths grows linearly with fuel burnup levels.

I.2 Independent Neutron Source

In this section, more details on independent neutron source from the UNF-ST&DARD code system, SORUCE-4C, and KAERI [6] will be discussed. Table I.1 shows the further quantified details of Fig. 8.4 calculated from the SORUCE-4C code.

Most of the ^{242}Cm, ^{244}Cm independent source contributions are from the spontaneous fission. To further provide more details for analysis, the hal-life and their corresponding decay mode of each nuclides are listed in the Table I.2.

The data shows that the half-life time of ^{244}Cm is much longer than the ^{242}Cm, and therefore it will dominates the independent neutron spectrum for longer time. Potentially, the $^{238}PuO_2$ will dominates the independent neutron spectrum after the ^{244}Cm decays away. However, it will also depend on the atomic density of the heavy nuclides. Note that the ^{241}Pu is only one of the transuranium nuclide that undergoes β-decay. Therefore, presence of large amount of ^{241}Pu is generally not a good news for nuclear system since the β particle can interfere the

Table I.1 Independent Neutron Source Contribution by Nuclide

Case	α source	Target Nuclide	(α,n)	Spontaneous Fission
1	$^{235}U/^{238}U$	$^{17}O/^{18}O$	0.69%	99.31%
2	^{238}Pu	$^{17}O/^{18}O$	84.20%	15.80%
3	^{239}Pu	$^{17}O/^{18}O$	99.96%	0.04%
4	^{240}Pu	$^{17}O/^{18}O$	12.21%	87.79%
5	^{241}Am	$^{17}O/^{18}O$	99.95%	0.05%
6	^{243}Am	$^{17}O/^{18}O$	99.52%	0.45%
7	^{241}Pu	$^{17}O/^{18}O$	99.85%	0.15%
8	^{242}Cm	$^{17}O/^{18}O$	16.20%	83.80%
9	^{244}Cm	$^{17}O/^{18}O$	0.71%	99.29%
10	^{252}Cf	$^{17}O/^{18}O$	$\sim 0.00\%$	$\sim 100.00\%$

Table I.2 α Emitter Decaying Mode and Half-Life Time [6]

Nuclide	Half-Lif Time	α-Decay	Spontaneous Fission	β-Decay
^{238}Pu	87.7 years	$\sim 100\%$	$1.97 \times 10^{-5}\%$	-
^{239}Pu	24110 years	$\sim 100\%$	$3 \times 10^{-8}\%$	-
^{240}Pu	6564 years	99.99943%	0.00057%	-
^{241}Pu	14.35 years	0.25%	-	99.75%
^{241}Am	432.2 years	$\sim 100\%$	$4 \times 10^{-8}\%$	-
^{243}Am	7370 years	$\sim 100\%$	$3.7 \times 10^{-7}\%$	-
^{242}Cm	162.8 days	$\sim 100\%$	-	-
^{244}Cm	18.10 years	$\sim 100\%$	-	-
^{252}Cf	2.645 years	$\sim 100\%$	-	-

electronics and cause damage on them.

Figs I.6 and I.7 further show the independent neutron spectrum of two other different transuranium oxides. For the $^{239}PuO_2$, the spontaneous fission spectrum is very similar to the thermal neutron induced fission spectrum. Potentially, we can use the same DRF coefficient to calculate the dose from spontaneous and thermal neutron induced fission neutrons. This can be further studied in the future.

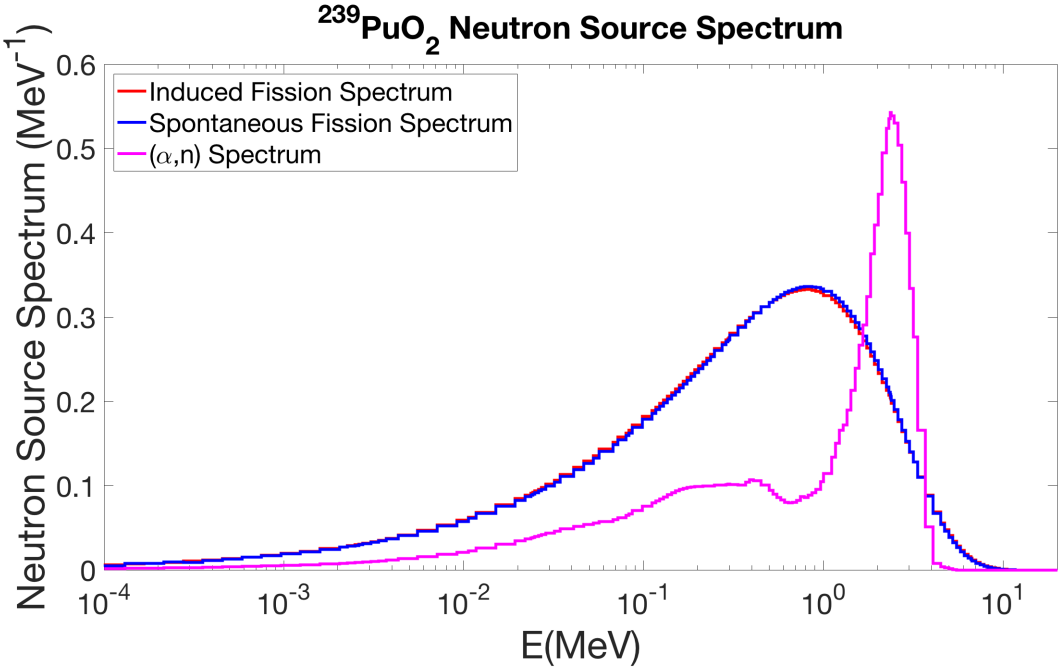

Figure I.6 $^{239}PuO_2$ Independent Source Spectrum

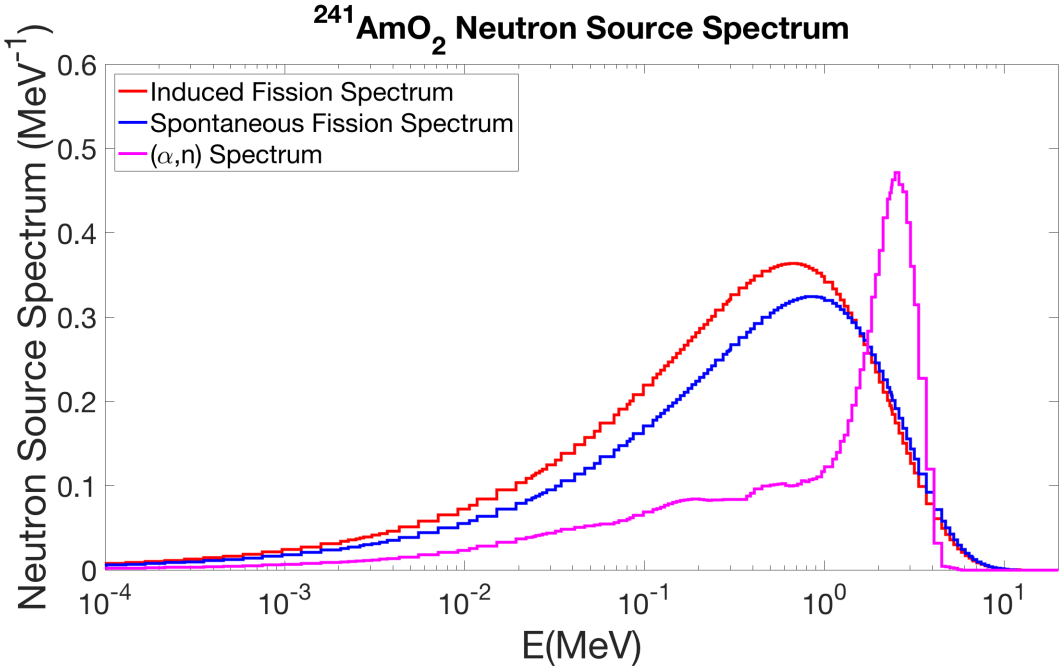

Figure I.7 $^{241}AmO_2$ Independent Source Spectrum

Appendix J

FOV Verification for Dry Storage Cask External Dosimetry

In this section, the FOV for independent neutron source and induced fission neutron source will be verified. The photon source real FOV will not be presented due to limitation of computation resources.

J.1 Independent Neutron Source

Here, the real FOV of independent neutron source for the dosimeter location and cask loading pattern shown in the Fig. 8.25 is presented. Fig. J.1 shows the FOV for the 0-degree and axial mid-plane (axial level 3) air dosimeter. Note that one axial level is 10.16 cm. Two assemblies with 5 axial levels are presented here.

The result shows that almost no contribution is observed from axial level 4 away from the dosimeter ($\sim$ 40 cm away). Further details on slice FOV are shown in the Figs J.2, J.3, and J.4. Note that the air dosimeter is located at the 19/36 overall axial level, which is corresponding to the axial level 3 in Fig. 8.10.

The FOV shows a lower contribution to some locations near the dosimeter. This is mainly because the relative lower burnup level of 37500 MWd/MTHM with smaller independent neutron source strength. The other locations are filled with fuel rods with burnup level of 46500 MWd/MTHM, which has larger independent neutron source, and therefore are making more contribution.

The results show that the FOV estimated by using importance function is appropriate for the dose calculation from independent neutron source.

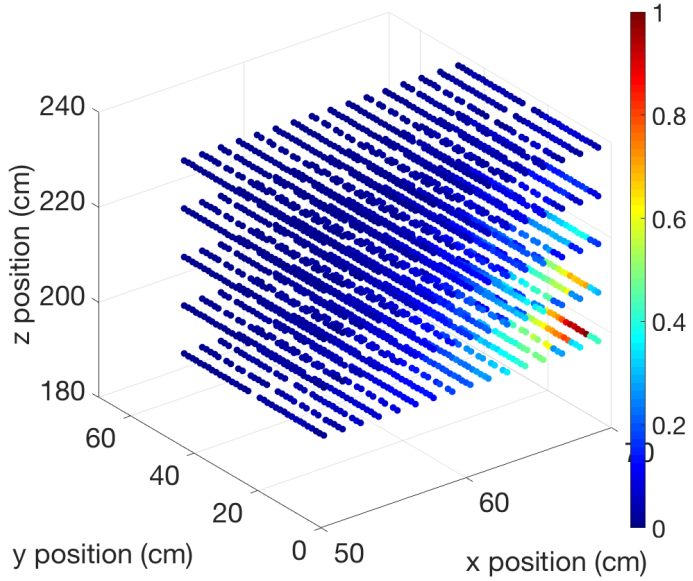

Figure J.1 Real FOV for 0-degree Axial Level 3: Independent Neutron Source (Scaled to Maximum 1)

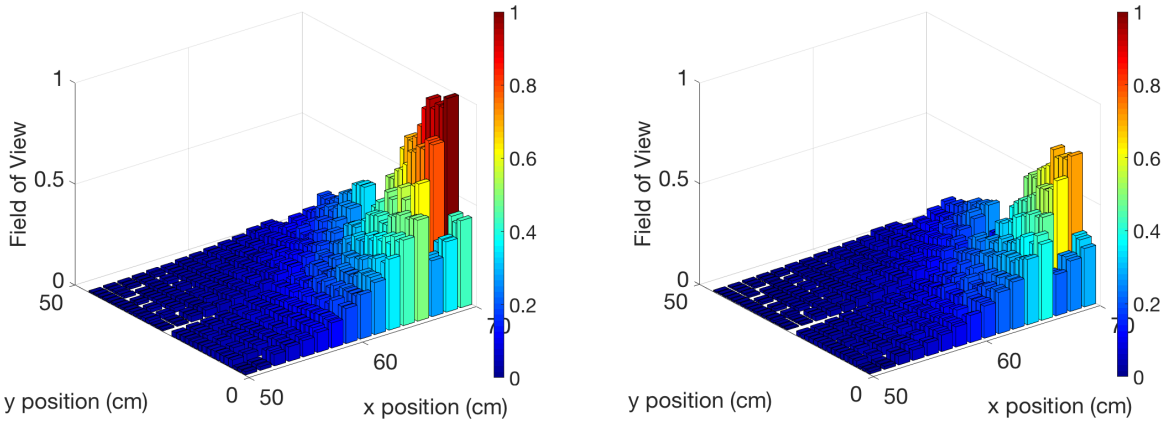

(a) Axial Level 19 **(b)** Axial Level 20

Figure J.2 Real FOV for Dosimeter at 0-degree Axial Level 3: Independent Neutron Source (Scaled to Maximum 1)

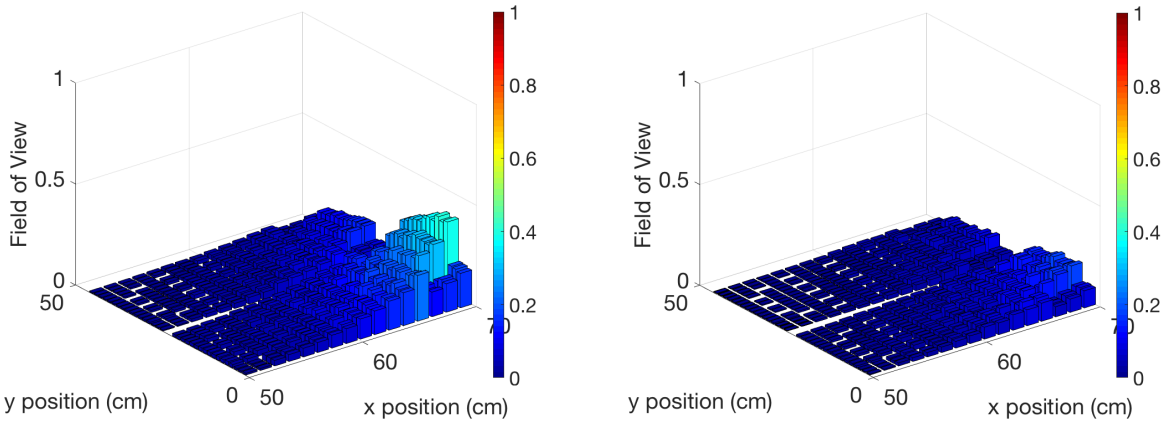

(a) Axial Level 21 **(b)** Axial Level 22

Figure J.3 Real FOV for Dosimeter at 0-degree Axial Level 3: Independent Neutron Source (Scaled to Maximum 1)

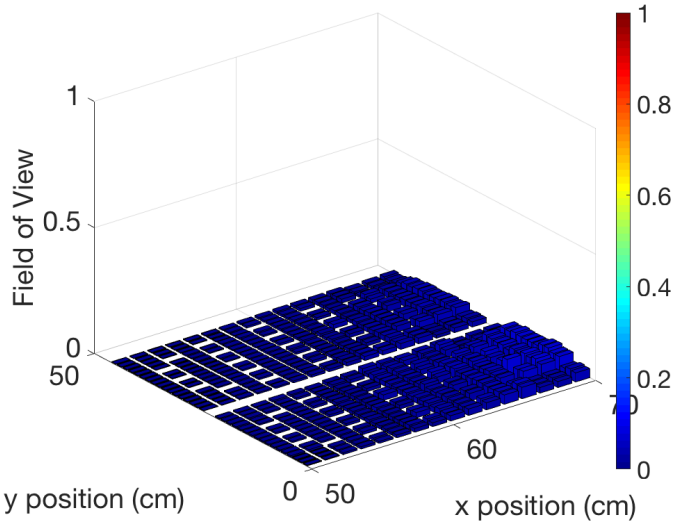

Figure J.4 Real FOV for Dosimeter at 0-degree Axial Level 3: Independent Neutron Source (Axial Level 23)

J.2 Thermal Neutron Induced Fission Neutron Source

In this section, the real FOV of 0-degree axial mid-plane (axial level 3) air dosimeter for thermal neutron induced fission neutron source is presented. Fig. J.5 shows the air dosimeter FOV from fission neutron source. Note that one more axial level is included for fission neutron source comparing to the independent neutron source.

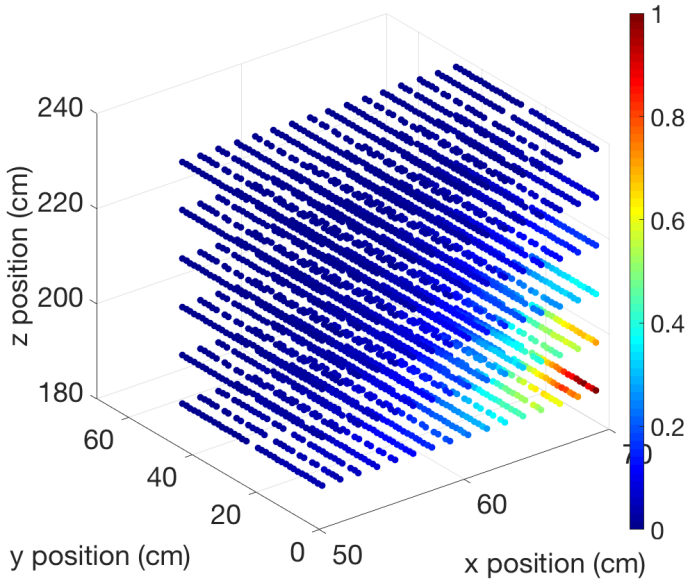

Figure J.5 Real FOV for 0-degree Axial Level 3: Induced Fission Neutron Source (Scaled to Maximum 1)

Similar to the independent neutron source, the contribution from axial level above 22 is considered small. It is also observed that the independent neutron source strength does not affect the FOV shape a lot. The DRF coefficients dominate the trend of FOV. Further detailed slice FOV are shown in the Figs. J.6, J.7, and J.8.

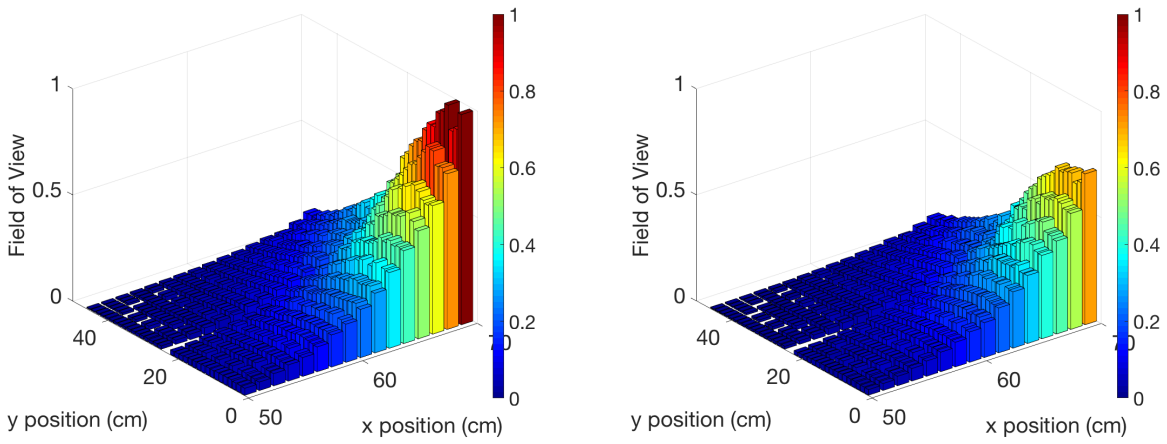

(a) Axial Level 19 **(b)** Axial Level 20

Figure J.6 Real FOV for Dosimeter at 0-degree Axial Level 3: Fission Neutron Source (Scaled to Maximum 1)

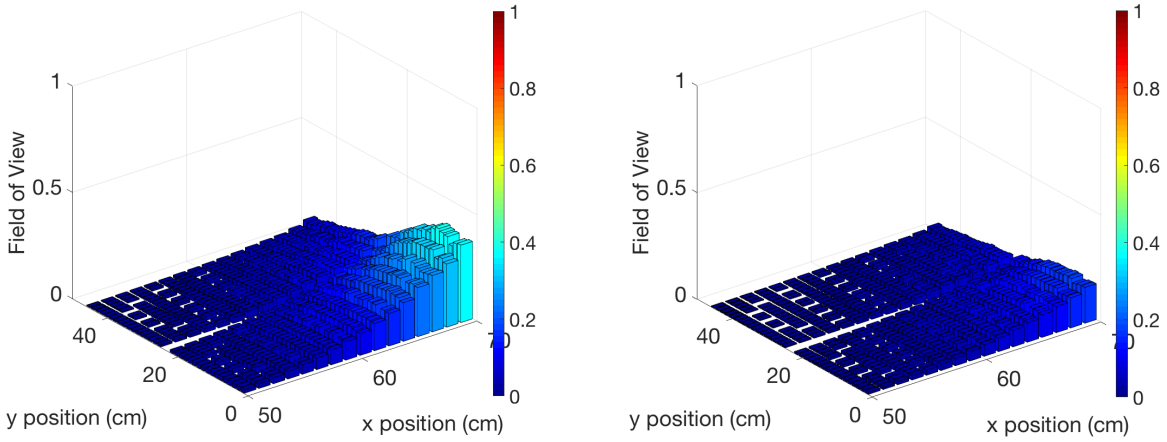

(a) Axial Level 21 **(b)** Axial Level 22

Figure J.7 Real FOV for Dosimeter at 0-degree Axial Level 3: Fission Neutron Source (Scaled to Maximum 1)

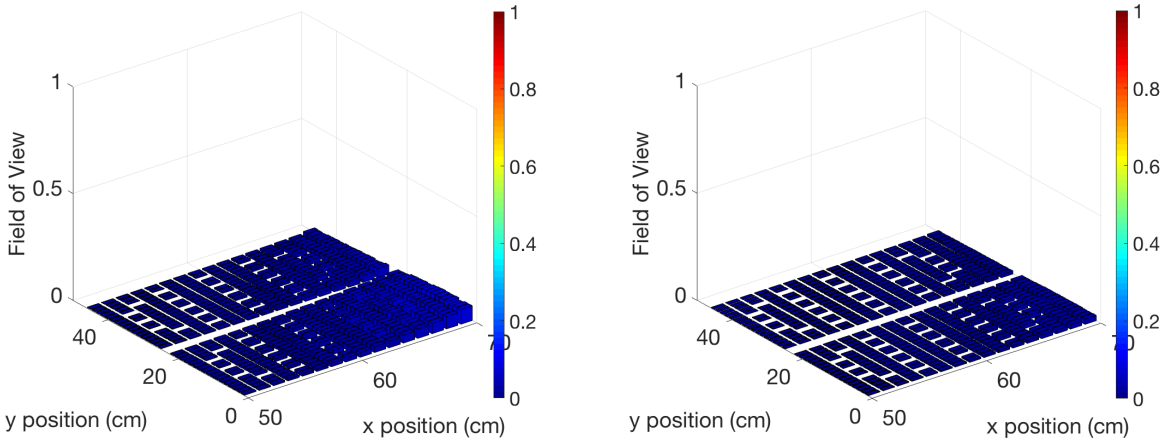

(a) Axial Level 23 **(b)** Axial Level 24

Figure J.8 Real FOV for Dosimeter at 0-degree Axial Level 3: Fission Neutron Source (Scaled to Maximum 1)

Appendix K

Dependency of Photon DRF Coefficient with Location and Energy

In this section, the variation of the photon DRF coefficient by fuel pellet location and energy are studied. Fig. K.1 shows the configuration of the 1D model we have in chapter 8 with fuel pellet ID.

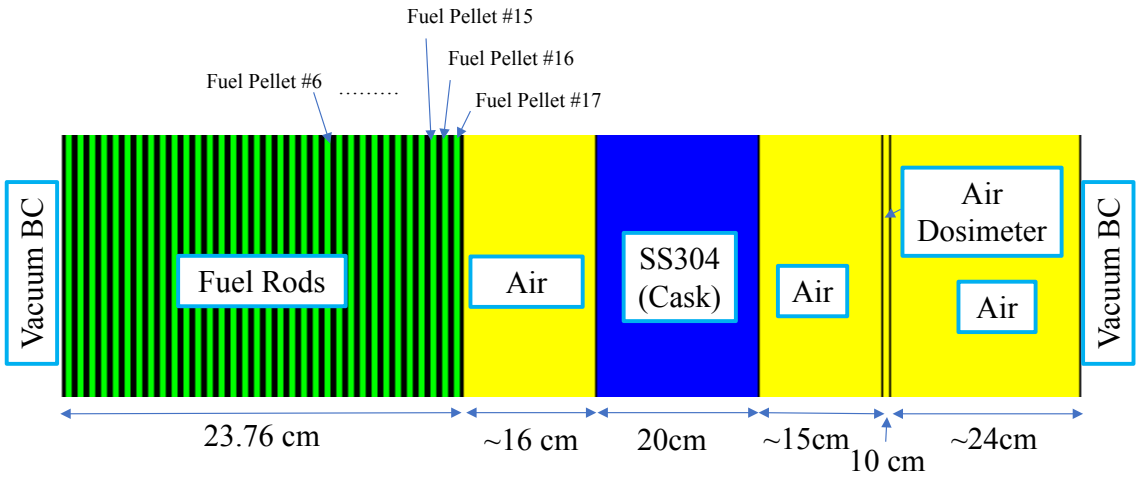

Figure K.1 1D GBC-32 Model with Fuel Pellet ID

The selected fuel composition here is 4 wt% UO_2 fresh fuel. The DRF coefficients are calculated by the MCNP5 code system with use of the CADIS methodology.

Fig. K.2 and K.3 show the trend of DRF coefficient by location and energy of the photon source. Note that the pink line with $\times$ sign is the 17^{th} fuel pellet.

It is observed that for photon with relatively low energy, i.e. 0.75 MeV, the DRF coefficients almost drop 2 orders of magnitude with 4 fuel pellet away. Therefore, most of the dose from

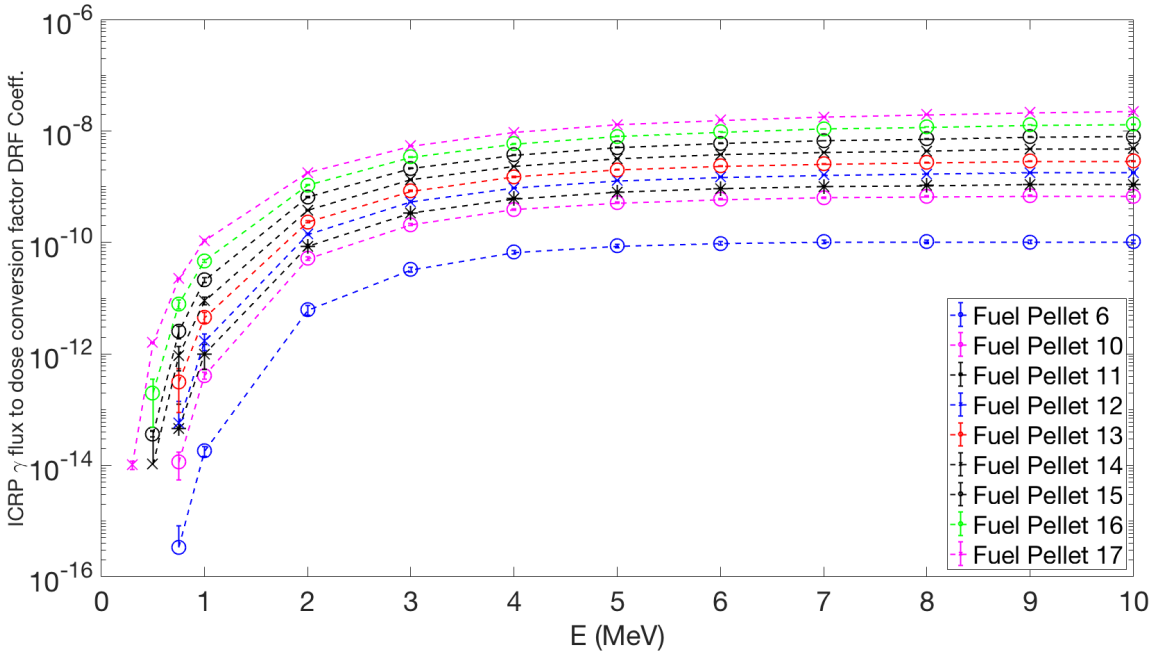

Figure K.2 Dependency of the Photon DRF Coefficients with Location and Energy - 1

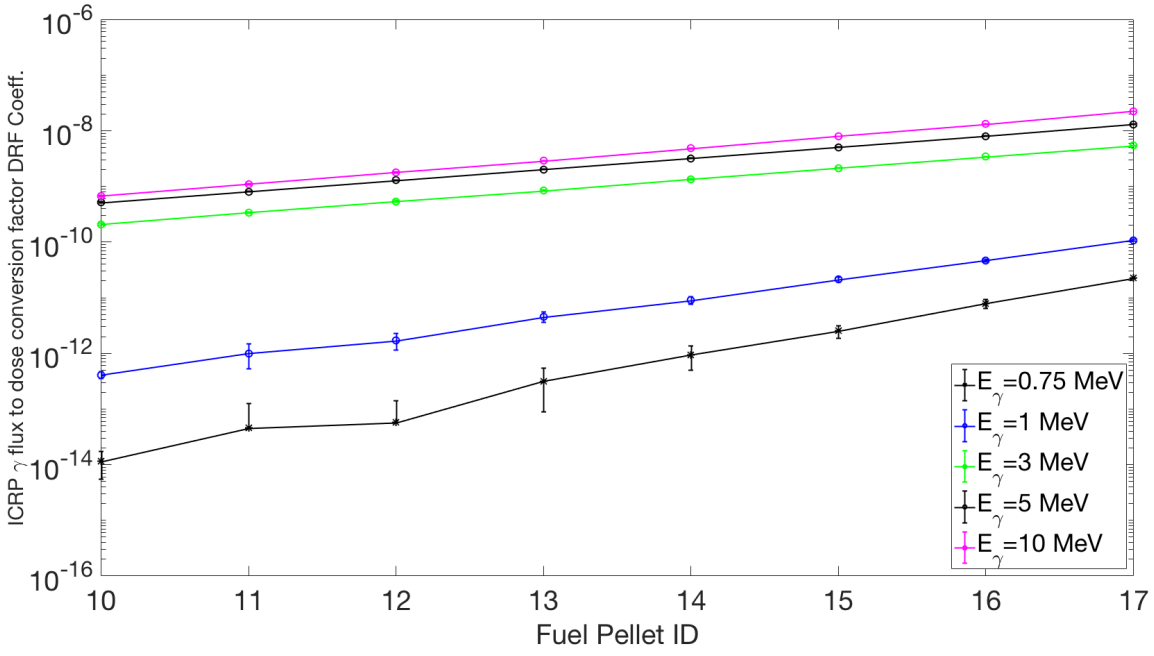

Figure K.3 Dependency of the Photon DRF Coefficients with Location and Energy - 2

photon are from those fuel pellet at the surface of fuel assembly. Fig. K.4 further shows the scaled photon DRF coefficient with maximum of 1.

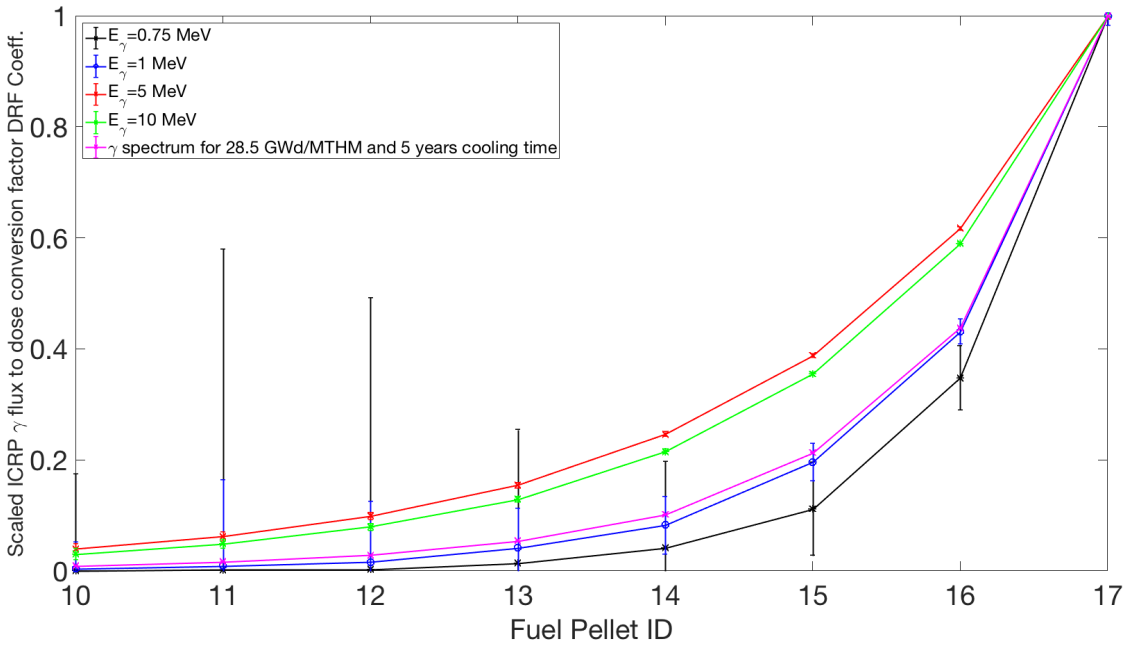

Figure K.4 Dependency of the Photon DRF Coefficients with Location and Energy - 3

The result further verified that only a few fuel pellets from the surface of fuel assembly are the main contributors of photon dose.